Vehicle Performance Analysis & Multi-Physical Optimization based on Innovative KPIs

Guido Napolitano Dell'Annunziata

Supervisors: Prof. Francesco Timpone
Prof. Flavio Farroni

Department of Industrial Engineering
University of Naples "Federico II"

This dissertation is submitted for the degree of
Doctor of Philosophy in Industrial Engineering

March 2023

Life is a game, not a time of slavery, and it's a good game if you play it with a heart open to hope. But one must expect some hard hitting and some tumbles in the mud; but that shouldn't stop him from getting right back on his feet and throwing himself back into the game, with the cheerful determination to play it for his team, and not just for himself. You are members of a large team, the largest ever of its kind, that is, a team of youth and service. Submerging all selfishness and promoting loyal collaboration, ***teamwork is the one that, in the end, will be successful.***

B.P.

To my father
and to my families,
my roots and my lymph

Declaration

I hereby declare that except where specific reference is made to the work of others, the contents of this dissertation are original and have not been submitted in whole or in part for consideration for any other degree or qualification in this, or any other university. This dissertation is my own work and contains nothing which is the outcome of work done in collaboration with others, except as specified in the text.

Guido Napolitano Dell'Annunziata
March 2023

Acknowledgements

This Ph.D. is the synthesis of three years full of experiences, discoveries, changes of course, teachings and skills acquired within the walls of the Industrial Engineering Department of the University of Naples Federico II. But the most important resource of this journey is undoubtedly the people I've had the good fortune to meet along the way, without whom this path would not have the same value. First of all, thanks to my supervisors, prof. Francesco Timpone and prof. Flavio Farroni, thank you for believing in me since the first day of this journey, for guiding and supporting me in the choices of these three years, for the opportunities you have been able to offer me and for the passion for research that you have passed on to me. Thanks to Prof. Valentina Donzella, supervisor of my visiting Ph.D. period abroad, for your welcome and for showing me how it is possible to give technical and human support to your team, running from one commitment to another. How not to thank all my colleagues, the old and new ones, for their constant support and inspiring motivation. Finally, thanks to my family, my lifelong friends, my chiefs and my scouts, you are my safe haven.

Abstract

Understanding and optimizing vehicle performance is a constant challenge in the motorsport environment. Each team tries to find original strategies and procedures to overtake their opponents on the track; precisely for this reason, the world of motorsport has always been a forerunner in the adoption of innovative engineering solutions, favoring a technological transfer toward the common road vehicle market.

In recent years, a lot of effort has been spent developing models able to describe the complex phenomena that occur during races. There are many different factors that affect the performance of a race car, but they can be synthesized into three macro-areas: (1) the vehicle itself with its subsystems, (2) the driver and (3) the external conditions, such as environmental conditions and road roughness. This Ph.D. thesis has been developed with the aim of combining all these relevant factors, exploiting the research outcoming of the last years in all the different areas explored within this work, providing new methodologies to understand vehicle behavior and offering effective procedures to optimize performance.

To achieve this ambitious goal, however, it is not possible to use only data from simulations and indoor tests; even with the most refined models and the most advanced testing procedures, it is very difficult to be able to faithfully reproduce all the interrelated phenomena that take part in defining the performance of a vehicle while it is racing. For this reason, all the activities that will be presented in this work are based on a large amount of

experimental data acquired on track during dedicated test sessions or races; this approach has been chosen to investigate real operating conditions.

In addition, considering the ever-increasing number of sensors installed on the vehicle and the heterogeneity of data to be analyzed, in order to correctly extract the information capable of characterizing the vehicle and its behavior, various data reduction and big data analysis techniques have been applied. In this complex scenario, in which different disciplines play a fundamental role, this work tries to put things in order, proposing innovative tools for studying vehicle behavior and robust procedures for evaluating robust KPIs capable of summarizing the external factors which, more or less directly, influence the two chosen target variables, the tire grip and the tire wear. These two parameters have been chosen because tire management is a key factor for winning races, since the latter are the only components capable of discharging the vehicle's power to the ground. For all these reasons, the thesis flow is structured as follows:

- **State of Art and Background:** starting from the main targets of the work and defining the overall approach and the toughest challenges, a wide literature study is presented, able to provide the main theoretical references used as a basis for the development of the various innovative approaches proposed within the thesis.

- **Tire-Road Forces Estimation:** the study of the interaction between tire and road is undoubtedly the basis from which to start in the study of vehicle performance. To this aim, an evolved version of an existing tool, the T.R.I.C.K. 2.0 has been developed. Thanks to a simple but effective vehicle model, starting from the real outdoor acquisitions, exploiting the most relevant sensors that are generally equipped on a high motorsport car, the tool is able to evaluate with a good level of accuracy the interaction forces, the slip indices and the dynamic camber.

- **Virtual Test Bench for Suspension Setup Optimization:** the suspension system is the main component that ensures the contact of the tires with the ground; for this reason, a further vehicle model has been developed with the intention of replacing the complex and expensive test benches, providing practical indications on how to modify the main parameters suspensions to reach the desired functioning of the wheel group.

- **Driver's Skills Characterization:** starting from data collected from different drivers, on the same vehicle and on the same track, several objective and generalized metrics have been defined to classify their capacity. The procedure developed can be applied in other fields giving useful suggestions about which are the weaknesses of different drivers and defining specific strategies to refine their abilities.

- **Further Phenomena Related to the Performance:** it is not enough to consider only the tire-road forces estimation, the suspension and the driver to have a complete overview of the factors that influence the overall behavior of the vehicle. Other quantities, such as temperatures, tires inflation pressure and contact patches have to be analyzed to understand what is happening during races. In addition, it is necessary to pay attention to the viscoelastic properties evaluation and road roughness characterization. For both these topics, new acquisition methods and processing procedures are presented and new KPIs with their effectiveness are illustrated.

- **Management of Acquired Data and Their Reduction:** a global case study, for which are available all the typology of data previously described, is exposed; after the organization of the dataset, carried out with different methods of data reduction, also the target variables, tire grip and wear, are described in detail.

- **Vehicle Performance Analysis and Optimization:** the influence of the different KPIs on the tire grip and wear is analyzed. In this phase, some techniques have been built in order to find correlations among all these parameters and to highlight mutual dependencies. Thanks to these analyses, it has been possible to find the optimal tire thermal working range, the effect of the roughness on the grip and the possibility to predict the wear, knowing few relevant information.

The obtained results confirm the validity of the chosen approaches, giving a substantial contribution to vehicle behavior overall comprehension and resulting in effective procedures usable to maximize motorsport team performance on the track.

Table of contents

Nomenclature

Acronyms/Abbreviations

ADAS Advanced Driver Assistance Systems

ANSI American National Standard Institute

ARB Anti-Roll Bar

CAN Controller Area Network

CDF Cumulative Distribution Function

CFD Computational Fluid Dynamics

CoG Center of Gravity

CRT Car Real Time

DIMRA Driver Identification and Metric Ranking Algorythm

DMA Dynamic Mechanical Analysis

DoF Degree of Freedom

FEM Finite Element Method

GNSS Global Navigation Satellite System

GPI Geographic Information System

GPS Global Positioning System

GUI Graphic User Interface

HDC Height Difference Correlation

HWR High Working Range

IR Infra-Red

ISO International Organization for Standardization

K&C Kinematic & Compliance

KMA K-Means Algorithm

KPI Key Performance Indicator

LSD Limited Slip Differential

LWR Low Working Range

ODE Ordinary Differential Equation

PCA Principal Component Analysis

PDE Partial Differential Equation

PDF Probability Density Function

PSD Power Spectral Density

RMS Root Mean Square

RWD Rear Wheel Drive

SSE Sum of Squared Error

SWIFT Short Wavelength Intermediate Frequency Tire model

T.R.I.C.K. Tire-Road Interaction Characterization & Knowledge

TPMS Temperature and Pressure Monitoring System

TTSP Time-Temperature Superposition Principle

VESevo Viscoelasticity Evaluation System evolved

WLF William-Landel-Ferry (theory)

General Quantities

α	Slip angle	(rad)
γ	Camber angle	(rad)
μ	Grip	$(-)$
μ_a	Grip due to adhesion contribution	$(-)$
μ_h	Grip due to hysteresis contribution	$(-)$
Ω	Angular velocity	(rad/s)
C_x	Tire braking stiffness	(N)
$C_{y\alpha}$	Tire cornering stiffness	(N/rad)
$C_{y\gamma}$	Tire stiffness with respect the camber thrust	(N/rad)
CP_{Area}	Contact patch area	(m^2)
D	Potential damping energy	(J)
E	Kinetic energy	(J)
F_a	Force due to adhesion contribution	(N)
F_c	Centrifugal force	(N)

F_h	Force due to hysteresis contribution	(N)
F_s	Side force	(N)
F_x	Global longitudinal interaction force	(N)
$F_{y\alpha}$	Cornering force	(N)
$F_{y\gamma}$	Camber thrust	(N)
F_y	Global lateral interaction force	(N)
F_z	Global vertical interaction force	(N)
FP	Friction power	(J/s)
FP_{tot}	Total friction power	(J/s)
g	Gravity acceleration	(m/s^2)
L	Lagrangian function	(J)
m	Mass	(kg)
M_x	Global roll moment	(Nm)
M_y	Global pitch moment	(Nm)
M_z	Global yaw moment	(Nm)
R	Effective rolling radius	(m)
s	Slip vector	(−)
s_x	Slip ratio	(−)
s_y	Slip angle	(rad)
t_p	Pneumatic trail	(m)

T_{Air}	External air temperature	(K)
T_{Inner}	Tire inner liner temperature	(K)
T_{Surf}	Tire tread surface temperature	(K)
T_{Track}	Track temperature	(K)
U	Potential energy	(J)
U_e	Potential elastic energy	(J)
U_g	Potential gravitational energy	(J)
V	Wheel center velocity	(m/s)
v	Forward velocity vector	(m/s)
v_s	Sliding velocity	(m/s)
V_x	x-axis component of the wheel center velocity	(m/s)
V_y	y-axis component of the wheel center velocity	(m/s)
$Wear_{Max}$	Wear maximum value	(−)
$Wear_{Mean}$	Wear mean value	(−)

T.R.I.C.K.

α_{Wing}	Wing inclination angle	(−)
β	Vehicle sideslip angle	(rad)
δ	Steering angle	(rad)
γ_{Stat}	Camber static angle	(rad)
μ	Friction coefficient	(−)

ϕ	Roll angle	(rad)
a	Front wheelbase	(m)
a_x	Longitudinal acceleration	$(\mathrm{m/s^2})$
a_y	Lateral acceleration	$(\mathrm{m/s^2})$
$Area_{Piston}$	Brake piston area	$(\mathrm{m^2})$
b	Rear wheelbase	(m)
C_p	Brake caliper coefficient	$(\mathrm{m^3})$
C_x	Drag coefficient	$(-)$
C_z	Downforce coefficient	$(-)$
d_{Laser}	Distance between rear laser sensors	(m)
F_{ARB}	Force acting on the anti-roll bar	(N)
$F_{B_{Eng}}$	Braking force related to the engine	(N)
F_B	Force related to the brake pressure	(N)
$F_{RollRes}$	Rolling resistance force	(N)
F_{SA}	Force acting on the shock absorber	(N)
F_{Steer}	Steering fictitious force	(N)
F_{WIR}	Wheel rotational inertia force	(N)
H_{Axle}	Axle height from the ground	(m)
H_{Laser}	Laser height measurement	(m)
k_ϕ	Roll stiffness	(N/m)

k_{ARB}	Anti-Roll Bar stiffness	(N/m)
k_{Spring}	Spring stiffness	(N/m)
k_{Tire}	Tire stiffness	(N/m)
k_{Z_0}	Experimental nominal tire stiffness coefficient	(N/m)
k_{Z_C}	Experimental camber coefficient for tire stiffness	(Nrad/m)
k_{Z_P}	Experimental internal pressure coefficient for tire stiffness	(Nbar/m)
k_{Z_V}	Experimental velocity coefficient for tire stiffness	(Nm/s^2)
m	Angular coefficient	$(-)$
m	Vehicle total mass	(kg)
m_v	Vehicle sprung mass	(kg)
MR_{ARB}	Anti-roll bar motion ratio	$(-)$
MR_{SA}	Shock absorber motion ratio	$(-)$
p_{Brake}	Brake pressure	(Pa)
P_{Tire}	Tire inflation pressure	(bar)
p_{xLaser}	Coordinate along x-axis of the laser sensor positioning	(m)
q	Intercept	$(-)$
R	Tire radius	(m)
r	Yaw rate	(rad/s)
R_{Disc}	Disc radius	(m)
$Roll$	Roll angle value for a lateral acceleration of 1 g	(rad)

S_{ARB}	Anti-roll bar displacement	(m)
S_{SA}	Shock absorber stroke	(m)
SC	Sensitivity coefficient for the aerodynamic coefficient	$(-)$
t	Vehicle track	(m)
U	Vehicle longitudinal velocity	(m/s)
V	Vehicle lateral velocity	(m/s)
V_{ref}	Vehicle reference velocity	(m/s)
AD	Anti-Dive coefficient	$(-)$
$Aerodown$	Axle downforce due to aerodynamics	(N)
$Aerodrag$	Axle drag force due to aerodynamics	(N)
AL	Anti-Lift coefficient	$(-)$
AS	Anti-Squat coefficient	$(-)$
$TotalDrag$	Total drag force	(N)
W	Static axle load	(N)

Virtual 7-Post

ϕ	Coordinate of the sprung mass rotation around y-axis	(deg)
σ_s	Shock absorber vertical damping	(Ns/m)
θ	Coordinate of the sprung mass rotation around x-axis	(deg)
a	Front wheelbase	(m)
b	Rear wheelbase	(m)

c	Front track	(m)
d	Rear track	(m)
d_{wire}	Wire diameter	(m)
f	Axial deformation of the spring	(m)
G	Tangential elastic modulus	(Pa)
I	Moment of inertia of section area	(kgm^2)
I_p	Moment of inertia of section area with respect to the neutral torsion axis	(kgm^2)
I_x	Inertia moment of sprung mass around x-axis	(kgm^2)
I_y	Inertia moment of sprung mass around y-axis	(kgm^2)
K_s	Suspension spring vertical stiffness	(N/m)
K_w	Tire vertical stiffness	(N/m)
l	Length of the beam	(m)
M_s	Sprung mass	(kg)
M_w	Unprung mass	(kg)
MR	Motion ratio	($-$)
n	number of turns in a spring	($-$)
R	Average diameter of the coil	(m)
s	Deformation of the spring	(m)
z_G	Coordinate of the center of gravity displacement	(m)

z_r	Coordinate of the road displacement	(m)
z_s	Coordinate of the sprung mass displacement	(m)
z_w	Coordinate of the unsprung mass displacement	(m)

Roughness

α	Magnification	$(-)$
β_M	Slope of the PSD for macro roughness	$(-)$
β_m	Slope of the PSD for micro roughness	$(-)$
δ	Dimension of the Eulerian space	$(-)$
$\Gamma_z(\lambda)$	Auto-correlation function	(m^2)
λ	Wavelength of the road profile	(m)
λ_{macro}	Characteristic wavelength of the road profile at a macro scale	(m)
λ_{micro}	Characteristic wavelength of the road profile at a micro scale	(m)
λ_x	Intersection point of the two scaling ranges	(m)
ω	Frequency	$(1/\mathrm{s})$
ω_{min}	Smallest frequency related to the largest length scale	$(1/\mathrm{s})$
ω_x	Crossing frequency between micro and macro roughness	$(1/\mathrm{s})$
$\Phi(z)$	Height distribution	$(-)$
σ	Standard deviation	$(-)$
$\xi_{\parallel}$	Parallel correlation length, equivalent to λ_{macro}	(m)
$\xi_{\perp}$	Normal correlation length	(m)

$C_z(\lambda)$	Height difference correlation function	(m^2)
C_{1D}	1D power spectral density	($-$)
C_{2D}	2D power spectral density	($-$)
D	Local fractal dimension	($-$)
f	Spatial frequency	(1/m)
$F_0(t)$	Greenwood-Williamson function	($-$)
$F_{3/2}(t_s)$	Greenwood-Williamson function	($-$)
H	Hurst coefficient	($-$)
H_M	Hurst coefficient for the fractal scaling of macro roughness	($-$)
H_m	Hurst coefficient for the fractal scaling of micro roughness	($-$)
L	Sample length	(m)
N_0	Zero crossing density	($-$)
N_p	Number of the peaks of the profile per unit length	($-$)
q	Magnitude of the wave vector	($-$)
R	Sphere curvature radius	(m)
R_a	Center line average	(m)
R_c	Mean height of the profile elements	(m)
R_p	Maximum profile peak height	(m)
R_q	Root mean square	(m)
R_v	Maximum profile valley height	(m)

R_z	Maximum height of the profile	(m)
RS_m	Mean width of the profile elements	(m)
s	Affine parameter	$(-)$
$S(f)$	Power spectral density	$(-)$
t	Normalized gap distance	$(-)$
v	Sliding velocity	(m/s)
X_{tj}	Width of the jth profile element	(m)
Z_{pj}	Height of the jth profile peak	(m)
Z_{tj}	Height of the jth profile element	(m)
Z_{vj}	Depth of the jth profile valley	(m)
Ku	Kurtosis	$(-)$
m	Mean value	$(-)$
$P(h)$	CDF value in correspondence of h	$(-)$
$p(z)$	PDF value in correspondence of z	$(-)$
Sk	Skewness	$(-)$
Sw	Skewness	$(-)$
z	Random variable	$(-)$
z^*	Standardized normal variable	$(-)$

Viscoelasticity

δ	Phase angle or hysteresis	(rad)

ε	Strain	$(-)$
η	Viscosity coefficient	(kg/ms)
ω	Stress-strain frequency	(rad/s)
ω_s	frequency of the damped motion of the VESevo rod	(rad/s)
σ	Stress	(Pa)
σ_c	Equivalent damping coefficient	(Ns/m)
a_T	Temperature shift factor	(K)
C_1	WLF first empirical constant	$(-)$
C_2	WLF second empirical constant	$(-)$
f	Solicitation frequency	(1/s)
J	Creep compliance function	(1/Pa)
K_c	Equivalent contact stiffness	(N/m)
T_g	Glass transition temperature	(K)
T_s	Shifted temperature	(K)
$tan\delta$	Loss factor	$(-)$
E	Relaxation modulus	(Pa)
E'	Storage modulus	(Pa)
E''	Loss modulus	(Pa)
E^*	Complex relaxation modulus	(Pa)
J'	Storage compliance	(1/Pa)

J''	Loss compliance	(1/Pa)
J^*	Complex dynamics compliance	(1/Pa)

Subscripts

0	Static or initial condition
$3RD$	Related to the third element
BR	Related to the anti-roll bar
avg	Average value
BR	Braking phase
BR	Related to the bump rubber
DT	Traction phase
M	Related to the roughness macro scale
m	Related to the roughness micro scale
max	Maximum value
std	Standard deviation
v	Along the vertical direction
x	Longitudinal direction
y	Lateral direction
y	Vertical direction
AD	Related to the Anti-Dive effect
AL	Related to the Anti-Lift effect

AS Related to the Anti-Squat effect

Dyn Relative to the dynamic condition

i Axle subscript: F for Front Axle, R for Rear Axle

j Side subscript: L for Left Side, R for Right Side

Range Range in which the quantity is evaluated

SA Evaluated with the shock absorber formulation

Stat Relative to the static condition

Chapter 1

Introduction & State of art

1.1 Background and Motivation

Finding the best strategy to optimize vehicle performance has always been one of the main targets in the motorsport sector [1]. Clearly, the characteristics of a racing vehicle are defined during the design phases in accordance with the design and other constraints imposed by the regulations, but creating the most powerful and lightest vehicle does not automatically mean being able to win a race or a championship. There are several factors that affect vehicle performance during races, not only strictly related to the car itself but connected also to what is happening around and inside the vehicle. To simplify, three-main categories could be identified to group all the phenomena that occur while driving a vehicle on the track (Figure 1.1), they could be linked to:

- the vehicle itself, with its components and subsystems;
- the driver's skills and behavior on track;
- the external factors, directly related to the specific conditions in which the race takes place.

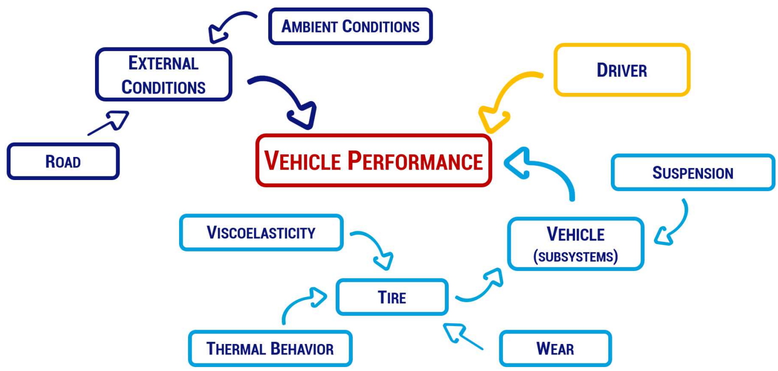

Fig. 1.1 Principal factors that affect vehicle performance

For what concerns the first point, all the components of the cars play a role in the definition of its final performance, trivially contributing to the definition of its overall weight, for example, but even the vehicle capable of generating the most power would not be successful if its interaction with the road is not optimized. The vehicle interaction with the track is ensured by the contact of tires with the road [2]; the holding of this contact is mainly related to the proper functioning of the suspension system that can be modified according to the track condition and topology [3]; for this reason, great attention is paid from the race engineers in the best setup definition, changing the dampers and the springs mounted on the vehicle and varying the tire characteristic angles. In addition, to optimize the tire-road interaction, thus maximizing the force exchanged from the vehicle to the road, it is necessary to understand tire behavior, studying how the tire properties change in different operating conditions. Tires, indeed, are composed of viscoelastic materials and their properties are not fixed, they could exert their maximum potential in a very narrow window, that is a combination of several different factors. In this already complex scenario, drivers have a fundamental role in vehicle management. Although they are generally professional drivers, the analysis of their driving behavior, aimed at identifying their peculiarities and their weaknesses, becomes an important aspect in the definition of diversified strategies capable of seeing the combination of vehicle and driver as a single system. Finally, it is necessary to point out that the vehicle is immersed in a variable environment, and the external conditions can change, also drastically, the ways in which the vehicle is running. Among all the external factors that influence the performance, the most relevant are the air and track temperatures, that influence directly the thermal balance of the vehicle and of the tires, and the track characteristics from a roughness point of view. Road roughness, in fact, has a direct impact on the tire-road interaction phenomenon, being responsible for the maximum friction levels observable on track.

In this articulated and complex context, in which the various factors are mutually dependent, it becomes of fundamental importance to define which are the main indicators that summarize the performance of the vehicle. Following the aim of this work, strongly related to the vehicle dynamics field, the most relevant parameters, that have a direct influence on the car lap-time, are surely the grip exerted by the tires and their degradation, which can be synthesized as the tire global wear.

1.1.1 Multidisciplinary Approach

Vehicle performance optimization is a complex problem that involves different disciplines and fields of application. In the last decades, several theories have been developed to explain and simplify the different phenomena described in the previous paragraph; in fact, it is possible to find different models capable of accurately explaining the viscoelastic behavior of a material [4, 5], different approaches for the study of road roughness characteristics [6, 7], extensive treatises on vehicle dynamics [8, 9], but there are few works in which all these aspects are combined each other with the aim of a complete analysis of all the factors that contribute to maximizing the performance of a vehicle [10]. Even fewer examples can be found in the literature in which this multidisciplinary approach is applied to real data collected on the track during races. This probably derives from the great paradigm shift that has taken place in the last 20 years, during which, thanks to even more powerful computing systems and reduced computational costs, virtual simulation environments have become fundamental for the study and development of reliable models able to represent reality, managing to re-create virtual digital twins in the real systems considered [11]. By combining all these different application fields, adopting different virtual models and using data obtained from simulators, it is quite complex to obtain reliable results capable of explaining with a good degree of approximation what really happens on the track, making it difficult to identify simple but effective strategies to improve performance during competitions. For this reason, the approach followed in the research activities that will be presented in the next chapters makes extensive use of different types of data acquired directly in real operating conditions or during outdoor test sessions and races, thanks to the collaboration with several industrial partners, which is the reason why for most of the results shown are dimensionless for confidentiality. Starting from the experimental data, the main idea has been to develop simple but effective models, tools and methodologies easy to use and applicable also on track, to obtain practical feedback to be used during race weekends. The close collaboration with the industrial partners gave the possibility to understand which are the real challenges with which every motorsport team has to face every day in order to maximize vehicle performance, focusing the research targets on the concrete overcome of the actual limits of the methodology commonly adopted in the motorsport sector.

1.1.2 Data Collection & Data Reduction

Due to the approach chosen, strongly based on the analysis of experimental data, it becomes essential to understand how to manage this large amount of data, extracting only the truly relevant information that can help to analyze the vehicle in maximum performance conditions. High-performance motorsport cars are the pinnacle of automobile technology, they are equipped with hundreds of sensors with a high level of accuracy that monitor every aspect of each vehicle. These devices also allow to transmit all the data in real-time to the team and the amount of data is millions of individual data points. For this reason, in this way, motorsport cars can be seen as rolling sensor networks, constantly gathering and transmitting information about the car and the driver to the rest of the racing team [12].

In the motorsport sector, data analytics influences the design of the cars, how they are driven and how the race is aired. Prior to the adoption of data analytics, the success or the failure of a race was entirely determined by the driver's split-second decisions on the track. By the 1970s, however, telemetry systems had shrunk in size and sophistication to the point where they could be installed in vehicles to provide information about their operation [13]. The amount of data in the motorsport field, connected to the variety of the same, makes the issue considerably complex and, for this reason, Big Data drives big decisions in this application scenario. Big Data locution generally refers to extremely large datasets that may be analyzed computationally to reveal patterns, trends, and associations, especially relating to human behavior and interactions. The opportunities offered by Big Data are undeniable since their main function is to provide the best possible representation of reality through data [14]. This data can be used for the development of every physical quantity in order to improve the vehicle behavior and it can be also used to align all the adjustments with the driver's attitude and his comfort feeling in the car. Since Big Data is a concept, applied to data, which does not conform to the normal structure of the traditional database, the technologies and the algorithms used to process this are innovative methodologies of analysis [15]. Thus, in trying to efficiently extract meaningful insights from such data sources quickly and easily, nowadays analytics has become inextricably vital to realize the full value of Big Data. Every detail can be examined to determine a variety of variables that are collected in data storage. The processing of this data has made it possible to carry out many studies in order to understand how to improve vehicle performance in the motorsport field, according to the different tracks and all the boundary conditions. The raw data collected are integrated into external software in order to create the so-called virtual channels, which represent the original telemetry according to a more understandable structure. Indeed, all the acquired data requires preliminary operations, such as data filtering, to make them more manageable. However, the main difficulty of this data is that even if it is connected to different aspects, it is mutually interrelated [16]. Thus, the telemetry quantities are not the only ones of interest to fully understand the behavior of the vehicle. For this reason, the influence of the track, characterized by its own road roughness, together with the viscoelastic characterization of the tire compound, are both particularly relevant since they greatly influence the performance of the car. It is, therefore, possible to state that automobile motorsport development is becoming ever more data-intensive since cars are evolving into mobile computing and data centers, which become ever more interconnected among each other [17].

The collected data allows motorsport teams to monitor information in real-time, but also to use it in order to simulate the car at different mechanical/aerodynamic conditions for maximizing its performance and to anticipate or investigate problems. The large amount of data, connected to their great variety, however, makes it difficult to extract information from these, especially because the combination of physical quantities of different natures is particularly complex due to the considerable variability dictated by the motorsport field. Hence, Big Data science finds great application in this context.

1.1.3 Target and Research Question

This thesis work aims to investigate almost all the different factors that affect vehicle performance. As already outlined in the previous paragraph, the complexity of this problem lies in the diversity of the phenomena that occur during the races and in the mutual dependencies that arise during vehicle functioning. For this reason, given the large number of data available, it was necessary to develop methodologies that would allow correct data processing by isolating the real information contained within the acquired data. In addition, not all the data obtained are indicative of the vehicle's maximum performance conditions or are not in a format that can be directly used for the purposes of this study, so further data reduction steps were necessary before building a functional database for the purposes of the activity. It is also relevant to point out that the presented activities are deeply linked to the motorsport sectors, but all the approaches used and the findings could be transposed to other scenarios, simply by shifting the performance parameter you want to optimize. If the final target is vehicle safety and passenger comfort, for example, it is still possible to use the tools and the methodology identified during this work, starting from different data and imposing different aims. Also for this reason, all the strategies proposed in this work try to be as simple as possible to broaden their field of application. In this elaborate scenario, the research questions to which this thesis tries to answer in the next chapters are the following:

- Is it possible to evaluate the interaction forces and other relevant quantities with a sufficient approximation starting directly from the data acquired on track? To this end, in Chapter 2 a simple but effective tool is presented; using an 8 DoF vehicle model, starting from several channels generally mounted on high-performance cars and from a detailed vehicle parameterization, different formulations have been built to evaluate tire-road interaction forces, slip indices and dynamic camber variations.

- Is there the possibility to reproduce the behavior of suspension test benches in order to characterize the suspension parameters and identify the best setup conditions? In Chapter 3 a virtual model able to reproduce the functioning of a 7-Post Rig is proposed; this model has been developed using lumped-elements methods, schematizing both the vehicle and the suspension behavior. Its effectiveness is assessed thanks to the presentation of a simple case study, in which several suspension configurations are analyzed.

- Starting from data acquired on track, is it possible to define objective and generalized metrics able to synthesize drivers' behaviors providing a sort of ranking of their abilities? To answer this question, in Chapter 4 an innovative methodology is exposed; using the data acquired from different drivers in the same conditions, several KPIs, related to the quantities acquired, have been obtained. Valuating their relevance, it has been possible to combine them to obtain a proper sorting of their skills.

- How can innovative acquisition and processing methodologies be developed to obtain robust data in actual operating conditions for those quantities not strictly related to the vehicle? In Chapter 5, this aspect is deepened for what concerns tire viscoelastic properties and road roughness characterization, overcoming the most common procedures generally used to obtain this kind of data.

- Given the multitude of data that influence vehicle performance, is it possible to extract the truly relevant information by building a reduced database capable of highlighting the vehicle's maximum performance conditions? To this purpose in Chapter 6, further techniques of data processing and data reduction have been presented, showing how an overall database that contains KPIs of different types which all contribute to the understanding of vehicle performance can be obtained.

- Finally, how the different phenomena analyzed can be combined to obtain practical information and highlight the mutual dependencies? Is it possible to define strategies that can be adopted to analyze the vehicle performance, both in terms of tire grip and wear? In Chapter 7, innovative methods have been defined with the aim to predict tire wear and to determine the optimal tire thermal working range, showing the effective variation of the viscoelastic properties and the effect of road roughness.

1.2 Tire Mechanics

The tire plays a fundamental role in the vehicle dynamics field and many automotive companies spend a lot of time and resources on the development of tire structures in order to improve their behavior when in contact with the road. Therefore, the tires must fulfill several functions [18, 3], such as providing sufficient traction for driving and braking maneuvers or adequate steering control and directional stability. For these purposes, the analysis of the tire mechanics is essential for comprehending the vehicle's performance.

1.2.1 Tire Reference System

An axis reference system needs to be defined to describe the phenomena involved in tire-road interaction and its forces and moments systems arising during the vehicle motion. One of the commonest used axis systems is recommended by ISO855 standard and it is shown in Figure 1.2 [19].

In this reference system, the road is considered flat and non-deformable. The x-axis is along the intersection line of the tire plane and the ground. The tire plane is defined as the plane made by narrowing the tire to a flat disk. The z-axis is perpendicular to the ground and upward, and the y-axis direction is chosen so that the axis system satisfies the right-hand rule.

The tire orientation is defined by two angles. The camber angle γ is the angle between the tire plane and the equatorial plane passing through the x-axis; the sideslip angle α is the angle between the x-axis and the forward velocity vector v, as shown in Figure 1.2.

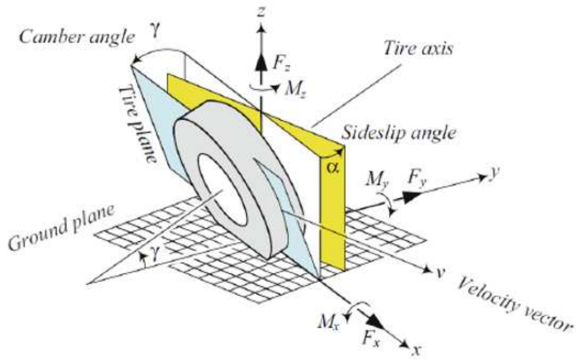

Fig. 1.2 Tire ISO reference system [19]

The resultant force system occurring during the tire-road interaction is assumed to be located at the center of the tire footprint and it can be decomposed along the x, y and z axes. Therefore, the interaction of the tire with the road generates a three-dimensional force system including three forces and moments:

- *Longitudinal force* F_x is the tangential force acting along the x-axis and it is also called forward force. This force is positive during acceleration maneuvers; otherwise is negative.
- *Normal force* F_z is the vertical force normal to the ground plane. It is also defined as wheel load. If the resultant force is upward, this magnitude is positive.
- *Lateral force* F_y is the force tangent to the ground and orthogonal to both F_x and F_z. This force is positive if its application direction matches with y-axis.
- *Roll moment* M_x is the longitudinal moment about the x-axis. It is also called overturning moment.

- *Pitch moment* M_y is the lateral moment about the y-axis and it is known as rolling resistance torque. This magnitude is positive if tends to turn the tire about the y-axis and moves it forward.

- *Yaw moment* M_z is the upward moment about the z-axis and it is defined as aligning moment or self-aligning moment.

1.2.2 Tire Kinematics

Let Q be a point on the rim axis y_c (Figure 1.3). The position of the rim with respect to the flat road depends only on the height h of the point Q and on the camber angle γ.

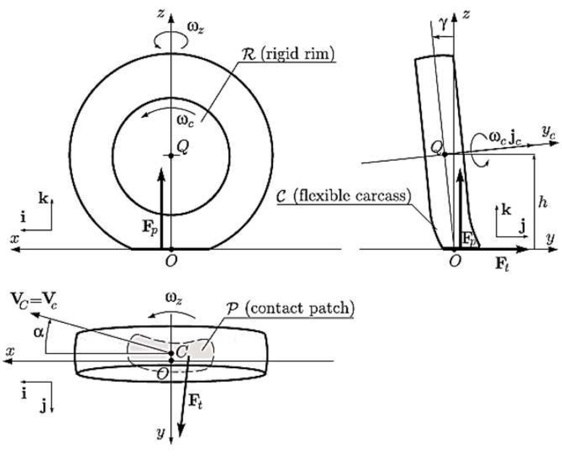

Fig. 1.3 Reference system planes

The latter is the angle between the rim axis and the road plane. The rim, being a rigid body, has a defined angular velocity Ω. Therefore, the velocity of any point P of the space moving together with the rim is given by the well–known equation:

$$V_P = V_Q + \Omega \times \overline{QP} \tag{1.1}$$

where V_Q is the velocity of the point Q and $\overline{QP}$ is the vector connecting Q to P. The three components of V_Q together with the Ω ones are the six parameters that completely determine the rim velocity field. The angle between the velocity V_C corresponding to the center of contact patch, which is parallel to the flat road, and the x-axis of the reference system is called slip angle α. The latter is fundamental in the lateral interaction between the tire and road. In order to describe the wheel motion, it is used to evaluate the following vectorial magnitude, also called slip:

$$s = \frac{V - \Omega \times R}{V_x} \tag{1.2}$$

where V is the wheel center velocity, which is parallel to the flat road, Ω is the angular velocity of the wheel, R is the effective rolling radius and V_x is the x-axis component of the wheel center velocity. The quantity $\Omega \times R$ is defined pure rolling velocity and matches with the wheel center velocity as soon as the tire works in free rolling conditions. Distinguishing the slip components along the x and y-axis, we can define the following magnitudes:

$$\begin{cases} s_x = \frac{V_x - \Omega R}{V_x} \\ s_y = \frac{V_y}{V_x} = \tan\alpha \approx \alpha \end{cases} \tag{1.3}$$

The first quantity is called longitudinal slip, whereas lateral slip is the second one. About the longitudinal slip, it is possible to differentiate the following cases:

- Wheel working in pure rolling condition: there are no differences between the wheel center and each rim point velocity;
- Wheel working in global slip condition (traction phase): the tire rotates among the wheel axis, but the vehicle does not move forward;
- Wheel working in global locking condition (braking phase): the tire behaves as a rigid body during the vehicle-braking phase;

However, taking into account what happens in the contact patch (Figure 1.4), the tire tread usually works in pseudo–slippage conditions.

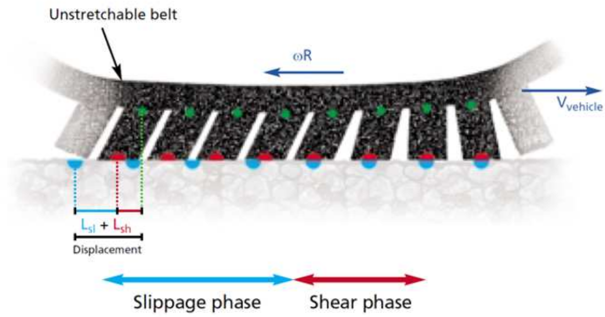

Fig. 1.4 Pseudo-slippage condition

Actually, the tread of a tire is deformable, whereas its belt is not stretchable. Consequently, for example, when a vehicle brakes, the road surface pulls the contact patch backward, but only the tread is distorted. The tread blocks recline, and this outcomes in a relative movement between the bottom of the rubber block, in contact with the road surface, and the belt. This is the shear phase (or pseudo–slippage), which occurs at the leading edge of the contact patch [20]. As the rubber tread block gets closer to the trailing edge of the contact patch, the stress increases and the rubber block, whilst remaining sheared, goes into effective slippage condition with the road surface. This means that a mismatch in the velocity value occurs between the points of the tread in contact with the road (red points, Figure 1.4) and the road surface ones (blue point).

1.2.3 Tire Dynamics

The tire plays a fundamental role in vehicle dynamics which in its turn is subjected to three different types of force fields: the gravitational forces field, the aerodynamic forces and the tire–road interaction forces. The interaction forces field refers to the phenomena occurring in the contact patch between the tire and the road. This field is due to the application of a torque – driving or braking – around the wheel axis and the force applied is transmitted to the road thanks to the tire contact patch. This force–torque system at a given point of the contact patch is statically equivalent to any set of forces or distributed load. Therefore, regardless of the degree of roughness of the road, the distributed normal and tangential loads in the contact patch yield a resultant force F and a resultant torque vector M.

$$
\begin{aligned}
F &= F_x i + F_y j + F_z k \\
M &= M_x i + M_y j + M_z k
\end{aligned} \tag{1.4}
$$

The resultant couple M is simply the moment around the point O, but any other point could be selected. The traditional components of the magnitudes in the Equations 1.4 are the following: F_x is the longitudinal force, F_y is the lateral force; F_z is the vertical load (or normal force); M_x is the over-tuning moment, M_y is the rolling resistance moment and M_z is the self–aligning torque [21, 22]. Thanks to the experimental tests carried out on tires and the physical–analytic models, it is possible to determine the tire–road interaction forces law. These expressions state that the vertical load depends on tire crushing, whereas the longitudinal and lateral forces on the corresponding slip factor, longitudinal and lateral slips, respectively. In the following paragraph, the longitudinal and lateral interactions will be briefly described [23].

Pure Longitudinal Interaction

The tire testing aims at the full identification of the functions that are the relationships between the motion and the position of the rim and the force and moment exchanged with the road in the contact patch. It is meaningful to perform experimental tests for the so-called pure slip conditions. It means setting that the longitudinal and lateral forces depend only on the corresponding slip factors and on the vertical load, whereas the self–aligning moment on the vertical load and lateral slip factor [21, 22, 24].

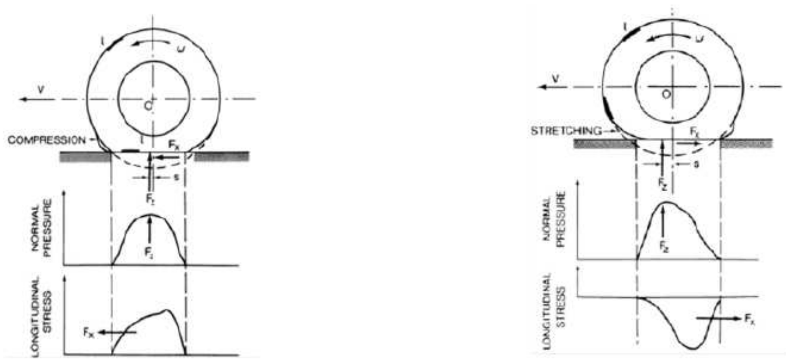

(a) Traction torque (b) Braking torque

Fig. 1.5 Longitudinal interaction physics

To comprehend the phenomena involved in the contact patch during the longitudinal interaction, it is possible to consider a vehicle that is going to brake. If no global sliding takes place on the contact patch, the relationship between the longitudinal force F_x and the longitudinal slip s_x can be considered as linear:

$$F_x = C_x s_x \tag{1.5}$$

where s_x can be $s_{x,DT}$ in traction phase or $s_{x,BT}$ in braking phase. C_x is the tire longitudinal stiffness, often called braking stiffness.

$$C_x = \left.\frac{\partial F_x}{\partial s_x}\right|_{s_x=0} \tag{1.6}$$

In Figure 1.6, the typical behavior of the longitudinal Force F_x as a function of the longitudinal slip under braking conditions, for several values of the vertical load F_z, is shown.

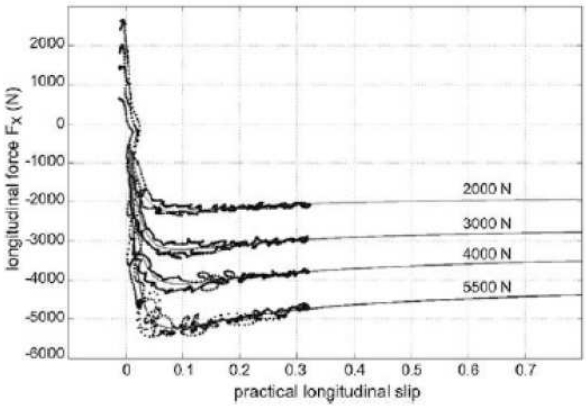

Fig. 1.6 Longitudinal interaction

It is important to point out that the longitudinal forces decrease as a linear function of the slippage ratio in a small range of longitudinal slip s_x. In this case, the longitudinal tire stiffness definition (Equation 1.6) is correct and the tire blocks work in adherence. Moreover, the vertical load influences the longitudinal force F_x: the latter grows less than proportionally with respect to the vertical one. Hence, the global longitudinal friction coefficient μ_x can be defined as the ratio between the value of the longitudinal force and the corresponding vertical load.

Pure Lateral Interaction

When a tire is not subject to any force perpendicular to the wheel plane, it will move along this last; if a side force F_s is applied to a wheel, a lateral force will be developed at the contact patch, and the tire will move along a path at an angle equal to the slip angle α with the wheel plane, mainly due to the lateral elasticity of the tire, as shown in Figure 1.7.

The lateral force developed at the tire/ground contact patch is usually called cornering force $F_{y\alpha}$ when the camber angle of the wheel is zero; the relationship between the cornering force and the slip angle is of fundamental

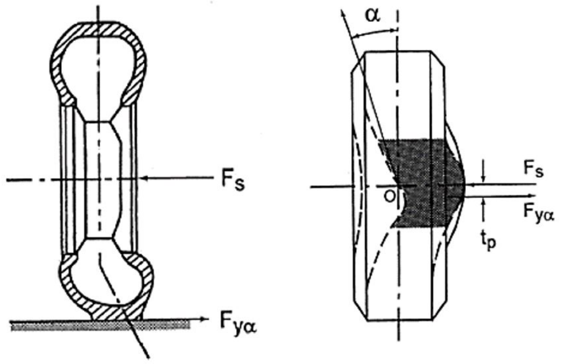

Fig. 1.7 Lateral interaction physics

importance to the directional control and stability of road vehicles. When the tire is moving at a uniform speed, the side force F_s applied at the wheel center and the cornering force $F_{y\alpha}$ developed in the ground plane are usually not collinear: at small slip angles, the cornering force in the ground plane is normally behind the applied side force, giving rise to a torque which tends to align the wheel plane with the direction of motion. This torque is called the "aligning" or "self-aligning torque", and it is one of the restoring moments which help the steered tire return to the original position after performing a curving maneuver. The distance t_p between the side force and the cornering force is called the "pneumatic trail", and the product of the cornering force and the pneumatic trail determines the self-aligning torque. To properly approach a vehicle within a turn, the driver has to act on the steering wheel. Every vehicle taking a turn is subjected to a side force, which tends to force it out of its curve. To keep the vehicle on the path, in each tire-road contact area must arise a centripetal force, F_y, which globally stabilizes the side force. The relationship between the cornering force and the slip angle is of fundamental importance to vehicle handling and stability on the road. Typical plots of the cornering force as a function of the slip angle show that for angles below a certain range, the lateral force is approximately proportional to the slip values.

Beyond them, the cornering force increases at a lower rate with an increment of the slip angle and reaches its maximum value as soon as the tire begins sliding laterally. It is clear from Figure 1.7 that for low slip angle values the lateral force increases linearly. Therefore, the relationship between the friction force and the corresponding kinematic parameter can be expressed as follows:

$$C_{y\alpha} = \left. \frac{\partial F_{y\alpha}}{\partial \alpha} \right|_{\alpha=0} \tag{1.7}$$

where $C_{y\alpha}$ is known as cornering stiffness. This quantity indicates the slope of the curve at the origin of the coordinate axis system. The cornering stiffness generally increases with the load, but the rate of increase declines as the load increases (see Figure 1.8). High-performance vehicles on a dry road will exhibit their maximum cornering ability using large tires operating at relatively light loads. Inflation pressure usually has a moderate effect on the cornering properties of a tire, but in general, cornering stiffness increases with an increase of the inflation pressure.

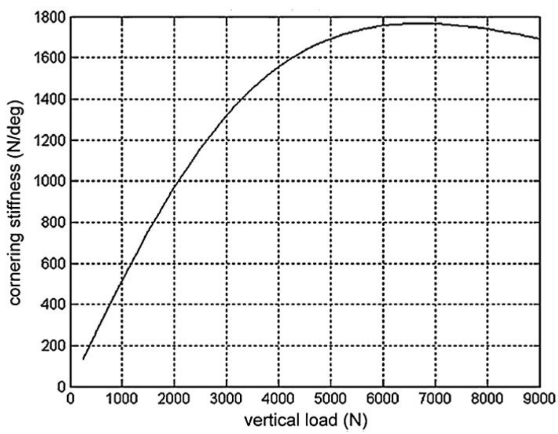

Fig. 1.8 Tire cornering stiffness

However, the relationship between the cornering stiffness and the normal load is non-linear (Figure 1.8); it means that the transfer of load from the inside to the outside tire during a turning maneuver will reduce the total cornering force that a pair of tires can perform, making so possible to act on the under/over steering behavior of the whole vehicle by modifying the value of the roll stiffness, able to manage the load transfers [3].

Camber Thrust

Camber causes a lateral force usually referred to as "camber thrust" $F_{y\gamma}$, and the development of this thrust may be explained in the following way: a free-rolling tire with a camber angle would revolve about point O, as shown in Fig. 1.9; however, the cambered tire in a vehicle is constrained to move in a straight line, developing therefore a lateral force in the direction of the camber in the ground plane. It has been shown that the camber thrust is approximately one-fifth the value of the cornering force obtained from an equivalent slip angle for a bias-ply tire and somewhat less for a radial-ply tire.

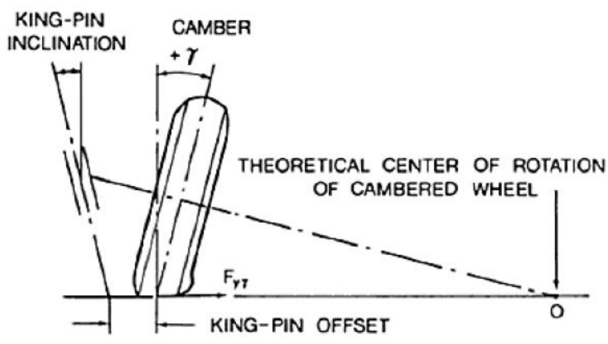

Fig. 1.9 Cambered tire behaviour

To provide a measure for comparing the camber characteristics of different tires, a parameter called "camber stiffness" is often used; it is defined as the derivative of the camber thrust with respect to the camber angle evaluated at zero camber angle:

$$C_{y\gamma} = \left.\frac{\partial F_{y\gamma}}{\partial \gamma}\right|_{\gamma=0} \tag{1.8}$$

Similarly to the cornering stiffness, normal load and inflation pressure have an influence on the camber stiffness. It has been calculated that for truck tires, the value of the camber stiffness is approximately one-tenth to one-fifth of that of the cornering stiffness under similar operating conditions. The total lateral force of a cambered tire operating at a certain slip angle is the sum of the cornering force $F_{y\alpha}$ and the camber thrust $F_{y\gamma}$:

$$F_y = F_{y\alpha} \pm F_{y\gamma} \tag{1.9}$$

If the cornering force and the camber thrust are in the same direction, the positive sign should be used in the above equation. For small slip and camber angles, the relationship between the cornering force and the slip angle and the one between the camber thrust and the camber angle are essentially linear; the total lateral force of a cambered tire at a slip angle can, therefore, be determined by:

$$F_y = C_{y\alpha}\alpha \pm F_{y\gamma}\gamma \tag{1.10}$$

As discussed previously, the lateral forces due to slip angle and camber angle produce a torque, but the component due to slip angle, however, is usually much greater and mainly responsible for the aligning torque acting on tires in ordinary driving conditions.

Interaction between Tangential Forces

In the discussion about the cornering behavior of tires, the effect of the longitudinal force has not been considered. However, quite often both the side force and the longitudinal force are present, such as braking in a turn. In general, tractive (or braking) effort will reduce the cornering force that can be generated for a given slip angle; the cornering force decreases gradually with an increase of the tractive or braking effort. At low values of tractive (or braking) effort, the decrease in the cornering force is mainly caused by the reduction of the cornering stiffness of the tire. A further increase of the tractive (or braking) force results in a pronounced decrease of the cornering force for a given slip angle. This is due to the mobilization of the available local adhesion by the tractive (or braking) effort, which reduces the amount of adhesion available in the lateral direction. It is interesting to point out that if an envelope around each family of curves of Figure 1.10 is drawn, a curve approximately semi-elliptical in shape may be obtained. This enveloping curve is often referred to as the friction ellipse.

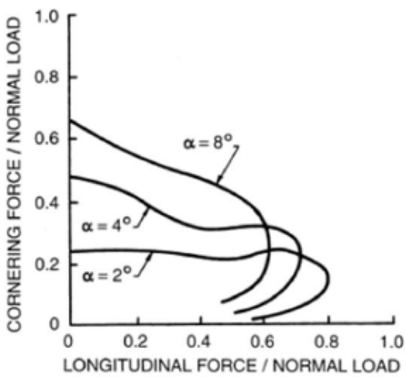

Fig. 1.10 Effect of longitudinal force on the cornering characteristics.

The friction ellipse concept is based on the assumption that the tire may slide on the ground in any direction if the resultant of the longitudinal force (either tractive or braking) and lateral (cornering) force reaches the maximum value defined by the coefficient of friction and by the normal load on the tire. However, the longitudinal and lateral force components may not exceed their respective maximum values $F_{x,max}$ and $F_{y,max}$, as shown in Figure 1.11. $F_{x,max}$ and $F_{y,max}$ can be identified from measured tire data and constitute respectively the major and minor axis of the friction ellipse.

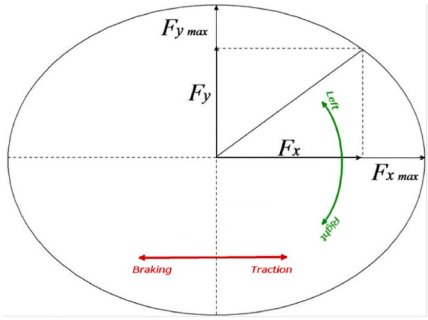

Fig. 1.11 Friction ellipse

The ellipse can be expressed also in terms of friction coefficients, also known as grip, defined as:

$$\mu_x = F_x/F_z \tag{1.11}$$

$$\mu_y = F_y/F_z \tag{1.12}$$

In which μ_x is the longitudinal static friction coefficient and μ_y is the lateral static friction coefficient.

1.3 Tire-Road Interaction Forces Estimation

One of the main challenges of vehicle dynamics is the accurate estimation of tire-road interaction forces. If available, such information could be harnessed in many favorable ways, e.g.: i) the enhancement of passenger safety and comfort, which is crucial these days especially with the advent of autonomous and semi-autonomous systems; ii) the maximization of vehicle and tire performance in high-end and motorsport applications.

Many studies have been conducted on this matter, featuring a wide variety of techniques. A rather common approach is the use of estimators and/or observers to obtain tire forces and slip angles from a number of easy-to-retrieve measurements and suitable vehicle and tire models [25, 26]. [27]

proposes an offline regression of force versus slip data (at given normal force and road surface) obtained from an Extended Kalman-Bucy Filter to estimate friction coefficient through a nominal tire model. In [28], an adaptive parameter estimator is put in place to discern different surfaces according to friction thresholds. In [29] tire forces and sideslip angle are estimated in real-time, accounting for nonlinearities by building and comparing an Extended Kalman Filter-based and an Unscented Kalman Filter-based estimator [30]. In [31], two models are employed for low and high frequencies in order to better capture dynamic changes of the slip angle. [32] focuses on the estimation of pneumatic trail as an early indicator of approaching lateral force peak. [33] uses optimal linear parametrization to fit a nonlinear Burckhardt tire model and obtain the tire-road friction coefficient. In [34], tire-road friction coefficients are estimated at individual wheels using a recursive least-squares parameter identification and testing outcomes using different hardware strategies.

While a tire model is required in most cases, it inevitably convoys inaccuracies, since at best the tire model is a suitable-enough approximation of the tire behavior. Within this perspective, in [35] a neural network with online parameter estimation is used to compensate model uncertainties. [36] presents a hybrid estimator using a combination of an Extended Kalman Filter and a neural network structure, with no tire road friction model, with simulation results showing a good ability to estimate lateral forces and grip potential.

Different sensor setups have been explored to perform estimation with a variety of measurements. For instance, [37] developed an estimator using yaw rate, longitudinal/lateral accelerations, steering angle and angular wheel velocities, all obtained from sensors that are already integrated in modern cars. Such sensors are also exploited in [38], which develops a two-stage Kalman Filter-based arrangement. Wheel rotational speeds and torques are required in [39] to obtain longitudinal and lateral tire-road force estimates. [40] presents an intelligent tire system with a tri-axial acceleration sensor installed onto the inner liner of the tire. Neural network techniques are used to then estimate tire forces thanks to a training procedure using a Flat-Trac test platform [41]. A similar approach is proposed in [42]. [43] incorporates a differential GPS in the traditional sensor setup to estimate velocities. [44] combines elementary diagnosis tools and new algebraic techniques for filtering and estimating derivatives of noisy signals, including the estimation of lateral forces from vertical force estimates using Kamm friction circle theory.

Another approach, based on the principle of using the vehicle as a moving lab, is tried out in [45], proposing the identification tool denoted as T.R.I.C.K. (Tire/Road Interaction Characterization & Knowledge) comprising of a vehicle model which processes experimental data and virtual sensor measurement to compute a number of virtual telemetry channels - thus providing quantitative insight on steady-state tire-road interaction. The scientific validity of the approach used lies in the development of a simple model, in which the main physical relationships for the study of vehicle dynamics have been implemented. The validation of the tool outputs has been carried out with the experimental data obtained from very expensive sensors that, for this reason, are generally not mounted during ordinary test sessions. [46] uses T.R.I.C.K. as a basis for another force estimation method that also accounts for the interaction between sprung mass and unsprung mass. In [47] the authors propose a slight expansion of T.R.I.C.K. with an improved estimation of roll angle and aerodynamic-related forces. To do so, laser sensors are introduced to measure the distance between the road and relevant locations on the vehicle during motion, similarly to [48] and [49] which are however related to two-wheeled vehicles. Adopting the same methodology used in the T.R.I.C.K., this thesis work proposes a wide extension of the tool adopting innovative sensors and formulas, as already presented in [47].

1.4 Vertical Ride Modeling

In the last years, suspensions have played a fundamental role in the motorsport and automotive industry. The growing need to reproduce with a high level of detail the phenomena concerning vehicle dynamics has given a strong impulse to the research in this field. One of the main tools for maximizing vehicle performance is the correct use of the suspensions which derives from the ability to predict its behavior in different working conditions; hence the need to build models capable of providing indications for the optimization of suspension setup, a key factor in the definition of the best setup of the whole vehicle. In order to study the vertical ride behavior of a vehicle, it is necessary to model properly both suspensions and tires; for their constitutive nature, it is simpler to schematize with a high level of accuracy the suspension systems using, for example, lumped-elements models whereas different strategies can be adopted to model tires, depending on the specific modeling goals.

To this aim, in the last decades, several tire models have been developed to reproduce faithfully vertical ride and the tire response on uneven roads [50–52] (Figure 1.12).

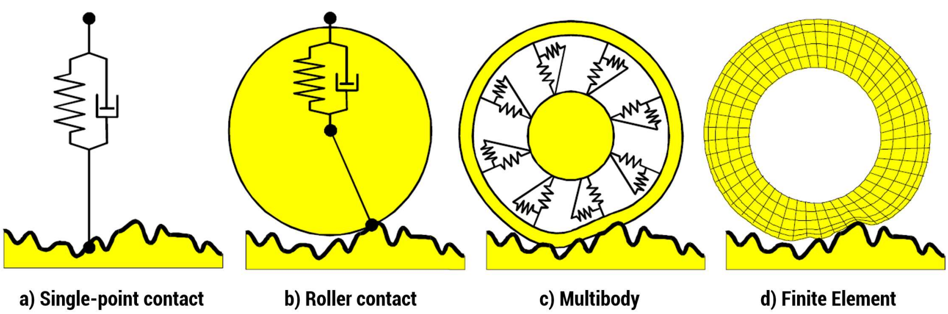

Fig. 1.12 Vertical ride models

The most extensively used model is the single-point contact model [50]; it is generally represented by a spring and damper in parallel. This approximation is valid for long wavelengths and gradual slope surface irregularities [53]. This model can be used on surfaces with random unevennesses generated by filtered white noise. Rolling over discrete obstacles (e.g. cleats) gives too high accelerations of the tire with a point contact model. Slightly increasing the complexity of the model, it is possible to find the roller contact model that consists of a rigid wheel rolling over the obstacles and one spring and damper. There is only one contact point, neglecting the special cases of road geometry where the rigid wheel has more than one contact point with the road. The contact point is not restricted to lie directly beneath the wheel axle. Small wavelength bumps are filtered out by this model and its representation is better than the single-point contact model [54, 55].

Another approach consists of the representation of the tire by means of a certain number of nodes physically interconnected to reproduce the degrees of freedom and constraints of the real structure [20, 56–58], normally denotes as multibody models. In the flexible ring model [59], also the tread-band is considered, which is modeled as a deformable beam, and radially and tangentially distributed sidewall stiffnesses. Owing to the bending of the tread-band the vertical stiffness in the center of the contact patch is lower than the stiffness at the edges of the contact patch. Even without the non-linear sidewall stiffnesses, this model is able to show the typical dip in the vertical force while rolling over cleats. The toroidal membrane tire model [53] is also classified as a flexible ring model. The flexible ring model is also indicated as adaptive footprint model as the deflection of the flexible carcass provides the model with an adaptive footprint. According to Kim et al. [60] and Oertel and Fandre [61] the SWIFT model [62–65], the FTire model [66] and the CDTire [67] are among the most commonly adopted multibody models in the automotive field, useful to study dynamic phenomena as braking, cornering, and driving on uneven pavement surfaces [68]. The SWIFT model is represented by means of a rigid ring model, able to describe the tire belt behavior, connected to two tire–road interaction sub-models by means of stiffness elements: an enveloping model to take into account of the road unevenness and a slip model. The SWIFT model aims to represent the tire dynamic behavior up to 100Hz range, where the tire belt remains quasi-rigid and circular. Finally, there are the finite elements models (FEM). These models are based on a detailed description of the tire structure and they can be used directly to calculate the dynamic forces of the tire rolling over obstacles at high velocities [69–71]. This type of models give the most reliable results, but they are high time-consuming and require a high computational cost. In particular, single-point contact and roller contact models can be easily used for real-time applications, such as hardware-in-the-loop and driver-in-the-loop, whereas for multibody and finite element models this is not always true, but depends by the model complexity.

For the purpose of this thesis, that was strictly related to suspension analysis and setup optimization, it is not necessary to use the more complex models which required a detailed tire schematization. In order to develop a tool that could be effectively used also on track to give fast feedback also during a race weekend, the simple-point contact model is adopted. In the Chapter 3 will be shown the effectiveness of the proposed approach.

1.5 Driving Style: Its Relevance and Applications

The study of the style of drivers is a topic of great interest that concerns various fields of application. It is important for the development of Advanced Driver Assistance Systems (ADAS) and of autonomous vehicles, to make predictions and statistical studies on road accidents or traffic, but also to find the right car configuration suitable for a driver for a track race. There are many studies in the literature, also listed below, that deal with the aforementioned areas, but the topic on which this work focuses is slightly different as it mainly investigates the differences between professional and non-professional drivers, whereas taking into consideration aspects of the driving style that are common

to the different research fields described above.
The reason for this interest lies in the importance that driving style has in the field of track racing, in fact it and all the features related, such as trajectories taken and the use of the pedals and steering, are decisive for the outcome of a lap on the track. The performance of a driver can be classified according to his driving style and this can also allow making a prediction on what the results will be in terms of lap time. Furthermore, knowledge about the differentiating skills between racing drivers and non-racing drivers could be useful for developing targeted training for amateur drivers based on what mistakes they usually make, but also professional drivers can benefit from it to identify what their weak points are and improve them. Due to the growing interest in the automotive and motorsport industries, many studies have been conducted on the analysis of pilots' driving style [72–74], although not many focus on the comparison between professional and amateur drivers, as this work does.

Analyzing the methodologies commonly adopted in this research field, the first criticality encountered was the lack of a consistent sample of field data, coming from laps ridden on track. This aspect can be noticed in the study of the pilots' style proposed by Segers [1], analyzed from different points of view, like comparisons of the use of steering wheel and pedals, but without a consistent amount of data to support the research from a statistical perspective.

Taking inspiration from Segers' work, in [75] the authors identify some metrics to classify drivers, in order to compare professional race drivers with a software developed for autonomous driving. The classification is based on acceleration, braking, gear shifting and steering with the aim of evaluating performance, smoothness and response for different corners, laps, or tracks. However, these metrics are used to highlight the differences with a software and not between professional and non-professional pilots. Another study involving a driving simulator is the one presented in [76], the authors developed the Driver Identification and Metric Ranking Algorithm (DIMRA) as a data-based method that, through the use of a set of lap-based metrics, allows objective judgment and identification of different drivers and enables to separate their driving styles using clustering methods.

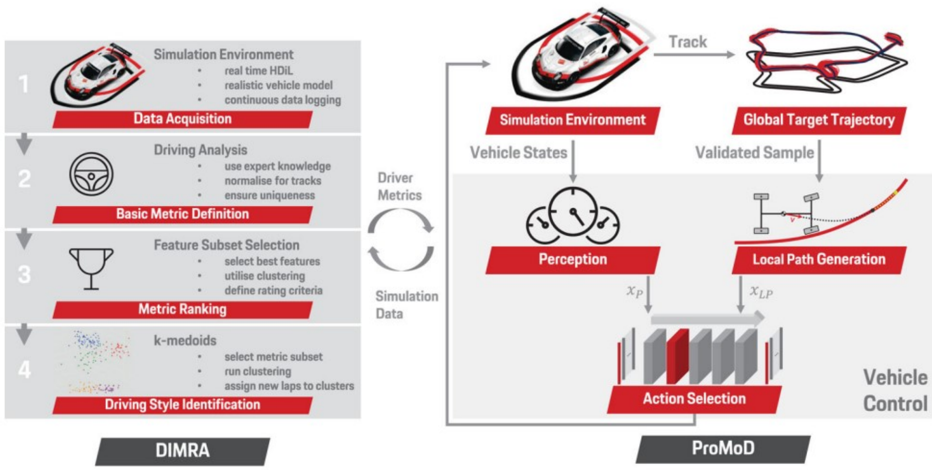

Fig. 1.13 Proposed Holistic Method to Assess and Model Race Driver Behaviour [76]

As mentioned, the use of a professional racing simulator to compare the behavior of drivers is widespread. It is used to compare human drivers (professionals and amateurs) and autonomous drivers under an aggressive driving scenario in terms of steering, use of pedals, trajectories [77] and also to study the processing of visual information of racing drivers compared to normal drivers [78]. Another paper that dealt with understanding and quantifying the differences in drivers is [79], where the authors investigate differences between race-car drivers and normal drivers in a high-speed driving task. The experiment was conducted in a race-car simulator and aspects concerning road departures, lateral acceleration, steering performance, the chosen path to negotiate the corner were analyzed.

Many other works base the identification of driving style on data from a simulator [80–83]. For example, in [84] a driving simulator was used to

get data of more or less skilled drivers in order to find an identifier of driving skill level and in [85] is presented a method to study and evaluate race drivers on a driver-in-the-loop simulator by analysing tire grip potential exploitation. What can be concluded therefore is that a considerable number of studies concerning the classification of the driving style of pilots, make use of a virtual driving simulator to acquire useful data for research. It is important to underline that no matter how valid these studies are, thanks also to the increasingly advanced simulation systems, but they cannot take into account a whole series of aspects and phenomena that can occur in the real world. For this reason, this research work is based on telemetry data obtained from laps on the track, because driving data acquired during real test sessions have the advantage of providing more realistic and detailed driving behavior in real-world settings, ensuring greater robustness of the results obtained.
Another aspect that emerged is that in the current research results, there are mainly two methods for driving style recognition: the subjective evaluation method and the statistical classification method. Finally, there is a really small amount of works that focused on identifying differences between professional drivers and not through parameters related to driving style. Research often focuses only on professional drivers or on the comparison between a human driver and an autonomous vehicle/software. Several studies in this area aim to develop and improve both driver assistance systems, to ensure greater safety, and autonomous vehicles, to make them more adaptable to the driver according to his driving style, in order to achieve better vehicle performance and driving pleasure [86–88]. Also widespread is the study of the effect that driving style can have on the fuel or energy consumption of vehicles [89, 90].

1.6 Viscoelasticity

Rubber is a fascinating material with unique properties that make it an essential component of a pneumatic tire: it is soft, elastic, resistant to cutting and scraping, with a high coefficient of friction and low permeability to gases. The characterization of tire tread viscoelasticity is a fundamental topic in the optimization of vehicle performance. All rubbery materials consist of long chain-like polymer molecules. The original elastomeric material (raw rubber) is basically a highly-viscous liquid but it can show elasticity because the long molecules are held together, at least temporarily, by being intertwined and entangled. The basic reaction in rubber processing is the joining of long molecules together by a few chemical bonds (crosslinks) to form a loose three-dimensional permanent molecular network. The shape becomes fixed and the material is transformed from a high-viscosity liquid into an elastic solid. This joining reaction is often termed "curing" because the material is no longer a viscous sticky liquid, or "vulcanization" because it is usually carried out with reagents that introduce sulfur crosslinks between the molecules. The main effect of this procedure is that the rubber becomes insoluble in each solvent, which affects the production system as the subsequent processing of these materials cannot provide for technological processes that require a flow of material; that is, it is not possible to use extruders, castings or similar techniques [91, 92].

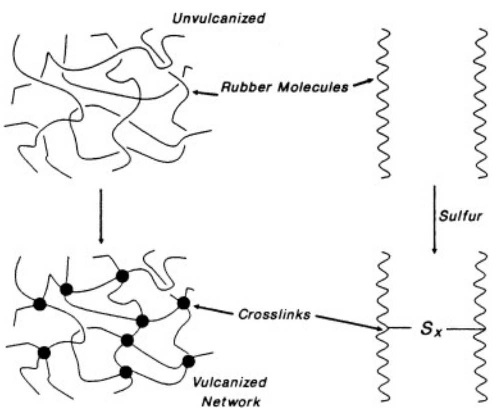

Fig. 1.14 Vulcanized Rubber Molecular Network

Viscoelastic materials do not show a linear relationship between stress and applied strain. Indeed, their behavior deviates from Hooke's law and exhibits elastic and viscous characteristics at the same time. The typical response of viscoelastic materials is characterized by a strong dependence on the rate of straining $d\varepsilon/dt$; the faster the stretching, the larger the stress required, as shown in the $\sigma - \varepsilon$ diagram represented in Figure 1.15, which is known as the stress-strain diagram.

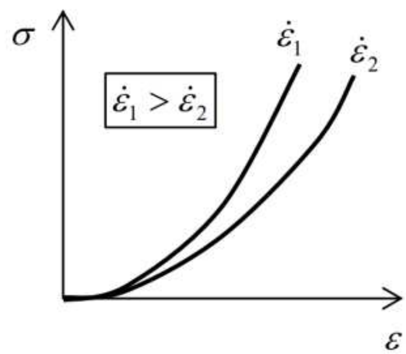

Fig. 1.15 Strain-stress diagram - $\frac{d\varepsilon}{dt}$ dependence

The effect of stretching shows that the viscoelastic materials depend on time; the most generic equation that describes this feature is Newton's Law [93, 94]:

$$\sigma = \eta \frac{d\varepsilon}{dt} \tag{1.13}$$

Newton's Law shows the connection between the stress and the strain rate through the viscosity coefficient η: every material which satisfies the equation 1.13 can be classified as a viscoelastic material. It is fundamental to underline that the viscoelastic materials, after removing any deforming force, return to their original shape, after a certain time period; contrariwise, when a perfectly elastic solid is subjected to a force, it distorts instantaneously in proportion to the applied load. In the last case, stress and deformation are immediate and the material behavior agrees with Hooke's Law.

A polymeric material, such as rubber, subjected to deformation cycles always describes a non-zero area on the diagram, even when the deformation cycle is carried out in a quasi-static manner and then, if the cycle is carried out suddenly, the area is significantly increased (as reported in Figure 1.16). These materials, in fact, in addition to exhibiting non-linear elastic trend, are characterized by a strong viscous behavior which corresponds to a high dependence of the area of the cycle by the speed of the deformations and they have an additional property called hysteresis, which results in a loss of mechanical energy which also manifests itself in deformation cycles conducted in a quasi-static manner. For this reason, polymeric materials are also called viscoelastic and hysteretic.

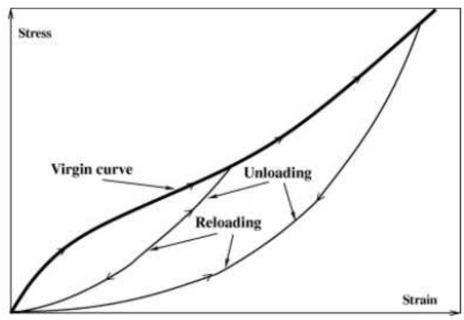

Fig. 1.16 Strain-stress diagram with hysteresis

To better understand the mechanical behavior in viscoelastic materials, two main types of experiments are usually carried out: transient and dynamic. As the transient material testing, two important categories are commonly performed: creep experiment and stress relaxation experiment [95].

The creep experiment involves loading a material at constant stress, maintaining that stress for a certain period of time and then removing the load. The response of a typical viscoelastic material to this test is shown in figure 1.17.

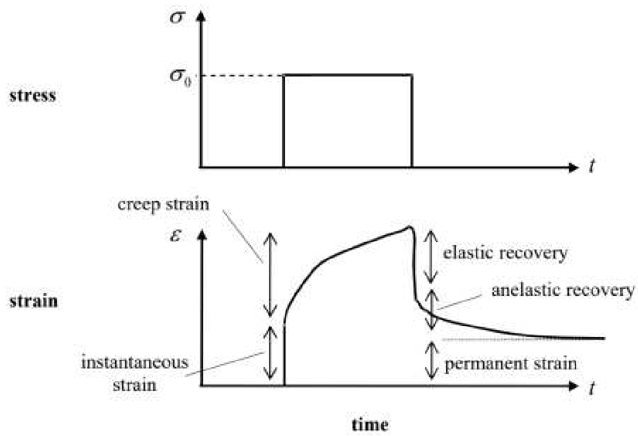

Fig. 1.17 Strain response to the creep experiment

First of all, there is an instantaneous elastic straining, followed by an ever-increasing strain over time known as creep strain. The creep strain usually increases with an ever-decreasing strain rate so that eventually a more-or-less constant-strain steady state is reached, but many materials often do not reach such a noticeable steady state, even after a very long time. Then, when the material is unloaded, the elastic strain is recovered immediately. After that, there is an anelastic recovery strain recovered over time; this anelastic strain is usually very small for metals but may be significant in polymeric materials. A permanent strain may then be left in the material.

The relationship between the stress and the strain during the creep experiment may be expressed through the creep compliance function J [93]:

$$J(t) = \frac{\varepsilon(t)}{\sigma_0} \tag{1.14}$$

The trend of the function $J(t)$ is shown in Figure 1.18.

The material behaves as a glassy solid if the load is applied with higher frequency values and it is similar to a rubbery solid if the load is applied quasi-statically. In the middle time–range, where the solid behaves as a viscoelastic material, the creep compliance shows a linear trend and it proportionally

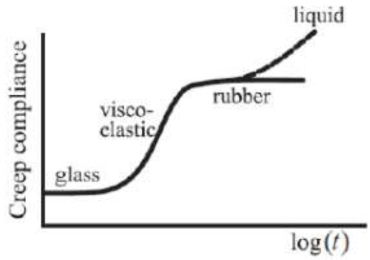

Fig. 1.18 Creep compliance

increases with time. Differently, the stress-relaxation experiment involves straining a material at constant strain and then maintaining that strain (Figure 1.19). The stress required to hold the viscoelastic material at the constant strain decrease over time. This phenomenon is called stress relaxation; it is due to a re-arrangement of the material on the molecular or micro-scale [96].

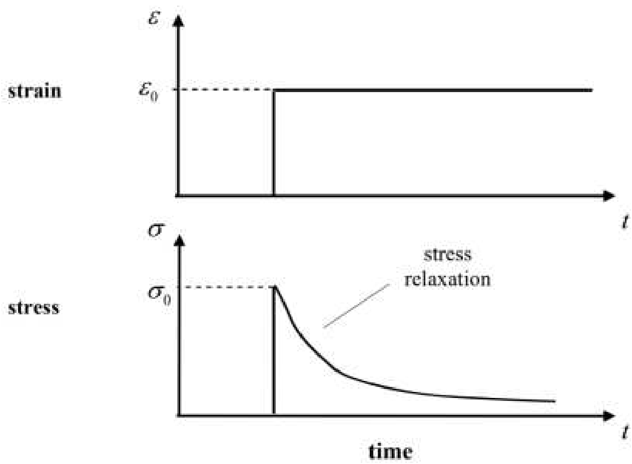

Fig. 1.19 Stress response to the stress relaxation experiment

Similarly for the creep compliance quantity, defined in the Equation 1.14, the relaxation modulus E is expressed as [93]:

$$E(t) = \frac{\sigma(t)}{\varepsilon_0} \tag{1.15}$$

The trend of the relaxation modulus is reported in Figure 1.20.

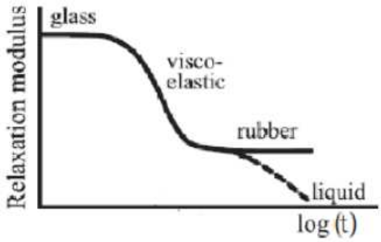

Fig. 1.20 Relaxation modulus

From Figure 1.20, it is possible to distinguish the glassy and rubbery plateaus and the linear trend, where the material exhibits viscoelastic behavior. These transient tests allow the characterization of the viscoelastic material reaction to a stress/strain load step. Differently, the dynamic test involves a repeating pattern of loading-unloading. It can be strain-controlled (with the resulting stress observed), as in Figure 1.21, or stress-controlled (with the resulting strain observed). The results of a cyclic test can be quite complex, due to the creep, stress-relaxation and permanent deformations. These phenomena are highlighted with non-overlapping cycles in the diagram shown in Figure 1.21.

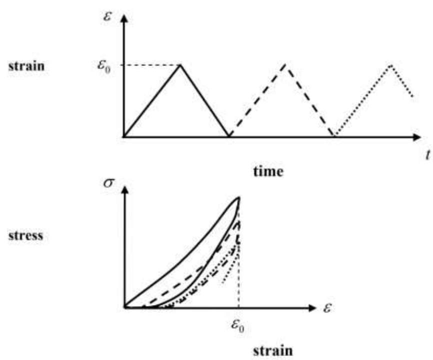

Fig. 1.21 Stress response to the cyclic test

In particular, it can be assumed that sinusoidal stresses or strains of constant frequency are applied to a sample until a steady sinusoidal strain or stress results, with a fixed phase angle between the input and the output (Figure 1.22). For example, for a sinusoidal shear strain:

$$\varepsilon(t) = \varepsilon_0 \sin(\omega t) \tag{1.16}$$

where ε_0 is the strain amplitude and ω is the angular frequency, the stress σ will oscillate sinusoidally as:

$$\sigma(t) = \sigma_0 \sin(\omega t + \delta) \tag{1.17}$$

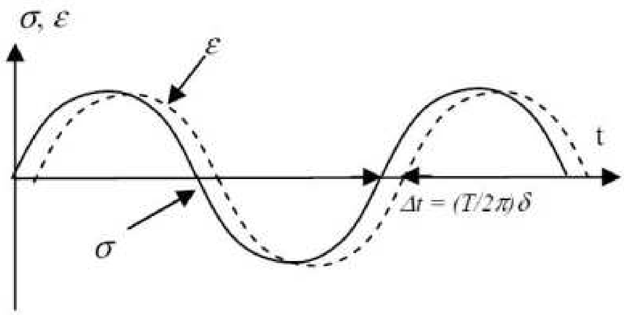

Fig. 1.22 Strain-stress phase

Using the trigonometric formula, the Equation 1.17 can be rewritten as:

$$\sigma(t) = \varepsilon_0[E'(\omega)\sin(\omega t) + E''(\omega)\cos(\omega t)] \tag{1.18}$$

where $E'(\omega) = (\sigma_0/\varepsilon_0)cos(\delta)$ is the storage modulus, while the loss modulus is $E''(\omega) = (\sigma_0/\varepsilon_0)sin(\delta)$. The first is a measure of the elastic energy stored and recovered, while the second is a measure of the dissipated energy as heat in cyclic deformation. The ratio $E''(\omega)/E'(\omega)$ is the $tan(\delta)$, also called loss factor where δ is the phase angle by which the strain lags behind the applied stress. Typical values of $tan(\delta)$ for rubber compounds at room temperature range from about 0.03 for a highly resilient, "springy" material with low energy dissipation to about 0.2 for a typical tread compound with relatively high dissipation [97]. The loss factor, $\tan(\delta)$, is directly linked to the way the material dissipates a part of energy provided by means of a load/stress time function. As a result of the phase lag between stress and strain, the dynamic stiffness can be defined as a complex number E^* [93]:

$$E^* = E'(\omega) + iE''(\omega) = (\sigma_0/\varepsilon_0)e^{i\delta} \tag{1.19}$$

In an analogous manner, the steady sinusoidal strain in response to the applied sinusoidal stress of constant frequency is expressed in terms of the (in phase) storage compliance $J'(\omega)$ and the loss compliance $J''(\omega)$ as:

$$\varepsilon(t) = \sigma_0[J'(\omega)\sin(\omega t) + J''(\omega)\cos(\omega t)] \tag{1.20}$$

where $J'(\omega) = (\varepsilon_0/\sigma_0)\cos(\delta)$ and $J''(\omega) = (\varepsilon_0/\sigma_0)\sin(\delta)$. The complex dynamics compliance J^* is defined as [93]:

$$J^* = J'(\omega) - iJ''(\omega) = (\varepsilon_0/\sigma_0)e^{-i\delta} \tag{1.21}$$

It is important to underline that all these quantities, which characterize the viscoelastic behavior, are a function of the frequency at which the sinusoidal load is applied.

1.7 Road Roughness

Road roughness is generally defined as an expression of irregularities in the pavement surface that affect the ride quality of a vehicle (Figure 1.23). In addition, since road roughness has a large influence on many physical phenomena, such as its influence on grip values and tire degradation, it is a fundamental theme in this thesis work to understand more about overall vehicle performance. Surface roughness most commonly refers to the variations in height of the surface relative to a reference plane. It is measured either along a single line profile or along a set of parallel line profiles (surface maps).

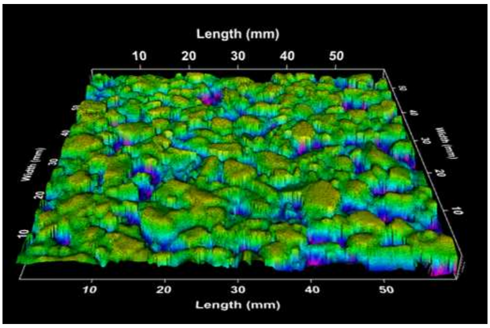

Fig. 1.23 Road roughness acquisition

Talking about road texture, it is possible to distinguish *macro-roughness* and *micro-roughness*. The first one represents the surface irregularities of longer wavelengths. The micro one, instead, is produced by fluctuations of short wavelengths characterized by asperities (local maxima) and valleys (local minima) of varying amplitudes and spacing [98]. To analyze the road texture, starting from its three-dimensional topography surface, many methods could be adopted for each surface topology. Commonly, statistical parameters are used to characterize the road roughness but it is usual to prefer a spectral analysis that allows for obtaining better results. In order to characterize road roughness several statistical parameters are adopted exploiting the concepts of amplitude probability distribution and density function.

The cumulative probability distribution function, or simply cumulative distribution function (CDF) [99], $P(h)$ associated with the random variable $z(x)$, which can take any value between $-\infty$ and $+\infty$ or z_{min} and z_{max} is defined as the probability of the event $z(x) \leq h$ and it is written as in Equation 1.22.

$$P(h) = Prob(z \leq h) \tag{1.22}$$

where $P(-\infty) = 0$ and $P(+\infty) = 1$. Generally, to describe the probability structure, it is used the probability density function (PDF), indicated with $p(z)$, which is defined as:

$$p(z) = \frac{dP(z)}{dz} \tag{1.23}$$

The cumulative probability distribution function is the integral of the probability density function $p(z)$:

$$P(z \leq h) = \int_{-\infty}^{h} p(z)dz = P(h) \tag{1.24}$$

$$P(h1 \leq z \leq h2) = \int_{h_1}^{h_2} p(z)dz = P(h_2) - P(h_1) \tag{1.25}$$

For what has been said, it is clear that:

$$\int_{-\infty}^{+\infty} p(z)dz = 1$$

The data, usually, tend to have a Gaussian or normal probability density function:

$$p(z) = \frac{1}{\sigma\sqrt{2\pi}} \exp\left[-\frac{(z-m)^2}{2\sigma^2}\right] \tag{1.26}$$

where σ is the standard deviation and m is the mean.

However, for simplicity, it is useful to plot the Gaussian function in terms of the standardized normal variable z^*:

$$z^* = \frac{(z-m)}{\sigma} \tag{1.27}$$

which has zero mean and unity standard deviation. In this way the normal probability density function is:

$$p(z^*) = \frac{1}{\sqrt{2\pi}} \exp\left[-\frac{(z^*)^2}{2}\right] \tag{1.28}$$

which is called the standardized Gaussian or the normal probability density function (Figure 1.24).

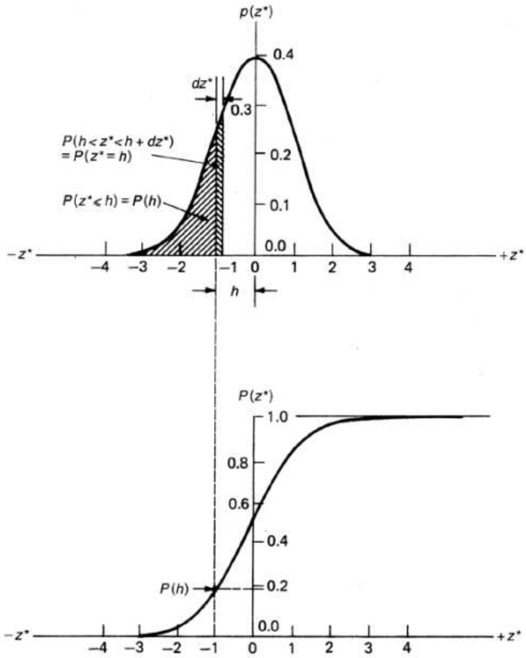

Fig. 1.24 Gaussian probability density function and gaussian probability distribution function

The shape of the probability density function is useful to define some important parameters, such as the skewness (*Sk* or *Sw*) and the kurtosis (*Ku*) [100]. The first one represents the degree of symmetry of the distribution function, while the latter refers to the peakedness of the distribution and it is a measure of the degree of pointedness or bluntness of a distribution function (Figure 1.25).

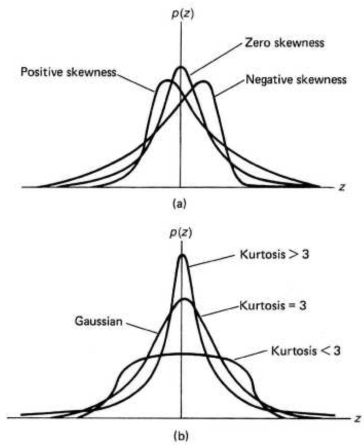

Fig. 1.25 Probability density functions - Skewness and Kurtosis

In particular, zero skewness reflects in symmetrical height distribution, profiles with positive skewness display valleys filled in or high peaks while profiles with negative skewness display peaks removed or deep scratches. For what concern kurtosis, if it is greater than 3, the profile has many high peaks and low valleys, while if it is less than 3, the profile has relatively few high peaks and low valleys [100] (Figure 1.26).

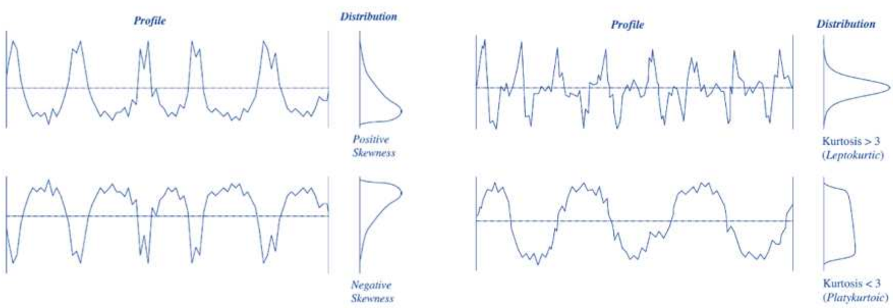

Fig. 1.26 Skewness and Kurtosis

Chapter 2

T.R.I.C.K. 2.0: an Evolved Tool for Vehicle Behavior Analysis Exploiting Advanced Sensors System

2.1 Introduction

The tool proposed in this chapter is the direct evolution of the T.R.I.C.K. tool developed by the UniNa research group in recent years. It was born with the aim to define a procedure able to estimate tire forces and slip indices during test sessions and to give, in a very short time, useful information to vehicle manufacturers and vehicle dynamics engineers about vehicle behavior, giving the possibility to improve vehicle performance. T.R.I.C.K. has been thought as a development tool to be employed in experimental activities with specifically instrumented testing vehicles, increasing the amount of information that track sessions can provide and collecting data useful to identify the parameters of interaction models used in the simulation. In particular, the main advantages that such kind of tool could bring to vehicle dynamic analysis are:

- absence of test bench campaign: while the standard procedure of tire characterization requires a lot of complex, bulky and expensive test benches to obtain a complete and detailed study of tires behavior, the tool's purpose is to consider the vehicle as a moving lab, and in this sense go to obtain all the data necessary for the study through track tests, saving costs and time;
- real thermal and frictional tire characterization: tire test rigs inevitably lead to the adoption of expedients that are useful for analyzing tires under controlled conditions, but which sometimes turn out to be quite far from reality. The possibility to test tires in real working conditions allows taking into account the real effect of frictional and thermal phenomena, usually neglected or badly evaluated [101, 102, 21];
- tire testing session results analysis: the use of a tool that allows making a comparison between the different tires tested in an objective way, is an additional resource to complement the subjective evaluation of the specialized test driver [103];
- race and test performances analysis: tires directly influence vehicle performances; consequently, a detailed analysis of the tangential interaction characteristics and of the effects that tires generate on the whole vehicle behavior can provide useful suggestions about the direction in which the performance improvement strategies should move. This last aspect is of fundamental importance for companies dealing with motorsport because by performing the vehicle races can be won;
- tire models parameters identification: with the availability of a wide data set, eventually acquired by means of dedicated track sessions, it is possible to predict the behavior of tires in all its possible working configurations; it allows to identify physical and empirical tire models parameters, tuning their output in order to fit the experimental ones [104, 105, 11];

- real-time tire behavior analysis: real-time knowledge of the tire dynamic behavior is a fundamental prerequisite for using electronic controls in vehicle dynamics, which are rapidly increasing their complexity and, consequently, the required accuracy of the measurement systems [106].

Maintaining these aims, the T.R.I.C.K. 2.0 wants to obtain more reliable results, in particular for what concerns forces estimation exploiting other sensors, generally equipped on high-performance vehicles, and considering further parameters that are in most cases available for motorsport teams.

2.2 T.R.I.C.K. - Tire/Road Interaction Characterization & Knowledge

A simplified overall scheme of the T.R.I.C.K. is shown in Figure 2.1. The tool is basically composed by a vehicle model able to process experimental signals acquired from the vehicle CAN bus and from sideslip angle estimation additional instrumentation, deeply described in the paragraph 4.2.2, providing a sort of virtual telemetry.

2.2.1 Basic Hypotheses and Reference System

The vehicle has been modeled using an 8-degree-of-freedom (DoF) quadricycle model, where:

- 3 DoF refer to in-plane vehicle body motions (longitudinal, lateral and yaw motions);
- 4 DoF refer to wheel rotations;
- 1 DoF refers to the steering angle

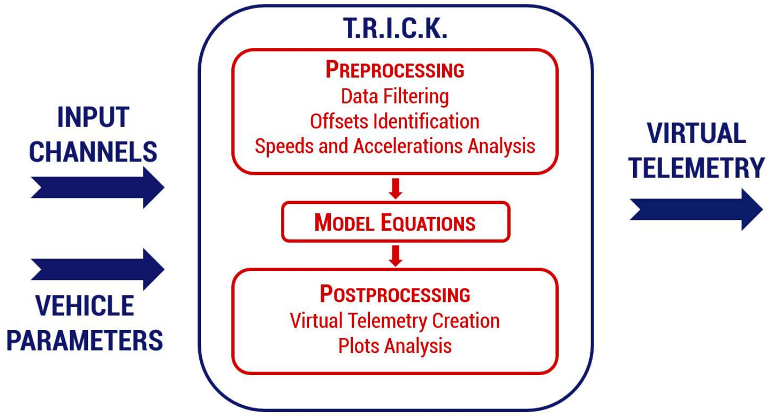

Fig. 2.1 T.R.I.C.K. tool block diagram

Moreover, suspensions and steering system kinematics and compliances are fixed and characterized by their own respective and invariable K&C curves, allowing to take into account roll angle, front and rear wheels toe and camber variations as a function of vehicle longitudinal and lateral accelerations. A wide and accurate description of vehicle characteristics, such as drag and downforce aerodynamics coefficients, tires rolling resistance parameters and Ackermann steering coefficients, gives the possibility to model dynamic effects commonly neglected because of their complexity, but essential in an interaction characterization activity. In order to describe the vehicle motions, two coordinate systems have been introduced: one earth-fixed $(x';y')$, the other $(x;y)$ jointed to the vehicle, as shown in Figure 2.2. With reference to the same Figure, v is the centre of gravity (CoG) absolute velocity referred to the earth-fixed axis system and U (longitudinal velocity) and V (lateral velocity) are its components in the vehicle axis system; r is the yaw rate evaluated in the earth fixed system, β is the vehicle sideslip angle, F_{xij} and F_{yij} are respectively longitudinal and lateral components of the tire-road interaction forces. The front and rear wheel tracks are indicated with t_F and t_R, while the distances from front and rear axle to the centre of gravity are represented by a

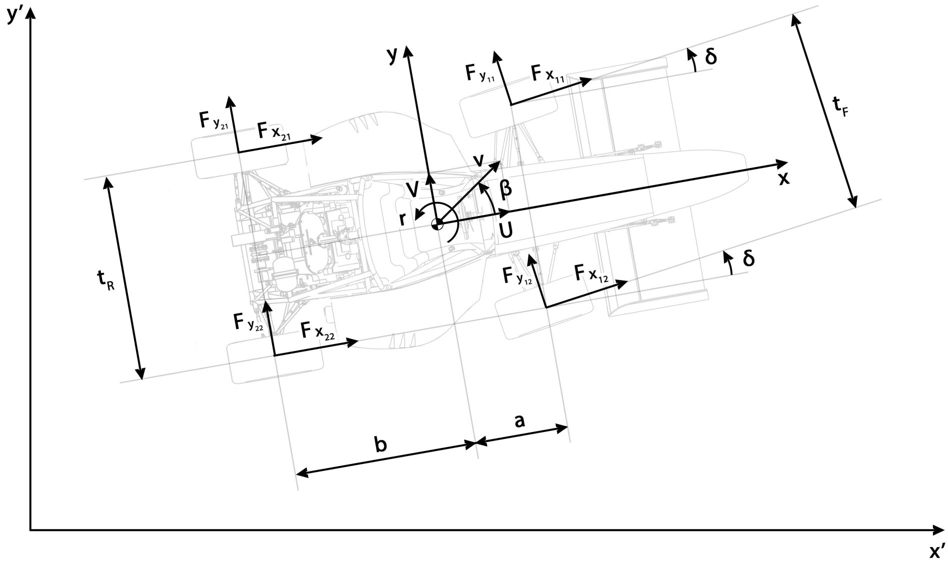

Fig. 2.2 Coordinate system

and b, respectively. The steer angle of the front tires is denoted by δ, while the rear tires are supposed non-steering. Vertical loads, for reason of coherence with the ISO reference system, are minor than 0 in ordinary condition of tire in contact with the road. Also the camber and the toe angles are considered in ISO reference system.

2.2.2 Input Channels and Parameters

The T.R.I.C.K. tool, in its first version, through a specifically developed graphical user interface (GUI), loads and processes twelve input channels exported from the acquiring system, composed by CAN bus and Optical Sensor, as MATLAB variables (files *.mat), properly named as in Table 2.1.

CAN bus wheel speed signal is expressed in terms of angular speed (rad/s) and measured using a phonic wheel: multiplying it by the effective rolling radius, manually set in the vehicle control unit during initialization, it can be obtained the values in terms of linear speed (m/s). To develop the

Table 2.1 T.R.I.C.K. tool input channels

Channels	**Input**	**Sensor**	**Unit**
time	Acquired Time	CAN-BUS	s
$gLat$	Vehicle Lateral Acceleration	CAN-BUS	m/s^2
$gLong$	Vehicle Longitudinal Acceleration	CAN-BUS	m/s^2
$vLat$	Vehicle Lateral Velocity	Opt. Sensor	m/s
$vLong$	Vehicle Longitudinal Velocity	Opt. Sensor	m/s
$nYaw$	Vehicle Yaw Rate	CAN-BUS	deg/s^2
$vWheelLong_{ij}$	Wheel Speed for the tire ij	CAN-BUS	m/s
$asteer$	Steering Angle	CAN-BUS	deg

new version of the tool, several additional acquired channels are added to these 11 input channels; they will be deeply described in the next paragraphs. In addition, to properly apply the vehicle model equations, it is necessary to know several design information of the vehicle, such as suspension characteristics, aerodynamics coefficients, tire specifications, geometry and masses parameters and so on [45].

2.2.3 Pre-Processing

After loading the input channels and the input parameters of the vehicle, the T.R.I.C.K. tool performs a series of operations before processing the data; these procedures make up the pre-processing phase, which is crucial in order to obtain good results.

The data acquired from the sensors are often subject to noise, electromagnetic disturbances, and high-frequency vibrations, so the information they provide to the tool could be not directly linked with the phenomena involved in vehicle dynamics field. For this reason, a preliminary essential operation is a filtering of the channels that have to be processed. For this purpose it is used a Butterworth filter, that is a type of signal processing filter designed to have a frequency response that is as flat as possible in the passband. In particular, it is used a third order, 5 Hz low-pass filter with a Nyquist normalizing frequency depending on sample rate, commonly equal to 50 or 100 Hz.

Vehicle on-board instrumentation is unavoidably installed with misalignments between its own reference system and the vehicle one; for this reason, it is possible that some procedures will be affected by miscalculations. To avoid that, it is necessary to detect and correct these misalignments or offsets. In detail, it is possible to identify a static and a dynamic offset, to fix them the tool provides two different procedures:

- to detect the static offsets, it is necessary to choose a range of acquisitions with the vehicle in stationary conditions; after that, the average values of lateral acceleration, longitudinal acceleration and longitudinal velocity channels are calculated within the selected range and these quantities are subtracted from the original signals. In this way the static offset is removed from the signals (Figure 2.3);

- to detect the dynamic offsets, it is necessary to choose a range of acquisitions in which the vehicle is on a straight line at constant speed (for example, on the pit lane); after that, the average values of steering angle, yaw rate and lateral velocity channels are calculated within the selected range and these quantities are subtracted from the original signals. In this way, the dynamic offset is removed from the signals (Figure 2.4).

Then, all the acquired quantities have to be reported to the CoG using transport equations.

2.2.4 Processing and Post-Processing

After the pre-processing operations, the T.R.I.C.K. tool uses several equations to estimate interaction forces, slip indices and dynamic camber angles (the most relevant are reported in appendix A). In particular, dynamic equations

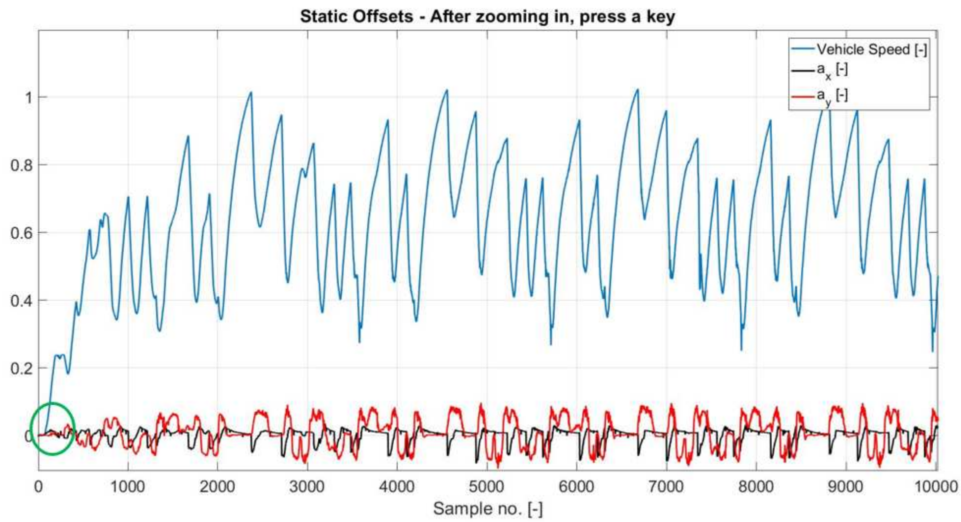

Fig. 2.3 Static offsets identification – in green circle, the range with the vehicle stationary

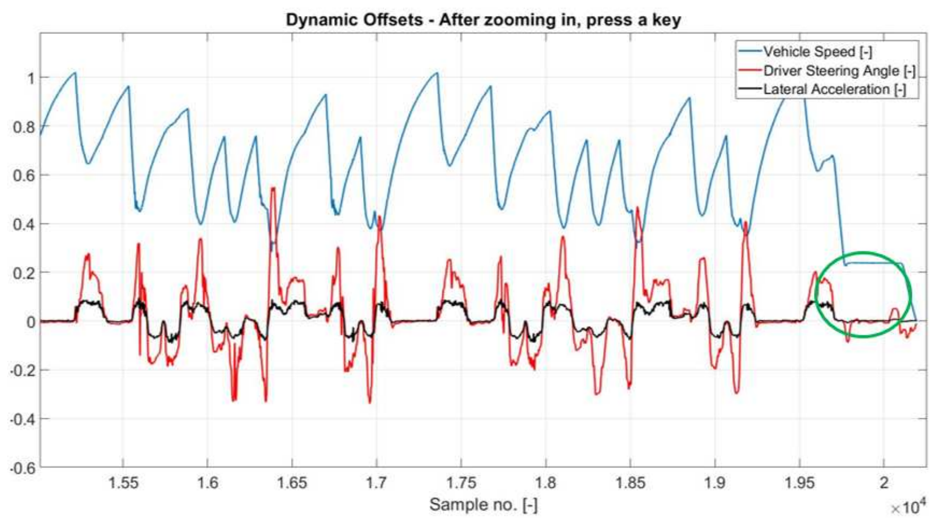

Fig. 2.4 Dynamic offsets identification – in green circle, the range in which the vehicle is on a straight line at constant speed

are used for forces evaluation, kinematic relations are adopted for the slips calculation and experimental-based formulas are used to estimate the camber variation from the static setup [3, 45]. In the proposed version of the T.R.I.C.K. 2.0 several formulations have been updated in order to obtain a better estimation of forces and camber angles. After the processing, all the processed data are stored in the form of virtual telemetry and the user can also visualize some relevant plots, shown in Figure 2.5, useful to perform a deep performance analysis of the reference tires and vehicle.

2.2.5 T.R.I.C.K. 2.0 - Novelties

The need to create a new version of the T.R.I.C.K. tool stems from the desire to use alternative formulations to those already present in the first release of the tool, in order to obtain results that reflect, in the closest way to reality, the dynamic behavior of the vehicle analyzed. T.R.I.C.K. 2.0 tool is designed for studying the dynamics of a racing car, which usually has a more advanced sensor system than the one required for the T.R.I.C.K. simulation. Moreover, vehicle manufacturers have additional information about the construction and performance characteristics of the car and conduct dedicated tests to analyze the behavior of certain components. In this way, it is possible to take advantage of all these additional factors to update the tool's processing phase (model equations), using formulations that allow for better results. In particular, these new sensors are considered:

- laser sensors for ride height measuring;
- potentiometers and load cells mounted on the shock absorbers;
- anti-roll bars' load cells;
- brake pressure sensors.

Thanks to the combined adoption of these acquired channels with additional parameters, it was possible to develop to obtain a better estimation of:

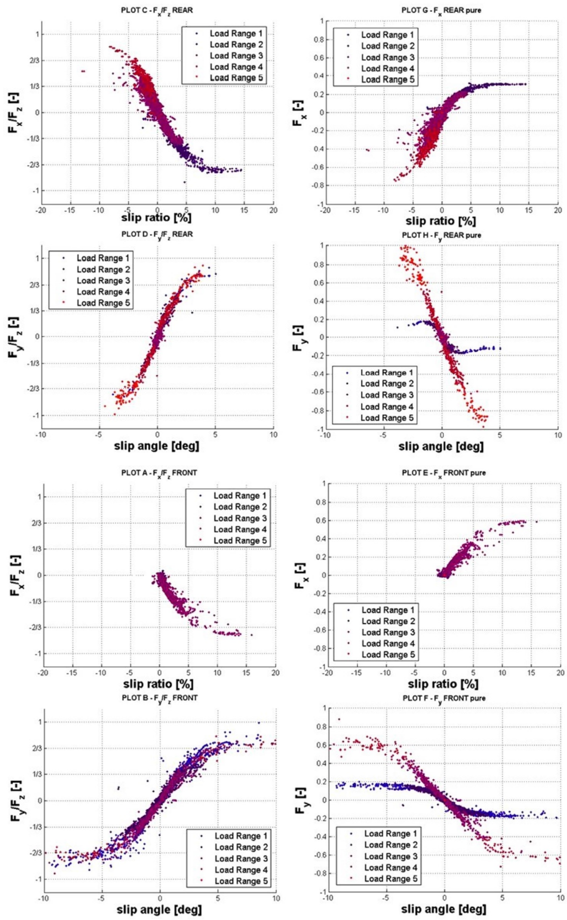

Fig. 2.5 Pure interactions - left column: grip, right column: interaction force [45]

- aerodynamic forces;
- roll angle;
- roll stiffness;
- vertical forces;
- dynamic camber angles;

- longitudinal and lateral forces.

All these new formulations have been validated using a high-performance simulator, which presents a much more complex vehicle model and a deep parameterization of all the vehicle subsystems. Finally, also the user experience had been improved, with a new GUI useful to carry out several checks on the acquired data and to give the possibility of choice among all the different formulations available. All the relevant GUI updates are shown in Figure 2.6, where it is possible to visualize the more complex information flow within the T.R.I.C.K. 2.0.

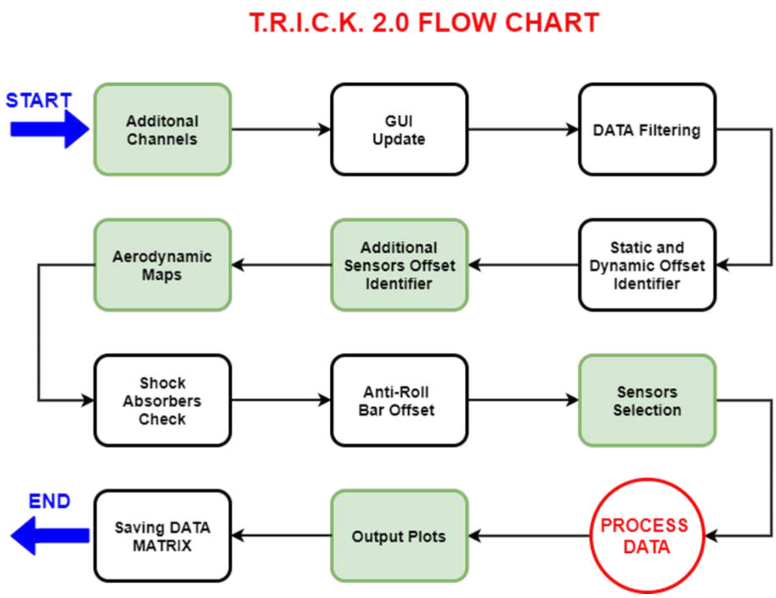

Fig. 2.6 T.R.I.C.K. 2.0 Flow chart, in green the GUI novelties

2.3 Roll Angle & Aerodynamic Forces Formulas

2.3.1 Laser Sensors

Lasers sensors are widely adopted in the motorsport sector to monitor the vehicle ride height variations, fundamental parameters to investigate the goodness of the car setup [107]. These sensors generally belong to the "rangefinders" category and are designed to measure object distance without contact through a laser beam, exploiting the principles of laser radiation: a laser pulse is sent in a narrow beam towards the target object and, measuring the time taken by the impulse to be reflected off the target and returned to the source, knowing the speed of light, it is possible to evaluate the distance accurately. Usually, these instruments are securely mounted on the vehicle, particularly on the bottom of the frame, so that the laser beam is directed perpendicular to the ground (in static conditions); this measurement technique is not appropriate for high precision sub-millimeters measurements whereas is often the best solution for measuring distances between moving objects, as in the considered case. In this work, laser sensors data are used to estimate roll angle and aerodynamic forces, as already presented in the previous paper [47], with the addition of a fully new formulation for the dynamic camber formulation, deeply treated in the section 2.4.4. To calculate the above-mentioned quantities, different laser sensors must be mounted in specific positions, in particular:

- for the roll angle, two sensors mounted at the same abscissa (along the x-axis) are needed; they must be installed symmetrically to the xz plane at the same height from the ground;
- two sensors are needed to evaluate the aerodynamic forces, mounted along the vehicle symmetry plane xz, near the position of the front and rear axles;

- finally to evaluate the camber angle, it is necessary to calculate the axles' dynamic height in order to estimate their variation, so the same configuration of the previous point is needed.

To summarize, to estimate the virtual channels just introduced, a minimum of three laser sensors should be installed on the vehicle:

- the first one fixed on the symmetry plane xz, the nearest possible to the front axle;
- the other two symmetrically mounted always to plane xz, as near as possible to the abscissa of the rear axle (clearly to define the positions of the sensors, their size should be taken into account).

Considering the pitch and roll motions that occur during ordinary vehicle movements, the heights acquired by the sensors vary causing the laser beam's inclination variation. Despite this, since the roll and pitch angles are small, of the order of a few degrees, this imperfect perpendicularity can be neglected.

2.3.2 Roll Angle Estimation

Within the tool the roll angle is used to assess the dynamic camber; in particular, in the first release of the T.R.I.C.K. it was evaluated as in the Equation 2.1, in which a_y is the lateral acceleration, g is the gravity acceleration and $Roll(g)$ is the value of the roll angle in correspondence of a lateral acceleration of 1 g. Clearly, in this way, the relation between roll angle and lateral acceleration is strictly linear.

$$\phi = \frac{a_y}{|g|} \cdot Roll(g) \tag{2.1}$$

Usually, the dependence between ϕ and a_y is not linear, it can be variable and it is a specific characteristic of the reference vehicle due to the suspension elements equipped. To overcome the limits of the previous formulation, adopting the laser sensors it is possible to evaluate the roll angle as in Equation 2.2.

$$\phi = \arctan(\frac{H_{LaserRL} - H_{LaserRR}}{d_{Laser}}) \tag{2.2}$$

Where $H_{LaserRL}$ and $H_{LaserRR}$ are, respectively the heights from the ground measured by the left and right laser sensors and d_{Laser} is the distance between them. With this approach, the evaluation of the roll angle is not more related to lateral acceleration, giving back more reliable results. In order to compare the roll angles found using the two described methods, it is necessary to fit linearly the signal obtained in the second case to get an approximate linear roll dependence from the lateral acceleration, as shown in Figure 2.7.

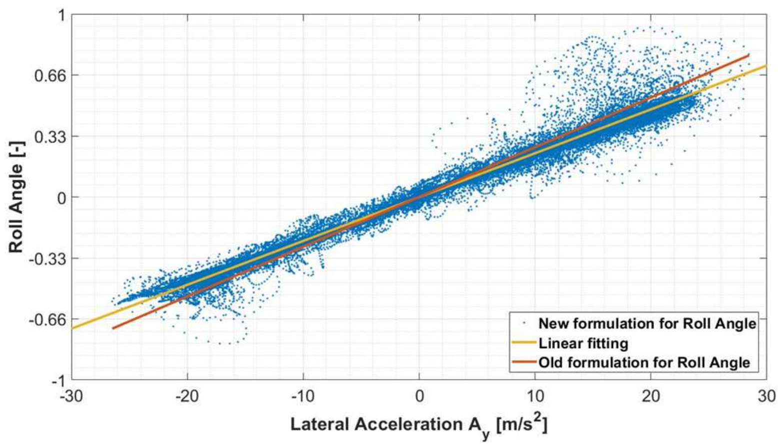

Fig. 2.7 Comparison between old and new roll angle formulation

In the figure, the fitting obtained from the formula has a lower slope than the original linear formulation, to better comprehend the global trend of the roll angle a further comparison was made in Figure 2.8 with the virtual channels provided by a simulator.

The comparison with simulator data shows that the new formulation is similar to the one implemented in the simulator, in which a more elaborate vehicle model is implemented. The analysis shows that a linear dependence

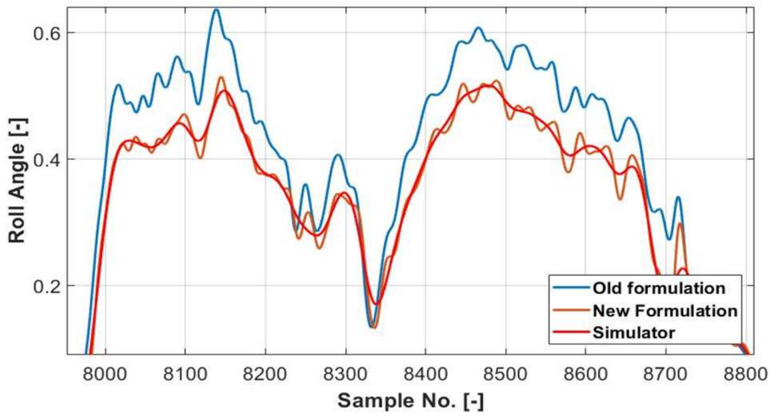

Fig. 2.8 Roll angle comparison among simulator, old and new formulation

roll angle - lateral acceleration is an appropriate approximation, but using the heights collected instantly by the laser allows to achieve a more reliable estimation of the roll angle with subsequent benefits shown in the following sections.

2.3.3 Aerodynamic Forces Calculation

Aerodynamic Maps

Several aerodynamic appendices are expressly designed to maximize race vehicles' performance on track. The adoption of front and rear wings, undertray and sidepods gives the possibility to control air flows around the vehicle to obtain specific aims [108, 109]. To properly design all these devices both CFD simulations and experimental tests were conducted [110]. Wind tunnels are the most useful equipment to study the real flow patterns around a true-scale vehicle. The possibility to carry out this kind of test is based on the so-called principle of reciprocity, which states that to evaluate the behavior of a flow pattern around a generic body, it is indifferent to move a body in a still fluid or to move the fluid around a stationary body [111]. The most functional outputs obtainable from wind tunnel testing are the aerodynamics maps, in which the aerodynamic coefficients (i.e. C_x, C_{zF}, C_{zR}) are defined as a function of several vehicle variable parameters, such as wings' flaps inclination angles and axles heights from the ground. Usually, to define these maps it is necessary to fix all the reference parameters except one that varies among all the possible operating conditions [112]. It should also be remembered that the aerodynamic maps have to be appropriately corrected because test conditions are not perfectly equal to those occurring in real driving conditions.

Generally, the variation of the aerodynamic coefficient is not linear, for this reason, to correctly implement the maps in the tool a series of lookup tables should be used, but this approach could be too expensive from a computational point of view, making the tool less flexible. To consider the wind tunnel outputs most easily, a linear approximation of the dependencies of the aerodynamic coefficients concerning the reference parameters was defined, identifying the average coefficient of variations. First of all, a preliminary split into two macro-categories of aerodynamic behavior has to be done; indeed, it is well known that in the motorsport world there are tracks for which aerodynamic contribution is more prevalent (high downforce circuits with few straight) than others (low downforce circuits with many straights and few corners). In the presented new version of the T.R.I.C.K. tool, the user can select the level of downforce corresponding to the track on which the telemetry is acquired to set properly the reference parameters and variation laws. Then, the information within the maps is used to determine the linear variation coefficients to correct the static values of C_x, C_{zF}, C_{zR}. In addition, to be able to evaluate these coefficients for each acquisition sample it is necessary to know the height of the vehicle from the ground during the driving phases, using the laser sensors.

Aerodynamic Forces

Combining the aero-maps with the information provided by the lasers, the following procedure for the evaluation of the aerodynamic forces has been developed. Firstly, several static conditions are defined as a reference for the subsequent evaluations:

- Drag coefficient C_{x0};
- Front axle downforce coefficient C_{zF_0};
- Rear axle downforce coefficient C_{zR_0};
- Wing inclination angle α_{Wing_0};
- Front axle height from the ground H_{AxleF_0};
- Rear axle height from the ground H_{AxleR_0}.

The last three quantities identify the reference static conditions of the car, from which deviations have to be evaluated. The wing inclination angle is assumed constant during vehicle motion so it depends only on the choice of the aerodynamic package adopted so that the variation $\Delta\alpha_{Wing}$ is fixed and is directly connected to the change of the flap inclination concerning the reference one. For what concerns the axles' height variations, to calculate them the signals acquired by the lasers have to be pre-processed because these sensors are generally not mounted at the same abscissa of the axles. First of all, the average value of the measurements obtained from the two rear lasers has to be calculated in order to know the height from the ground at the xz symmetry plane, as shown in Equation 2.3. This preliminary operation is not needed for the front sensor, already located on the symmetry plane.

$$H_{LaserR} = \frac{H_{LaserRL} + H_{LaserRR}}{2} \tag{2.3}$$

H_{LaserF} and H_{LaserR} represent the dynamic height signals in the position in which the sensors are installed. Starting from these, through a graphic procedure it is possible to evaluate the heights of the axles. Starting from the static heights of the sensors H_{LaserF_0} and H_{LaserR_0} it is possible to derive the equation of the line passing through them (Equations 2.4 and 2.5):

$$m = \frac{H_{LaserF_0} - H_{LaserR_0}}{p_{xLaserR} - p_{xLaserF}} \tag{2.4}$$

and:

$$q = H_{LaserR} - m p_{xLaserR} \tag{2.5}$$

Where m is the angular coefficient of this ideal line, q is the intercept with the z-axis. Having defined the line of equation $y = mx + q$, replacing x with the abscissas of the two axles, their heights from the ground can be determined (Equations 2.6 and 2.7).

$$H_{AxleF} = ma + q \tag{2.6}$$

$$H_{AxleR} = m(-b) + q \tag{2.7}$$

After these operations, the parameters of the reference variations can be evaluated (Equations 2.8, 2.9 and 2.10).

$$\Delta\alpha_{Wing} = \alpha_{Wing} - \alpha_{Wing_0} \tag{2.8}$$

$$\Delta H_{AxleF} = H_{AxleF} - H_{AxleF_0} \tag{2.9}$$

$$\Delta H_{AxleR} = H_{AxleR} - H_{AxleR_0} \tag{2.10}$$

Starting from the information of the aero-maps, for each aerodynamic coefficient, three linear sensitivity coefficients have been settled, referring to the three parameters just described, for a total of nine coefficients. Referring to C_x, they are:

- $SC_{x-\alpha Wing}$ for a unitary variation of the wing inclination angle, expressed in degree;

- SC_{x-H_F} for a unitary variation of the front axle height, expressed in mm;
- SC_{x-H_R} for a unitary variation of the rear axle height, expressed in mm.

The same applies to C_{zF} and C_{zF}. Finally, the aerodynamic coefficients can be evaluated as in the Equations 2.11, 2.12 and 2.13.

$$C_x = C_{x0} + SC_{x-\alpha Wing}\Delta\alpha_{Wing} + SC_{x-H_F}\Delta H_{AxleF} + SC_{x-H_R}\Delta H_{AxleR} \quad (2.11)$$

$$C_{zF} = C_{zF0} + SC_{zF-\alpha Wing}\Delta\alpha_{Wing} + SC_{zF-H_F}\Delta H_{AxleF} + SC_{zF-H_R}\Delta H_{AxleR} \quad (2.12)$$

$$C_{zF} = C_{zR0} + SC_{zR-\alpha Wing}\Delta\alpha_{Wing} + SC_{zR-H_F}\Delta H_{AxleF} + SC_{zR-H_R}\Delta H_{AxleR} \quad (2.13)$$

Introducing the aerodynamic coefficient variability it is possible to highlight that the downforces and the drag have a quadratic dependence from the vehicle CoG longitudinal velocity and a non-linear dependence on the corresponding aerodynamic coefficient; this non-linear dependence comes out from the fact that each coefficient depends linearly from three different uncorrelated vehicles parameters, resulting in a more complex non-linear variability. In order to assess the improvements made taking into account the variability of the aerodynamic coefficients as just described, several comparisons were made among simulator and T.R.I.C.K. formulations with and without aero-maps to highlight the variations in forces calculation.

From Figure 2.9 it is possible to point out that the presented new formulation follows the simulator trends slightly better. However, the best improvements in aerodynamic forces estimation are obtained for the front downforce; indeed, as shown in Figure 2.10, the previous formula implemented was not able to estimate the force fluctuations that occur at the end of the straights due to vehicle's heights from the ground changes, a direct consequence of the longitudinal load transfers. For the rear downforce (Figure 2.11), the

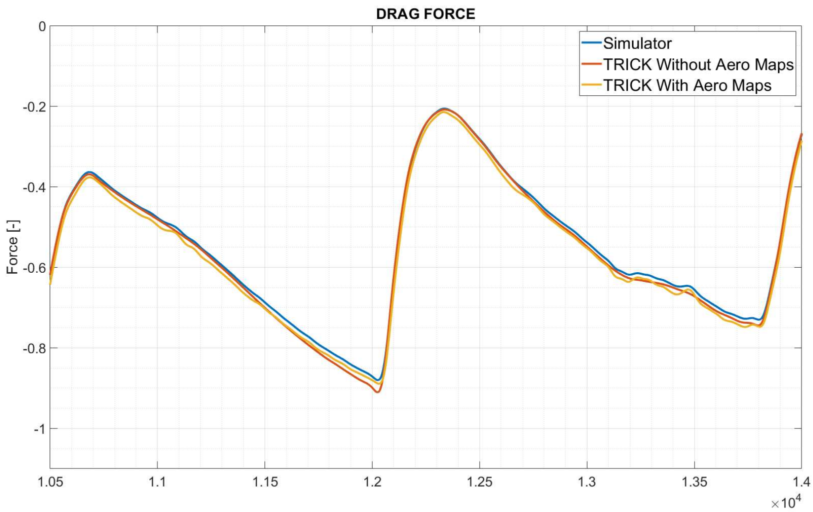

Fig. 2.9 Drag Force - Comparison among simulator, T.R.I.C.K. with and without aerodynamic maps [47]

improvements are less evident but still present. The small differences between simulator and T.R.I.C.K. 2.0 could be further reduced by carrying out more reliable wind tunnel tests or correcting in a more robust way the aero-maps information to bridge the gap between test and real operating conditions. Despite that, the formulation just represents a noticeable overcoming of the formula adopted in the first version of the tool.

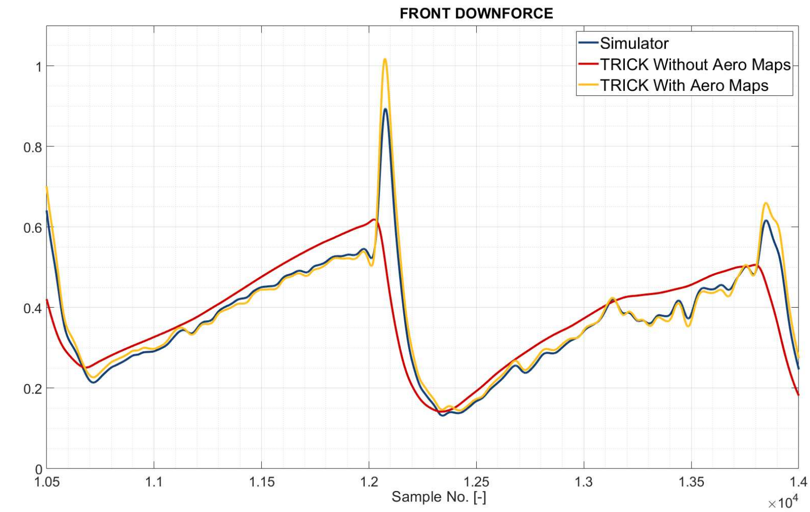

Fig. 2.10 Front Downforce - Comparison among simulator, T.R.I.C.K. with and without aerodynamic maps [47]

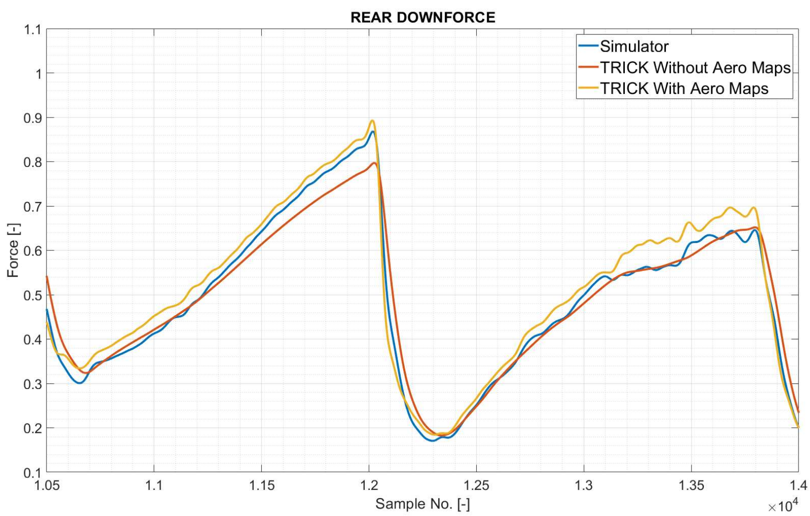

Fig. 2.11 Rear Downforce - Comparison among simulator, T.R.I.C.K. with and without aerodynamic maps [47]

2.4 Vertical Force Formulation

Vertical forces estimation is a fundamental task to properly characterize the tire-road interaction. An accurate F_z evaluation has to take into account all the different phenomena that occur during the vehicle motion, such as lateral and longitudinal load transfers, axles' height variations, dynamic variation of the suspension geometry. The classical formulation of the first release of the T.R.I.C.K. tool was based on the global equilibrium equations, calculated on the simplified eight-degree-of-freedom vehicle model (see appendix A); this approach, while allowing a good estimation of the vertical forces, neglected the presence of some dynamic phenomena. One of the main aims of the T.R.I.C.K. 2.0 is to overcome the limits of the previous formulation, exploiting the presence of additional sensors already installed on a race vehicle and using the further information provided, to obtain a more reliable estimation of the vertical forces in all the different operating conditions. In particular, in the presented formulation, the main novelty is constituted by the information acquired by potentiometers and load cells installed on the shock absorbers and on the anti-roll bars. To correctly interpret the data acquired by the additional sensors several procedures have been developed to identify and remove the offsets, verify the consistency of the signals acquired and isolate the real additional information provided by these sensors. After these preliminary operations, the new formulation is presented, paying attention to the possible implications related to the suspension geometry that is generally adopted for a race car. Finally, an innovative camber formulation, based on the information provided by laser sensors and load cells, is presented to overcome the limit of the old camber formulation.

2.4.1 Roll Stiffness Evaluation considering Tire Stiffness

Roll stiffness evaluation is a preliminary task necessary to properly evaluate the vertical load transfer. Before carrying out this activity, roll stiffness was evaluated within the T.R.I.C.K. as in the Equation 2.14:

$$k_\phi = k_{\phi F} + k_{\phi R} = (\frac{k_{spring_F}}{MR^2_{SA_F}} + k_{ARB_F}) + (\frac{k_{spring_R}}{MR^2_{SA_R}} + k_{ARB_R}) \tag{2.14}$$

Where $k_{\phi F}$ and $k_{\phi R}$ are, respectively, the front and rear axle roll stiffness, k_{spring_i} is the spring stiffness (for the springs mounted on the axle, expressed in (N/mm)), MR_{SA_i} it the shock absorber motion ratio and, finally, k_{ARB_i} is anti-roll bar (ARB) stiffness, reported to the ground and expressed in (N/mm). Using the Equation 2.14, for each axle the roll stiffness scheme adopted is shown in Figure 2.12a.

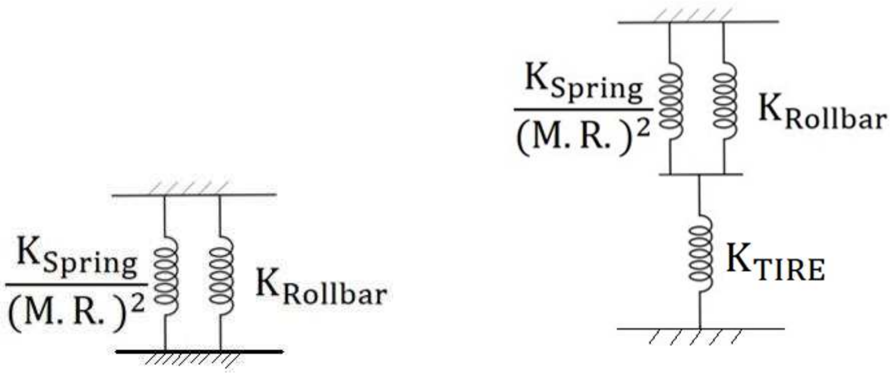

(a) Old (b) New

Fig. 2.12 K_ϕ single axle stiffness schemes

The novelty of this work is to consider the contribution of tire stiffness to the overall roll axle stiffness calculation. Indeed, tires for their own structure have a stiffness that can be considered as in series to the parallel between the spring and ARB stiffness, as illustrated in Figure 2.12b. To correctly evaluate the tire stiffness, an empirical formulation was considered. Equation 2.15 is based on several experimental coefficients (k_{ZP_i}, $k_{Z_{o_i}}$, k_{ZC_i} and k_{ZV_i}) that links the tires stiffness to some relevant tire information such as internal tire

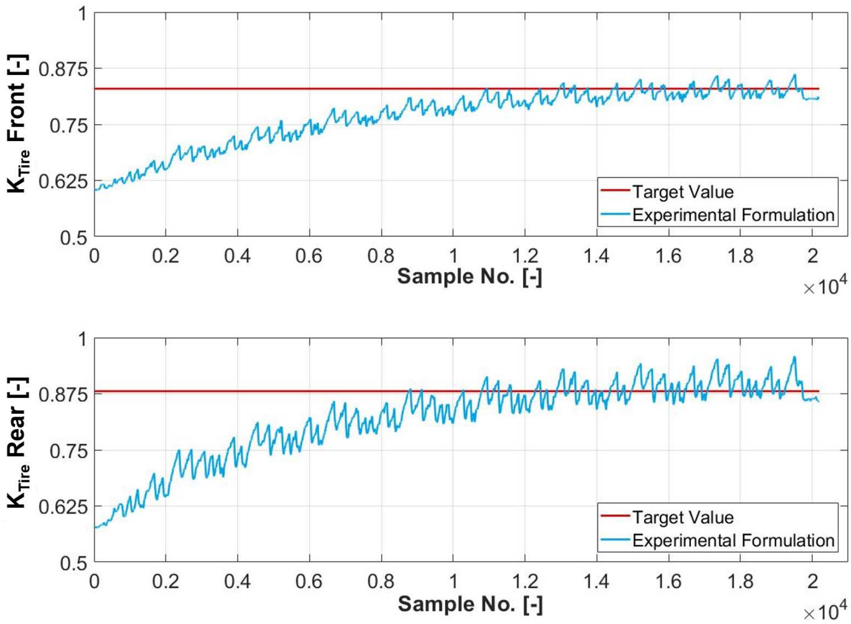

Fig. 2.13 K_{Tire} trend compared with the optimal target value

pressure, camber and velocity. For simplicity, it has been chosen to consider equal the stiffness of the tires of the same axle.

$$k_{Tire_i} = \frac{k_{Z_{o_i}} + k_{ZP_i} \cdot P_{Tire_i} - k_{ZC_i} |\gamma_{Stat_i}| + k_{ZV_i} \cdot (V^2 - V_{ref}^2)}{1000} \tag{2.15}$$

In Figure 2.13 a comparison between k_{Tire} trends estimated using this experimental formula and the target value, provided by the vehicle manufacturer, is shown. The proposed stiffness formulation is able to approximate in a good way the target values, considering all the stiffness variations related to the changes of the operating conditions, both at the beginning of the run (tire not in the optimal working range) and also within a single lap (related to the vehicle handling). Consequently, considering also the tire stiffness, the k_ϕ axle roll stiffness is evaluated according to Equation 2.16. The tire stiffness calculation coupled with the new axle roll formulation leads to a more precise estimation of the roll stiffness target value, resulting in a more reliable evaluation of the vertical load transfers.

$$k_{\phi_i} = \frac{k_{Tire_i} \cdot (\frac{k_{spring_i}}{MR^2_{SA_i}} + k_{ARB_i})}{k_{Tire_i} + (\frac{k_{spring_i}}{MR^2_{SA_i}} + k_{ARB_i})} \tag{2.16}$$

2.4.2 Shock Absorber and Antiroll-Bar Load Cells & Potentiometers

To analyze in detail the behavior of the shock absorbers, it is necessary to install on each of them a dedicated sensor system, generally consisting of a pair of sensors, a load cell and a potentiometer. The load cell reads the force acting on the suspension during the various motion conditions whereas the potentiometer acquires the stroke of the spring and/or the shock absorber instantly. To completely characterize the vehicle suspensions behavior, four load cells and four potentiometers are required, for a total of eight additional instruments; the first ones are used to calculate the vertical loads acting on the single wheels, while the position sensors can be utilized to verify the reliability of forces acquisitions. The force signals supplied by these sensors are instantaneous, unlike the contributions due to lateral load transfers that do not occur instantaneously but are affected by a delay that is generally neglected. Because of this effect, the classical formulation (described in appendix A) based on the forces balance has obvious limitations. The main issue of using these sensors in determining vertical forces is that they could present an offset that must be identified and eliminated in the right way in order to have real and precise measurements. Furthermore, the breaking or incorrect action of a single load cell compromises the use of the formulation that will be presented in the following paragraphs.

Combined Check Procedure with Potentiometers and Load Cells

Before using the load cells acquisitions, it would be advisable to check that these are working correctly, this control is possible if the additional potentiometer channels are available. The force acting on the shock absorber F_{SA} and its stroke S_{SA} are linked by the relationship expressed in Equation 2.17:

$$k_{Spring} = \frac{F_{SA}}{S_{SA}} \tag{2.17}$$

In which k_{Spring} is the stiffness of the spring mounted on the suspension considered; this value is known because it is one of the vehicle parameters defined in the initializer. Usually, k_{Spring} is not constant, but no grave mistakes are made considering it fixed. The ratio expressed in Equation 2.17 remains unchanged even if the acquisitions are affected by offset, for this reason, it was decided to do this check as the first operation before proceeding with the new formulation. For each corner a linear fitting of the acting force is performed with respect to the spring stroke; in this way, it is possible to obtain the slope value of the interpolating line which should just be equal to the design spring stiffness.

As shown in Figure 2.14, if the sensors work correctly the procedure returns values comparable with those present in the initializer, with errors always lower than 10%. Possible high mistakes are therefore attributable to the incorrect working of the sensors (load cells and/or potentiometers) or to an incorrect vehicle parameterization.

Offset Removal Procedures

Generally, the sensors are not installed perfectly, due to some misalignments or inaccurate positioning; in these cases, the measurements could be affected by offsets. An offset is present when the measured value is not equal to zero in a specific condition in which the inspected quantity must be zero. For what

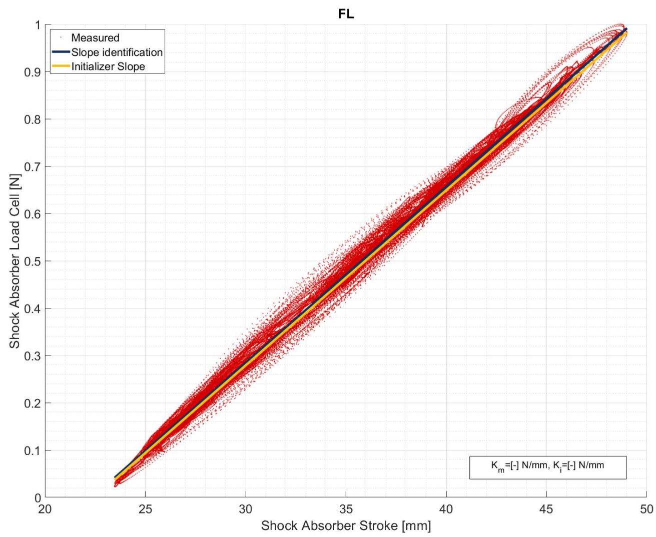

Fig. 2.14 Comparison between the linear fitting obtained from the sensors and the design spring stiffness value

concerns shock absorbers load cells, in case of zero longitudinal and lateral acceleration, the Equations 2.18, 2.19 and 2.20 must be verified.

$$m_v = \frac{F_{SA_{FL}} + F_{SA_{FR}}}{MR_{SA_F}} + \frac{F_{SA_{RL}} + F_{SA_{RR}}}{MR_{SA_R}} \tag{2.18}$$

$$F_{ARB_F} = 0 \tag{2.19}$$

$$F_{ARB_R} = 0 \tag{2.20}$$

Where m_v is the vehicle sprung mass $F_{SA_{ij}}$ is the shock absorber load cell acquisitions on the corner ij, MR_{SA_F} and MR_{SA_R} are the suspension motion ratios and F_{ARB_i} is the anti-roll bar load. In particular, the suspension motion ratio MR_{SA_i} is defined as in the equation 2.21.

$$MR_{SA_i} = \frac{\Delta z_{ij}}{S_{SA_{ij}}} = \frac{F_{SA_{ij}}}{F_{z_{ij}}} \tag{2.21}$$

In which Δz_{ij} is the vertical bump, $S_{SA_{ij}}$ is the spring stroke, $F_{SA_{ij}}$ is the force acting on the shock absorber read thanks to the load cell mounted and $F_{z_{ij}}$ is the vertical force, all these quantities refer to the generic corner ij. In most cases, the Equation 2.18 is not verified because of the offsets that affect load cells acquisitions. To overcome this inconvenience, a new offset identifying and zeroing procedure has been developed in this new version of the tool to remove potentiometers and load cell offsets. This operation is useful also to evaluate the static laser sensors' height (already discussed in Section 2.3) whereas for the ARB load cells offset another procedure has been developed and it will be discussed later in this section. To correctly identify the offset it is necessary to identify an acquisition range in which lateral and longitudinal accelerations are equal to zero. This condition occurs when the vehicle is standing still and when it is moving at constant speed, for example in pit lane. This second case allows determining the offsets more precisely because suspensions internal friction is negligible in this condition.

After these considerations, it is possible to split the load cells acquisition in the contributions highlighted in the Equation 2.22, where W_i is the static load, $Aerodown_i$ is the downforce, both referred to the axle i, $\Delta F^{DYN}_{SA_{ij}}$ is the load acting on the suspension ij due mainly to the lateral load transfer and in general to the dynamic running of the vehicle and $\Delta F^{Offset}_{SA_{ij}}$ is the load cell offset, always for the shock absorber ij.

$$\frac{F_{SA_{ij}}}{MR_{SA_{ij}}} = \frac{W_i}{2} + \frac{Aerodown_i}{2} + \Delta F^{DYN}_{SA_{ij}} + \Delta F^{Offset}_{SA_{ij}} \tag{2.22}$$

In pit lane, or in any other chosen range for the dynamic offset identification, the $\Delta F^{DYN}_{SA_{ij}}$ contribution is equal to zero, so in this condition, it is possible to evaluate $\Delta F_{SA_{ij}}^{Offset}$ (Equation 2.23).

$$\Delta F_{SA_{ij}}^{Offset} = mean\left|\frac{F_{SA_{ij}}}{MR_{SA_{ij}}} - \frac{W_i}{2} - \frac{Aerodown_i}{2}\right|_{Range} \tag{2.23}$$

After that, it is possible to evaluate $\Delta F_{SA_{ij}}^{DYN}$, which represents the real additional information provided by the load cells (Equation 2.24).

$$\Delta F_{SA_{ij}}^{DYN} = \frac{F_{SA_{ij}}}{MR_{SA_{ij}}} - \frac{W_i}{2} - \frac{Aerodown_i}{2} - \Delta F_{SA_{ij}}^{Offset} \tag{2.24}$$

After determining the contribution due to the dynamic forces acting on the shock absorbers, it is possible to focus the attention on the anti-roll bars that, usually, present a single load cell mounted on one side. The position in which this sensor is installed depends on the vehicle geometry and on how the bar is mounted. To be used in the calculation of the vertical forces, the signal read by the load cell must be divided by 2 and must be grounded using the motion ratio of the bars, defined as in Equation 2.25.

$$MR_{ARB_i} = \frac{\Delta z_{ij}}{S_{ARB_i}} = \frac{\frac{F_{ARB_i}}{2}}{F_{z_{ARB_{ij}}}} \tag{2.25}$$

In which Δz_{ij} is the bump for the generic wheel, S_{ARB_i} is the displacement of the bar with respect to its undeformed position (generally referred to as the blade position), F_{ARB_i} is the force acting on the anti-roll read thanks to the load cell mounted and, finally, $F_{z_{ARB_{ij}}}$ is the vertical force on the wheel ij due to the anti-roll bar action. In a similar way to what has been just seen with the load cells of the shock absorbers, also the sensors mounted and ARB are generally affected by offset. To remove them, in this case, it is necessary to find the relationship between the load acting on the anti-roll bar and the lateral acceleration. The side on which the sensor is installed affects the sign of this correlation; if the mounting side is unknown, it can be

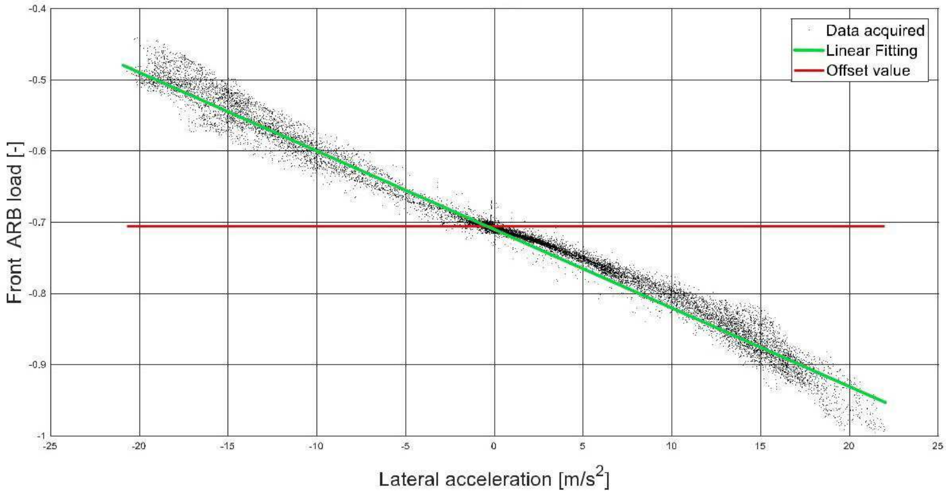

Fig. 2.15 Anti-roll Bar Force vs Lateral Acceleration, in the graph also the linear fitting and the offset value are shown

determined from this procedure. It is possible to synthesize the correlation between force and acceleration through a linear fitting (Figure 2.15) which returns two coefficients m and q, respectively slope and intercept of the least square fitting line. q represents the ARB load cells offsets and, therefore, the ARB forces reported to the ground can be evaluated as in the Equation 2.26.

$$F_{z_{ARB_{ij}}} = \frac{F_{ARB_{ij}} - q_i}{MR_{ARB_i}} \cdot \frac{1}{2} \cdot \frac{m_i}{|m_i|} \tag{2.26}$$

2.4.3 Vertical Forces Formulation and 'Anti Geometry' Effects

Having determined all the contributions provided by the load cells, it is possible to write the new vertical forces formulation (Equation 2.27).

$$F_{z_{ij}-SA} = \frac{W_i}{2} + \frac{Aerodown_i}{2} + \Delta F_{SA_{ij}}^{DYN} + F_{z_{ARB_{ij}}} \tag{2.27}$$

The application of this formula leads to a better estimation of the vertical forces only if all the loads pass through the suspension, as it happens in classic suspensions [113]; in most cases, however, race cars are designed with more performing suspensions with specific geometries useful to transfer part of the loads directly on the chassis to reduce some undesired body motions. The center of gravity (CoG) is the center of rotation for any acceleration or braking input. Because the front and rear suspensions are generally different in type and/or trim, the axles behave differently, resulting in dissimilar pitch motions depending on how the driving and braking forces are transmitted. To differentiate the various pitching modes of the car body subject to longitudinal accelerations, four terms are commonly used:

- Lift: lifting the front of the car under acceleration (for front-wheel-driven and four-wheel-driven cars);
- Squat: lowering the rear under acceleration (for rear-wheel-driven cars);
- Dive: lowering the front and lifting the rear under braking (for all vehicles with braking on both axles);
- Pitch: generic pitching, not directly connected to a specific maneuver, i.e. simultaneous and opposite shaking of the front and rear axles;

To prevent and minimize these rotations, an opposing force needs to be applied to the CoG; this opposite force comes from the anti-geometry specifically designed for the suspension systems. The 'anti-effects' in suspension systems describe the longitudinal to vertical force coupling between the sprung and the unsprung masses [114]. It results purely from the angle or slope of the side view virtual swing arm. However, it has been found that lateral forces also contribute to these effects by stressing the vehicle suspension system and thus producing vertical forces on them. As for the longitudinal anti-effects, also the lateral one can be obtained by designing the suspension arms with specific angles, which allow contrasting the diving or the lifting of the front or rear axle due to lateral forces. A common misconception is that anti-geometry controls or affects wheel loading where more squat on accelerating will give more rear wheel loading. Actually, wheel loading remains the same regardless of anti-geometry as the total longitudinal load transfer under steady state acceleration or braking is a function of the wheelbase, braking or acceleration force and center of gravity height. Anti-geometry gives the possibility to understand which is the amount of load going through the springs and the pitch attitude of the car. If a suspension has 100% anti, all the longitudinal load transfer is carried by the control arms and none by the suspension springs, so the suspension does not deflect when braking or accelerating. If the suspensions are designed with an anti-geometry, this implies that part of the load transfer does not act on the shock absorbers and, therefore, it is not acquired by the load cells.

In order to evaluate the vertical forces properly, taking into account also the anti-effects, the following procedure is implemented in the T.R.I.C.K. 2.0:

1. First of all, the vertical forces are evaluated without considering anti-effects, adopting the original formulation of the T.R.I.C.K. based on equilibrium equations.

2. Then, the F_z forces are used to evaluate the lateral and the longitudinal forces, adopting the classic formulation or the one illustrated in the next paragraph.

3. Finally, once calculated the tangential forces, the contribution of the anti-effects can be taken into account, calculating the so-called longitudinal and lateral jacking forces, obtained by multiplying the longitudinal and lateral forces by the particular angles with which the suspension has been designed according to the concepts of anti's geometries. These contributions vary in type and sign depending on the dynamic condition in which the vehicle is operating.

According to this procedure, it is possible to evaluate the longitudinal jacking forces:

- For deceleration maneuvers (measured $a_x < 0$, Anti-Dive and Anti-Lift effects):

$$F_{zFj_{AD-Fx}} = AD_{Fx} \cdot F_{x_{Fj}} \tag{2.28}$$

$$F_{zRj_{AL-Fx}} = AL_{Rx} \cdot F_{x_{Rj}} \tag{2.29}$$

- For acceleration maneuvers (measured $a_x > 0$, Anti-Squat effect):

$$F_{zRj_{AS-Fx}} = AS_{Rx} \cdot F_{x_{Rj}} \tag{2.30}$$

In the same way, it is possible to evaluate the lateral jacking forces:

- For front wheels:

$$F_{zFL_{AD-Fy}} = \pm AD_{Fy} \cdot F_{y_{FL}} \tag{2.31}$$

$$F_{zFR_{AD-Fy}} = \mp AD_{Fy} \cdot F_{y_{FR}} \tag{2.32}$$

In which, for Equation 2.31, the plus sign is used when $F_{zFL-SA} > F_{zFR-SA}$, while the sign minus is used in Equation 2.32 in the same condition.

- For front wheels:

$$F_{zRL_{AL-Fy}} = \pm AL_{Ry} \cdot F_{y_{RL}} \tag{2.33}$$

$$F_{zRR_{AL-Fy}} = \mp AL_{Ry} \cdot F_{y_{RR}} \tag{2.34}$$

In which, for Equation 2.33, the plus sign is used when $F_{zRL-SA} > F_{zRR-SA}$, while the sign minus is used in Equation 2.34 in the same condition.

Finally, the various contributions are added together to obtain the final value of the vertical forces:

$$\begin{cases} F_{zFL} = F_{zFL-SA} + F_{zFL_{AD-Fx}} + F_{zFL_{AD-Fy}} \\ F_{zFR} = F_{zFR-SA} + F_{zFR_{AD-Fx}} + F_{zFR_{AD-Fy}} \\ F_{zRL} = F_{zRL-SA} + F_{zRL_{AL-Fx}} + F_{zRL_{AS-Fx}} + F_{zRL_{AL-Fy}} \\ F_{zRR} = F_{zRR-SA} + F_{zRR_{AL-Fx}} + F_{zRR_{AS-Fx}} + F_{zRR_{AL-Fy}} \end{cases} \tag{2.35}$$

Modeling the anti-effects using the methodology just described is fundamental to obtain a substantial improvement in vertical forces estimation, leading to better visualization of the global adhesion ellipses. This is because considering these effects, it is possible to evaluate contributions that are not read by the load cell sensors, partially neglected adopting the classical formulation based only on the equilibrium equations.

2.4.4 Camber Angle Evaluation

Camber angle is one of the most relevant tire characteristic angles; it is defined as the inclination angle between the tire's equatorial plane and the road's vertical plane. Tires are generally mounted with a camber angle not equal to zero to improve the overall vehicle performance in lateral dynamics, overcoming the issues related to the adoption of a toe angle different from zero [115, 116]. A precise estimation of the dynamic variation of the camber angle is fundamental to understand the vehicle behavior and how it changes during the run, giving helpful information about functioning. In the previous version of the tool a formulation to estimate the camber angle was already present; although this formulation was based on physical phenomena directly related to the camber, it was characterized by excessive simplifications. In order to better approximate dynamic camber trend, within the T.R.I.C.K. 2.0 a new formula has been implemented, it is based on experimental evidence which links specific vehicle parameters to experimental coefficients, as it is shown in Equation 2.36.

$$\gamma_{Dyn_{ij}} = \gamma_{Stat_{ij}} + \phi C1_i + \Delta H_{Axle_i} C2_{ij} + F_{y^{ij}} C3_i + \delta C4_i \qquad (2.36)$$

In which $\gamma_{Stat_{ij}}$ is the static camber angle (deg), ϕ is the roll angle (deg), ΔH_{Axle_i} is the vertical axle displacement (mm), $F_{y^{ij}}$ is the lateral force acting on the tire (N), δ is the steering angle (deg), $C1_i$, $C2_{ij}$, $C3_i$ and $C4_i$ are the experimental coefficients and their units of measurement are respectively (deg/deg), (deg/mm), (deg/N) and (deg/deg); these coefficients allow the conversion of the previous contributions into a camber variation. After a consistency check on the signs of the different contributions for each corner, the study focused on the estimation of the vertical displacement ΔH_{Axle_i}, exploiting the additional sensors mounted on the vehicle already presented in the previous sections. Different strategies to evaluate ΔH_{Axle_i} have been compared, leading to different ways of evaluating the camber angle:

- Classic Camber Formulation, in which ΔH_{Axle_i} is estimated as the product between vehicle speed and a sort of medium axle displacement provided by the manufacturer (constant and indicated as lowering aero);

- Laser Sensors Camber Formulation, the laser sensors are used to determine the axles' vertical displacement over time;

- Potentiometers Camber Formulation, in which starting from the shock absorbers' displacements measured by the potentiometers, through the motion ratio, it is possible to evaluate ΔH_{Axle_i};

- Load Cells Camber Formulation, similarly to what has been done with potentiometers, vertical displacements can be evaluated starting from the forces acquired by the shock absorbers' load cells.

All these methods to evaluate the vertical axles displacements represent a concrete overcome of the classic formulation and can be used interchangeably depending on the sensors available.

2.5 Tangential Force Formulation

One of the most consistent improvements in the T.R.I.C.K.2.0 tool is strictly related to the evaluation of the tangential forces, which affect the adherence ellipses evaluation. First, an in-depth analysis of the switch conditions between the acceleration and braking phases was carried out to eliminate the discontinuities present in the values of the evaluated loads. Subsequently, the new formulation for the longitudinal forces is presented; it is based on the use of brake pressure sensors installed on the vehicle. In this new approach these sensors, together with knowledge of specific vehicle's braking system parameters, help in the distribution of longitudinal forces among the four corners. Finally, the Limited Slip Differential's role in tangential force distribution is shown, focusing attention on the effects on longitudinal and lateral force explication.

2.5.1 Longitudinal Forces Formulation Switch

In the original version of the T.R.I.C.K. tool, there are two formulations for calculating longitudinal forces, one for traction maneuvers and one for braking phases, as illustrated in appendix A. The switch between these two is only a function of lateral acceleration. It has been observed that, in correspondence with the change of sign of the lateral acceleration, all the longitudinal forces exhibited a discontinuity.

To understand why the discontinuities highlighted in Figure 2.16 occur, the physical behavior of the vehicle during the transition phase between braking and acceleration was analyzed in detail. It has been noticed that the vehicle is still in the acceleration phase when the torque supplied by the engine is greater than all the passive resistances acting on the car. These passive resistances consist of aero-drag force, rolling resistance and rolling inertia of all four wheels. Thanks to this consideration, the switch between the formulations has been changed according to Equation 2.37, which identifies

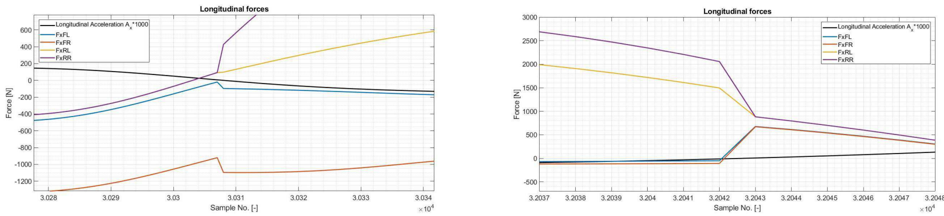

(a) Transition from positive to negative acceleration

(b) Transition from negative to positive acceleration

Fig. 2.16 Discontinuity of longitudinal forces due to acceleration's sign change

an acceleration maneuver. $F_{RollRes_{ij}}$ and $F_{WIR_{RL}}$ identify, respectively, the rolling resistance and the wheel rotational inertia for the generic corner ij.

$$ma_x \geq Aerodrag + F_{RollRes_{FL}} + F_{RollRes_{FR}} + F_{RollRes_{RL}} + F_{RollRes_{RR}} + \\ + F_{WIR_{FL}} + F_{WIR_{FR}} + F_{WIR_{RL}} + F_{WIR_{RR}} \quad (2.37)$$

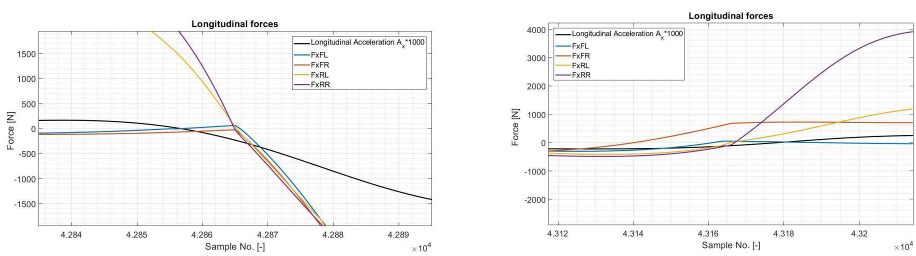

(a) Transition from acceleration to braking maneuver

(b) Transition from braking to acceleration maneuver

Fig. 2.17 Longitudinal forces due to acceleration's variation with the new switch condition

As it is possible to see from Figure 2.17, adopting the new switch condition, the change of sign of the longitudinal acceleration no longer causes the discontinuities detected with the original formulation. This result is obtained because the switch does not occur in that condition. The change of the formulations occurs for longitudinal acceleration values less than zero, but in correspondence of the switch condition, there is only a change of forces' slope without discontinuity, as it is possible to see in the graphs. In correspondence with the switch condition, therefore, only angular points are observed, which are not real but cannot be eliminated due to the simplifying assumptions on which the tool is based.

2.5.2 Brake Pressure Sensors & Longitudinal Forces calculation

To develop a new formulation for the evaluation of the longitudinal forces, a further step has been carried out for what concerns the vehicle total drag definition, as it is possible to see in Equation 2.38.

$$\begin{aligned} TotalDrag = Aerodrag &+ F_{RollRes_{FL}} + F_{RollRes_{FR}} + F_{RollRes_{RL}} + F_{RollRes_{RR}} + \\ &+ F_{WIR_{FL}} + F_{WIR_{FR}} + F_{WIR_{RL}} + F_{WIR_{RR}} + \\ &+ F_{Steer_{FL}} + F_{Steer_{FR}} + F_{Steer_{RL}} + F_{Steer_{RR}} \end{aligned} \tag{2.38}$$

Considering the switch proposed in Equation 2.37, this definition of the global vehicle aero-drag takes into account also the $F_{Steer_{ij}}$ contribution. These additional forces, neglected in the first release of the tool, are fundamental for the right writing of the equilibrium equations; indeed, they consider the "internal" contributions due to the steering system compliance, generally not considered when overall vehicle equations are written. These forces represent the longitudinal component of the force that the tire exerts along the orthogonal direction to itself, if the tire is in free rolling condition during a steering maneuver (on the rear wheels this contribution is minimal). Generally, the tire is not in free rolling, but the error committed with this assumption still leads to a better estimation of the longitudinal forces, if compared with the classical approach in which this phenomenon is not considered.

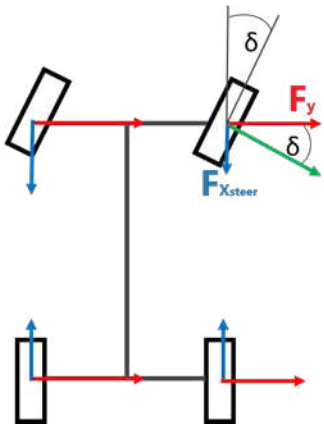

Fig. 2.18 Graphic representation of the $F_{Steer_{ij}}$ contribution

From the consideration made above, it is possible to evaluate $F_{Steer_{ij}}$ as in Equation 2.39.

$$F_{Steer_{ij}} = F_{y_{ij}} tan(\delta_{ij}) \tag{2.39}$$

With reference to Figure 2.18, the green arrow is the force that arises in the orthogonal direction of the steering tire and of which $F_{Steer_{ij}}$ represents the longitudinal component. Thanks to this consideration it is possible to define two conditions for the longitudinal forces evaluation:

- Traction Maneuver if $a_x > TotalDrag/m$: in this case the formulation remains unchanged and it is possible to evaluate the longitudinal forces as in Equations 2.40 to 2.43. Traction shall be distributed between the two driving wheels according to the vertical load acting on them.

$$F_{x_{FL}} = F_{RollRes_{FL}} + F_{WIR_{FL}} + F_{Steer_{FL}} \tag{2.40}$$

$$F_{x_{FR}} = F_{RollRes_{FR}} + F_{WIR_{FR}} + F_{Steer_{FR}} \tag{2.41}$$

$$F_{x_{RL}} = F_{RollRes_{RL}} + F_{WIR_{RL}} + F_{Steer_{RL}} + (ma_x - TotalDrag) \cdot \frac{F_{z_{RL}}}{F_{z_{RL}} + F_{z_{RR}}} \tag{2.42}$$

$$F_{x_{RR}} = F_{RollRes_{RR}} + F_{WIR_{RR}} + F_{Steer_{RR}} + (ma_x - TotalDrag) \cdot \frac{F_{z_{RR}}}{F_{z_{RL}} + F_{z_{RR}}} \tag{2.43}$$

- Braking Maneuver if $a_x \leq TotalDrag/m$: to evaluate the distribution of the braking forces, the knowledge of some parameters of the braking system, provided by the manufacturer, is necessary. This information is coupled with the signals acquired from the brake pressure sensors that measure the relative braking pressure on the two axles. Using the signal of these sensors, installed on the braking lines, after a preliminary filtering operation, it is possible to take into account the real distribution of the braking forces of the vehicle among the four corners. The brake caliper coefficient C_{p_i} is defined as in Equation 2.44, in which A is a conversion factor, μ_i is the friction coefficient of the brake caliper, $Area_{Piston_i}$ and R_{Disc_i} are respectively the piston area and the brake disc radius.

$$C_{p_i} = A\mu_i Area_{Piston_i} R_{Disc_i} \tag{2.44}$$

Using this coefficient and the brake pressure signals, it is possible to obtain the longitudinal forces related to the brake pressures for each axle, as illustrated in Equation 2.45.

$$F_{xB_i} = p_{Brake_i} \cdot \frac{C_{p_i}}{R_i} \tag{2.45}$$

In addition, among the braking forces, also the contribution related to the braking force exerts by the engine, $F_{XB_{Eng}}$, has to be considered; it influences directly the braking forces on the rear axle, for a rear wheel drive vehicle. After the definition of these forces that represent the braking effect, the forces on the four corners during the braking phase can be written as in Equations 2.46 to 2.49. The detailed description of the terms that appear within them if left to the following subsection, in which also the contribution of the Limited Slip Differential will be analyzed.

$$F_{x_{FL}} = F_{RollRes_{FL}} + F_{WIR_{FL}} + F_{Steer_{FL}} + \\ + \frac{1}{2} \cdot (ma_x - TotalDrag) \cdot \frac{F_{xB_F}}{F_{xB_F} + F_{xB_R} + F_{xB_{Eng}}} \quad (2.46)$$

$$F_{x_{FR}} = F_{RollRes_{FR}} + F_{WIR_{FR}} + F_{Steer_{FR}} + \\ + \frac{1}{2} \cdot (ma_x - TotalDrag) \cdot \frac{F_{xB_F}}{F_{xB_F} + F_{xB_R} + F_{xB_{Eng}}} \quad (2.47)$$

$$F_{x_{RL}} = F_{RollRes_{RL}} + F_{WIR_{RL}} + F_{Steer_{RL}} + \\ + (ma_x - TotalDrag) \cdot \frac{F_{xB_R} + F_{xB_{Eng}}}{F_{xB_F} + F_{xB_R} + F_{xB_{Eng}}} \cdot \frac{F_{z_{RL}}}{F_{z_{RL}} + F_{z_{RR}}} \quad (2.48)$$

$$F_{x_{RR}} = F_{RollRes_{RR}} + F_{WIR_{RR}} + F_{Steer_{RR}} + \\ + (ma_x - TotalDrag) \cdot \frac{F_{xB_R} + F_{xB_{Eng}}}{F_{xB_F} + F_{xB_R} + F_{xB_{Eng}}} \cdot \frac{F_{z_{RR}}}{F_{z_{RL}} + F_{z_{RR}}} \quad (2.49)$$

2.5.3 Limited Slip Differential Effects on Tangential Forces

The vehicle taken as reference in this research activity, as well as many other racing vehicles, mounts a Limited Slip Differential (LSD) (Figure 2.19), different from the classic one, also called open differential. This kind of differential allows limiting the relative motion between the two axle shafts, which is very useful in particular situations such as when one of the two wheels slides, always ensuring traction [117]; the most evident advantage is in curves, both in terms of traction and trajectory.

Taking into account the effects of the LSD, it is possible to resume Equations from 2.46 to 2.49, making some considerations about the terms that constitute them. The first three terms of each equation $F_{RollRes_{ij}} + F_{WIR_{ij}} + F_{Steer_{ij}}$ represent the resistance to the advancement and these terms are present on all the four wheels but they are slightly different for each wheel. The quantity $(ma_x - TotalDrag)$ is a negative term because the vehicle is in braking conditions and it indicates the difference between the driving force and the resistances. This difference for the front wheels is equally divided between right and left, according to the impact of F_{xB_F} on the sum of F_{xB}; for the rear wheels, instead, the formulation is different due to the presence of the LSD. Indeed, the ratio $\frac{F_{xB_R}+F_{XB_{Eng}}}{F_{xB_F}+F_{XB_R}+F_{XB_{Eng}}}$ represents the work that the differential does in distributing the forces between the two rear wheels, also taking into account the maximum torque limit that can be transferred by the differential between one wheel and the other. Considering Figure 2.20, the blue curve represents the transferable torque limit, beyond which the differential locks, as a function of the input torque. Under braking conditions (input torque <0), all the points belonging to the area under the curve represent points where the differential works correctly and distributes the longitudinal forces according to the Equations 2.48 and 2.49. The points on the line represent the transferable torque limit, following the equation of the line with angular

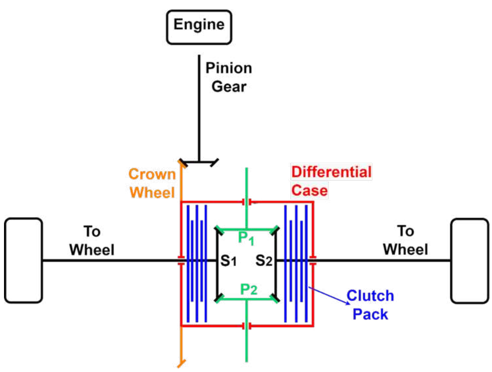

Fig. 2.19 Limited Slip Differential gear scheme

coefficients m_{LSD}, which depends on the engine characteristics, whereas the points above the line have no physical meaning.

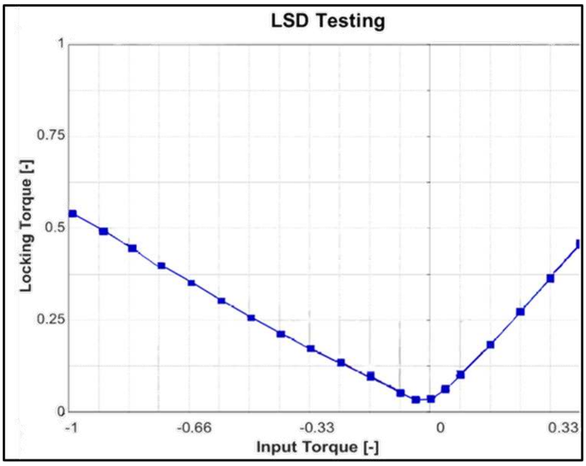

Fig. 2.20 Torque analysis for a generic Limited Slip Differential

When the difference between the braking forces at the rear is greater than the maximum transferable force, according to the previous image, it is as if the braking force is above the line limit, so the physical sense is lost. The longitudinal forces formulation for rear wheels in this condition then changes according to Equations 2.50 and 2.51.

$$\begin{aligned} F_{xRL} = {} & F_{RollRes_{RL}} + F_{WIR_{RL}} + F_{Steer_{RL}} + \\ & + (ma_x - TotalDrag) \cdot \frac{1}{2} \frac{F_{xB_R} + F_{xB_{Eng}}}{F_{xB_F} + F_{xB_R} + F_{xB_{Eng}}} \pm m_{LSD} F_{xB_{Eng}} \end{aligned} \tag{2.50}$$

$$\begin{aligned} F_{xRR} = {} & F_{RollRes_{RR}} + F_{WIR_{RR}} + F_{Steer_{RR}} + \\ & + (ma_x - TotalDrag) \cdot \frac{1}{2} \frac{F_{xB_R} + F_{xB_{Eng}}}{F_{xB_F} + F_{xB_R} + F_{xB_{Eng}}} \mp m_{LSD} F_{xB_{Eng}} \end{aligned} \tag{2.51}$$

In which $m_{LSD} F_{xB_{Eng}}$ is precisely the maximum transferable braking force and it is taken with the positive or negative sign depending on which is the faster wheel. The force just described is also responsible for the effect that LSD has on the lateral forces F_y (Figure 2.21); causing a difference between the longitudinal forces, a yaw torque is generated, which must be balanced by an opposite yaw torque caused by a variation of the lateral forces $(\Delta F y)$. Therefore, it will be an additional contribution to add or subtract (depending on the driving conditions) to the F_y formulation which must be considered.

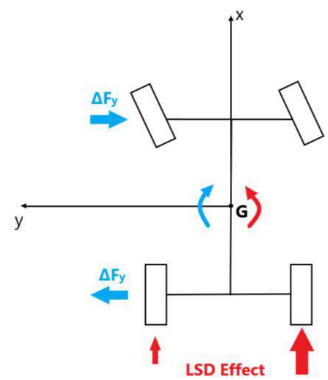

Fig. 2.21 Limited Slip Differential effect on the lateral forces F_y

2.6 Results & Validation

All the new formulations introduced in this work in the previous section represent an alternative to those already existing in the first version of T.R.I.C.K. and not a replacement; consequently, there will be more ways to determine a specific quantity. For this reason, at the end of all the operations of the pre-processing phase (data loading in the tool, identification and cancellation of the offsets, check on the values of the sensors and so on) the user is given the possibility to choose the formulations to be adopted for the simulation in question through an intuitive control panel (Figure 2.22).

In particular, the user can choose how to evaluate the following quantities:

- Roll Angle
- Aerodynamic Forces
- Roll Stiffness
- Vertical Forces
- Camber Angle

In the following paragraphs, several comparisons between the classical formulations and new ones will be presented to assess the improvement made in this new version of the tool. All the comparisons take as reference the data provided by a simulator, in which a detailed digital twin of the reference vehicle is implemented; this virtual vehicle model is much more complex than the one introduced in the T.R.I.C.K 2.0, constituting a reliable reference to evaluate the tool performance. Finally, it is important to underline that, for industrial confidential agreement, all the plots and the diagrams will be provided as resized.

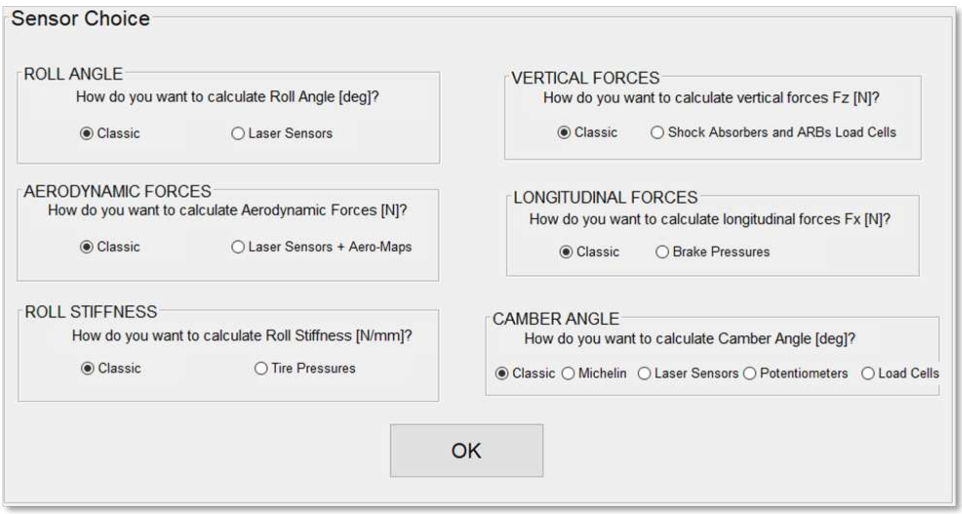

Fig. 2.22 Sensor choice panel representation in the T.R.I.C.K. 2.0 GUI

2.6.1 Camber Angles

As already illustrated in paragraph 2.4.4, the dynamic camber angle has been evaluated using the experimental Equation 2.36. In particular, there are four different methods to estimate ΔH_{Axle_i}, all examined in Figure 2.23. The figure always shows the same tire (Front Left) for the same stretch of simulation, but clearly, the data obtained are representative of the other tires and conditions. From the Figure 2.23 it is possible to make some considerations:

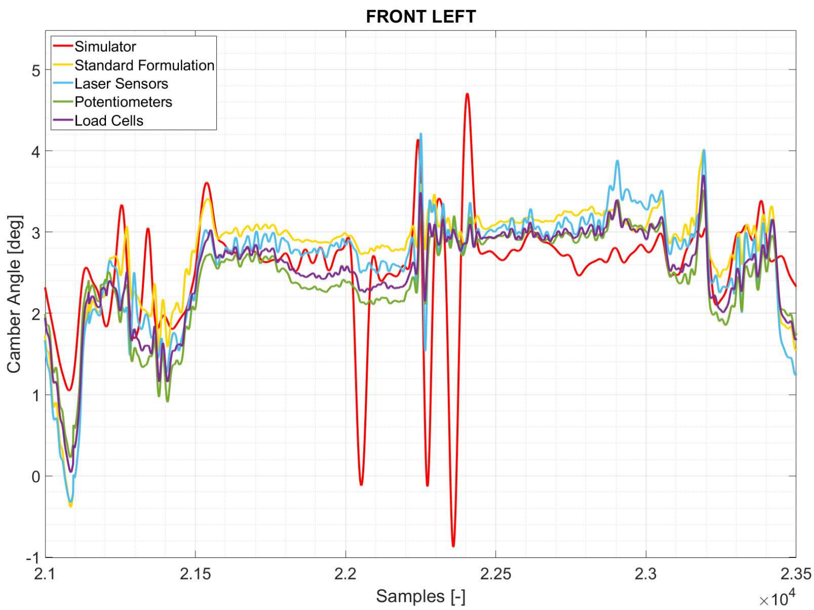

Fig. 2.23 Global comparison among the different ways to estimate the camber angle and the simulator run

- the Classic Formulation discretely approximates the camber trend, but is based on a fixed parameter, the lowering aero, less reliable than the sensors;
- the formulation that involves the use of laser sensors is valid in straight stretches, but tends to lose meaning if there are changes during the run

(road pit, lateral slope changes or curves), probably because this sensor, although filtered, is more sensitive than the others (it presents higher spikes);

- finally, the formulations with potentiometers and shock absorbers load cells are the most conservative as they never have values that are too far from those typical of dynamic camber. In particular, the potentiometer formulation seems slightly better as it is characterized by a cleaner signal and it is the one that overall provides a result closer to the simulator one on the four corners.

2.6.2 Tire/Road Interaction Forces

In the purpose of verifying the new considerations introduced in the previous chapter about the study of F_x, F_y and F_z forces, it was decided to realize a comparison among many simulation files, each of these obtained through the use of combinations from different formulations. Using the sensor choice panel already presented and changing four of the six switches available (aerodynamic forces, roll stiffness, vertical forces and longitudinal forces), sixteen different possibilities to evaluate the tire-road interaction forces are obtained; for brevity, only two cases are reported in the following figures: the one in which all the classical formulation are adopted and the other one in which all the additional sensors are available and functioning.

Longitudinal Forces

For what concerns the longitudinal forces, also the classical formulation was updated with the new switch discussed in section 2.5.1; then a comparison among the classical F_x formulation (T.R.I.C.K. Baseline), the one obtained using pressure sensors and the longitudinal forces obtained from the simulator was performed (Figure 2.24). In addition to the forces plot, there is also an acceleration plot, useful for understanding the vehicle's operating condition.

As can be seen from Figure 2.24, for two different tires, the use of pressure

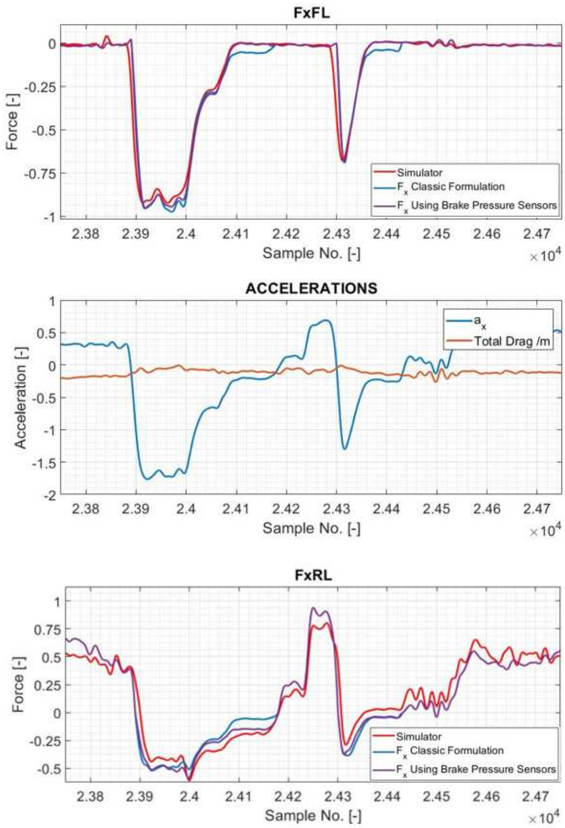

Fig. 2.24 F_x comparison between classical and brake pressure formulations for Front Left and Rear Left tires

sensors leads to an improvement in the F_x trend compared to the simulator data. In particular, while in traction condition $a_x > TotalDrag/m$ the compared trends are identical, it is in braking $a_x < TotalDrag/m$ and in the transition from braking to acceleration that the effect of the sensors can be noticed, with a deviation from the reference more contained. This happens because in this new formulation during braking is also taken into account the effect of LSD. In particular, the relative error between the estimated forces and the simulator is reduced on the average of the 8% for the front tires and od the 20% for the rear tires.

Lateral Forces

The only change made in the F_y formulation is related to the consideration of the LSD effects which causes a torque balanced through a lateral forces variation. Indeed, as it is possible to see in Figure 2.25, between the classical

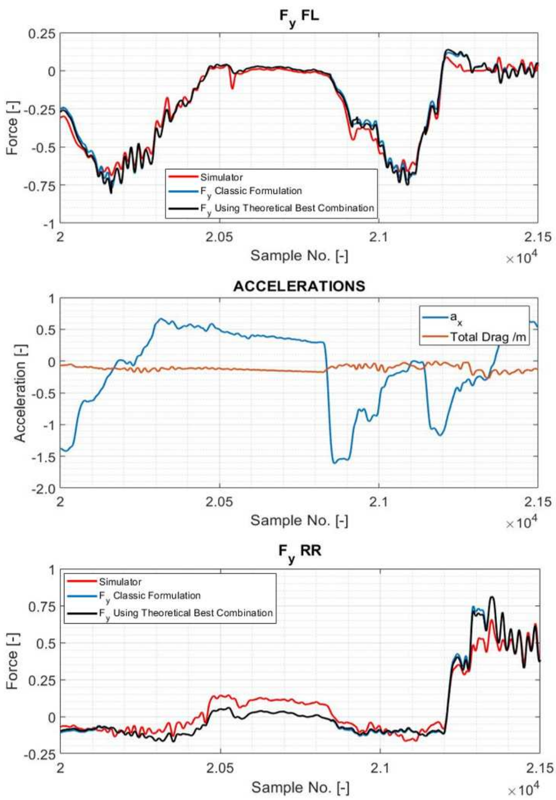

Fig. 2.25 F_y comparison between classical and best theoretical formulations for Front Left and Rear Left tires

formulation (in blue) and the theoretical best combination, using all the additional sensors (in black), there are only small differences. The improvements are noticeable only under braking conditions because the effect of the LSD is implemented only in combination with the use of the braking pressure; in this case, the estimated forces follow slightly better simulator trends.

Vertical Forces

As seen in section 2.4, in T.R.I.C.K. 2.0 it was chosen to evaluate the vertical forces using the load cells mounted on the vehicle's shock absorbers and anti-roll bars. From Figure 2.26 it can be observed how the use of the formulation

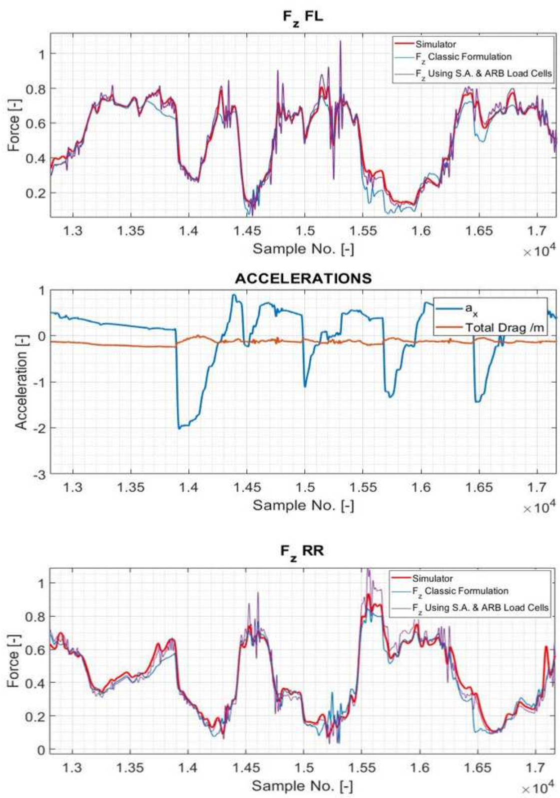

Fig. 2.26 F_z comparison between classical and shock absorbers and ARB formulations for Front Left and Rear Left tires

that considers the sensors, although characterized by a more evident noise, is able to ensure a more consistent trend if compared with the reference simulator data, and this can be found both in braking and acceleration conditions.

The improvements obtained with this new formulation are also attributable to the implementation of the anti-effects within the Fz formulation. Taking these effects into consideration, in fact, some contributions are added to the calculation of the vertical forces, that would otherwise be neglected because the forces generated by the anti-geometries act on the suspension arms and therefore could not be read by the sensors. It should also be highlighted that a complete vertical forces analysis has taken place with the implementation of the tire stiffness, calculated by the tire pressure sensors, within the calculation of the roll stiffness. Unfortunately, the simulator runs do not have any information about tire pressure sensors, so it is only possible to verify this aspect for a real run.

2.6.3 Interaction Curves

In order to provide a complete overview of the results achieved with the T.R.I.C.K. 2.0, also the longitudinal and lateral interaction curves are reported. In particular, to highlight the longitudinal behavior of the tires, the diagrams $F_{x_{ij}}/F_{z_{ij}}$ vs Slip Ratio $s_{x_{ij}}$ for each corner are visible in Figure 2.27, whereas lateral characteristics, in four $F_{y_{ij}}/F_{z_{ij}}$ vs Slip Angle α_{ij} plots are shown in Figure 2.28. In both figures are compared, for the four corners, the classic formulations (T.R.I.C.K. Baseline) with the new version of the tool, using all the new formulations simultaneously. As can be observed at first sight in both figures, the curves obtained using the new formulations better approximate those provided by the simulator. In particular, Figure 2.27 shows the grip behavior of each tire in different thermal and interaction conditions (pure and combined); since the vehicle is rear-wheel drive, front wheels only provide information regarding braking. The reason why it is considered that the new trends (in yellow) are more accurate than the original ones is also linked to the more conservative values obtained in terms of grip both in traction

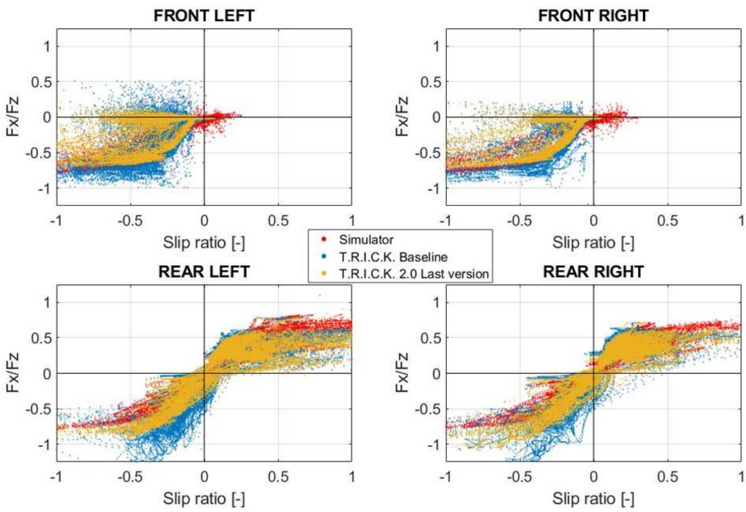

Fig. 2.27 Comparison of the tires' longitudinal characteristics between old and new tool version

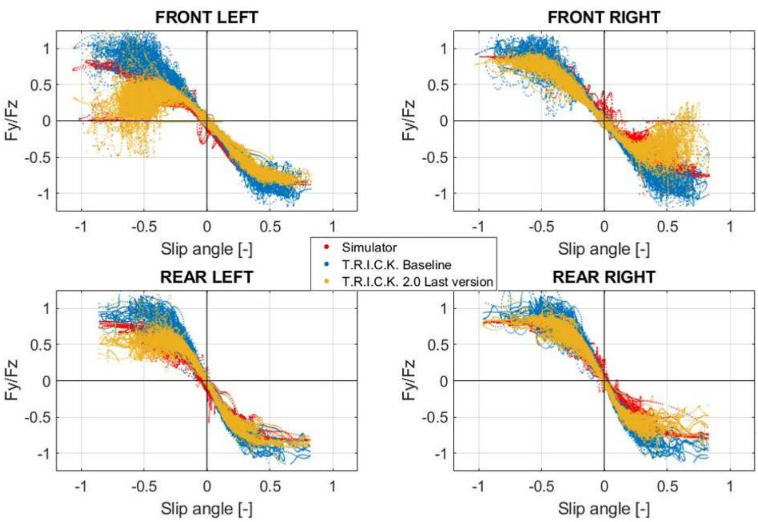

Fig. 2.28 Comparison of the tires' lateral characteristics between old and new tool version

and in braking: the grip values achieved from the basic version of the tool (blue curve) are considered unreliable because they are too high. This is probably due to an underestimation of the vertical load transfers evaluated with the old formulations, which causes the curve to rise for high slip values. This confirms that the new formulations concerning longitudinal and vertical forces help to converge toward a more realistic estimation, in accordance with the reference considered. Similar considerations apply to Figure 2.28; also in this case, despite the front wheels trend, that in conditions of high slip angles is not accurate if compared with the simulator values, the new trends are considered more reliable because they show more conservative and more real values in terms of lateral grip.

2.6.4 Adherence Ellipses

Finally, to conclude the analysis of the results obtainable with the T.R.I.C.K. 2.0 tool the adherence ellipses for each corner are reported. The adherence ellipse is virtually present underneath each tire it identifies the domain within which it is possible to work under adherence conditions. The ellipse, in the presented case, is expressed in terms of friction coefficients (Fx/Fz= longitudinal static friction coefficient, Fy/Fz= lateral static friction coefficient); its semi-axles represent the availability of grip in one direction or another. The adherence ellipses reported in Figure 2.29 are obtained from the simulator data, from the T.R.I.C.K. Baseline formulations and from the T.R.I.C.K. 2.0 new formulations, all used simultaneously.

Considering the ellipses obtained with the classical formulation, they deviate strongly both in shape and size from that obtained with the simulator, with a high deviation especially in braking conditions in curves (combined longitudinal and lateral interaction). This is mainly due to the fact that in the classical formulation several aspects related to the evaluation of tangential and vertical forces are not taken into account, such as the use of additional sensors or the desire to consider other aspects like the effect of the self-locking

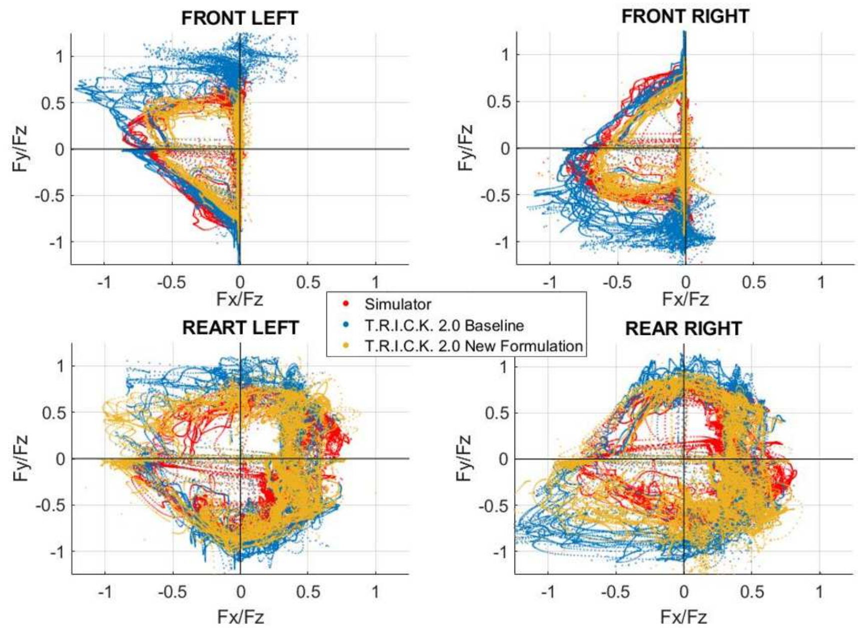

Fig. 2.29 Comparison of the tires' lateral characteristics between old and new tool version

differential for the tangential forces or the anti-effects for the vertical ones. For what concerns the ellipses obtained from the T.R.I.C.K. 2.0, it can be observed a considerable reduction in the area covered by the ellipses and a trend closer to the ellipse of the simulator; in particular, there is a clear improvement for the pure lateral (vertical axis), while a trend perhaps even too conservative as regards the front corners. The combined use of the load cells for the vertical force formulation and the brake pressure sensors used for the Fx formulation, involves, for all the adherence ellipses, a trend close to that of the simulator, confirming the advantages of using these sensors in the new formulations introduced. Moreover, these new formulas do not interfere with each other but rather converge toward a result very close to that provided by the simulator. The same concepts have been extended to real runs, where, although not having the simulator data as a reference, the same trends were found with the ellipses obtained with the new formulation characterized by a much smaller area than those obtained in the Baseline case (Figure 2.30).

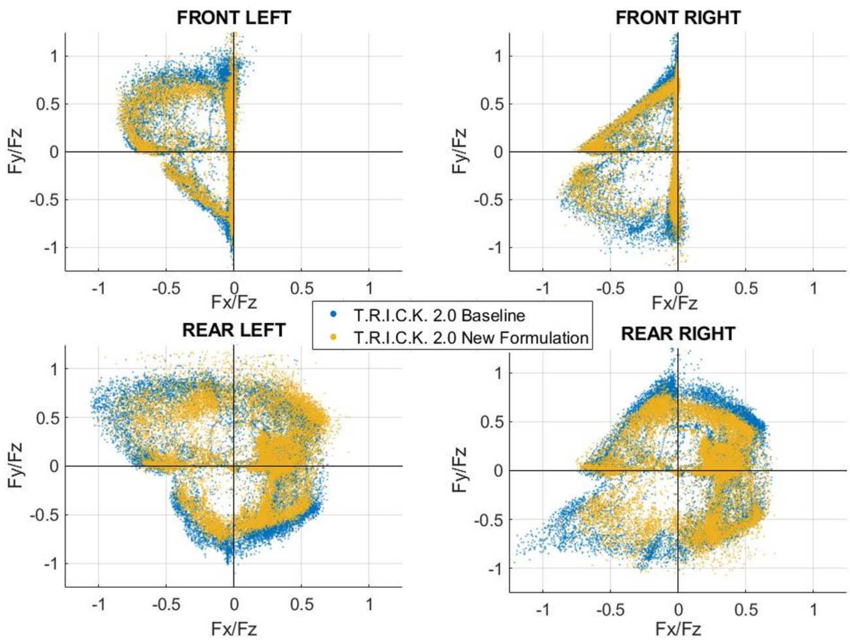

Fig. 2.30 Comparison of the tires' lateral characteristics between old and new tool version

2.6.5 Final Considerations

In this chapter, an evolved version of the T.R.I.C.K. tool has been presented; the T.R.I.C.K. 2.0 is born with the aim of overcoming the formulation already inserted in the tool to obtain a better estimation of the interaction force and dynamic camber angle. This is made possible through the use of additional sensors and parameters, generally adopted and known in high-level motorsport contexts. Thanks to the comparison of the results with the reference data provided by the simulator, it is possible to assess that this new version represents a concrete step forward for a better comprehension of the tire-road interaction phenomena, giving more reliable feedback on how the vehicle is working on track. In addition, the modularity of the tool gives to the user the possibility to choose the best approach to evaluate the interaction forces using all the information available in that particular test session, highlighting also eventual sensors malfunctioning. The simultaneous use of all the new formulations implemented leads to a sort of convergence toward the target, represented by the simulator, giving further confirmation of the goodness of the procedures presented in the previous paragraphs. The tool, in this new shape, is a powerful instrument to investigate vehicle and tires' performance and to understand the better operating conditions. Some further improvements can be obtained with more precise vehicle parameterization and carrying out dedicated outdoor test sessions to validate the estimation of the forces using specific sensors, such as dynamometric wheels.

Chapter 3

Virtual 7-Post Rig for Suspension Setup Optimization

3.1 Introduction

Talking about the vehicle's design, it is common to imagine the vehicle of interest that is tested on several types of benches in different ways in order to determine its strength, durability and performance. Some of these test benches are widely used by almost all the big manufacturers of vehicles both for common use and for motorsport applications. For a single vehicle, several test benches can be used, even extremely different from each other, in order to assess its global behavior and those of its components: the performance and the reliability of the endothermic, electric or hybrid engine, the goodness of the aerodynamic solutions of the vehicle, if this has a low drag coefficient and, in motorsport, if this has a high downforce; the suspensions' response from both the kinematics and dynamic point of view.

In the automotive industry, as well as in the motorsport field, vehicle dynamics modeling and simulation is one of the most important methodologies for handling and ride performance evaluation [118, 119]. Test rigs cannot always be exploited as they require a rarely sustainable economic expenditure, constituting often a limiting factor. For this reason, test benches can be exploited by the teams for a limited period, with consequent problems related to the replicability of the tests, which are sometimes slow and laborious. A further disadvantage is the possibility that during a test the vehicle may be damaged due to the stresses imposed by the actuators, inevitably bringing additional costs to the car manufacturer.

To cope with the limitations described, it was decided to combine real tests with a virtual simulation environment that anticipates what is expected to be obtained from the test bench. The virtual simulator is then introduced for a preventive and symbiotic study of all the systems that make up the vehicle, such as the engine, the chassis, the body (the aerodynamic surfaces) or suspension systems [120], in order to obtain several advantages over tests conducted with a test bench. Despite this, test benches remain a valuable tool and therefore support simulators if necessary. One of the advantages of simulations through virtual models is to study the vehicle even before the prototype is designed by simply entering input parameters that characterize it [121].

In addition, it is possible to carry out various real tests without having problems with their replicability, identifying all possible scenarios of interest and eliminating in advance those that gave unwanted results in virtual simulations. An additional advantage brought by the virtual simulation is the speed with which simulations can be made without needing the vehicle (or auxiliary systems). In the context of racing, the virtual model can be exploited at any time before the race, thus performing rapid analysis and whenever it is necessary, conditions impossible to replicate using a real test bench.

In recent years so-called "virtual test rigs" have become more and more important in the development process of cars. Originally, the idea was to substitute expensive durability tests with computer simulations. Meanwhile, the focus has changed towards a more cooperative usage of numerical and laboratory rig simulation. In early development stages, when no physical prototypes are available yet, numerical simulation is used to analyze and optimize the design, also when the cost of this test becomes more expensive to increase the performance of the cars in the motorsport sector [122]. In particular, this chapter focuses on the development of a virtual model able to reproduce the behavior of a real 7-post test bench in order to give useful output suggestions on how to optimize suspension setup before or during race weekend.

3.2 Post Shaker Rigs

Post shaker rigs are a specific type among all the Suspension Kinematics and Compliance test rigs and they are one of the most important measuring facilities in the automobile industry, which support chassis engineers for chassis tuning and development as well as vehicle dynamics simulations [123]. These rigs apply vertical loads, also at high-frequency, to the tested vehicle to analyze its response, typically on a specific road or track profile. Several versions of these rigs involve the use of 4/5/7 actuators or even more, depending on the degrees of freedom to be checked on the vehicle. In the following paragraphs, two of the most famous and used rigs will be exposed, the 4-Post and the 7-Post

3.2.1 4-Post

The simplest configuration for a Post Shaker Rig is the Four Post Shaker Rig. A hydraulic actuator called platforms is located underneath each wheel to push up on the tire, creating the four posts; each platform can be activated in a vertical vibrating mode to reproduce the vibrations induced by the road profile when running. As a matter of fact, the platforms are fitted on special hydraulic actuators connected to a hydraulic power unit and driven by a complex computer-controlled system (Figure 3.1) [124].

Fig. 3.1 4-Post Rig

These four actuators, known as wheel pans, move up and down in a controlled displacement to generate the asperities of a road surface being simulated or move across a frequency band in a controlled sweep to gain a general overview of the vehicle's behavior across its expected operating range. Profiles of roads can also be created for more specific purposes such as discrete profiles (striking a curb or pothole) or pink noise profiles to study specific energy inputs. 4-posters were and still are used in the vehicle industry to simulate chassis vertical dynamics as the vehicle travels over a rough road, by generating forces at the tire contact patches using electro-hydraulic servo-actuators. They are also used to characterize the suspension by exciting the 4-wheel patches, with either sine-sweeps or randomly (white noise). Control of the actuators can be operated in position, acceleration or force mode, in this configuration all the inertial load transfers and aerodynamic forces are not considered.

3.2.2 7-Post

Expanding upon the 4-post rig, the 7-post configuration adds three additional hydraulic actuators, like in Figure 3.2, in order to create aerodynamic forces and other movements in the racing car, the hydraulic actuators were rigidly fixed to the frame by means of three brackets [125]. The additional hydraulic actuators are called also aeroloaders. While the 4 posts push up on the tires, these three further actuators pull down on the chassis to apply the loads seen on the track and to take into account inertial effects deriving by braking and turning [126]; in this way, the vertical dynamics of a vehicle can be accurately simulated even for an entire lap [127]. The three aeroloader actuators present different problems: mechanically they are similar to the wheel actuators, although, they must track the motion of the sprung mass of the car, even when it goes into resonance, without varying the applied load.

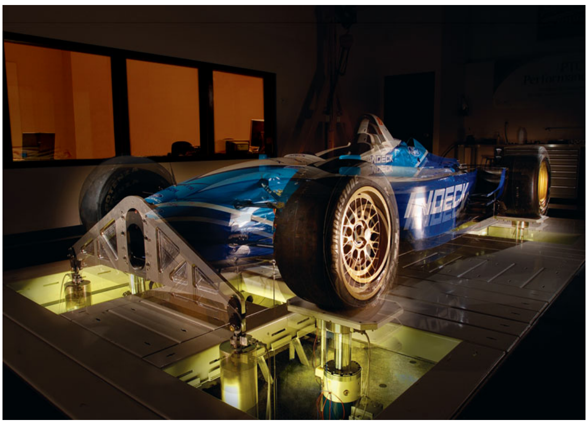

Fig. 3.2 7-Post Rig

Through the use of the 7 actuators, a 7-post can be used to accurately reproduce the vertical loads seen by a vehicle on track or road, allowing the faithful reproduction of the track's asperities in a controlled environment, measuring the effects of tuning changes on the vehicle. The rig enables to conduct several tests, the simplest are quasi-static suspension characteristics tests, yielding load/displacement curves for suspensions, roll control systems and allowing suspension kinematics to be measured with appropriate sensors [123]. The 7-post shaker enables the engineering staff of a race team to gain a better understanding of the dynamics of the vehicle. Resonance tests of the whole car on its suspension and tires are performed using sine sweeps and random excitation [127]. The fact that the tire is not rolling, as the damping of a static tire is less than a rotating one.

The 7-post machine offers the most rigorous way of testing a real suspension and how it interacts with the car. It is generally accepted that minimizing the variation in normal load will result in improved handling due to the minimization in lateral and longitudinal forces. Playing back a track profile on a 7-post shaker allows the engineer to study the effects of damping changes on the normal load variation at each tire.

3.2.3 4-post / 7-post Testing Measurements

The normal force of the tire on the wheel pan, known as the contact patch load, is measured to study how the tire load varies relative to load inputs, known as Contact Patch Load Variation. The load seen at the contact patch will increase as the tire is pushed up due to gravity and the reaction force of the suspension, such as when hitting a bump, and will decrease after. Contact patch load variation can loosely be viewed as a measure of tire efficiency or mechanical grip, and it is traditionally accepted that the less the load on the tire changes relative to excitation, the more grip the tire will make. Shaker rig testing is an extremely effective method of analyzing contact patch load variation, which is a valuable parameter for damper tuning.

Through the use of instrumentation mounted on the wheel pans, on the suspensions and on the body, the response of the sprung mass is also analyzed in heave (up and down), pitch (front to back) and roll (left to right). In most cases, roll response is negligible because the suspensions are symmetrical. Reducing the pitch response reduces weight transfer between the front and rear improving mechanical grip and also reduces aerodynamic Center of Pressure movements, improving aerodynamic grip.

The use of a 7-post or 4-post test rig depends on the type of vehicle to be tested; a 4-post configuration is often used for road cars and low-aero race cars where each tire is on an individual actuator. Using the 4-post also requires a less complex setup; the car can be rolled onto the shaker rig and after attaching six accelerometers testing can begin. When aerodynamic loads become prevalent, the 7-post is used. It requires an additional chassis mounting structure to attach the three additional actuators which must be designed and built prior to arriving at the rig. With the 7-post configuration, a complete lap can be replayed by the actuators.

3.2.4 Inputs & Outputs

The inputs under the wheel pans can be simple repetitive vibrations or representations of real roads. While undergoing input from the road, sophisticated dynamic measurement devices provide insight on how the system is working. Generally, unwanted noises and vibrations entering the passenger compartment are the focus of these investigations. Normally a sine wave under all wheel pans in phase (operating in unison) is used to excite the vehicle. However, it is possible to run the tests in any manner: exciting one wheel at time, or the two fronts out of phase with the two rears, which is pitch input, or the right sides out of phase with the lefts, which is roll input. It is possible to run inputs from recordings from actual on-track test sessions. Normally, wheel travels from actual test-session recordings are re-created in the lab. By using the correct deflections indicated by wheel travel with the same springs and bars as those used in the track test, the loads will be correct. Deflections are used because race teams seldom have vertical loads as a measurement.

The aeroloaders simulate other forces on the car such as the squashing from inertia loads as the car rolls through a banked turn or deflections due to aerodynamic loading. By adjusting the load on the three downforce rams, it is possible to simulate any combination of roll, heave or pitch displacement to recreate specific conditions seen on the track and repeat that condition.

To summarize, the 7-post rig requires as input signals:

- four vertical road movements under the wheels, one for each;
- rolling motion due to aerodynamic loads;
- rolling motion due to inertia induced by load transfers;
- pitch motion due to aerodynamic loads;
- pitch motion due to inertia induced by load transfers.

The instrumentation typically measures accelerations, displacements and forces. The vertical accelerations of the sprung and unsprung components are of particular interest because they show the natural frequencies of the system. The forces exchanged between tire and road are relevant because they can give information to understand the effects on grip. After the test, the post-rig returns as output:

- four vertical wheel movements, with associated speeds, accelerations and forces exchanged between tires and road;
- body vertical movements, with associated spped and accelerations;
- body roll motion with relative angular velocity, acceleration and force;
- body pitch motion with relative angular velocity, acceleration and force.

Grip can be seen as the ability of the tires to stay in contact with the road. The seven-post shaker rig gives the possibility to simulate real operating conditions and repeat this over and over while changing the shocks, springs, sway bars, tire pressures, nose weight, etc. until a combination that provides the least load variation in the tires is found. The shaker is not able to simulate lateral forces because tires only see vertical loads. There are some differences in tires' vertical spring rate when operating at a slip angle (around a turn) versus no slip angle (rolling straight ahead); teams can measure the effect of lateral forces on grip by performing a second test with the best shock proposals learned from sessions on the shaker rig. The same input/output scheme is adopted in the virtual 7-Post model that will be presented in the following paragraphs in order to obtain a model with a functioning really similar to those of the real test bench.

3.3 Virtual Modeling of a 7-Post Test Rig

Running of tests on a virtual 7-post test rig help to reduce testing time on the actual seven-post test rig already discussed in paragraph 3.2.2, and give the possibility to evaluate the performance of a given vehicle, apriori. Moreover, the development of a more complete nonlinear vehicle model, with the possibility of an asymmetrically tuned damper, will offer racing teams the capability of maximizing the damper curves, while keeping the tire vertical load variation low. In [126], a linearized vehicle model was developed for the purpose of analyzing race vehicle characteristics for tracked race vehicles. In [118], a frequency domain analysis for damper tuning and optimization with the use of the 7-Post is described; this approach has improved and expanded in [127] with the use of inputs deriving from test sessions on track for the improvement of the vehicle setup and behavior.

7-post test application, however, is not limited to racing vehicles, but can also be used to characterize everyday road vehicles. While in racing applications the main objective is to maximize the vertical force of the tires on the road, the most important criterion for a passenger car is passenger comfort. By adjusting the suspension to reduce transmissibility, passenger comfort is increased, but at the expense of road-holding behavior. However, an optimal compromise can be found for both scenarios. Using a virtual 7-post to simulate vehicle behavior and analyzing its response under different operating conditions can determine if a vehicle is well designed, even before the actual prototype is produced, saving time and financial resources over multiple iterations of design [128]. To this aim, during this work great attention was paid on how effectively model a virtual 7-post, able to reproduce its complete behavior and properly characterize the vehicle suspension system, defining the best setup configuration in order to maximize performance.

3.3.1 Vehicle Modeling

The approach adopted to model the vehicle is based on lumped-element. The lumped-element model (also called lumped-parameter model, or lumped-component model) simplifies the description of the behavior of spatially distributed physical systems, such as a vehicle, into a topology consisting of discrete entities that approximate the behavior of the distributed system under certain assumptions [129]. This approach is really useful in mechanical multibody systems modeling because it allows simplifying the model itself considering just all the relevant parts of the system, decoupling the different behavior of the components. This may be contrasted to distributed parameter systems or models in which the behavior is distributed spatially and cannot be considered as localized into discrete entities. Mathematically speaking, the simplification reduces the state space of the system to a finite dimension, and the partial differential equations (PDEs) [130] of the continuous (infinite-dimensional) time and space model of the physical system into ordinary differential equations (ODEs) with a finite number of parameters [131].

If on the one hand, a very strong simplification of a continuous system in a finite one is made, leading to have an equally strong diversity of results from the real ones, on the other hand, this methodology allows having a set of differential equations that are easier to solve and manipulate. The continuous system is divided into an appropriate number of elements of finite dimensions, the mass of each of which is concentrated in one or more points of the element, while the parts that connect them are considered as elasticity without mass.

Finally, if simplifications have been made following particular strategies, they do not lead to an excessive diversity of results and, in these cases, it can be extremely convenient to adopt this kind of models. For this reason, the Lumped-element model was adopted, which returns the best trade-off between modeling simplicity and goodness of results.

3.3.2 Full Car Model

The model used to simulate the 7-Post behavior is the direct evolution of the simplest model for simulating vehicle dynamics, the Quarter car model [132]. It is a single-suspension model and it is generally utilized to study the vertical dynamics in order to define the best damping characteristics of the shock absorber as a compromise between comfort and road-holding. Indeed, when a generic forcing is applied on the system, it causes a vertical acceleration of the sprung mass and an oscillation of the force exchanged by the unsprung mass with the ground [133]. The acceleration amplitude shall be reduced to a minimum for adequate comfort, while the amplitude of the oscillation shall be reduced to a minimum to ensure adequate road-holding. These minimizations are obtained by appropriately setting the damping value [134, 135]; the appropriate adjustment of the stiffness and damping values also reduces vibration and noise problems resulting from other vehicle subsystems [136].

In order to obtain a model that allows a more accurate study of the dynamics of the vehicle, especially of the vertical one to emulate a real 7-Post rig, the scheme represented in Figure 3.3 is adopted; this scheme is associate to a well-known literature model, called Full-car model [137].

It is a model consisting of five masses, one of which represents the suspended mass of the vehicle, while the remaining represent the unsprung masses of the vehicle; each of the latter collects the wheel and the part of the suspension that is not suspended in the real vehicle. Each of the four unsprung masses is connected to the suspended mass by a spring and a

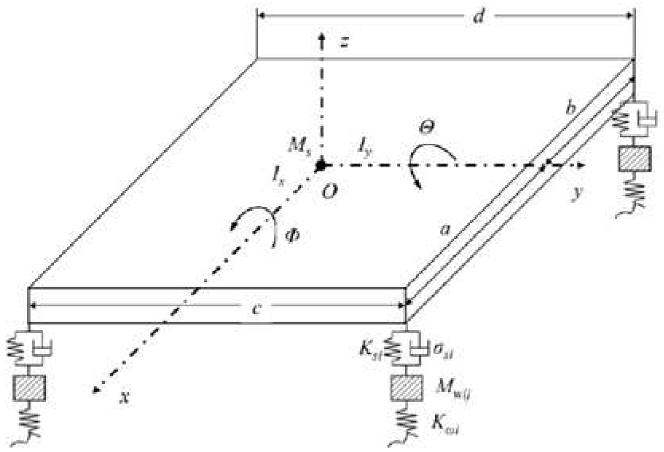

Fig. 3.3 Full car model

damper representing an independent suspension. On the other hand, the connection between each of the four unsprung masses and the ground is limited to a spring representing the vertical stiffness of the tire, the damping provided by the latter is considered negligible with regard to the simplified model described. To study the motions of the latter, a body-fixed reference system levorotatory is adopted, the z-axis indicates the vertical axis, facing up, through the center of gravity of the suspended mass, the orthogonal axis to z-axis one, consistent with the direction of the vehicle, on which the vehicle wheelbase is projected, is the x axis, and with the letter y is indicated the axis which forms with the other two the desired body-fixed reference system right-handed and orthogonal. With reference to the Full-car model, the x-axis is confused with the rolling axis and the y-axis with the pitch axis [3].

The system is characterized by a total of seven DoF, each of the unsprung masses is able to move exclusively on the z-axis, this allows studying the motion of:

1. Front left wheels displacement on z-axis;

2. Front right wheels displacement on z-axis;

3. Rear left wheels displacement on z-axis;

4. Rear right wheels displacement on z-axis.

and all that ensues, such as speed, acceleration and forces exchanged with the road through the stiffness of the tires. In particular, the vertical movement of the four wheels can be schematized as a bump, if the wheel displacement produces a compression of the suspension, or as a rebound, if the wheel displacement produces an extension of the suspension. The suspended mass can move on the same axis and rotate around the axes x and y thus being able to study the following body motions:

5. Heave, the motion of the body on the z-axis;

6. Roll, the rotation of the body around the x-axis;

7. Pitch, the rotation of the body around the y-axis.

3.3.3 Modeling Approaches

The equations of motion can be derived using two approaches:

- Lagrangian approach: It is based on the Lagrangian observation of the phenomena found on the stationary-action principle which requires that the action functional of the system (a numerical value describing how a physical system has changed over time) remain at a stationary point throughout the time evolution of the system. This constraint allows the calculation of the equations of motion of the system using the well-known Lagrange's equations [138].

- Eulerian approach: It is based on Eulerian observation of the phenomena which considers the evaluation of a point of space and is observed the evolution of all the particles that pass through that point. It is a way of looking at particle motion that focuses on specific locations in the space through which the particle flows as time passes. This constraint allows the calculation of the equations of motion based on the equilibrium concept. [139].

With both approaches, it is possible to derive a set of equations that are apparently different, but they contain the same identical terms with the same signs, unless for the consideration of the weight force in the Lagrangian approach. The difference lies in the fact that the weight force for the equilibrium equations can be neglected because it forms together with the reaction exchanged by the road of the systems equivalent to zero, that is, self-balancing.

Considering that it is in our interest to study the vertical forces exchanged between tires and road, with the Lagrangian approach it is possible to obtain equations that take into account also the effect of the static vertical loads due to the gravitational forces. For this reason, these equations are implemented in the final model and the method used to derive them, for brevity, is the only one presented in the next paragraph.

3.3.4 Model's Equations Derived with the Lagrangian Approach

Lagrangian mechanics describes a mechanical system with a pair (M, L), consisting of a configuration space M and a smooth function L within that space called Lagrangian. By convention, $L = E - U$ where E and U are the kinetic and potential energy of the system, respectively.

To write the equations of motion with the Lagrangian approach it is necessary to define the following quantities:

- q_h = generic Lagrangian coordinate;
- F_s = external force applied in the generic point P_s;
- δP_s = infinitesimal displacement of the generic point P_s;

- $Q_h = \sum_{s=1}^{\nu} F_s^e \frac{\partial P_s}{\partial q_h}$ = Lagrangian component of the external force.

Using these definitions, it possible to write the Lagrange's equation (Equation 3.1

$$\sum_{h=1}^{n} \left(-\frac{d}{dt}\frac{\partial L}{\partial \dot{q}_h} + \frac{\partial L}{\partial q_h} + Q_h\right) \cdot \delta q_h = 0 \tag{3.1}$$

The previous writing is valid for any given moment of time and for each of the n sets of virtual displacements. It follows that the Lagrange equation can be dissolved into n second-order differential equations, in number equal to the degrees of freedom of the system. These equations are given below:

$$\frac{d}{dt}\frac{\partial L}{\partial \dot{q}_1} - \frac{\partial L}{\partial q_1} = Q_1$$

$$\frac{d}{dt}\frac{\partial L}{\partial \dot{q}_2} - \frac{\partial L}{\partial q_2} = Q_2$$

$$\ldots$$

$$\frac{d}{dt}\frac{\partial L}{\partial \dot{q}_n} - \frac{\partial L}{\partial q_n} = Q_n \tag{3.2}$$

In order to solve the Lagrange equations referring to the body-fixed reference system in Figure 3.3. Like any model, to simplify both logical and analytical reasoning it is useful to introduce a series of hypotheses in order to make the system easier to treat. The assumptions that are adopted are given below:

- The internal damping of the tire is neglected. This assumption is valid since its value is much smaller than that of the suspension and also decreases as the roll speed increases.

- It is believed that the vehicle is symmetrical with respect to the xz plane in such a way as to take into account the central y-axis of inertia and therefore the inertia products I_{xy} and I_{yz} are canceled.

- The case is supposed to be rigid in such a way that it is possible to obtain the moments of inertia I_x and I_y.

It is necessary to write the expressions related to the kinetic energy and the energy associated with each of the forces acting on it. Called m the mass and $\dot{x}$ the speed, the kinetic energy can be expressed as in the Equation 3.3

$$E = \frac{1}{2}m\dot{x}^2 \tag{3.3}$$

Called K the stiffness of the spring and x its displacement, the expression relating to the energy associated with the elastic forces is reported in Equation 3.4

$$U_e = \frac{1}{2}Kx^2 \tag{3.4}$$

Indicated with g the gravitational acceleration, the energy associated with the weight force is expressed in Equation 3.5.

$$U_g = mgx \tag{3.5}$$

Finally, called σ the value of damping, the expression relating to the energy associated with the dissipative force of viscous nature is reported in Equation 3.6 [126].

$$D = \frac{1}{2}\sigma\dot{x}^2 \tag{3.6}$$

After these preliminary definitions, it is possible to write the Equations relating to kinetic energy and the energy associated with the exchanged forces for the full car model.

Kinetic Energy

$$E = \frac{1}{2}M_s\dot{z}_G^2 + \frac{1}{2}[I_x\dot{\varphi}^2 + I_y\dot{\theta}^2] + \frac{1}{2}M_{wf}\dot{z}_{wfr}^2 + \frac{1}{2}M_{wf}\dot{z}_{wfl}^2 + \\ + \frac{1}{2}M_{wr}\dot{z}_{wrr}^2 + \frac{1}{2}M_{wr}\dot{z}_{wrl}^2 \quad (3.7)$$

Elastic Forces Energy

$$U_e = \frac{1}{2}K_{sf}(z_{sfr} - z_{wfr})^2 + \frac{1}{2}K_{sr}(z_{srr} - z_{wrr})^2 + \\ + \frac{1}{2}K_{sf}(z_{sfl} - z_{wfl})^2 + \frac{1}{2}K_{sr}(z_{srl} - z_{wrl})^2 + \frac{1}{2}K_{wf}(z_{wfr} - z_{rfr})^2 + \\ + \frac{1}{2}K_{wr}(z_{wrr} - z_{rrr})^2 + \frac{1}{2}K_{wf}(z_{wfl} - z_{rfl})^2 + \frac{1}{2}K_{wr}(z_{wrl} - z_{rrl})^2 \quad (3.8)$$

Weight Forces Energy

$$U_g = g(M_s z_G + M_{wf}z_{wfr} + M_{wf}z_{wfl} + M_{wr}z_{wrr} + M_{wr}z_{wrl}) \quad (3.9)$$

Dissipative Forces Energy

$$D = \frac{1}{2}\sigma_{sf}(\dot{z}_{sfr} - \dot{z}_{wfr})^2 + \frac{1}{2}\sigma_{sr}(\dot{z}_{srr} - \dot{z}_{wrr})^2 + \frac{1}{2}\sigma_{sf}(\dot{z}_{sfl} - \dot{z}_{wfl})^2 + \\ + \frac{1}{2}\sigma_{sr}(\dot{z}_{srl} - \dot{z}_{wrl})^2 \quad (3.10)$$

The equations are written using additional coordinates to the seven independent characteristics of the system. In order to obtain a system that counts as many equations as there are degrees of freedom, the congruence equations are used, which are the mathematical relationships among the parameters that describe the vehicle motion. They involve positions, velocities and accelerations, without consideration of the masses nor the forces that caused the motion [3]. The auxiliary coordinates are expressed as a function of the independent ones; it should be noted that in the equations that follow the sinuses of the angles have been confused with the angles themselves.

Congruence Equations

$$z_{sfl} = z_G - a\theta + c\varphi \tag{3.11}$$

$$\dot{z}_{sfl} = \dot{z}_G - a\dot{\theta} + c\dot{\varphi} \tag{3.12}$$

$$z_{sfr} = z_G - a\theta - c\varphi \tag{3.13}$$

$$\dot{z}_{sfr} = \dot{z}_G - a\dot{\theta} - c\dot{\varphi} \tag{3.14}$$

$$z_{srl} = z_G + b\theta + d\varphi \tag{3.15}$$

$$\dot{z}_{srl} = \dot{z}_G + b\dot{\theta} + d\dot{\varphi} \tag{3.16}$$

$$z_{srr} = z_G + b\theta - d\varphi \tag{3.17}$$

$$\dot{z}_{srr} = \dot{z}_G + b\dot{\theta} - d\dot{\varphi} \tag{3.18}$$

These equations are used to determine the position, speed and, if desired, the acceleration of the body at the four wheel centers of the vehicle. They are formulated considering the bounce motion of the body combined with that of rolling and pitch. Signs are given by convention considering positive counter-clockwise and negative clockwise rotations. Taking advantage of the equations related to kinetic energy and exchanged forces, expressed in the most explicit and extensive form, and the equations of congruence, it is possible to derive the seven equations that describe the motion of the system under consideration.

Body Bounce

The following Equation 3.19 is linked to the rebound motion, that is the motion along the z-axis of the sprung mass.

$$\begin{aligned}M_s\ddot{z}_G = &-(K_{sfr}+K_{srr}+K_{sfl}+K_{srl})z_G-(\sigma_{sfr}+\sigma_{srr}+\sigma_{sfl}+\sigma_{srl})\dot{z}_G\\&+(cK_{sfr}+\ dK_{srr}-cK_{sfl}-dK_{srl})\varphi+(c\sigma_{sfr}+d\sigma_{srr}-c\sigma_{sfl}-d\sigma_{srl}\ )\dot{\varphi}\\&+(aK_{sfr}+aK_{sfl}-bK_{srr}-bK_{srl})\theta+(a\sigma_{sfr}+a\sigma_{sfl}-b\sigma_{srr}-b\sigma_{srl})\dot{\theta}\\&+K_{sfl}z_{wfl}+K_{sfr}z_{wfr}+K_{srl}z_{wrl}+K_{srr}z_{wrl}+\sigma_{sfl}\dot{z}_{wfl}+\sigma_{sfr}\dot{z}_{wfr}\\&+\sigma_{srl}\dot{z}_{wrl}+\sigma_{srr}\dot{z}_{wrr}-M_sg\end{aligned}\tag{3.19}$$

This equation takes into account the suspended mass and acceleration of the center of gravity on z-axis; the coefficients of stiffness and vertical damping of the four suspensions; the coordinate of the center of gravity displacement on z-axis and its speed; geometric values of the front and rear wheelbase, front and rear track; values of the coordinates of the mass rotation suspended around the x and y-axis; the coordinates of the unsprung mass displacement at the angle ij on z-axis and their angular speed; finally, it takes into account the effect of gravitational acceleration.

Body Pitch

The following Equation 3.20 is linked to the pitch motion, that is the rotation around the y-axis of the sprung mass. This equation takes into account the inertia moment of sprung mass around y and angular acceleration of the sprung mass around y-axis; the coefficients of stiffness and vertical damping of the four suspensions; the coordinate of the center of gravity displacement on z-axis and its speed; geometric values of the front and rear wheelbase, front and rear track; values of the coordinates of the mass rotation suspended around the x and y-axis; finally, it considers the coordinates of the unsprung mass displacement at the angle ij on z-axis and their angular speed.

$$\begin{aligned} I_y\ddot{\theta} = {} & (aK_{sfr} - bK_{srr} + aK_{sfl} - bK_{srl})z_G + (a\sigma_{sfr} - b\sigma_{srr} + a\sigma_{sfl} - b\sigma_{srl})\dot{z}_G \\ & + (-acK_{sfr} + bdK_{srr} + acK_{sfl} - bdK_{srl})\varphi + \\ & (-ac\sigma_{sfr} + bd\sigma_{srr} + ac\sigma_{sfl} - bd\sigma_{srl})\dot{\varphi} \\ & - (a^2K_{sfr} + a^2K_{sfl} + b^2K_{srr} + b^2K_{srl})\theta - (a^2\sigma_{sfr} + a^2\sigma_{sfl} + b^2\sigma_{srr} + b^2\sigma_{srl})\dot{\theta} \\ & - aK_{sfl}z_{wfl} - aK_{sfr}z_{wfr} + bK_{srl}z_{wrl} + bK_{srr}z_{wrr} - a\sigma_{sfl}\dot{z}_{wfl} - a\sigma_{sfr}\dot{z}_{wfr} \\ & + b\sigma_{srl}\dot{z}_{wrl} + b\sigma_{srr}\dot{z}_{wrr} \end{aligned} \tag{3.20}$$

Body Roll

The following Equation 3.21 is linked to the roll motion, that is the rotation around the x-axis of the sprung mass.

$$\begin{aligned} I_x\ddot{\varphi} = {} & (cK_{sfr} + dK_{srr} - cK_{sfl} - dK_{srl})z_G + (c\sigma_{sfr} + d\sigma_{srr} - c\sigma_{sfl} - d\sigma_{srl})\dot{z}_G \\ & + (-acK_{sfr} + bdK_{srr} + acK_{sfl} - bdK_{srl})\theta + \\ & (-ac\sigma_{sfr} + bd\sigma_{srr} + ac\sigma_{sfl} - bd\sigma_{srl})\dot{\theta} \\ & - (c^2K_{sfr} + c^2K_{sfl} + d^2K_{srr} + d^2K_{srl})\varphi - (c^2\sigma_{sfr} + c^2\sigma_{sfl} + d^2\sigma_{srr} + d^2\sigma_{srl})\dot{\varphi} \\ & + cK_{sfl}z_{wfl} - cK_{sfr}z_{wfr} + dK_{srl}z_{wrl} - dK_{srr}z_{wrl} - c\sigma_{sfl}\dot{z}_{wfl} - c\sigma_{sfr}\dot{z}_{wfr} \\ & + d\sigma_{srl}\dot{z}_{wrl} + d\sigma_{srr}\dot{z}_{wrr} \end{aligned} \tag{3.21}$$

This equation takes into account the inertia moment of sprung mass around x and angular acceleration of the sprung mass around x-axis; the coefficients of stiffness and vertical damping of the four suspensions; the coordinate of the center of gravity displacement on z-axis and its speed; geometric values of the front and rear wheelbase, front and rear track; values of the coordinates of the mass rotation suspended around the x and y-axis; finally, it takes into account the coordinates of the unsprung mass displacement at the angle ij on z-axis and their angular speed.

Wheels Bounce

The following equations are linked to the rebound motions of the wheels, that is the motion along the z-axis of the unsprung mass.

$$M_{wfr}\ddot{z}_{wfr} = K_{sfr}(z_G - a\theta - c\varphi - z_{wfr}) + \sigma_{sfr}(\dot{z}_G - a\dot{\theta} - c\dot{\varphi} - \dot{z}_{wfr}) \\ - K_{wfr}(z_{wfr} - z_{rfr}) - M_{wfr}g \quad (3.22)$$

$$M_{wfl}\ddot{z}_{wfl} = K_{sfl}(z_G - a\theta + c\varphi - z_{wfl}) + \sigma_{sfl}(\dot{z}_G - a\dot{\theta} + c\dot{\varphi} - \dot{z}_{wfl}) \\ - K_{wfl}(z_{wfl} - z_{rfl}) - M_{wfl}g \quad (3.23)$$

$$M_{wrr}\ddot{z}_{wrr} = K_{srr}(z_G + b\theta - d\varphi - z_{wrr}) + \sigma_{srr}(\dot{z}_G + b\dot{\theta} - d\dot{\varphi} - \dot{z}_{wrr}) \\ - K_{wrr}(z_{wrr} - z_{rrr}) - M_{wrr}g \quad (3.24)$$

$$M_{wrl}\ddot{z}_{wrlr} = K_{srl}(z_G + b\theta + d\varphi - z_{wrl}) + \sigma_{srl}(\dot{z}_G + b\dot{\theta} + d\dot{\varphi} - \dot{z}_{wrl}) \\ - K_{wrl}(z_{wrl} - z_{rrl}) - M_{wrl}g \quad (3.25)$$

These equations take into account the terms relating to the vehicle wheels, such as the mass of the four wheels and their acceleration on the z-axis;

the four wheels' stiffness (neglecting the damping coefficients); and the coordinate of the unsprung mass displacement at the ij-corner on z-axis. They also take into account the terms relating to the suspension connected at each wheel, such as the coefficients of stiffness and vertical damping. Also the coordinate of the center of gravity displacement on z-axis and its speed, geometric values of the front and rear wheelbase, front and rear track, values of the coordinates of the mass rotation suspended around the x and y-axis are considered; in addition, they take into account the effect of gravitational acceleration; finally, it is possible to find relevant terms such as the coordinate of the road displacement at the ij-tire on z-axis.

3.4 Model Implementation

3.4.1 Nomenclature

Before proceeding to the implementation of the equations of motion relating to the seven degrees of freedom in the model, a nomenclature was defined in order to uniquely determine the parameters introduced. It should be noted that the following nomenclature in Tab. 3.1 is the same used in the Simulink model and has been introduced so as to be explicit and immediate to understand.

Parameters	**UoM**	**Nomenclature**
Gravitational acceleration	m/s^2	g
Front suspension stiffness	N/m	kSpringFront
Rear suspension stiffness	N/m	kSpringRear
Front tire stiffness	N/m	kTyreFront
Rear tire stiffness	N/m	kTyreRear
Front suspension damping coefficient	$N \cdot s/m$	dampFL dampFR
Rear suspension damping coefficient	$N \cdot s/m$	dampRL dampRR
Sprung mass	kg	mSprung

Front unsprung mass	kg	mWheelFront
Rear unsprung mass	kg	mWheelRear
Front wheelbase	m	lFrontWheelbase
Rear wheelbase	m	lRearWheelbase
Front track	m	lFrontTrack
Rear track	m	lRearTrack
Moment of inertia of sprung mass around x-axis	$kg \cdot m^2$	JxxCar
Moment of inertia of sprung mass around y-axis	$kg \cdot m^2$	JyyCar
Moment of inertia of sprung mass around z-axis	$kg \cdot m^2$	JzzCar
Sprung mass rotation around x-axis	rad	aRollBody
Sprung mass rotation around y-axis	rad	aPitchBody
Sprung mass velocity around x-axis	rad/s	nRollBody
Sprung mass velocity around y-axis	rad/s	nPitchBody
Center of gravity displacement on z-axis	m	zCG
Center of gravity velocity on z-axis	m/s^2	vCGVert
Front left unsprung mass displacement on z-axis	m	zWheelFL
Front right unsprung mass displacement on z-axis	m	zWheelFR
Rear left unsprung mass displacement on z-axis	m	zWheelRL
Rear right unsprung mass displacement on z-axis	m	zWheelRR
Front left unsprung mass velocity on z-axis	m/s^2	vWheelFLVert
Front right unsprung mass velocity on z-axis	m/s^2	vWheelFRVert
Rear left unsprung mass velocity on z-axis	m/s^2	vWheelRLVert
Rear right unsprung mass velocity on z-axis	m/s^2	vWheelRRVert

Front left shock absorber velocity	m/s^2	vSAFLVer
Front right shock absorber velocity	m/s^2	vSAFRVer
Rear left shock absorber velocity	m/s^2	vSARLVer
Rear right shock absorber velocity	m/s^2	vSARRVer
Front left tire vertical force	N	FzWheelFL
Front right tire vertical force	N	FzWheelFR
Rear left tire vertical force	N	FzWheelRL
Rear right tire vertical force	N	FzWheelRR
Road displacement under front left tire	mm	zRoadFL
Road displacement under front right tire	mm	zRoadFR
Road displacement under rear left tire	mm	zRoadRL
Road displacement under rear right tire	mm	zRoadRR
Front motion ratio	(-)	MotioRatioFront
Rear motion ratio	(-)	MotioRatioRear

Table 3.1 Nomenclature

For what concern the Motion Ratio, it can be expressed as the ratio of the force F_v exerted on the z-axis placed vertically to the force F exerted along the direction on which the suspension lies; it can also be expressed in terms of deformation. Precisely as the ratio between s, that is the deformation that the spring undergoes in the direction of the suspension, and s_v, which represents the deformation of the spring along the vertical direction.

$$MR = \frac{F_v}{F} = \frac{s}{s_v} \tag{3.26}$$

Using the above definition, it was derived the relationship between the vertical stiffness K_v and the stiffness of the spring K, which is assumed constant.

$$K_v = K \cdot MR^2 \tag{3.27}$$

For the creation of the already described model, the following simplyfing assumptions on some of the vehicle parameters were made :

- It is assumed constant stiffness K for the springs. Consequently, spring interactions as elastic forces are assumed as linear functions of the deformations and sliding speeds of the shock absorbers respectively. However, this approach could be improved by inserting non-linear stiffness;
- The behavior of the tires is assumed linear in the radial direction so that the vertical force exchanged with the road varies linearly with the crushing of the tires; this hypothesis is valid only for small movements. This approach could also be improved by inserting a law of variation of stiffness with load;
- The inertia products of the case are constant during the motion.

3.4.2 Model Interface

The simulator's graphical interface, provided by the Simulink environment, consists of several block layouts, which allow the motion equations introduced in paragraph 3.3.4 to be visually represented. The model structure aims to have a clear view of how the blocks are used and how they interact. An example of a provision that represents the model in its entirety is shown in Figure 3.4.

One color is assigned to each typology of block, chosen among an appropriate selection to outline which are inputs or outputs, or data that originates from or is addressed to the Workspace. It was also defined a legend to describe the meaning of the different colors, thanks to which it is possible to understand the functionality of a certain block simply by observing the color (Figure 3.5).

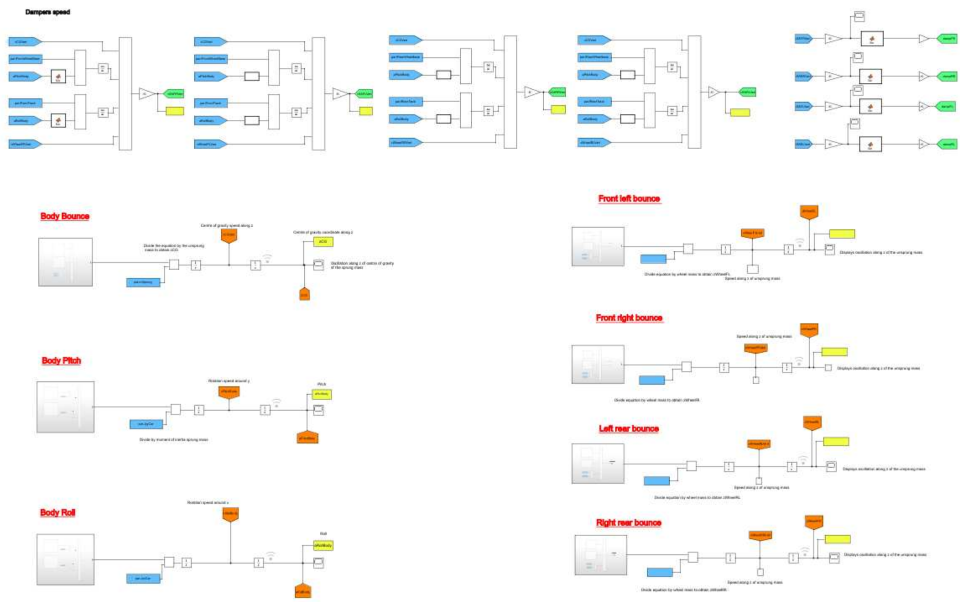

Fig. 3.4 7-DoF vehicle model - Simulink Graph

	Data:	*Color:*
Main window	Input	Light blue
	Output	Orange
	Goto blocks	Light green
	To Workspace blocks	Yellow
Secondary windows	Input	Light blue
	Output	Gray
	To Workspace blocks	Yellow
	Input from main window	Orange
	From Workspace blocks	Green

Fig. 3.5 Legend

Vertical Forces Determination

The stiffness of the tires is fundamental for the study of the vertical forces to the road, because of the interaction that exists instant by instant between wheel and road. The followings are the equations used in the model for the calculation of $FzWheelFR$, $FzWheelFL$, $FzWheelRR$ and $FzWheelRL$, in which the subscript j refers to the generic wheel (right or left) of an axle:

$$FzWheelFj = kTyreFront(zWheelFj - zRoadFj) \tag{3.28}$$

$$FzWheelRj = kTyreRear(zWheelRj - zRoadRj) \tag{3.29}$$

Damping Coefficient Determination

A more complex procedure is needed to consider the damping of the suspensions, because it is not a constant value but varies according to an empirical exponential function obtained thanks to the considerations made below. The points through which the damping curve passes, for the front and rear suspension, are visible in Figures 3.6 and 3.7 and provided by the dampers manufacturer.

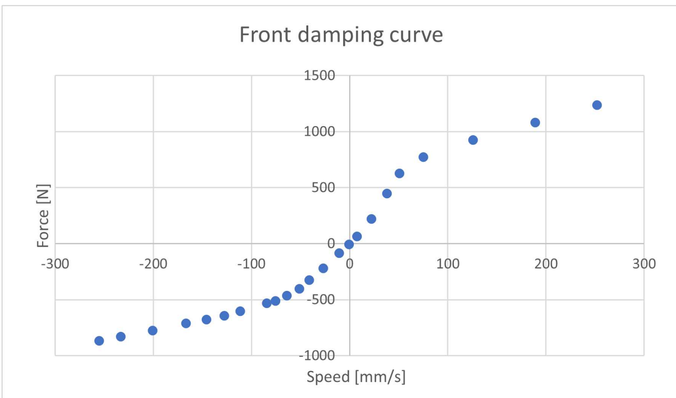

Fig. 3.6 Front damping points

From these points it is possible to obtain the function of a curve that best approximates the known damping points, using specific curve fitting toolboxes. For both front and rear suspension the positive points (on the x-axis) were divided from the negative points to facilitate the identification,

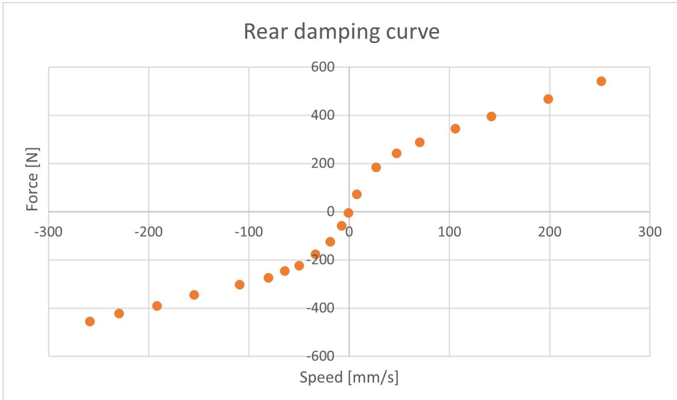

Fig. 3.7 Rear damping points

thus obtaining four exponential functions each dependent on the parameters a, b, c and d.

$$y = A \cdot e^{B \cdot u} + C \cdot e^{D \cdot u} \tag{3.30}$$

In Figures 3.8 and 3.9 it is possible to visualize the fitted curves obtained from the damping points.

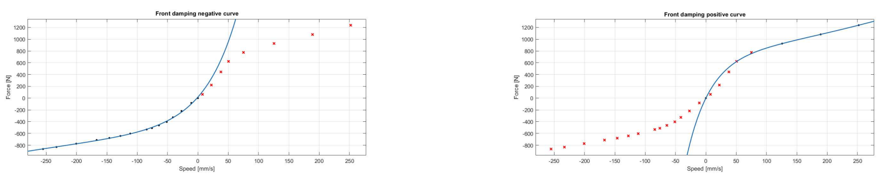

(a) Front damping negative curve

(b) Front damping positive curve

Fig. 3.8 Front damping fitted curves

The obtained functions are not directly implementable in the model, because the equations enter with a speed in the diagram and return with a force. It is necessary to implement the derived functions, because the value of the damping coefficient is nothing more than the incremental ratio of the function just described, that is the value of the slope of the curve at each point of the curve, which not having a linear trend, returns variable values.

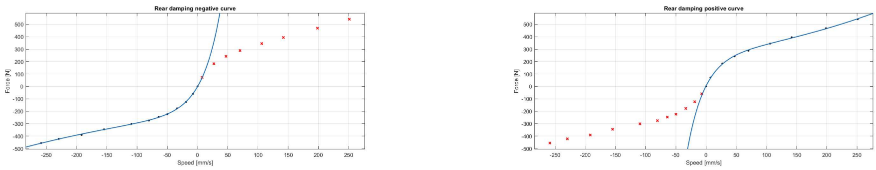

(a) Rear damping negative curve (b) Rear damping positive curve

Fig. 3.9 Rear damping fitted curves

Therefore, the derived functions have been used in the model and evaluated by identifying the following parameters:

- u which corresponds to the sliding speed of the suspension assessed along the z-axis.
- A, B, C, D represent constant parameters, obtained with the fitting procedure.

From the Equation 3.31, it is possible to understand that the characteristic damping value of the suspension depends only from a single input parameter that corresponds to the sliding speed of the suspension (if $u = 0 \Rightarrow \sigma = 0$).

$$y = B \cdot A \cdot e^{B \cdot u} + D \cdot C \cdot e^{D \cdot u} \tag{3.31}$$

Applying the above formula, it was derived the value of the damping of the suspension evaluated along the vertical axis, expressed in $[\frac{N \cdot s}{mm}]$. By converting the result obtained in $[\frac{N \cdot s}{m}]$, after applying the Motion Ratio, the damping value placed on the axis of the suspension is available. In summary, knowing u, it is evaluated the value of y and, finally, after converting the value into the unit of measurement of the international system, the Motion Ratio is applied. The following procedure is used to calculate $dampFR$, $dampFL$, $dampRR$ and $dampRL$:

$$y = y(u) \tag{3.32}$$

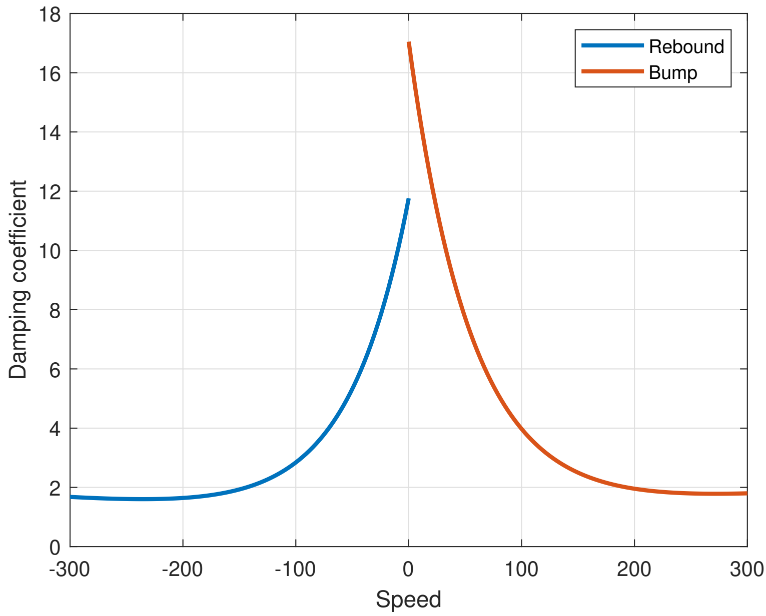

Fig. 3.10 Damping coefficient - Speed

$$\sigma = \frac{\sigma_v}{MR^2} \tag{3.33}$$

$$\sigma = \frac{y \cdot 1000}{MR^2} \tag{3.34}$$

3.4.3 Model User Interface

In order to make the interaction with the software as user-friendly as possible, a file mask has been introduced to manage the entire simulation process through a sequence of instructions written in the MATLAB programming language. The set of instructions is executed automatically; the user has to wait for the answer from the software, without programming the instructions to give to the model. It is not necessary, indeed, to modify the blocks, to provide the representation or to the saving of the results, through the Mask file, the process is driven entirely, and the user must simply start the script. The mask file is composed of several sections, each of which has its purpose:

- Load data: in this section, the user has the possibility to choose the inputs and references data to load and process with the model;
- Vehicle initialization: here, the user has the possibility to choose the file containing all the information (parameters) concerning the vehicle;
- 7-Post virtual model: represents the section in which the model is launched and simulated the process automatically;
- Post-processing: it includes all the post-simulation phases: the creation of structured variables in output, visualization of the graphs of the variables of interest and saving the outputs produced during the simulation.

The output data returned by the model are listed in Table 3.2.

Definition	**Name**
Center of Gravity displacement on z-axis	zCG
Sprung mass rotation around x-axis	aRollBody
Sprung mass rotation around y-axis	aPitchBody
Front left Unsprung mass displacement on z-axis	zWheelFL
Front right Unsprung mass displacement on z-axis	zWheelFR
Rear left Unsprung mass displacement on z-axis	zWheelRL
Rear right Unsprung mass displacement on z-axis	zWheelRR
Front left tire vertical Force	FzWheelFL
Front right tire vertical Force	FzWheelFR
Rear left tire vertical Force	FzWheelRL
Rear right tire vertical Force	FzWheelRR

Table 3.2 Output Signals

To properly parametrize the vehicle to be simulated, a minimum number of parameters are needed to start the simulation; they are listed in Table 3.3.

Definition	**Name**
Front Motion Ratio	MotionRatioFront
Rear Motion Ratio	MotionRatioRear
Front suspension stiffness	kSpringFront
Rear suspension stiffness	kSpringRear
Front suspension vertical stiffness	kSpringFrontVert
Rear suspension vertical stiffness	kSpringReatVert
Front tire stiffness	kTyreFront
Rear tire stiffness	kTyre Rear
Front wheelbase	lFrontWheelBase
Rear wheelbase	lRearWheelBase
Front track	lFrontTrack
Rear track	lRearTrack
Sprung mass	mSprung
Front unsprung mass	mWheelFront
Rear unsprung mass	mWheelRear
Moment of Inertia of sprung mass around x-axis	JxxCar
Moment of Inertia of sprung mass around y-axis	JyyCar

Table 3.3 Vehicle Parameter Required

Other vehicle parameters can be considered, in particular for what concerns the suspension system; these will be deepened in the next paragraph.

3.5 Suspension Modeling

The model described allows a fairly accurate study of the vertical dynamics of a vehicle. It is necessary to estimate as accurately as possible the stiffness of each of the four springs (Figure 3.3) which connect the suspended mass to its four unsprung masses. In this study, it was assumed that the vehicle is equipped, at both axles, with several different elastic elements, so that the overall stiffness is obtained as a combination of various contributions [140]. Except in the case of springs, the other elements exert their stiffness only under particular conditions of relative motion of the suspended mass with respect to the unsprung mass.

3.5.1 Stiffness of the Elastic Elements

In [141], the elastic elements that could be part of the suspension system of a vehicle have been described from the constructive point of view. For the purpose of this study, since the chosen model is lumped elements model, it is important to know only the stiffness of these organs. Therefore, attention will not be paid to the distinction between the various types of spring construction rather than anti-roll bars, but exclusively to the stiffness that they explain.

Spring Stiffness

The spring, to which reference will be made, is the cylindrical helix compression spring. This, in its normal use, is subjected to direct compressive forces along its axis. Assuming one of the extremes of the spring fixed on a plane and the other subjected to an axial force F statically applied, it is possible to draw on a diagram the relationship between the force F and the axial deformation f suffered by the spring. The spring stiffness K is defined as the slope of the curve $F(f)$ [142], as indicated in Equation 3.35.

$$K = \frac{dF}{df} \tag{3.35}$$

For a cylindrical helix spring, the stiffness is usually constant throughout its normal range of use. This behavior is defined as linear, as there is proportionality between the applied force and the deformation, with a constant of proportionality equal to the stiffness K. However, there are cases where the springs, with a variable distance between the turns or with variable wire diameter, have a not constant stiffness. Knowing the geometric quantities of the spring and the elastic modulus G of the material, it is possible to calculate the stiffness. In the case of spring with linear elastic behavior, indicating with d_{wire} the diameter of the wire, R the average diameter of the coil and n the number of turns, the formula for the stiffness evaluation is exposed in Equation 3.36:

$$K = \frac{G \cdot d_{wire}^4}{64 \cdot n \cdot R^3} \tag{3.36}$$

A spring mounted on a vehicle in static condition is already loaded with a certain amount, called preload, which is a function of the car's weight on a single wheel. In some cases, it is possible to add a preload to the spring, in order to make height corrections or weight balance. For a spring with constant stiffness, the addition of a preload does not change the response of the element in terms of elastic reactions.

Bump Rubber Stiffness

The bump rubber is an elastic element with no constant stiffness and the response that it provides, in terms of reaction, is a function of the compression magnitude. Generally, the mathematical equation that binds the force to the deformation is not known. However, the constructors usually provide experimental curves in which the stiffness, or force, is related to compression. An example of these curves is shown in Figure 3.11; because of their task, common practice is to consider these elements with a trend of increasing stiffness.

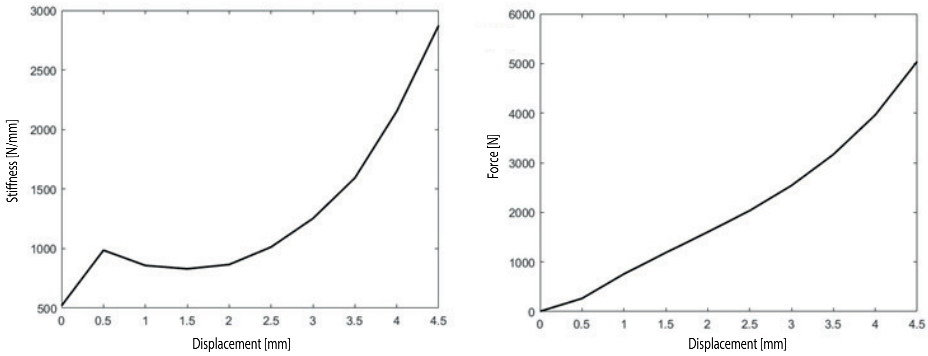

Fig. 3.11 Experimental curves of a bump rubber

Stiffness of the Third Element

As regards the stiffness of the third element, since it is composed essentially of a spring, a bump rubber or a combination of these two, the same applies as discussed in paragraphs 3.5.1 and 3.5.1. The stiffness of the spring is assumed constant, while the bump rubber's one is assumed variable. A simplified assumption is to not consider the preload of the spring, in fact, it can be assumed that the third element acts exclusively when a positive excursion of equal size for the two wheels of the same axle occurs (with reference to the signs used in the diagram of Figure 3.3).

Stiffness of the Anti-Roll Bar

For the Anti Roll Bar (ARB) stiffness evaluation, it is essential to know its type and its geometric sizes. In fact, for a U or T anti-roll bar, assuming a circular section full of material, the torsional stiffness is calculated as in Equation 3.37 [143].

$$K_T = \frac{G \cdot I_p}{l} = \frac{G}{l}\frac{\pi \cdot d^4}{32} \tag{3.37}$$

Where G is the modulus of tangential elasticity of the material, l is the length of the bar section that actually deforms, I_p is the moment of inertia of section area with respect to the neutral torsion axis, and d is the diameter of the straight section.
However, in the case of Z anti-roll bar and in the hypothesis of constant section, each blade can be schematized like a cantilever with the well-known beam theory, so the bending stiffness is calculated as in Equation 3.38.

$$K_Z = \frac{3 \cdot E \cdot I}{l^3} = \frac{G}{l}\frac{\pi \cdot d^4}{32} \tag{3.38}$$

Where E is the normal modulus of elasticity of the material, I is the moment of inertia of section area, and l is the length of the beam. Moreover, there are some construction solutions that allow more corrections, consisting of mixing of these elements, such as the use of blades in place of the rigid arms of an anti-roll bar U, T or Z.
It is clear that if the task is to achieve a model of the suspension system as general as possible, so that it can be used for any vehicle, it is essential to unbind that from the specific type of construction. This means that the torsional and/or flexural stiffness of the components of the anti-roll bar cannot be implemented in the model. Instead, a single stiffness equivalent to the single wheel that takes into account the entire anti-roll system will have to be introduced. This stiffness equivalent to the wheel, in fact, depends not only on the elastic elements or on a mix of them but also on the various lever ratios that transmit the elastic reaction of the bar to the wheel. In order to eliminate any dependence, it was preferred to take into account only this single stiffness parameter referred to the single wheel, without the need to divide it by two. That is because the anti-roll bar acts on the entire axle rather than on a single corner.

In order to make the modeling as generic as possible, it will be considered that the stiffness to the single wheel due to the anti-roll system is not constant, but variable depending on the amount of roll. Therefore, it will be assumed to know the trend curve of the stiffness equivalent to the wheel as a function of the rolling angle, an example of this trend is shown in Figure 3.12

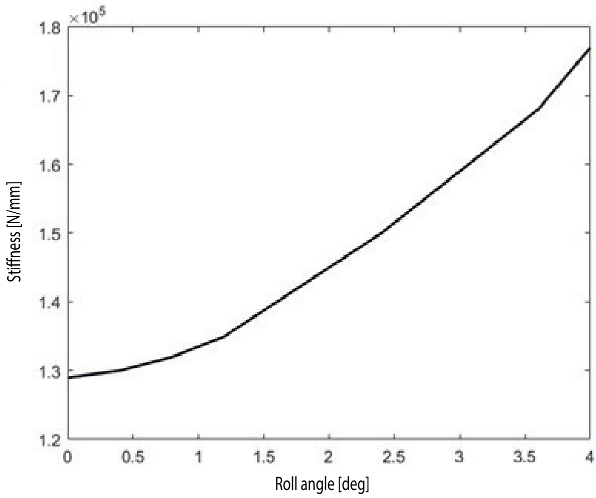

Fig. 3.12 Stiffness of Anti-Roll Bar

3.5.2 Motion Ratio

The spring and the damper, with its limit bump rubber, are very often not installed along the z-axis as defined in the reference system of the full car model. However, for parameterization, it is necessary to know the stiffness along this axis and not the one on the actual axis to which the elastic element belongs. In motorsport, where unequal-length wishbones suspension schemes are usually used, the spring is activated via a lever called Rocker. The rocker is driven by a rod that acts as a tie rod, defining the so-called Pull System [144]. The parameter that allows relating the movements along the axis of the spring with those along the z-axis, is the Motion Ratio (MR) which is a simple lever ratio.

Introducing the following parameters:

- $\delta x_s =$ Infinitesimal displacement on the direction on which the spring lies;
- $\delta z_w =$ Infinitesimal displacement of the wheel on z-axis;
- $F_s =$ Force on the direction on which the spring lies;
- $F_z =$ Force on z-axis;
- $K_s =$ Stiffness of the spring, assumed as constant;
- $K_z =$ Stiffness of the spring on z-axis.

The Motion Ratio is defined as in [145]:

$$MR = \lim_{\delta z_w \to 0} \left(\frac{\delta x_s}{\delta z_w} \right) \tag{3.39}$$

The principle of virtual works states that [146]:

$$F_s \cdot \delta x_s = F_z \cdot \delta z_w \tag{3.40}$$

From which it is obtained that:

$$F_z = \frac{F_s \cdot \delta x_s}{\delta z_w} = F_s \cdot MR \tag{3.41}$$

For determining the equivalent stiffness of the spring on z-axis, there may occur two cases:

Constant MR

$$K_z = \frac{dF_z}{dz_w} = MR \frac{dF_s}{dz_w} = MR \frac{dF_s}{dx_s} \frac{dx_s}{dz_w} = MR^2 \cdot K_s \tag{3.42}$$

Variable MR

$$K_z = \frac{dF_z}{dz_w} = \frac{d}{dz_w}(F_s \cdot MR) = MR\frac{dF_s}{dz_w} + F_s\frac{dMR}{dz_w} \tag{3.43}$$

On the right side of the equal, the first term in Equation 3.43 is the same in Equation 3.42, but there is a second new term. Ultimately:

$$K_z = MR^2 \cdot K_s + F_s\frac{dMR}{dz_w} \tag{3.44}$$

It is found that, in the case of variable Motion Ratio, the equivalent stiffness along the z-axis is the sum of two contributions, where the second is a differential term. Generally, the latter tends to be positive in order to generate an increase in stiffness during an upward wheel travel. In cases where the variation of the Motion Ratio is very marked, and the reaction of the spring is high, the second contribution becomes a term that cannot be neglected. In the model, a variable Motion Ratio has been considered, and it has been assumed to know the trend as a function of the wheel excursion, as reported in Figure 3.13.

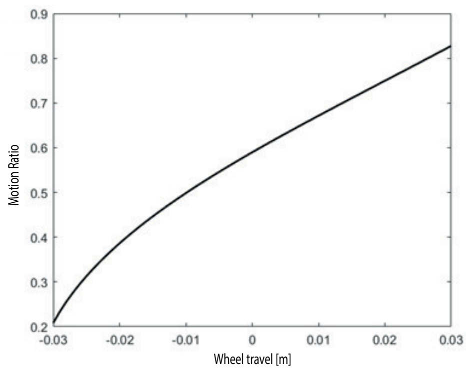

Fig. 3.13 Variable motion ratio

3.5.3 Suspension Nomenclature

For suspension modeling, it is necessary to introduce all the parameters that make it up, such as the parameters which take into account the stiffness of the suspension elements and the parameters that influence them. These parameters are visible in Table 3.4.

Parameters	**UoM**	**Nomenclature**
Vertical equivalent stiffness to the wheel of ARB	N/m	kARBFront kARBRear
Vertical equivalent stiffness of Third element	N/m	k3rdFront k3rdRear
Vertical equivalent stiffness of Bump Rubber	N/m	kBRFront kBRRear
Vertical equivalent stiffness of 3rd element Bump Rubber	N/m	kBR3Front kBR3Rear
Coordinate of the displacement of the suspended mass at the front not unsprung mass right and left on z-axis	m	zSuspendedFL zSuspendedFR
Coordinate of the displacement of the suspended mass at the rear not unsprung mass right and left on z-axis	m	zSuspendedRL zSuspendedRR
Front and Rear Third element Motion Ratio	(-)	MotionRatio3rdFront MotionRatio3rdRear
Difference: $zSuspendedFR - zWheelFR$ in static vehicle conditions	m	DeltaStaticFront
Difference: $zSuspendedRR - zWheelRR$ in static vehicle conditions	m	DeltaStaticRear
Front and rear suspension Bump Rubber activation threshold	m	BRActivationFront BRActivationRear
Front and rear 3rd element Bump Rubber activation threshold	m	BR3rdActivationFront BR3rdActivationRear
Force exerted along the direction of the suspension spring axis and the third element	N	FSpring F3rdSpring

Table 3.4 Suspension Nomenclature

3.5.4 Suspension Model Implementation

This section is focused on the evaluation of the equivalent stiffness to the wheel. Therefore, the stiffness of the suspension system was modeled in the Simulink environment. A vehicle commonly has two axles, but the model description will refer only to the front axle, since the treatment for the rear axle is entirely similar. In order to extend the applicability of the model to a wider range of vehicles, the most complex possible configuration of elastic elements has been evaluated; this takes into account the presence for each wheel of Spring and Bump Rubber, whereas for each axle of a third element with a bump rubber and an anti-roll bar.

The result is that the stiffness of the third element and anti-roll bar affects both wheels of the same axle, unlike the spring which gives a stiffness contribution exclusively on a single corner. Considering these assumptions, it follows that the stiffness involving an axle can be schematized, as shown in Figure 3.14. The next paragraphs will analyze each of the blocks that make up the scheme.

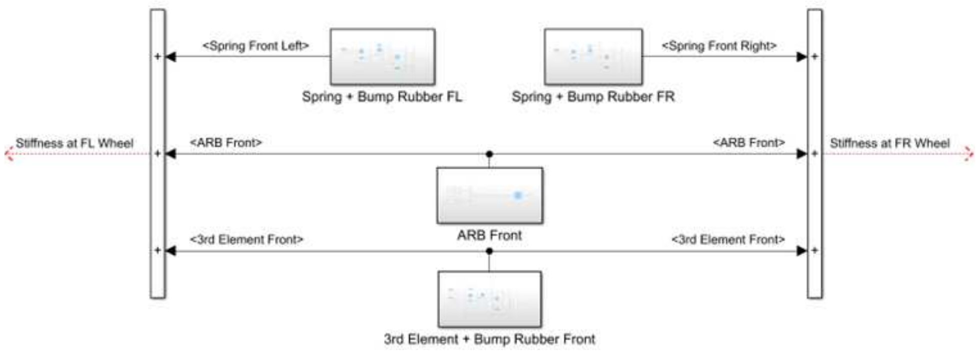

Fig. 3.14 Front axle stiffness model

Spring and Bump Rubber Modeling

The Spring and the relative bump rubber modeling is focused on the following assumptions, some of them has already been mentioned in paragraph 3.5.1:

- The spring stiffness is constant;
- The Bump Rubber stiffness is variable;
- The Motion Ratio is variable with the wheel travel.

Since the Motion Ratio variation is usually expressed as a function of the wheel travel in the static conditions, it was necessary to introduce $DeltStaticF$ in the input model parameters, which is the difference between $zSuspendedFL$ and $zWheelFL$ in the static condition of the vehicle. This parameter is essential to derive the positive (bump) or negative (rebound) values. The blocks scheme to determine the bump/rebound is shown in Figure 3.15.

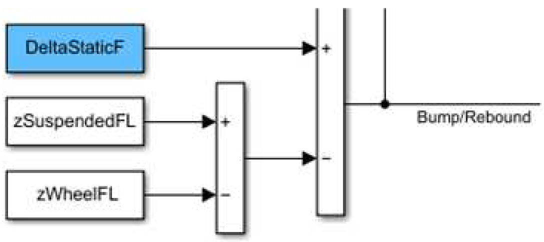

Fig. 3.15 Bump/Rebound model

It is necessary to combine the effective spring travel to the bump/rebound value. In the model, it was made through a look-up table, which describes spring travel value as a function of the wheel travel. The curve trend can be calculated:

- if the MR is constant, using Equation 3.42:

$$x_s = MR \cdot z_w \tag{3.45}$$

- if the MR is variable, using Equation 3.43:

$$x_s = \int MR(z) \cdot dz_w \tag{3.46}$$

To obtain the real spring travel, the eventual spring preload should be considered too. To simplify, in the model was assumed the absence of an additional preload in addition to the standard load due to the vehicle's weight. Although it is present, the suspensions static displacement does not cause a calculation error in the model since the spring travel curves, which are referred to the static condition and not to the relaxed spring condition, take intrinsically into account of the suspension static displacement effect. Knowing the actual compression of the spring, it was possible to evaluate when the bump rubber comes into action. In this regard, the $BRActivationF$ parameter has been introduced, indicating the maximum compression threshold after which the bump rubber begins to compress. The following difference has therefore been implemented as in Equation 3.47:

$$spring_{compression} - BRActivation = BumpRubber_{compression} \tag{3.47}$$

The following conditions have been subsequently introduced:

$$\begin{cases} if \quad BumpRubber\_compression < 0 \quad \Rightarrow \quad K = 0 \\ if \quad BumpRubber\_compression > 0 \quad \Rightarrow \quad K = kBRFront \end{cases} \tag{3.48}$$

The $kBRFront$ stiffness was evaluated through a new lookup table which reports the bump rubber stiffness as a function of its travel. Therefore, the switch, while the bump rubber is not in action, returns a zero value of the stiffness. When the bump rubber starts to travel, the switch returns an associated stiffness value. The condition expressed in Equation 3.48 was modeled as in Figure 3.16.

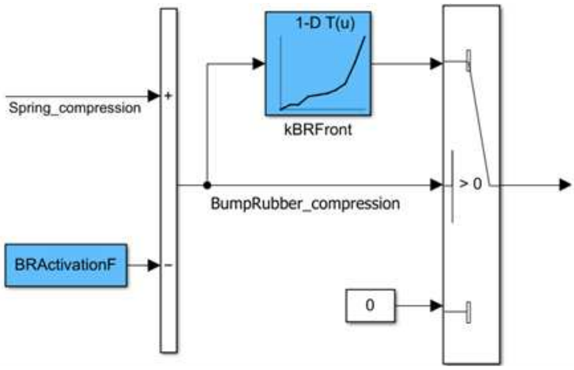

Fig. 3.16 Bump rubber stiffness model

Therefore, because stiffnesses are in parallel, it was possible to sum the stiffnesses of the bump rubber to that of the spring, as shown in Figure 3.17.

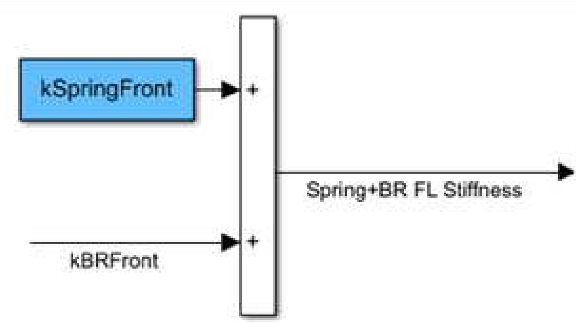

Fig. 3.17 Bump rubber and spring stiffness sum model

Knowing the total stiffness along the direction where lies the spring axis, called *Spring+BR FL Stiffness*, it was necessary to determine the equivalent stiffness along z-axis. Looking at Equation 3.44, it is evident that the equivalent stiffness to the wheel is made by two contributes called in the model as *Basic Stiffness* and *Rising Rate Stiffness*. The first one is easily evaluable by deriving the MR entering the bump value in the relative lookup table, squaring it and multiplying it by the total stiffness (Spring+BR FL Stiffness). To determine the second contribution it is needed to know the force exerted by the spring along its direction, which is determinable through installed sensors on the spring during the vehicle testing [147]. The blocks scheme representing Equation 3.44 is shown in Figure 3.18.

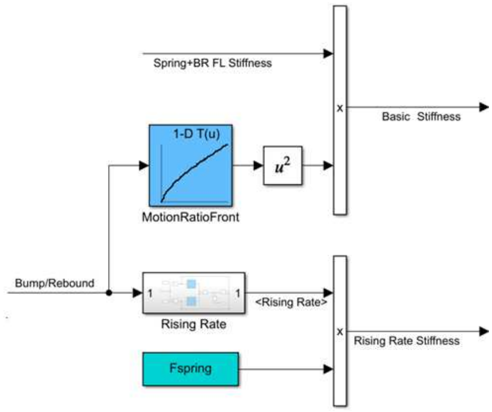

Fig. 3.18 Model to evaluate the equivalent stiffness to the wheel

The evaluation of spatial derivative in Equation 3.44 was made by applying the derivative definition, i.e. the incremental ratio. Using the bump value ± 0.00001 m, it was possible to evaluate the MR value in these two points and, thereafter, the incremental ratio, called Rising Rate. The blocks scheme is shown in Figure 3.19.

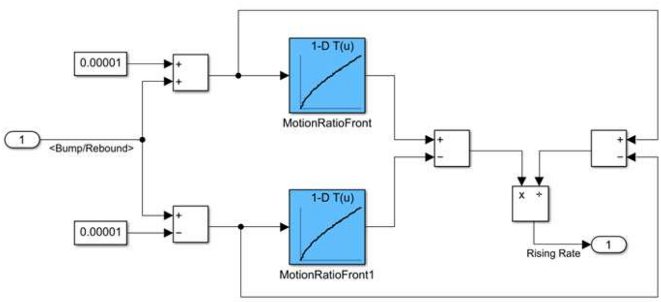

Fig. 3.19 Incremental ratio model

Finally, adding the basic stiffness and the rising rate stiffness the stiffness equivalent to the wheel due to the spring and its bump rubber was determined.

Third Element and Bump Rubber Modeling

The spring and bump rubber modeling of the third element is based on the following assumptions:

- Spring stiffness is constant;
- Bump Rubber stiffness is variable;
- MR is variable in function of the wheel travel;
- The spring is not preloaded in the static condition;
- $DeltaStaticF$ assumes the same value for each wheel of the same axle, this means that in the static vehicle conditions it is verified the condition expressed in Equation 3.49.

$$DeltaStaticF = zSuspendedFR - zWheelFR = zSuspendedFL - zWheelFL \tag{3.49}$$

Made the assumption that the third element spring is not preloaded when the vehicle is in the static condition, it is engaged only when a bump of the same entity for each wheel occurs; thus, it is needed to determine the bump entity for each wheel. The blocks scheme is shown in Figure 3.20.

The same entity bump condition of the two wheels, implemented in Figure 3.21, can be obtained by:

1. Taking the minimum between the two bump values (which can eventually be rebound values too);
2. Verifying if this value is more than zero.

Then, in the model has been included a switch that returns a non-zero value only when the minimum value is more than zero, i.e. when both the wheels are having a bump. In addition, taking the minimum value of the bump between each wheel means considering the common displacement

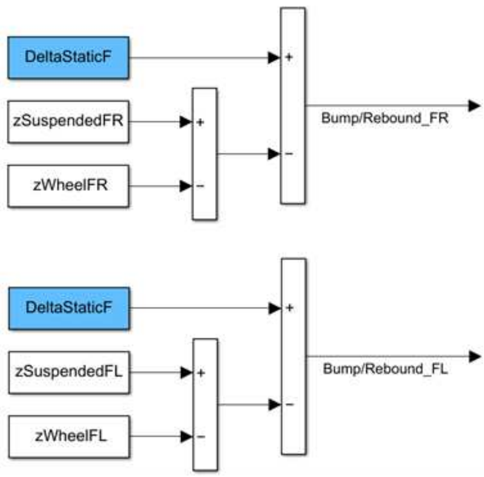

Fig. 3.20 Positive wheels travel for the wheels of an axle

entity of the two wheels. In the overall model, despite the switch has been entered at the end of the scheme, it fulfills exactly the task described above. In fact, it establishes that only when the minimum value is more than zero, the procedure returns a correct value; while, when the value is less than zero, the third element does not exert any stiffness.

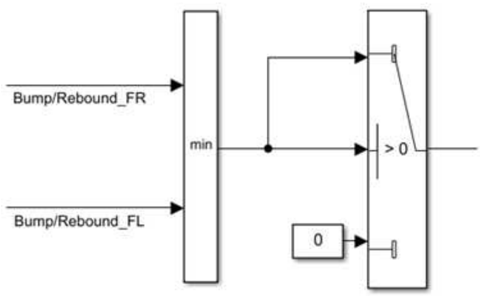

Fig. 3.21 Equal bump model for each wheels

Subsequently, as it is shown in Figure 3.22, the modeling scheme for the third element and bump rubber is really similar to Spring and Bump rubber already described in the paragraph 3.5.4.

The only differences between them are:

- In the previous case, both bump and rebound for the wheels' travel were considered, instead, now it is considered only the positive value of the wheels' travel, i.e. the common bump;
- Given that the third element stiffness is distributed on both wheels of the axle, it was necessary to divide the stiffness value by two.

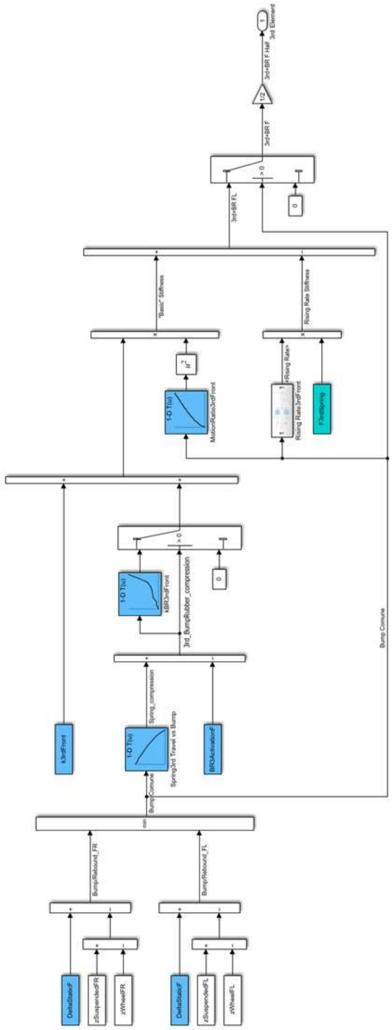

Fig. 3.22 Model to evaluate the equivalent stiffness to the wheel from third element and bump rubber

3.5.5 Anti-Roll Bar Modeling

In paragraph 3.5.1, some considerations have been made regarding the anti-roll bar stiffness, here taken again into account. The assumption was to consider known the trend of the equivalent stiffness to the wheel, explicated by the anti-roll system as a function of the roll angle. Therefore, it is necessary to estimate that angle:

$$\varphi = \arctan\left(\frac{|(zSuspendedFL - zWheelFL) - (zSuspendedFR - zWheelFR)|}{lFrontTrack}\right) \tag{3.50}$$

Because the functioning of the anti-roll bar is independent from the direction in which the vehicle rolls, the roll angle is evaluated as absolute value. In this way, it is assumed that the stiffness explicate by the system is the same for both rolling directions. Knowing the roll angle, it is possible to enter the look-up table with the roll angle value and to estimate the equivalent stiffness to the wheel given by the anti-roll system. It is important to underline, as already mentioned in paragraph 3.5.1, that despite the fact that also the anti-roll bar physically distributes its stiffness on both wheels, there is no division by two in the model. This is because it was assumed that the stiffness value can be directly considered on a single wheel.

In Figure 3.23 is reported the calculation scheme that reports the anti-roll bar modeling.

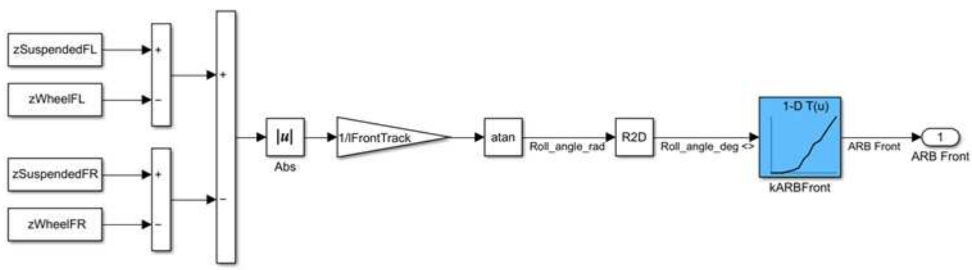

Fig. 3.23 Model to evaluate the equivalent stiffness to the wheel from Anti-roll bar

3.5.6 Equivalent stiffness at the wheel

The value of the equivalent stiffness at the wheel is evaluable as the sum of three contributes:

- Spring and Bump Rubber;
- Half of the Third Element and Bump Rubber;
- Anti Roll Bar;

Because all the elements are connected in parallel and their determination has already been described in the paragraphs 3.5.4, 3.5.4 and 3.5.5.

In Figure 3.24 it is shown the modeling of this sum operation followed by the equivalent stiffness relationship, described in Equation 3.51.

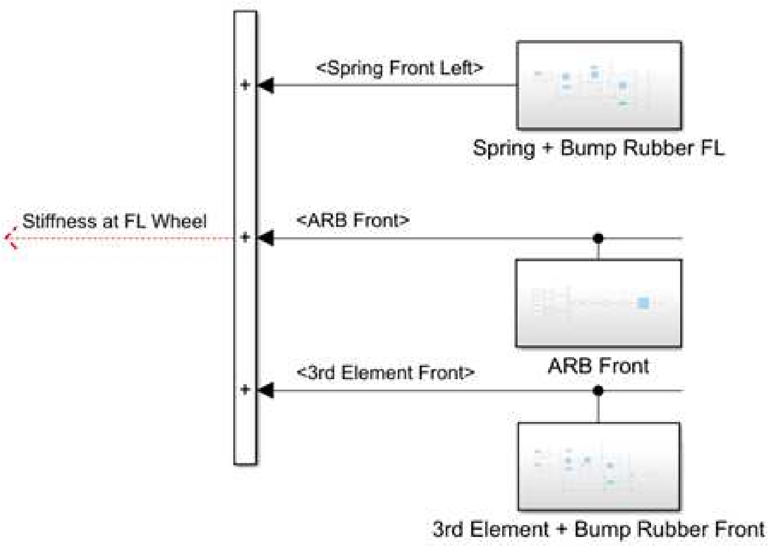

Fig. 3.24 Front left wheel stiffness model

$$K_z = \frac{K_s}{MR_s^2} + \frac{K_{BR}}{MR_{BR}^2} + \frac{K_{ARB}}{MR_{ARB}^2} + \frac{K_{3RD}}{MR_{3RD}^2} \tag{3.51}$$

Looking at subscripts:

- z refers to z-axis direction;
- s refers to *spring*;
- *ARB* refers to *Anti Roll Bar*;
- 3*RD* refers to *Third Element*.

3.6 Model Validation

In order to validate the model discussed in this chapter, a series of analyses were carried out, several simulations were launched with the same vehicle but different speeds and obstacles like bumps, holes, symmetrical and not. For brevity only few examples of simulation will be shown, deepening the parameters to be given to the model for the launch and how the output will be compared with the reference data.

To validate the model a reference vehicle has been chosen; all the parameters needed to characterize the vehicle are reported in Table 3.1. As already mentioned, the stiffness of the springs and the tires are assumed constant as well as the motion ratio; in addition, the inertia products of the case are constant during the motion.

Name	**Value**	**UoM**
MotionRatioFront	1.413	(-)
MotionRatioRear	1.147	(-)
kSpringFront	32860	N/m
kSpringRear	17400	N/m
kTyreFront	280000	N/m
kTyre Rear	280000	N/m
lFrontWheelBase	1.036	m
lRearWheelBase	1.274	m

lFrontTrack	1.495	m
lRearTrack	1.505	m
mSprung	1101	kg
mWheelFront	50	kg
mWheelRear	50	kg
JxxCar	204	$kg \cdot m^2$
JyyCar	1116	$kg \cdot m^2$

Table 3.5 Vehicle parameter

It is important to specify that the damping coefficients, already mentioned in paragraph 3.4.2, are different for the front and rear axles. These, together with the numerical value of the gravitational acceleration (9.81 m/s^2), are the only parameters needed to characterize the vehicle in the presented model. The other input needed concerns the road profile.

The choice of tracks to be used during the simulations is intimately linked to the aims of the study and to the peculiarities of the developed model. In fact, since the vertical dynamics of the vehicle is the main target of this study, straight tracks are adopted, in order to not introduce the contributions related to the corners (load transfers and yaw angles). Perfectly flat roads are modeled, excluding the holes and bumps to be taken into account; in other words, the roughness of the asphalt is not considered.

Bumps that are modeled for purposes similar to those of this study are frequently attributed to shapes derived from circumference or sine wave [135, 148]. In this case, a sine wave in the range from [0,π] has been modeled with h as the maximum height of the bump. The sine wave equation is given below:

$$z = h \cdot \sin(\omega \cdot t) \tag{3.52}$$

Where t is the walking time of the bump and the pulsation ω is derived from the following equation:

$$\omega = \frac{2 \cdot \pi}{t} \tag{3.53}$$

In Figure 3.25 the representation of a generic bump shape as a function of the time is shown.

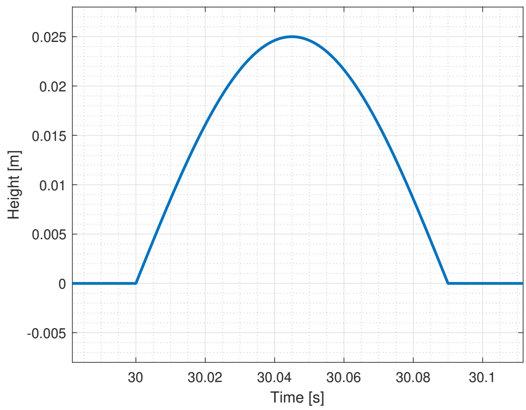

Fig. 3.25 Sine wave bump

In order to have a comparison with a virtual 7-post model, the results of several simulations performed using the model implemented in MATLAB/Simulink are compared with results obtained from CarRealTime [149], which is a commercial software widely used to study the dynamics of road vehicles and competition.

CarRealTime (CRT) is a virtual environment that could simulate some conditions similar to the functioning of a 7-post test rig. In CRT the parameterization of the vehicle can take place with greater or lesser accuracy, depending on the design needs and available data, as well as the definition of the road. The latest can be flat or littered with road surface imperfections with different characteristic dimensions. This simulation environment is also able to easily interact with other popular software dedicated to vehicle dynamics.

The simulations are conducted using the same vehicle used for the Virtual 7-Post model.

3.6.1 Validation on Bumps

In this paragraph the validation on a defined bump is analyzed, in both symmetrical and asymmetrical conditions. In particular, the chosen bump has the following characteristics:

- Height = 0.05 m
- Length = 2.5 m
- Vehicle velocity at the impact instant = 60 km/h

In the asymmetrical condition the bump impact only under the left side of the vehicle. For the validation of the model, the comparison of the virtual 7-Post with the reference from CRT is shown for the CoG and the four wheels center displacement (for symmetrical asperities only two wheels are reported).

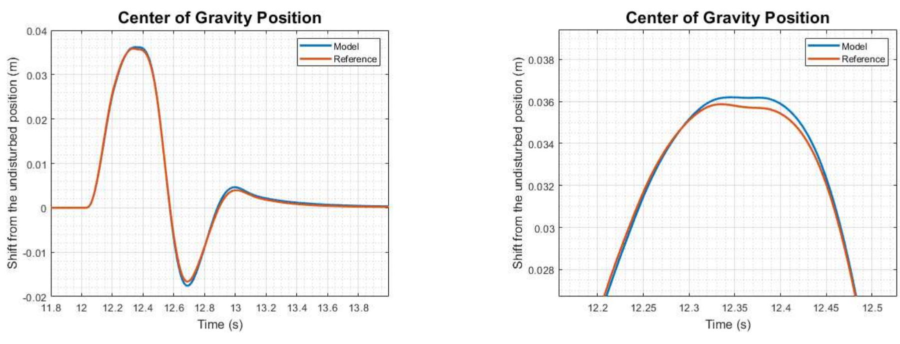

(a) CoG displacement (b) CoG displacement detail

Fig. 3.26 Center of gravity displacement on symmetrical bump

Starting from the symmetrical bump, from Figure 3.26 it is possible to notice how the 7-Post virtual model is able to reproduce faithfully the CoG variation, following the reference in its entire dynamics, with just slight deviation in the extreme conditions (peaks and valley). The same behavior can be observed also in Figure 3.27 for what concerns the wheel's center displacements.

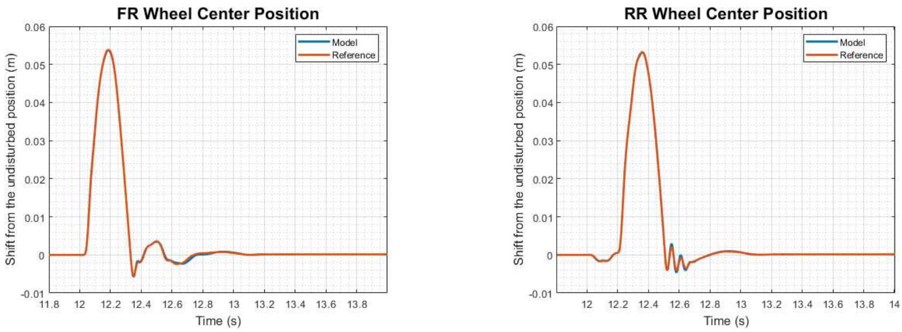

(a) FR wheel center displacement (b) RR wheel center displacement

Fig. 3.27 Wheel centers displacement on symmetrical bump

Moving to the asymmetrical bump, Figure 3.28 shows that the model is able to reproduce the overall center of gravity behaviors, with slightly more marked deviations from the reference in the final section of the perturbation.

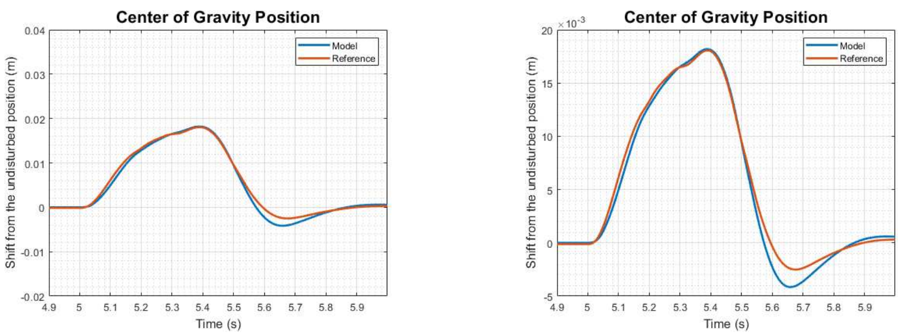

(a) CoG displacement (b) CoG displacement detail

Fig. 3.28 Center of gravity displacement on asymmetrical bump

This is strictly related to the displacement of the wheels' center, shown in Figure 3.29; the model is able to reproduce the variation with a good level of approximation, with few slight deviations in particular for the wheels that do not impact on the bump. This could be related to a not-perfect parameterization of the vehicle for what concerns its rolling behavior, with some inaccuracies in the definition of the suspension and vehicle characteristics.

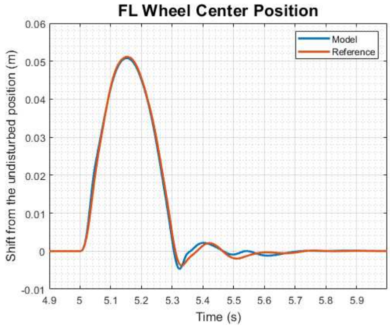

(a) FL wheel center displacement

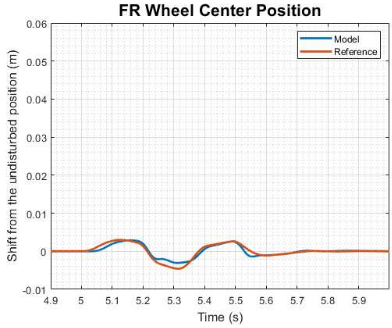

(b) FR wheel center displacement

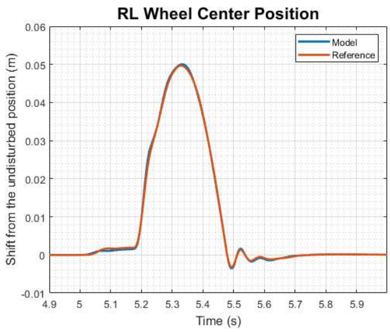

(c) RL wheel center displacement

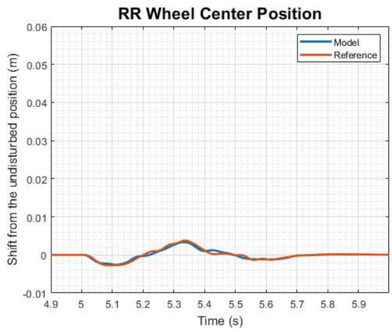

(d) RR wheel center displacement

Fig. 3.29 Wheel centers displacement on asymmetrical bump

3.6.2 Validation on Holes

Following the same approach used in the previous paragraph, the model has been validated also on different holes. For brevity, just two comparisons on a specific hole, both symmetrical and asymmetrical are reported. The chosen hole has the following characteristics:

- Height $= -0.025$ m

- Length = 5 m
- Vehicle velocity at the impact instant = 100 km/h

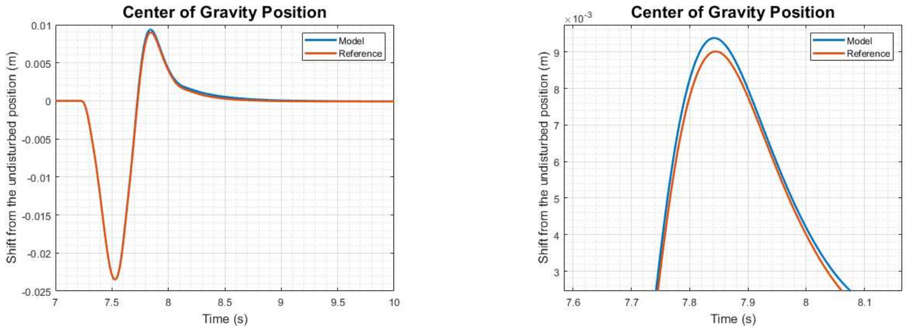

(a) CoG displacement (b) CoG displacement detail

Fig. 3.30 Center of gravity displacement on symmetrical hole

For the symmetrical hole can be done the same considerations already made for the symmetrical bump, from Figure 3.30 it is possible to notice how the 7-Post virtual model is able to reproduce faithfully the CoG variation, following the reference in its entire dynamics, with just slight deviation on the highest peak. The same behavior can be observed also in Figure 3.31 for what concerns the wheel's center displacements, where only small deviations are visible at the end of the simulation.

For the asymmetrical hole, Figure 3.32 shows that the model is able to reproduce the overall center of gravity behaviors, with slightly more marked deviations from the reference in the final section of the perturbation. Also in this case, the behavior of the CoG is strictly related to the displacement of the wheels' center, shown in Figure 3.33; the model is able to reproduce the variation with a good level of approximation, with few slight deviations in particular for the wheels that do not impact on the bump. This could be related to a not-perfect parameterization of the vehicle for what concerns its rolling behavior, with some inaccuracies in the definition of the suspension and vehicle characteristics..

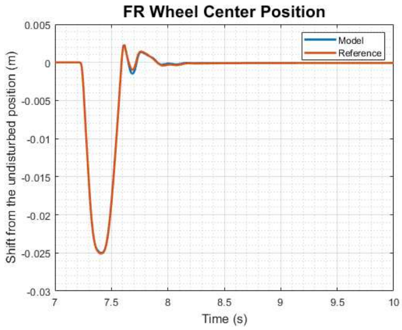

(a) FR wheel center displacement

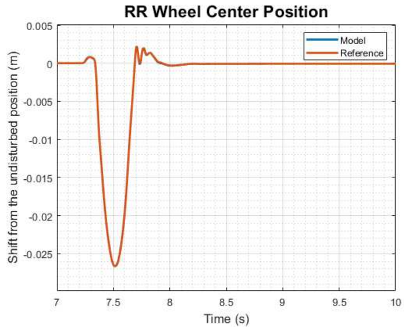

(b) RR wheel center displacement

Fig. 3.31 Wheel centers displacement on symmetrical hole

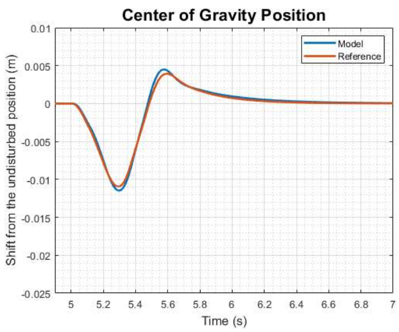

(a) CoG displacement

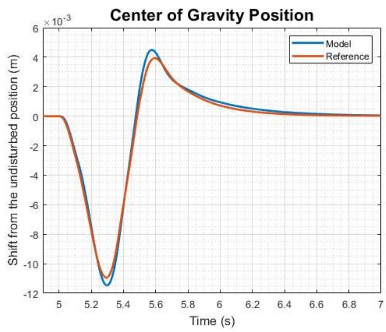

(b) CoG displacement detail

Fig. 3.32 Center of gravity displacement on asymmetrical hole

3.7 Case Study

Finally, in order to assess the model potentiality in suspension parameters optimization, a simplified case study has been built. Using the same symmetrical bump, already presented in paragraph 3.6.1, several simulations have been carried out varying both the spring stiffness and the damping curve of the shock absorber, choosing among commercial components compatible with the reference vehicle. In particular, three values of spring stiffness have been defined:

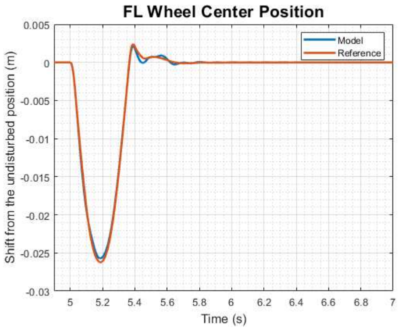

(a) FL wheel center displacement

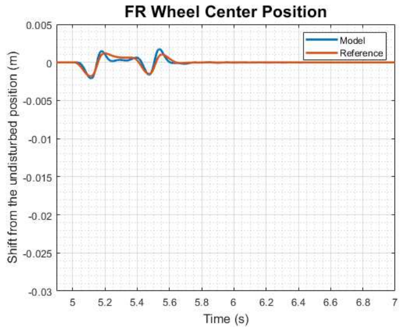

(b) FR wheel center displacement

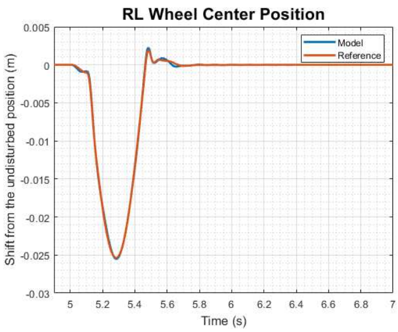

(c) RL wheel center displacement

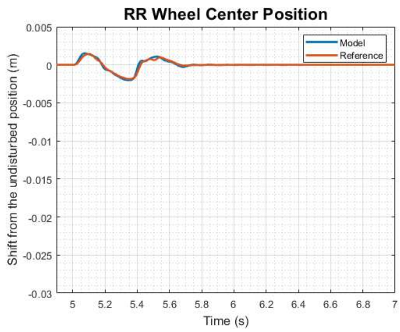

(d) RR wheel center displacement

Fig. 3.33 Wheel centers displacement on asymmetrical hole

- case a: $K_s = 120000$ N/m, with a reduction of the 20% with respect to the nominal value;
- case b: $K_s = 150000$ N/m, the nominal value adopted in the validation phase;
- case c: $K_s = 180000$ N/m, with an increase of the 20% with respect to the nominal value;

The same consideration was made for the damping curves of shock absorbers, defining three different conditions:

- case α: with a reduction of the 20% with respect to the nominal damping curve;

- case β: the nominal damping adopted in the validation phase;
- case γ: with an increase of the 20% with respect to the nominal damping curve;

The same springs and the same shock absorbers are adopted simultaneously on all four corners, resulting, globally, in nine different combinations. Then, two different studies have been carried out, comparing all the different configurations; the first one focuses attention on the CoG displacements, in order to find the best configuration that reduces it, to obtain the best ride performance; the second one, instead, aims to find the solution that maximizes the passenger comfort, studying the CoG vertical accelerations. For the first analysis, referring to Figure 3.34, the configuration that shows the overall minimum CoG position variation is the $a-\gamma$, with the lowest value of spring stiffness and the highest level of damping. In addition, it is also possible to see how this condition presents a reduced oscillation time if compared with the other simulations.

In the second case, analyzing Figure 3.35, it is possible to state that the configuration that presents the minor interval of CoG vertical acceleration is the $a-\alpha$, with the lowest value of spring stiffness and the lowest level of damping. Clearly, the best configuration depends on several factors involved in this simplified case study: the vehicle itself, the longitudinal velocity of the vehicle during the impact, the shape of the asperities and the suspensions parameterization. The combination of all these factors makes the definition of the best suspension setups quite complex, but, as shown by the results of the case study, the developed Virtual 7-Post model can provide interesting insights, simplifying the performance optimization process. It is also possible to define more complex road inputs and further configurations of the suspension system, to create cases as close to the reality with motorsport teams face every day.

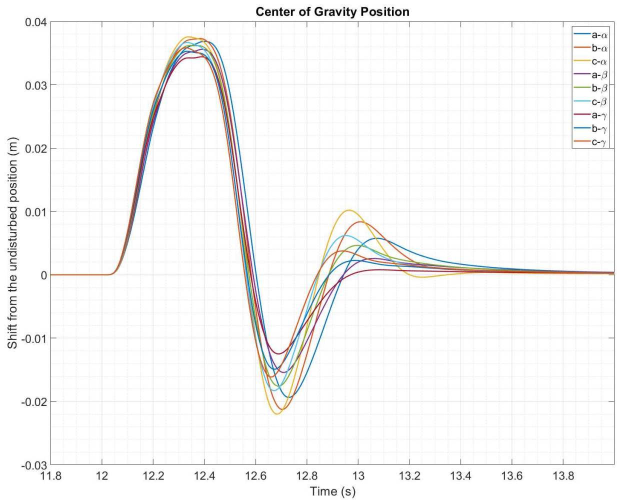

(a) CoG displacement for all the configurations

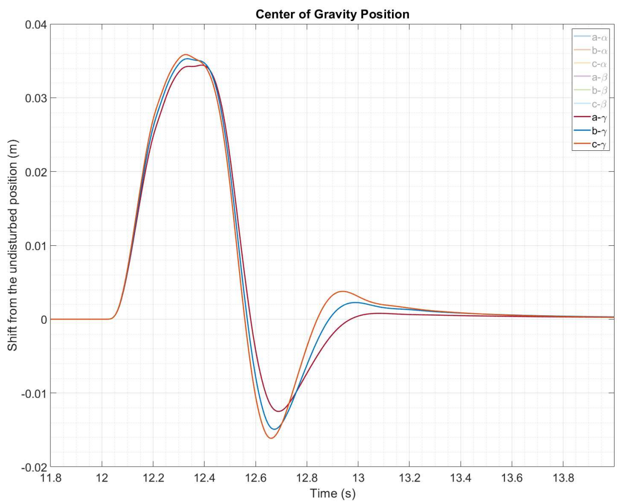

(b) CoG displacement for only 3 configurations (to highlight the best one)

Fig. 3.34 CoG displacement for all the 9 combinations

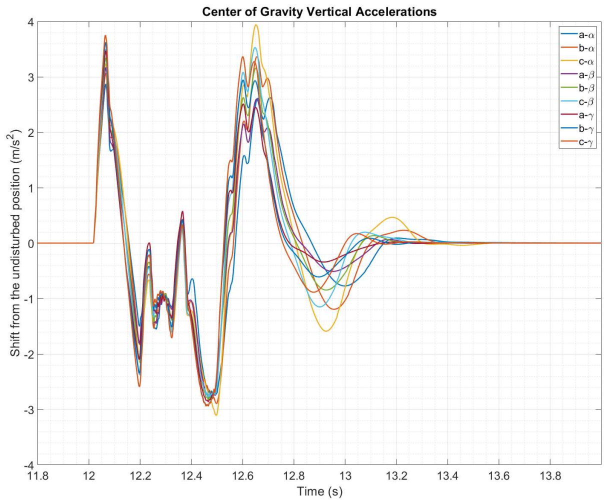

(a) CoG acceleration for all the configurations

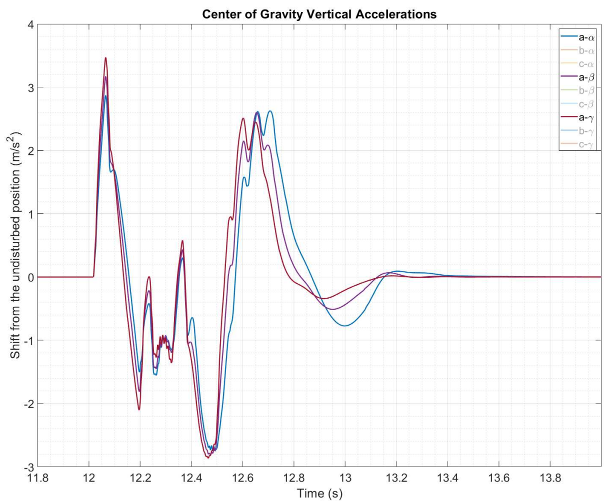

(b) CoG acceleration for only 3 configurations (to highlight the best one)

Fig. 3.35 CoG acceleration for all the 9 combinations

3.7.1 Final Considerations

In this Chapter, a lumped parameters model, developed in the MATLAB/Simulink environment, has been presented. Inside it, there is an insight into suspension modeling, so that the equivalent stiffness of the suspension is not considered as a vehicle parameter, but every stiffness of each elastic element could be considered. This will allow during the vehicle setup to find the best compromise for each suspension element, with a high level of accuracy on the corresponding stiffness value. It follows that it will be possible to make a multiplicity of simulations, being able to change several parameters, in search of the best compromise, without incurring in all the times and costs related to the real bench, as highlighted in the case study. For model validation, a more complex software that could create virtual reference data has been adopted. The comparison with the reference data gave positive feedback on the accuracy of the model; the model results deviate from the reference with small errors, due to the simplified assumptions introduced in the modeling phase. In order to improve the performance of the model, further developments could be related to the implementation of the following new features:

- to simulate and model also the forces due to aerodynamic loads and the inertia contributions with a more specific definition of the model equations;
- to consider the damping of the tire, in order to have a more accurate analysis;
- to include wheel angles and suspension geometry in the model, in order to implement also lateral force interactions effect in the analysis.

The introduction of the updates just described will lead to the development of software increasingly complete and able to compete with other existing tools. In addition, to completely validate the presented model, it will be necessary to make other comparisons, with real data, coming from outdoor acquisitions or from a real 7-Post test bench.

Chapter 4

Driving Style Characterization

4.1 Introduction

As already discussed in paragraph 1.5, driver style identification is one of the main topics in different scenarios. In order to highlight the driver's effect on the vehicle performance, aiming to be as objective as possible, this work relies mainly on the statistical methods which have a stronger generalization capability so that they can recognize the driving behavior easily and accurately. Furthermore, the ambition is to identify metrics that are as generalized as possible, therefore independent from the track topology and the vehicle used, so they can be applied in any context. The final aim of this research activity is to find a driver classification criterion starting from metrics, objective and applicable in every context (regardless of the circuit topology and the vehicle driven), starting only from vehicle data analysis, without any prior knowledge of the drivers. Indeed, studying driving style, decisive for the outcome of a lap, can help predict the results in terms of lap time and knowledge about the differentiating skills among racing and non-racing drivers can be useful for developing targeted training for amateurs based on what mistakes they usually make, but also for established drivers to identify what their weak points are and improve themselves. Therefore, although aware of the difficulty of a universal classification since the guide is nondeterministic and influenced by numerous accidental factors, the idea was to look at the vehicle plus man system as an unknown dynamic system whose behaviors are investigated and quantified through objective KPIs. In addition, modeling the behavior of drivers, acquiring and objectifying their characteristics, can also be helpful for exploring the human mind and body to deeply understand how it reacts to sudden stimuli that can arise in various situations, sometimes even critical, on the track.

To reach these targets, a novel methodology (Figure 4.1), quite different from those commonly used in literature, has been developed. The main principles on which this thesis' approach is based are:

- use of field data acquired on a real race car and not in a simulator environment, in order to better reflect the conditions that the drivers actually face on the track;
- classify the driving style with metrics that are objective and generalized, applicable to a driver of any experience, to any vehicle and on any circuit;
- focus the entire work on differentiating between professional and amateur drivers through parameters related to driving style.

Although in the literature there are studies with some of the characteristics mentioned above, it is believed that a work that simultaneously blends all these aspects together is original and innovative in this field of research.

The methodology proposed was applied for the analysis of three macro-topics, fundamental for the development of this research:

1. information obtainable from acquired data;
2. study of trajectories and repeatability;
3. analysis of the tire grip limit conditions.

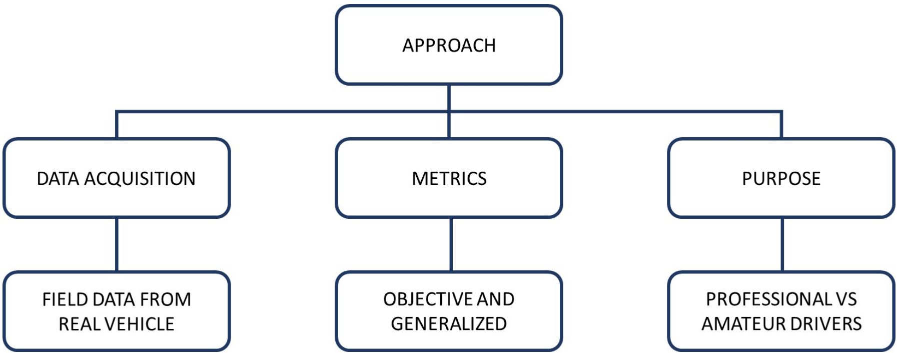

Fig. 4.1 Proposed approach

4.1.1 Telemetry-based Metrics

Many works in the literature focus on the identification of metrics obtainable from acquired data without invasive processing operations. In [150], a classification algorithm for professional drivers based mainly on data obtained from the pedals is implemented, such as throttle gradient or brake activation/deactivation, time delay between throttle and brake, braking distance, showing how different drivers can have different styles from this point of view while achieving similar results in terms of performance (e.g. lap times). One possible application suggested is the analysis of the driving style at a driver-in-the-loop-simulator. Similar metrics can be found in [151] in which the authors try to identify and validate a classification algorithm for drivers based on their driving style on three different datasets collected from 3 race seasons. They came to the conclusion that driving style can be distinguished automatically based on metrics describing the control inputs: brake, throttle and steering, in line with the aim of the study which was to provide methods helping with setting up race cars specifically for individual drivers. From all these studies described [76–78, 150, 151], it emerged that one of the factors that most influences a race on the track is the use of the pedals, therefore in order to identify the differences between the drivers, a study on throttle and brake is certainly necessary.

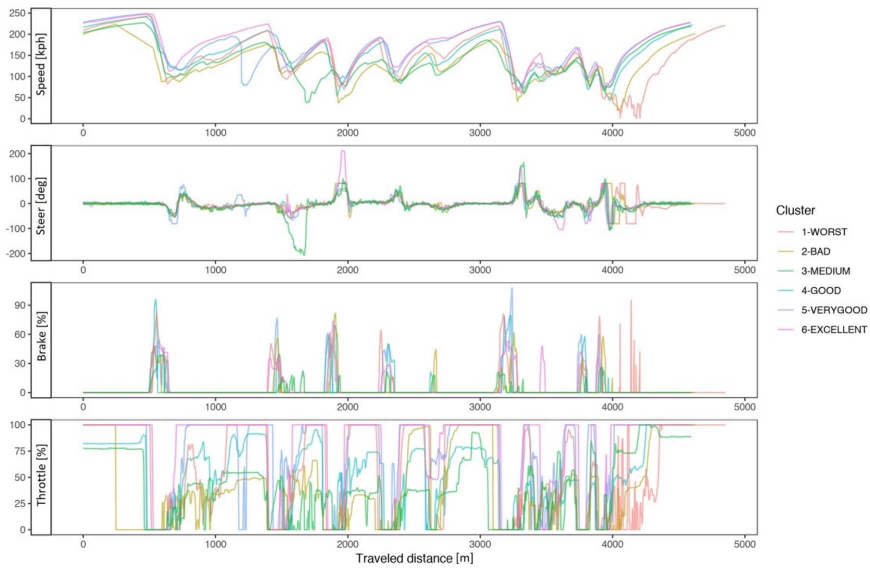

Fig. 4.2 Best lap times by performance level [77]

As mentioned, [77] used different metrics to differentiate the drivers, among these many were based on brake and throttle, being this among the main inputs that determine the outcome of a lap on the track. These metrics included mean, median and quartiles of brake or throttle, throttle speed (which with the steering speed are indicative of control activity in the corners), brake point and brake release relative to the start of the segment and percentage of full throttle (Figure 4.2). Similarly to [77], also in [78] the throttle variance and the mean steering speed were used as measures of control activity and consistency when driving in corners. Furthermore, the maximum brake pedal position on a scale of 0 (minimum) to 100% (maximum) was used as a measure of braking performance and the time at 0% and 100% throttle also brought out differences between the drivers. The time from the initial brake pedal actuation to the maximum brake pedal position during a braking maneuver was used as a measure of brake efficiency. Some of the indicators that emerged from both these works have been very useful for the development of this research task.

The use of brake and throttle is closely linked to the speeds and accelerations that the driver is able to obtain on the track. While there is little to say about speed, clearly the goal is to try to go as fast as possible in any sector of the circuit, on its first and second derivatives (acceleration and jerk) a more in-depth study can be made to understand the driving style of the drivers. Imposing the right acceleration or deceleration is crucial to be able to follow an optimal trajectory and take the curves in the best possible way. In particular when cornering, the right combination of longitudinal and lateral acceleration is what allows a driver to optimize the distance traveled and the speed reached to obtain the best lap time. In this regard, a very explanatory graph that allows seeing how the driver manages the accelerations is the ‘G-G Diagram’ which can be used as a driver performance indicator [139, 152–154]. Ideally, the driver should exploit the full potential of the vehicle by operating at or near the acceleration limits, however, the latter depends on a number of factors, including the characteristics of the engine, the gear, the tire-road friction coefficient.

As mentioned above, also jerk (the first derivative of acceleration) can be used to highlight style differences between pilots [155]. For example, in [156] the authors examined whether vehicle jerk contains information that could be potentially used to identify aggressive drivers. They hypothesized that the vehicle jerk indicates how smoothly a driver accelerates and decelerates the vehicle, and aggressive drivers may use large jerk (above a pre-defined threshold) more often by operating the gas and brake pedal compared to normal drivers. For their research they used two jerk-based metrics indicative of the use of a large positive or negative jerk during acceleration and braking respectively. In the end, for their case studies, these metrics were found to be effective in identifying aggressive drivers, but also in distinguishing speeding and non-speeding drivers. Additional metrics relating to jerk, both longitudinal and lateral, were introduced in [157], to be able to distinguish the drivers based on their driving style. The authors claim that the most relevant information is encoded in the frequency and variability of accelerations, thus they measured the standard deviation of the acceleration and jerk distributions over time and used them as an additional classification parameter.

Also the vehicle development is a subject closely linked to identifying the style of the drivers and several studies have provided interesting insights in this area. This topic is the basis of the study presented in [79], whose purpose was to compare professional and amateur pilots to help improving ADAS systems. The methodology adopted was to use data easily obtainable from telemetry and then develop metrics (in this case related to the steering) to evaluate the drivers, which is precisely the philosophy behind this project. In [84], the authors argue that information about driver's driving skill can be used to adapt vehicle control parameters to facilitate the specific driver's needs in terms of vehicle-performance and driving pleasure. In particular, with the use of a driving simulator, specific maneuvers were carried out in which the drivers were asked to give only steering inputs, maintaining the speed fixed. This is because the method was based on the coefficients of the discrete Fourier transform (DFT) of the steering wheel angle and the preliminary results showed that this parameter was reasonably effective in differentiating expert drivers from low-skill drivers. Also in [86] was developed a driving style identification method, applied to improve vehicle performance, in this case to develop adaptability of drivers and enable an automatic transmission gear decision system to meet the requirements of the driver's various personalities. This study conducts theoretical and experimental research on identifying the driving style based on the driver's dynamic requirement (related to driving resistance and its change rate). The authors analyzed the subjective factors (e.g. driver's personality) and objective ones (e.g. road conditions) affecting driving style, they also used exponential smoothing to establish the predictive model that could be used to identify the driving style based on the historical driver's dynamic demand data and they arrived at a general classification in sports, moderate, and economical types for driving styles. Finally, real vehicle tests were designed to verify the correctness and feasibility of the proposed method, which reflects the process that has been followed during this thesis work.

Finally, it is important to present a study that, at least in part, reflects the methodology that was followed during the presented research work: in [85] the philosophy adopted was to identify metrics that were more explanatory than the traditional ones, as lap time or average velocity, because although powerful, these metrics are closely related to the track and the vehicle and they do not always show where and why lap time differences occur. Therefore, the authors focused more on vehicle-trajectory and handling performance and they developed an algorithm to evaluate how far the driver or the vehicle is from the optimum, which is given by the maximum horizontal acceleration while retaining the trajectory or having the highest possible tire forces, respectively. This algorithm outputs an optimized vehicle state vector and by correlating the accelerations and real forces with those optimized, metrics that index the performance of the driver are obtained. These metrics made it possible to draw more detailed conclusions about the nature of the differences between the drivers in line with the stated purpose of this work which was to provide evaluation methods for drivers which allow general, track independent, conclusions on the driving style and point out areas for performance improvement. The aim was closely linked to that of this activity, which, however, is focused more on emphasizing the differences between professional drivers and not, rather than on improving the performance of the pilots based on optimization in a simulation environment.

It can be concluded that the processing of telemetry to derive metrics from them is certainly the approach that best suits this research project. The various studies presented have offered an overview of which are the parameters that, in a more or less direct way, can be obtained from the acquired data and during the presentation of this work, others indicators, specifically identified to differentiate the drivers, will be described. However, in order to be able to face the problem at 360° and take into consideration every aspect that is involved in a race on the track, there are still two fundamental topics to be explored: the study of the optimal trajectory to be taken on the track and the dynamic aspects related to the physical limits of the vehicle and the tires.

4.1.2 Trajectory Analysis

The study and comparison of trajectories between professional and non-professional drivers are also of great interest to the aim of this work. Various issues are involved in this study, such as the identification of curves in a circuit, the concept of the ‘racing line’ as the best trajectory to be taken to obtain the best time, the trade-off between radius of curvature and cornering speed. A literature review was therefore carried out also in this case to find other relevant research activities that investigate these topics.

Since the biggest differences between drivers occur in corners rather than straights, the identification of the curves of the circuit was the first task deepened. To date, many approaches have been developed to extract curve information from commercial satellite imagery, Global Positioning System survey data, laser-scanning data, and AutoCAD digital maps. However, as pointed out in [158], the existing approaches based on different data sources have proved their effectiveness in the extraction of curve information, but they require costly data collection or extraction or extensive manual labor. This complexity is beyond the scope of this work since it is searched only a rough subdivision of the circuit to then deepen other issues. Also the method presented by [158] and then used by [159], turned out to be not properly suitable for the purpose of this work. In [158] is presented a fully automated method for the extraction of curve data from geographic information system (GIS) roadway maps and the calculation of their length, radius, and central angle. Even if it is quite simple since there is only one adjustable parameter of the curve identification algorithm, that is the threshold of the bearing angle, this method is probably more usable for roads than for a circuit, as a matter of fact it is proposed in to solve curve safety issues related to lane departure crashes. In any case, these latest studies have offered an interesting insight into the identification of curves, such as the definition of some specific features (the point of curvature, the point of tangency, etc.). Despite this, the path chosen in this thesis to locate the curves was different; it was in fact decided to proceed by analyzing the different phases that a driver goes through when taking a corner and then making a subdivision of the curves based on the behavior of a professional driver. In order to divide the trajectory followed by the driver into different phases and then proceed with the identification of the starting and ending points of the curves on the circuit, great help was provided by the previously mentioned work of [85]. Here, to analyze driver performance independent from a specific track section, control states were defined based on the driver's inputs. The authors used three boolean variables to describe if the brake pedal, throttle pedal or steering wheel angle were active and their combination resulted in four control states: Pure brake (Braking), Trail brake (Turn Entry), Pure steer (Mid Corner), Throttle steer (Turn Exit). They did not consider other possible states because they were not relevant to their study, while in this activity other combinations were also added.

Another fundamental aspect linked to trajectories and driving performance is the 'Racing Line', defined as the perfect trajectory to follow to minimize lap time. The trajectory of the racing line depends on the severity of the corner, how long the following straight is and what kind of car is being driven. The racing line should be taken as follows: race to maximum capacity at the braking point, move the vision to the apex point, turn-in the car at the turn-in point, make the apex of the ideal racing line, begin to introduce the accelerator and finally open up steering to the corner's exit point. This description of the perfect racing line is provided by [160]: here the authors describe an optimal control-based strategy to find a trajectory of the car minimizing the traveling time subject to steering and tire limits. In an application for a 90° maneuver, the resulting minimum time trajectory had the following features: first, the car accelerates in the first straight portion of the track, then, it moves toward the outside edge of the corner (first kissing point), brakes, and turns into the corner through the apex point; finally, the car starts the exit from the corner, approaches to the second kissing point, and accelerates with maximum traction force. Always with the aim of identifying the optimal racing line, [161, 162] developed two optimization algorithms to find the minimum time trajectory taking into account not only the geometry of the circuit but also the dynamics of the vehicle. Both studies state that the optimal trajectory is the best compromise between the one that leads to the shortest distance traveled and the one that allows achieving the highest speeds (least curvature track). What determines the weight between these two solutions is the vehicle's dynamic behavior (the tires' performances, the braking/driving torque available, maximum achievable speed).

All these studies have offered a general overview of which is the optimal racing line to follow, but it is clear that it is strictly a function of the shape of the track in question, as well as of the vehicle available [163]. During the research activity, these studies have been taken as a reference to get an idea of what the optimal trajectory could be and how close to it the trajectories undertaken by professional and non-professional drivers are. There are several studies on algorithms that try to find the best trajectory to follow for different fields of application [164–166], but this was not what was of interest in the context of this thesis as there is no absolute best trajectory, in fact two drivers could adopt different choices based on their style but still get the same performances. Instead, the analysis that was carried out the most was that of comparing the trajectories followed by the drivers, especially when cornering. In this regard, for example, [167] makes interesting comparisons between the trajectories, plotting the lateral deviation of the racing lines from the track center line as a function of the distance along the center line. These comparisons are then deepened on the different sections of the circuit to fully understand the differences between the trajectories. In this study, the comparison was conducted between the trajectory of a driver and those generated by two algorithms, but clearly, this procedure can also be applied to the comparison between multiple drivers, in fact, this is what has been done in this thesis project.

This method of comparison was also used in [168]. In this study, the statistical dispersion of professional car drivers' trajectories was examined to quantify the repeatability of their performance. The driven paths were mapped to the track center line in terms of distance along the center line and lateral offset from the center line and with the help of statistical indicators and path curvature, comparisons were made between the driven paths of different drivers, both on the entire lap and on the individual curves (Figure 4.3).

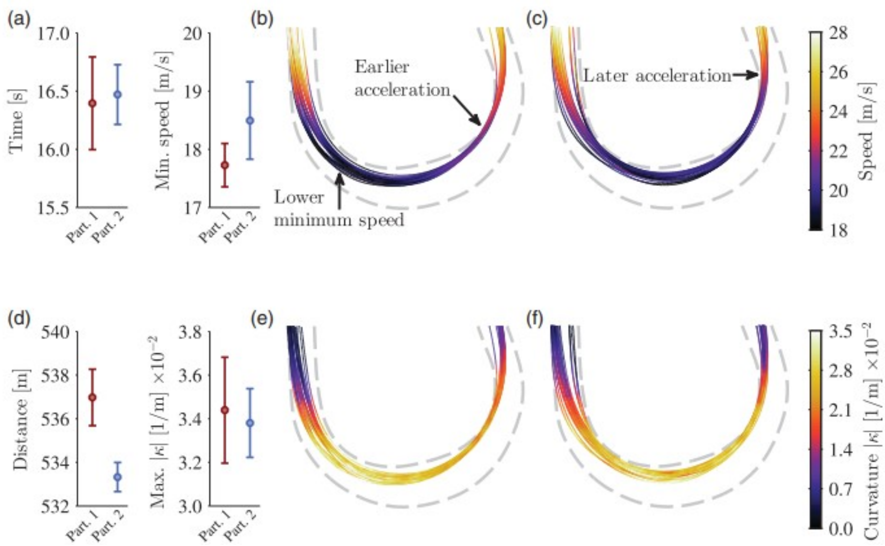

Fig. 4.3 Cornering comparison - (a) Median segment time and minimum speed. (b) Participant 1: speed. (c) Participant 2: speed. (d) Median segment distance and maximum curvature. (e) Participant 1: curvature. (f) Participant 2: curvature [168]

The authors, with their case study, were able to show that professional drivers exhibit highly repeatable paths at specific points around the track and that two professional drivers may have two different styles, in terms of path followed and speed profile, but still achieve similar lap times. This study offered many interesting insights on how to compare pilots' trajectories and how to quantify results with statistical indicators. Having analyzed all the facets of the trajectories, the next paragraph will describe a final decisive aspect for the outcome of a lap on the track, that is, how much the driver is able to exploit the potential of the vehicle by pushing to the limit of grip.

4.1.3 Grip Conditions and Tire Limits

One of the conditions necessary to be able to get the most out of a racing car is to work close to the grip limit conditions. A good driver is someone who is able to recognize the limits of the vehicle he drives to understand how far he can go and optimize performance to the maximum; on the other hand, an amateur driver cannot recognize when the wheels are about to lose traction, so either pushes too far by making mistakes or stops pushing as soon as he feels he is losing control of the vehicle. It is therefore clear that, in order to highlight differences between drivers, an investigation of the conditions in which they work in terms of grip and slip indices could be very appropriate. In literature there are several studies that investigate the link between tire performance and limits; one of the aspects that emerges is how important it is to work near the edges of the 'tire friction circle (ellipse)' [139, 3, 169], which is a diagram that combines the longitudinal and lateral force.

The friction circle represents the force-producing limit of the tire for a given set of operating conditions (load, surface, temperature, etc.); in general, a circle is a close approximation to the boundary of the diagram that represents the maximum force that the tire can generate under these operating conditions. The applications are varied, in [154] the authors use this type of approach to investigate the strategies that professional drivers apply to utilize as much of the car's tire force as possible and then they extend these results to develop autonomous vehicles. A study more focused on inexperienced drivers is the one described in [83], where optimal ranges of slip ratios and slip angles in which a driver should work with a racing vehicle are proposed and aspects relating to the training of amateur drivers thanks to the analysis of telemetry data obtained from a simulator are also investigated. In fact, the slip angle and slip ratio values achieved give an indication of how far the driver pushes himself to the limits of grip and so how much he exploits the potential of the car. Therefore they can also be used as a comparison index between professional and amateur pilots, as it is done in [85]. Furthermore, the percentage of saturation of the tire is also used as a yardstick between more or less experienced drivers [77]. The saturation shows the percentage of tire utilization, when 100% is reached the tire will start slipping; this means that keeping the saturation to 100% represents the ideal utilization of the tires' capabilities.

Returning to the activity presented, it is clear that to evaluate the performance of the drivers, identifying the grip limits and the tire saturation conditions would have been useful, but this would have required an in-depth study on the vehicle and on the dynamics of the road tire contact [170, 171] that deviates a little from the thesis approach. Indeed, to identify the limit conditions it is necessary to take into account many aspects that are closely related to the vehicle, the tires used and the contact conditions that inevitably affect the generality of the approach. Therefore, it was decided to extract global information on the vehicle's behavior from the telemetry data, thanks to the help of the T.R.I.C.K. tool, deeply described in Chapter 2, to study the interaction characteristic curves and from these make some general considerations on the pilots' style.

4.2 Data Acquisition & Outdoor Test Session

The studies carried out for the research activity described in this chapter were conducted on vehicle data acquired from track tests, thus reflecting the real behavior of amateur drivers for the first time on a circuit. In fact, especially for novices, the use of a driving simulator could have provided greater confidence given the lack of risk of injury, thus altering the veracity of their behavior. That said, the vehicle and the equipped instrumentation, the data processing and the test plan will be described accurately.

4.2.1 Vehicle

The vehicle used was a Fiat 124 Spider 1.4 MultiAir 140 hp MT, year 2017 (Figure 4.4). It is a two-seater car produced from the year 2016 by FIAT car manufacturer and the model chosen for the tests was the Cabrio one (Figure 4.5) and its main characteristics are described in Table 4.1.

Fig. 4.4 Fiat 124 Spider

It has a turbocharged inline 4 cylinder engine, petrol motor, which produces a maximum power of 140 hp (103 kW) at 5000 rpm and a maximum torque of 240 Nm at 2250 rpm. The power is transmitted to the road by

Table 4.1 Vehicle characteristics

Parameter Name	Value	Units
Vehicle mass	1197.5	kg
Unsprung mass	200	kg
Wheel Base	2.31	m
X CG	1.088	m
Front Track	1.495	m
Rear Track	1.505	m
CG height	0.489	m
Front RollCenter Height	0.0767	m
Rear RollCenter Height	0.2084	m
RollCenter Height	0.1387	m
Roll Rate	4.406	deg/g
Pitch Rate	1.365	deg/g
Z Inertia Moment	950	Kg*m^2
X Inertia Moment	730	Kg*m^2
Front section area	2.13	m^2
Front control unit roll rad	0.292	m
Rear control unit roll rad	0.292	m
Front spring Stiffness	43.34724	N/mm
Rear spring stiffness	20.0973636	N/mm
Front motion ratio	1.388	[]
Rear motion ratio	1.107	[]
Nominal steer ratio	14.2	[]
Front static camber	0.3	deg
Rear static camber	0	deg
Optical long position	-1.022	m
Optical lat position	0	m

the rear wheel drive (RWD) with a 6 speed manual gearbox with central lever. For what concerns the suspension system, the 124 Spider is equipped at the front with a double wishbone suspension with a stabilizer bar, coaxial spring-damper assembly and attachment on the lower element and at the rear with a five-arm multilink system with a coaxial damper spring group. As for the braking system, it includes vented discs at the front and discs at the rear, all with a diameter of 280 mm. The tires equipped were Toyo Proxes R888R 195/50R16, which are summer track tires, homologated for the road

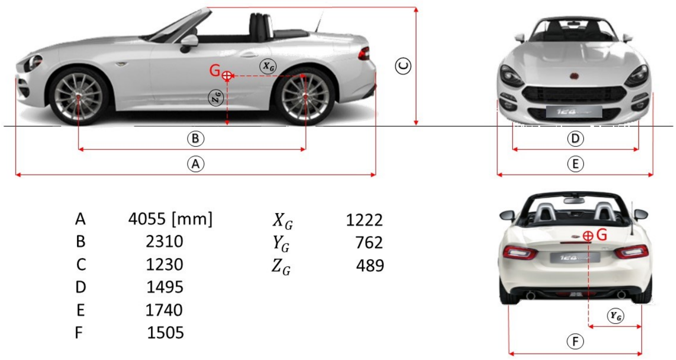

Fig. 4.5 Vehicle geometric parameters

and suitable for sports cars, that offer the best performance on dry asphalt, conditions in which the outdoor tests were conducted.

It should also be noted that to allow drivers to make the most of the car's performance by freely demonstrating their skills, the controls have been deactivated.

4.2.2 Instrumentation & Processing

The term 'data acquisition' refers to the process of measuring physical phenomena and their recording in order to subsequently analyze them. For the present research, four sensor systems were used:

1. Controller Area Network (CAN bus) integrated into the vehicle [172–174]; it provides data relating to percentage of throttle, brake pressure, gear engaged, steering angle and angular wheels' speed.

2. An inertial platform which, using accelerometers and gyroscopes, allows precise measurements of vehicle accelerations. Furthermore, measurements from high-grade kinematic global navigation satellite system (GNSS) receivers update the position and velocity navigated by the inertial sensors (Figure 4.6).

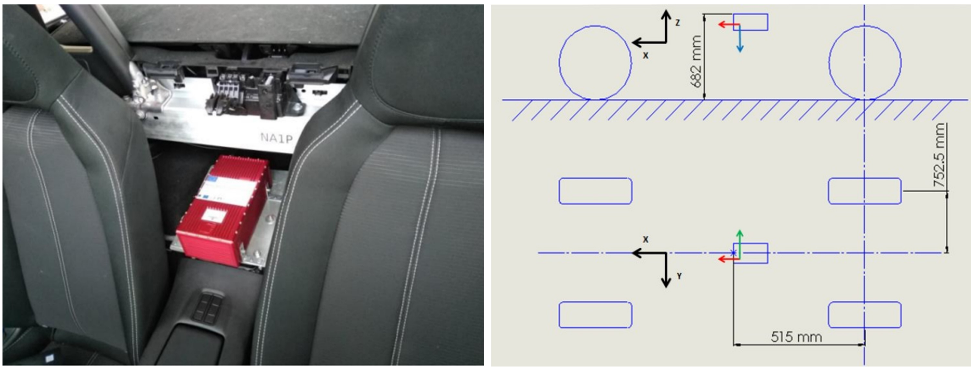

Fig. 4.6 Positioning of the inertial platform

3. An optical sensor which allows non-contact measurement of speed and slip angle. This instrument enables direct measurement of lateral and longitudinal components of the velocity vector of the wheels, to also obtain the tire slip indices (Figure 4.7).

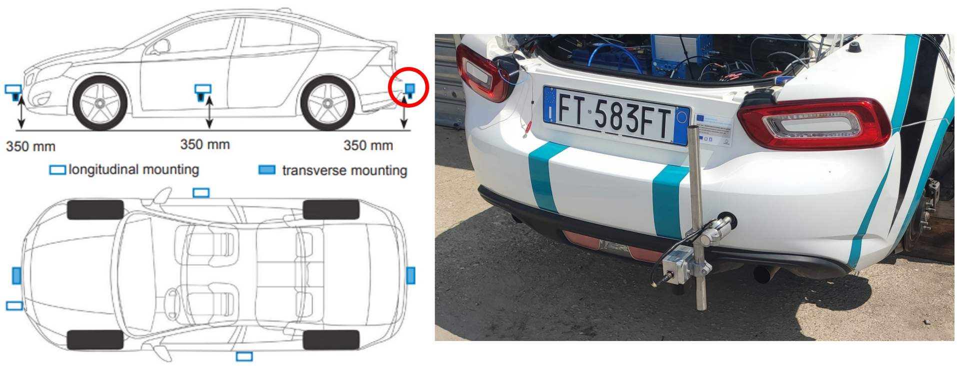

Fig. 4.7 Optical sensor mounting position

4. A complete data acquisition system capable of receiving various signals such as analogue, CAN, counter, encoder and digital. All the channels, passing through the acquisition system, are synchronized with microsecond precision.

All these devices used were connected together (Figure 4.8) and they provided several acquired channels, listed in Table 4.2, with a large amount of data, which required processing operations, differing from each other in terms of units of measurement and sampling frequency, coming from different instruments. Furthermore, all the channels have been modified to respect the conventions of the ISO reference system.

Table 4.2 List of acquired signals

SIGNAL	DEVICE
xCG: Centre of Gravity Longitude	OxTS
yCG: Centre of Gravity Latitude	OxTS
zCG: Centre of Gravity Altitude	OxTS
Vehicle Longitudinal Velocity	S-Motion
Vehicle Lateral Velocity	S-Motion
Vehicle Longitudinal Acceleration	OxTS
Vehicle Lateral Acceleration	OxTS
Vehicle Vertical Acceleration	OxTS
Yaw Rate	OxTS
Roll Rate	OxTS
Pitch Rate	OxTS
Steer Angle	CAN veicolo
Throttle Percentage	CAN veicolo
Brake Pressure	CAN veicolo
Gear Innested	CAN veicolo
Front Right Wheel Speed	CAN veicolo
Front Left Wheel Speed	CAN veicolo
Rear Right Wheel Speed	CAN veicolo
Rear Left Wheel Speed	CAN veicolo
Time	Processing Operations
Distance	Processing Operations

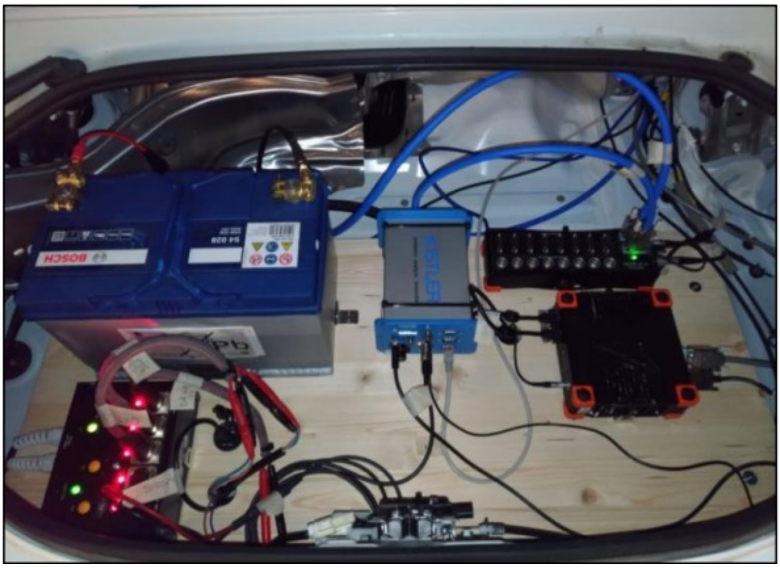

(a) Hardware fixed in the vehicle rear trunk

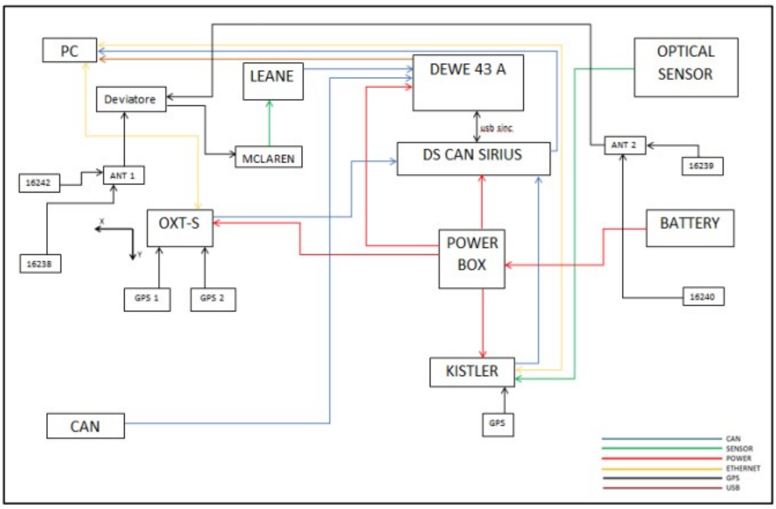

(b) Complete wiring of hardware devices installed

Fig. 4.8 Devices connection

4.2.3 Outdoor Test Session

Planning a testing session is essential for its success, the choice of instrumentation, vehicle, circuit and drivers to be compared must be carefully studied taking into account what the desired outcomes are and which parameters should be used to judge them [175, 176].

The circuit chosen to carry out the tests was the 'Circuito del Sele' in Battipaglia (SA). It is a flat circuit, thus chosen to avoid banking effects and facilitate inexperienced pilots, characterized by a track length of 1700 m, 6 curves and a straight of 400 m, with a maximum speed of around 135 km/h, allowing minimum lap times around 72 s (Figure 4.9). Thanks to the

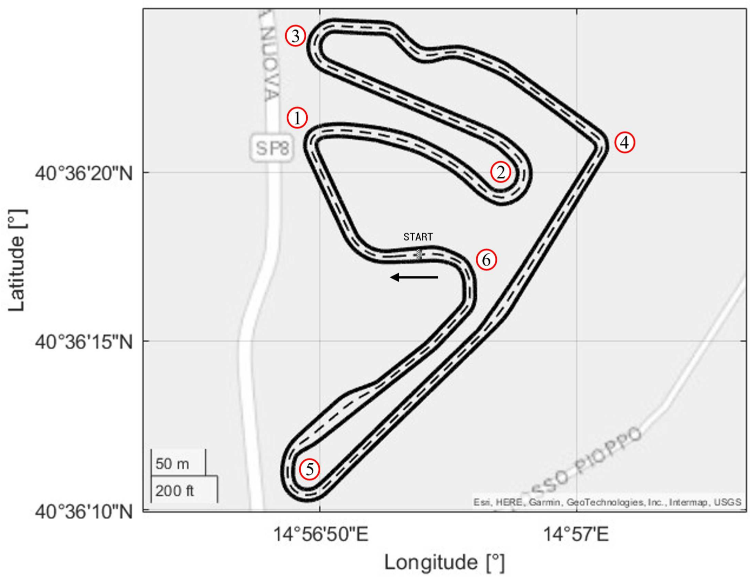

Fig. 4.9 Sele circuit topology

coordinates of the vehicle's center of gravity, obtained from GPS sensors, and the two track boundaries coordinates, obtained by points from Google Earth, it was possible to reproduce the circuit and drivers' trajectories for each lap in MATLAB environment (Figure 4.10).

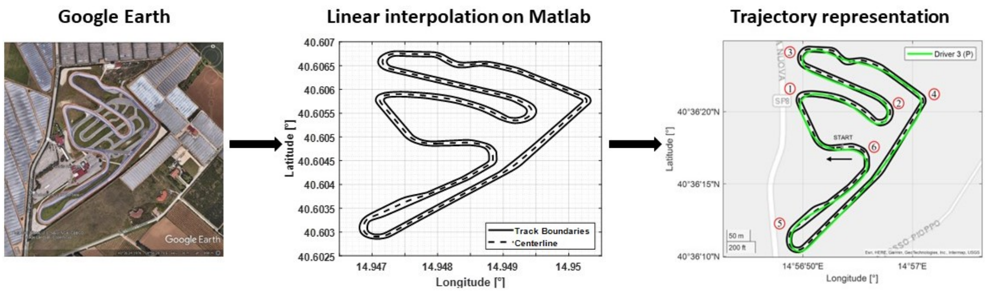

Fig. 4.10 Sele circuit and MATLAB representation

To correctly conduct the tests, particular attention was paid to the choice of the group of drivers: a total of 13 were selected, including two professionals (indicated by (P) in the following figures). By 'professional driver' it is meant a pilot who has a long experience on track; the remaining 11 drivers, on the other hand, were all amateurs, selected so that 6 had never had any experience on track while the remaining 5 had just a couple of experiences. All the drivers selected were males, for a more rigorous comparison with the professionals, with an age ranging between 22 and 56.

As for the test session, participants were instructed to drive the fastest lap time possible, and, in order to have comparable data, they have been put in the same driving conditions: dry track; same setup; same fuel level and track lighting; controls deactivated and tires in the stable performance region, after having been scrubbed from their brand new conditions, still far from the wear performance decay.

For the two professional drivers, 6 laps have been planned with an intermediate cool down, while for each non-professional driver, 10 laps have been planned, organized as shown in Figure 4.11 ('Max Performance' is a lap in which the driver pushes hard to get the best time, while 'Cool Down' is a tire-cooling lap).

The difference between the two categories is linked to the decision to introduce, for the amateurs, two intermediate laps in which they were accom-

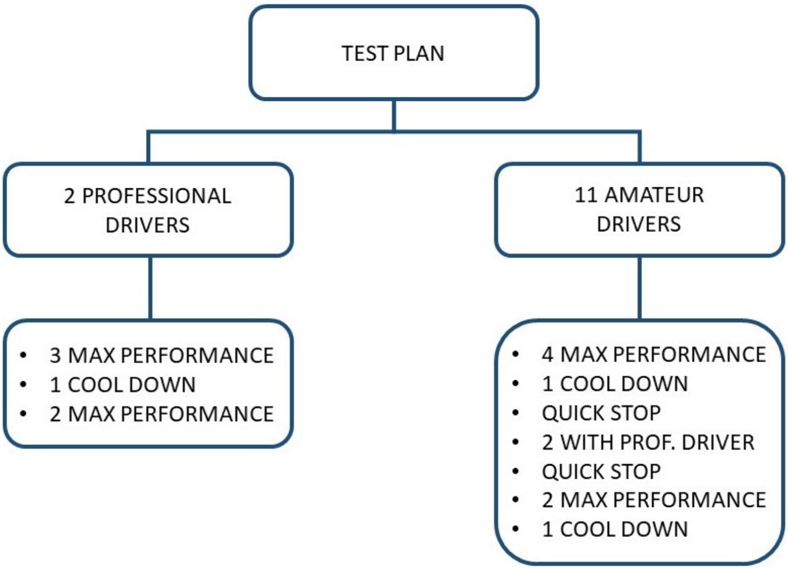

Fig. 4.11 Test plan

panied by one of two involved professional driver to receive instructions, to see if just two laps allowed the amateur driver to improve his style. Furthermore, given the greater probability of inexperienced drivers making mistakes, it was decided to plan for them for more laps to guarantee a fair number of acceptable laps among all drivers with greater certainty. After the test session, all the collected data has been processed using the T.R.I.C.K. 2.0 tool, performing all the operation already described in Chapter 2

4.3 Metrics from Direct Driver Interaction

Substantial differences can be found between driving in an urban environment and driving on track: while in the first case the guide must be responsible, paying attention to other road users, vice-versa, on track, the vehicle should be exploited to the maximum maintaining excellent levels of safety and appropriately managing posture, gaze and tires according to the weather and road conditions.

Aware of all the different aspects involved in driving on track, in this section, the attention is focused mainly on those controlled directly by the driver, hence it will deal with trajectories, gear shifting and steering.

4.3.1 Trajectory Studies: Racing Line and Curve Travelling

The first macro topic analyzed was the study of the trajectories because it touches different points that involve the driving style, especially related to corners' strategy, allowing to make both qualitative and quantitative considerations on the differences among pilots. Before starting this analysis, however, it was essential to get an idea of how to drive on track, so in-depth research was conducted on topics such as the best trajectory to take and how to tackle the curves in the correct way. Some researchers state that the optimal trajectory is the best compromise between the one that leads to the shortest distance traveled and the one that allows achieving the highest speeds (least curvature track), but, actually, no absolute best racing line exists, in fact, two drivers could get similar performance with different choices and it is also strictly a function of the shape of the track, as well as of the vehicle available [163]. Moreover, the problem of trajectory optimization is not only of a geometric nature but involves numerous aspects related to vehicle dynamics, including grip, car aerodynamics, power of the car engine and so on.

Therefore, during the research activity, these studies have been taken as a reference to get an idea of what the optimal trajectory could be, but then the approach was mainly to compare the trajectories of the pilots, similar to what is done in [168] where the authors examined the statistical dispersion of professional car drivers' trajectories to quantify the repeatability of their performance.

From a first global comparison of the trajectories of all the drivers, it emerged a higher standardization for the professional drivers who always follow the same line, as illustrated in Figure 4.12; on the other hand, the amateurs, in addition to going off the track more than once, often change the way of approaching curves, where the differences are more evident (Figure 4.13).

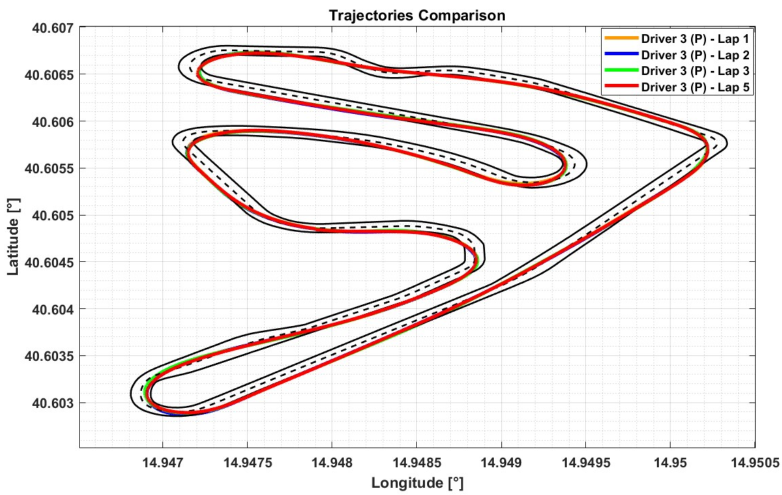

Fig. 4.12 Trajectories comparison - Driver 3 (P)

Although the repeatability of the single driver over several laps is not necessarily an indicator of better performance, it allows underlining the greater awareness of expert drivers on how to drive on track, which translates into better management of the vehicle, in terms of steering, pedals and gearbox, thus influencing, even if indirectly, the outcome of the lap. Indeed, in order to identify parameters that would allow to objectively compare the drivers, for

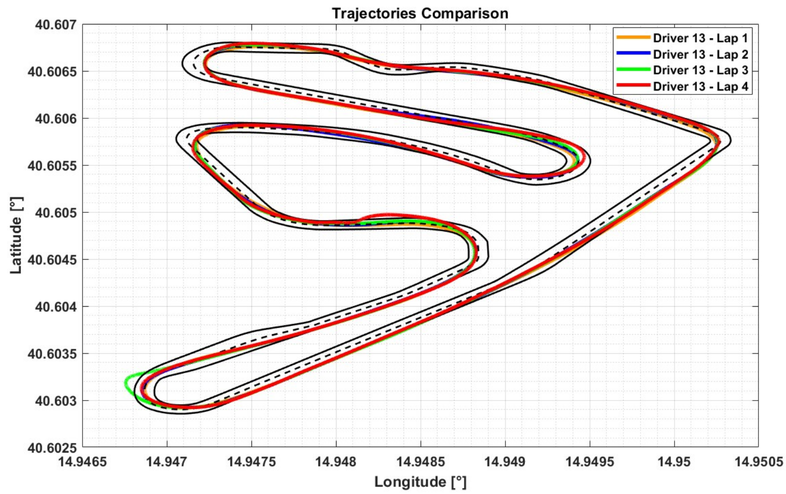

Fig. 4.13 Trajectories comparison - Driver 13

each lap of each driver some characteristic distances, function of trajectories, have been identified ([167]):

- the distances of the centerline and of the racing line from the two track boundaries;
- the distance between centerline and racing line.

In addition, to obtain adequate plots of the trend of these distances, a virtual distance channel was calculated on the basis of the centerline, in order to make the graphs between the different drivers comparable. All these distances were obtained using the 'Haversine Formula', described in equation (4.1), that allows calculating the shortest distance between two points over the earth's surface [177–179].

$$a = \sin^2\left(\frac{\Delta\phi}{2}\right) + \cos\phi_1 \cdot \cos\phi_2 \cdot \sin^2\left(\frac{\Delta\lambda}{2}\right) \tag{4.1a}$$

$$c = 2 \cdot atan2\left(\sqrt{a}, \sqrt{(1-a)}\right) \tag{4.1b}$$

$$d = R \cdot c \tag{4.1c}$$

Where ϕ and λ are latitude and longitude in radiant, R is Earth's radius (mean radius 6371000 m) and d is the distance required.

An example is shown in Figure 4.14 where the beginning and end of the curves are also indicated.

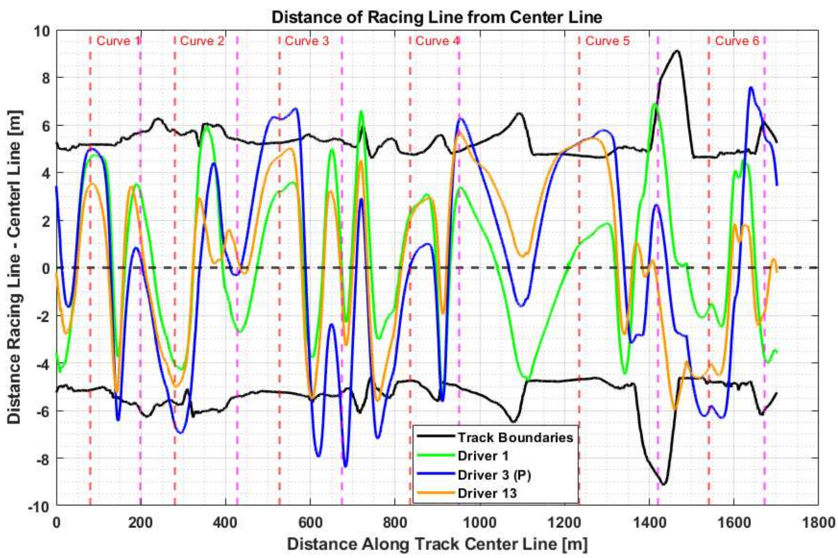

Fig. 4.14 Comparison of racing line distances from centerline. Observation: the distance of the track boundaries from the centerline is not constant because of the variable track width.

As expected, the main differences occur in the corners, particularly evident in turns 5 and 6 which proved to be the most difficult; therefore, insights into the individual curves from which to extract general evaluations will be presented below. First of all, it was necessary to identify the starting and ending points of the curves and to do this, reference was made to the different phases that follow one another during a lap on track. In order to identify them, three boolean variables were used to describe whether the brake pedal, accelerator pedal and steering wheel are active or not. In particular, these assume a unitary value if, respectively, the brake pressure is higher than 10 bar, the throttle percentage is higher than 10% and if the steering angle is higher than 10°, otherwise they assume a value of 0.

$$B_{brake} = \begin{cases} 1, & \text{if pBrake} \geq 10\text{bar} \\ 0, & \text{otherwise} \end{cases} \tag{4.2}$$

$$B_{throttle} = \begin{cases} 1, & \text{if rThrottle} \geq 10\% \\ 0, & \text{otherwise} \end{cases} \tag{4.3}$$

$$B_{steer} = \begin{cases} 1, & \text{if steerAngle} \geq 10^\circ \\ 0, & \text{otherwise} \end{cases} \tag{4.4}$$

To identify the curves, the trajectory of the generic lap has been divided into six sector types (Figure 4.15) based on the type of maneuver in progress with the same principle described in [85]:

- Pure braking
- Trail braking
- Pure steering
- Pure throttle
- Throttle steer
- Other

From this division, it was decided to select the start of the pure braking phase as the start of the curve, while the end of the throttle steer phase as the end of the curve. Then, assuming that the correct driving style is that of the

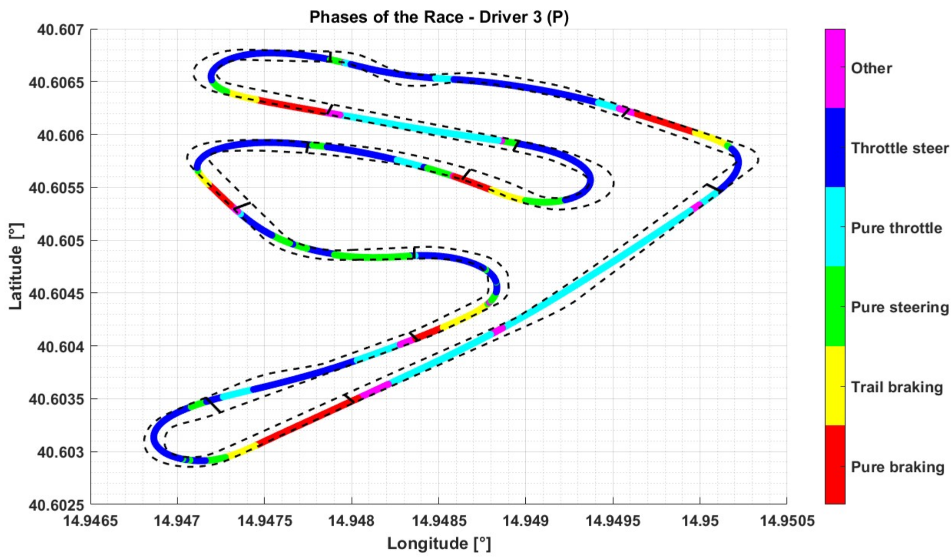

Fig. 4.15 Different phases of the race.

professional driver, the coordinates of the start and end of curves have been identified by averaging over five laps of the professional driver 3, following the procedure illustrated in Figure 4.16.

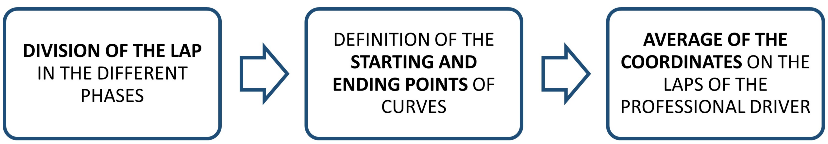

Fig. 4.16 Identification of the curves of the circuit

At this point, it was possible to deepen the study of the trajectories on the individual curves by making a comparison of the distances of the racing line from the centerline previously evaluated. An example is shown in Figure 4.17 for curve 5: as usually happens also in the first three corners, the professional driver tends to take the corner wider, then cut more, in order to apply the brake pedal as late as possible and to maximize the acceleration potential of the vehicle coming out of the corners. However, as for the exit, curve 5 is very variable, especially for amateurs drivers, probably because it is after a long straight, so it is more difficult to manage the trajectory.

Although these qualitative comparisons are very useful and interesting, the underlying problem was that they are closely linked to the circuit topology, while the research goal was to identify general metrics applicable for any track. This is why the next approach was to quantify the variability of the distances calculated for all the laps of the individual drivers and use it as an index of repeatability of the drivers' trajectory.

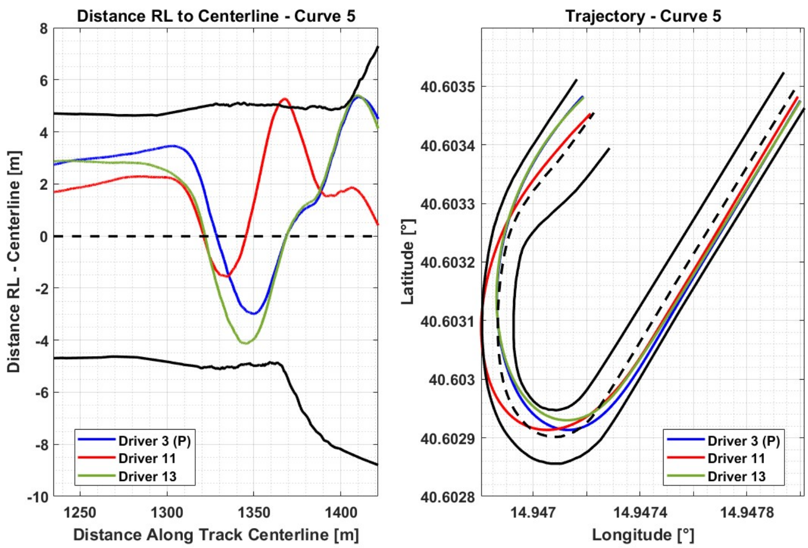

Fig. 4.17 Detailed comparison of trajectories - Curve 5

To evaluate the variability, the absolute standard deviation of the racing line-centerline (RL-CL) distance channels was calculated among all laps of the same drivers, for all the single acquired points in order to create a standard deviation channel for the entire length of the circuit. The reasoning behind this procedure is that a lower standard deviation indicates a greater

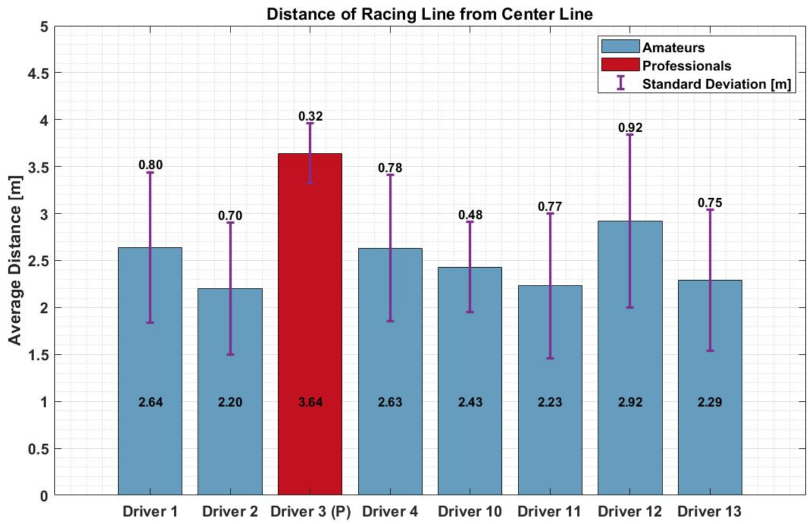

Fig. 4.18 RL-CL distance - Average and standard deviation

repeatability of the driver, meaning that he always tends to travel the same trajectory.

However, to quantify the difference between the drivers, the average value of the standard deviation channel was evaluated and the comparison results for the different drivers are shown in Figure 4.18.

As can be seen, professional driver 3 has a significantly lower average standard deviation than the other drivers, therefore this parameter identified proved to be effective in distinguishing experienced drivers from amateur ones.

4.3.2 Apex Points Analysis

To further analyze the strategy with which the different drivers approached the curves, three different procedures can be identified depending on the position of the apex point, that is the point where the car is closest to the inside edge of the corner and is determined by the racing line chosen by the driver. The three different possible situations are (Fig. 4.19):

(a) Mid-corner Apex: the apex is located in the middle of the corner, which allows the driver to maintain a straight-line speed as long as possible without sacrificing corner exit speed. In this case the corner radius is at its minimum in the middle of the corner and the corner radius trace is symmetrical;

(b) Late Apex: late corner entry results in a late apex and, by performing the largest amount of turning at the corner entry (minimum corner radius in the early part of the corner), the car is in a better position for the exit, which makes it easier to accelerate out of the corner. However, the drawback of a late apex is sacrificing corner entry speed;

(c) Early Apex: an early corner entry results in an early apex. The driver turns the steering wheel more (to decrease the radius of the path) at the corner exit, which inevitably sacrifices the corner exit speed. In this case, the minimum corner radius is reached in the later stage of the corner.

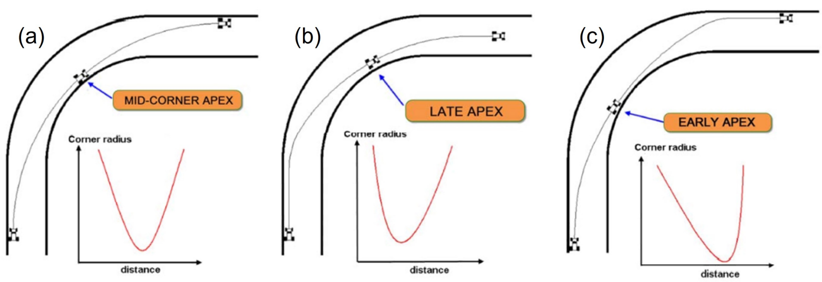

Fig. 4.19 Different cornering strategies. (a) Mid-corner apex (b) Late apex (c) Early apex

To sum up:

- a constant radius corner, one defined by one single radius, favors an apex placed close to the middle of the corner;
- a decreasing radius corner, where the latter part of the turn is tighter, normally requires a late apex;
- in an increasing radius corner, the apex is placed earlier.

Having identified the apex points for each corner as those which minimize the distance of the racing line from the inside track boundary, the laps of the different drivers were then compared to assess the type of strategy used at each curve. Taking curve 6 as an example (Figure 4.20), it can be seen that the professional driver uses a 'late-apex strategy' and exits not too wide; this allows him to tighten the trajectory and to be in a good position for the next corner; on the other hand, the inexperienced driver 11 does not follow a single strategy and he often tends to widen the trajectory too much, but an interesting observation is that for the two laps (8-9) made after the advice of the professional driver, he corrected his trajectory by approaching the professional driver. So at least for trajectory choice, the two laps with an experienced driver at the side proved effective. In order to quantify and objectify the better repeatability of a professional driver also from the point of view of curve management, it was calculated the areas of the circumferences that contain all the apex points collected in the different laps of the same driver on the individual curves, which are visibly different in Figure 4.20. A smaller area indicates greater proximity of apex points, thus higher repeatability, and extending the procedure on all six curves and to other drivers, professional pilots showed to always fall into the top 3 as minor area values.

Downstream of these results, it can be said that the area enclosing the apex points is also an effective metric for identifying a driver's style, even if it is not completely general since it is also related to the geometry of the

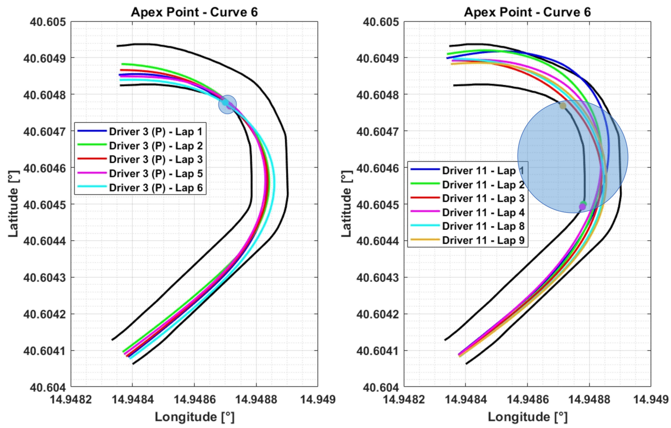

Fig. 4.20 Comparison of areas enclosing the apex points in curve 6 - Driver 3 (P) vs Driver 11

curve. In general, the analysis provided quantitative evidence to support the qualitative notion about race car driver higher repeatability.

4.3.3 Gear Study

In addition to the difficulty of managing the corners, another problem that emerged from the analysis of drivers' comments and sensations was their interaction with the gearbox, which is therefore explored in this paragraph, taking into account that it was further complicated by the presence of a manual gearbox with central lever.

First, professional drivers showed strong consistency in shifting, facing all the corners in second gear and the straights in third, except for the longest one in which they also inserted the fourth. On the other hand, amateurs showed a strong irregularity in the changes and some of them also made frequent errors in the initial phase of the curves where the downshifting of the gear often was not perfect (Figure 4.21).

Consequentially, the aspect investigated was the uniformity with which the drivers make the changes. To do this, the speeds in correspondence with

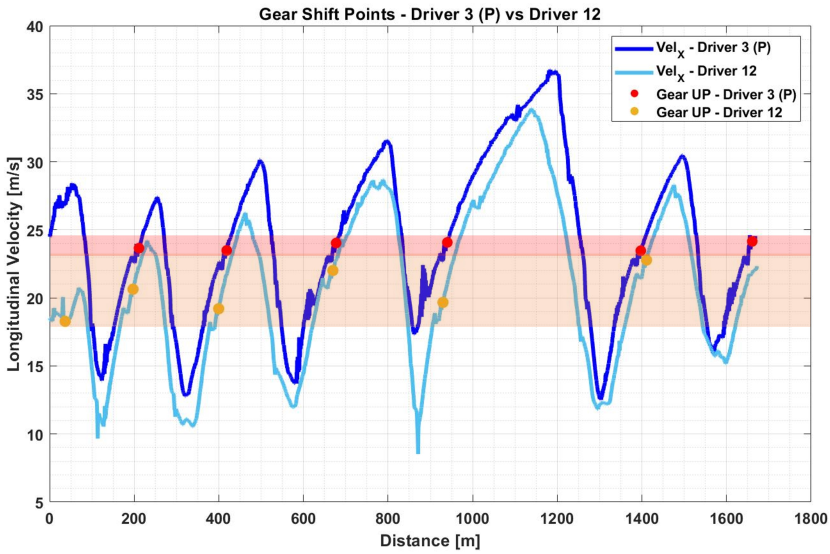

Fig. 4.21 Comparison of 2to3 gear up-shifting points - Driver 3 (P) vs Driver 12

the changes were collected for all the laps of the drivers, they were grouped by type of shift (2to3, 3to4) and then the variability of these speeds was evaluated using the standard deviation (Figures 4.22 - 4.23).

In both cases, it is very evident that racing drivers have greater precision and consistency proven by lower standard deviation values. Furthermore, the irregularity of amateur drivers is particularly high in 3to4 gearshifts, probably because often inexperienced drivers make this change in areas of the track where it is not necessary. The problem just mentioned is confirmed by the average shifting speed values, which are more or less in line among all the drivers for the 2to3 shift, but those in the 3to4 gearbox are much more variable and are often very low for amateurs compared to the speed at which the two professional drivers change.

To further explore the differences, the number of engine revolutions before the up-shifts was calculated and compared among drivers. In Figure 4.24 all

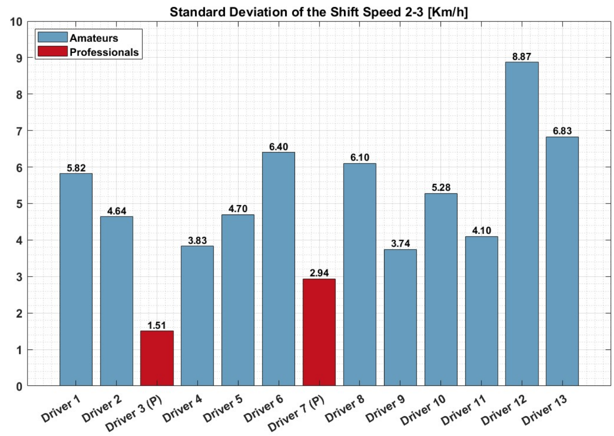

Fig. 4.22 Standard deviation (2to3)

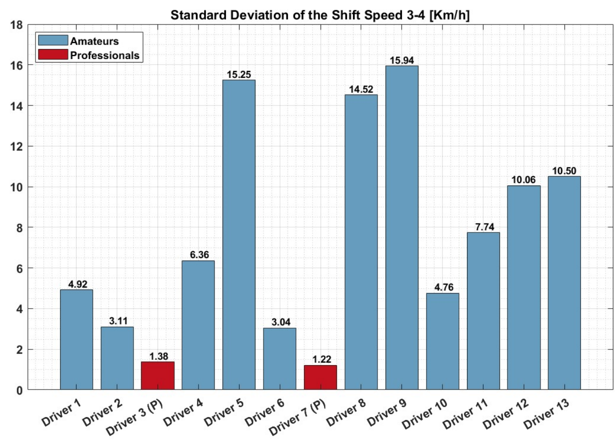

Fig. 4.23 Standard deviation (3to4)

the rpm, regardless of the type of gear change, for five laps of drivers 3 (P) and 12 are collected; each dot represents one of the changes of the single driver and, apart from a higher dispersion for the amateur driver, the professional driver shows gear changes at higher rpm, reaching higher shifting speed. Also, it is evident the strong variability that the amateur driver 12 shows, there is no defined rpm range in which he operates. This is further proved by the

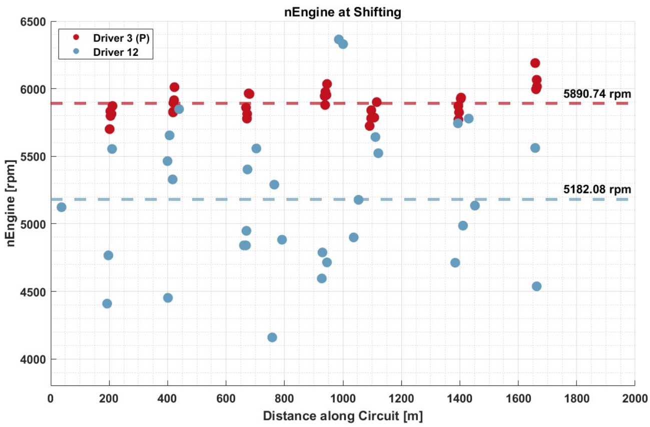

Fig. 4.24 Engine rpm over one lap - Driver 3 (P) vs 12

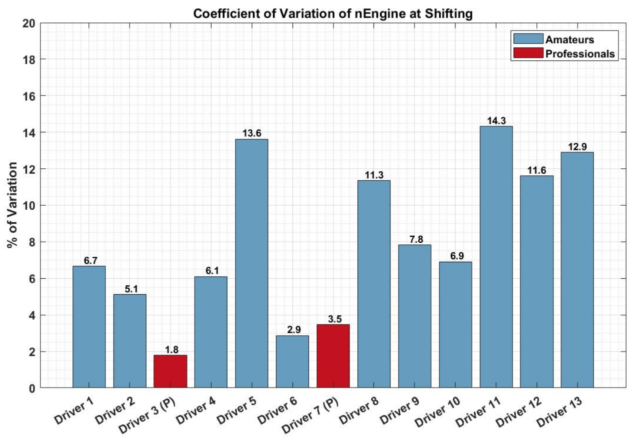

Fig. 4.25 Coefficient of variation of engine rpm

significantly lower coefficient of variation values for professional drivers (Figure 4.25).

4.3.4 Gear Chart

In order to generalize this result, the gear charts of the various pilots were also analyzed. The 'Gear Chart' is a purely kinematic diagram based on the equation (4.5).

$$n_m = \frac{(V \cdot 60 \cdot \tau_t \cdot \tau_p)}{(2\pi \cdot R_e \cdot 3.6)} \tag{4.5}$$

Where n_m is the number of engine revolutions, V is the forward speed in Km/h, τ_t and τ_p are, respectively, the transmission ratios to the gearbox and to the bridge and R_e is the effective rolling radius.

Figures 4.26 and 4.27 compare two representative graphs of a single lap of a professional and an amateur driver. The single graph was obtained by plotting the theoretical gear chart (six lines for six gears) and superimposing the actual one on it in black. The theoretical gear chart was obtained from the kinematic equation (4.5), where, as the gears varied, the bridge ratio was kept fixed and the gearbox ratio varied. Then a speed range suitable for the vehicle under examination of 0-200 Km/h was established and the theoretical rpm values were obtained from equation (4.5), delimited in the range 1000 rpm - 6500 rpm specific for the Fiat 124.

This graph allows to understand what is the range of rpm and speed covered over the entire lap and thus it was decided to evaluate the area underlying the gear chart for the pilot's working interval and use this as an indicator of exploitation of the car's potential. In fact, by comparing the areas of driver 3 (P) and driver 13 for one of their laps (Figures 4.26 - 4.27), the inexperienced driver (12) presents an area 20% smaller than the professional because he does not push the car to its maximum capacity, especially in 3rd gear, thus reaching lower values of rpm and speed.

It was then decided to make this comparison of areas between all the drivers, averaging the value over all the laps of the same driver. The results are shown in Figure 4.28: considering the combination of higher area values and lower coefficient of variation, the two professional drivers collide in the top 3, demonstrating that the area under the gear chart is also a valid indicator of the driver's performance. In this context, the amateur driver 6 also proved to be particularly good.

Finally, it should be noted that the best performance of professional drivers was also confirmed by the shorter time spent driving, also proving their greater ability to manage a manual gearbox.

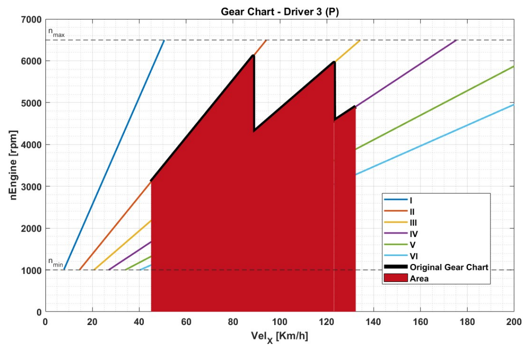

Fig. 4.26 Area under the gear chart - Driver 3 (P)

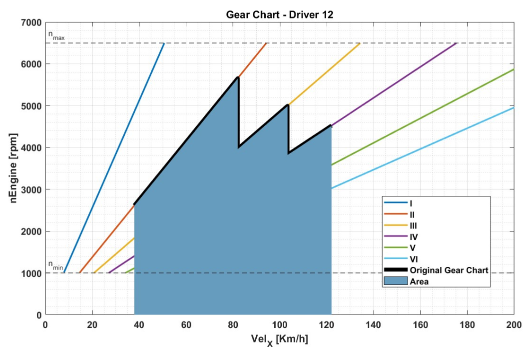

Fig. 4.27 Area under the gear chart - Driver 12

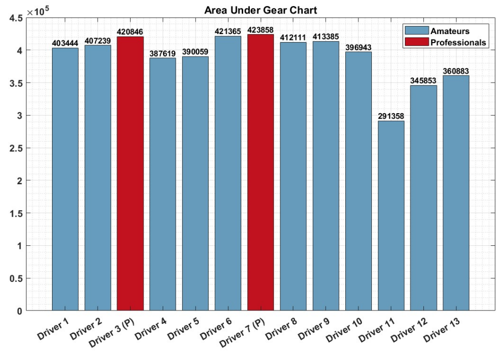

Fig. 4.28 Average areas under the gear chart

4.3.5 Steering Analysis

The next step was to analyze the steering management by the drivers. Steering is decisive in the outcome of a lap; in fact, it affects the direction of the vehicle but also the speed and grip that it has with the ground: if the driver steers more, the vehicle is committed more in lateral dynamic reducing the grip available in the longitudinal direction and therefore the longitudinal acceleration that can be demanded, resulting in a lower forward speed. Aside from some general guidelines, there is no unique optimal way to manage the steering, since different styles can involve a more or less gentle use of the steering wheel, still leading to similar results. However, both from tests and the literature study, the difficulty of inexperienced drivers in managing the steering emerged, leading them to make cornering corrections that affect the final performance (Figure 4.29).

To quantify the steering irregularities and thus be able to numerically compare the steering variability for the drivers, a low pass filter was applied to the steering channel and the filtered signal was identified with the aim of calculating the differences between the two (Figures 4.30 and 4.31). In particular, a frequency of 0.5Hz and an order of 3 were chosen, as this was the best compromise between signal cleanliness and effectiveness in highlighting the differences.

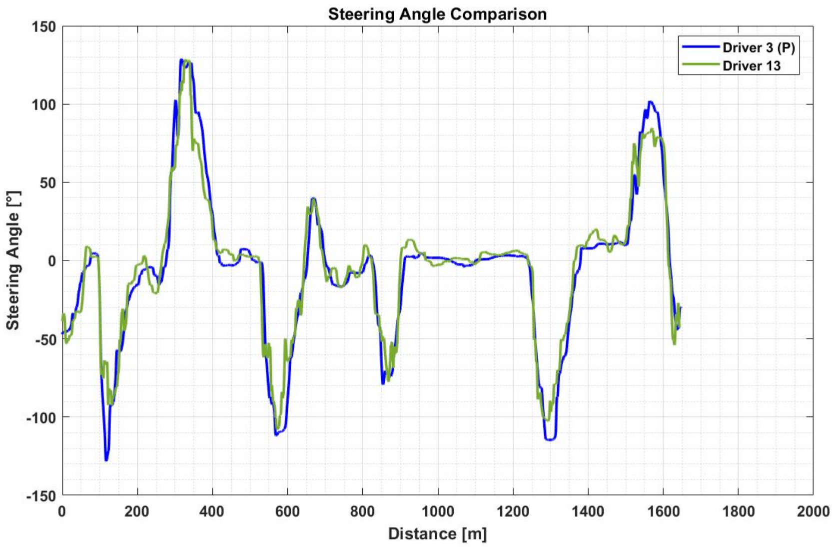

Fig. 4.29 Steering signal comparison between professional driver (3) and amateur driver 13

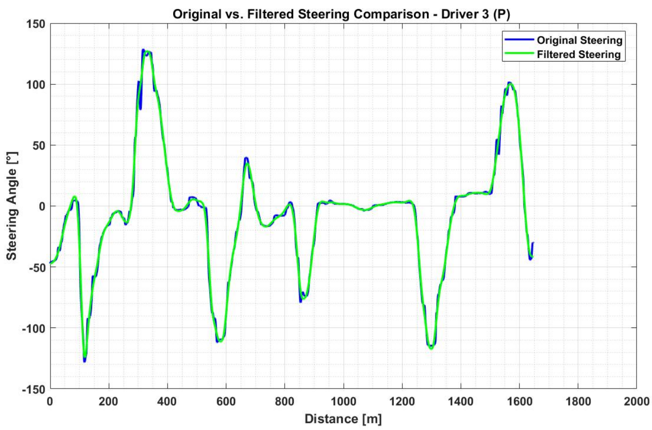

Fig. 4.30 Comparison between original and filtered steering channels - Driver 3 (P)

The idea was to evaluate for each sampled point the difference between the original steering angle and the filtered one, then add the differences over

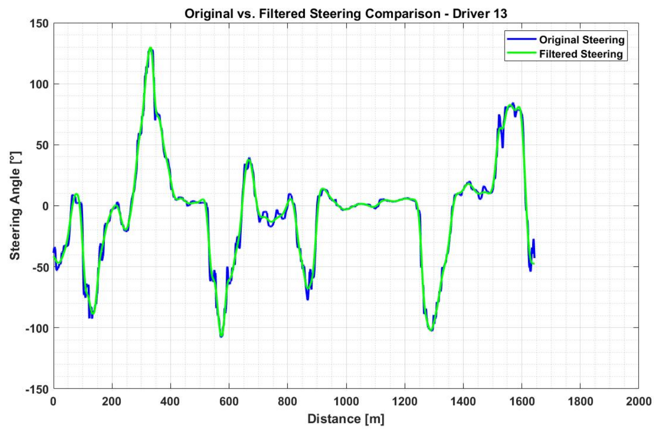

Fig. 4.31 Comparison between original and filtered steering channels - Driver 13

the entire lap and thus have an index that quantifies the steering irregularity in the lap. Obviously, the greater this sum of differences, the greater the irregularity, but to make these values comparable on all laps, a standardization was done by dividing them by the amount of the samples of the lap, otherwise a simple addition would have distorted the result as the number of summed values would not have been the same; Figure 4.32 shows a summary scheme of the procedure.

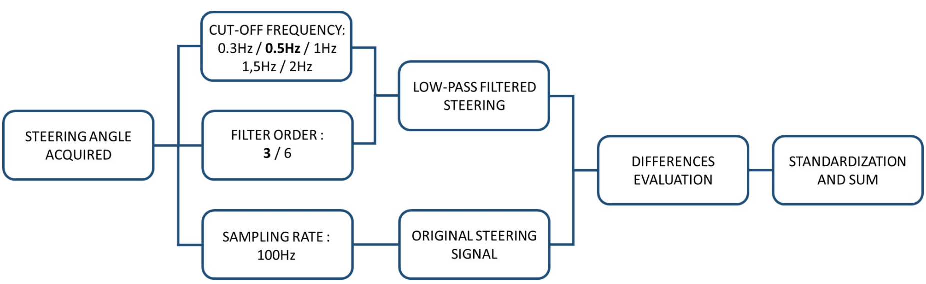

Fig. 4.32 Procedure followed for the analysis of steering irregularity

Professional drivers generally demonstrated greater regularity, with less sudden variations in the steering angle, but the true effectiveness of this parameter can be perceived by considering its combination with others, such as the average cornering speed and the average cornering steering values, from which more systematic differences among drivers can be noted, especially the ability of professional drivers to navigate corners in more critical speed and steering conditions, maintaining greater control. Indeed, the results obtained considering only the differences between filtered and unfiltered signals did not absolutely confirm the supremacy of the professional driver (Figure 4.33).

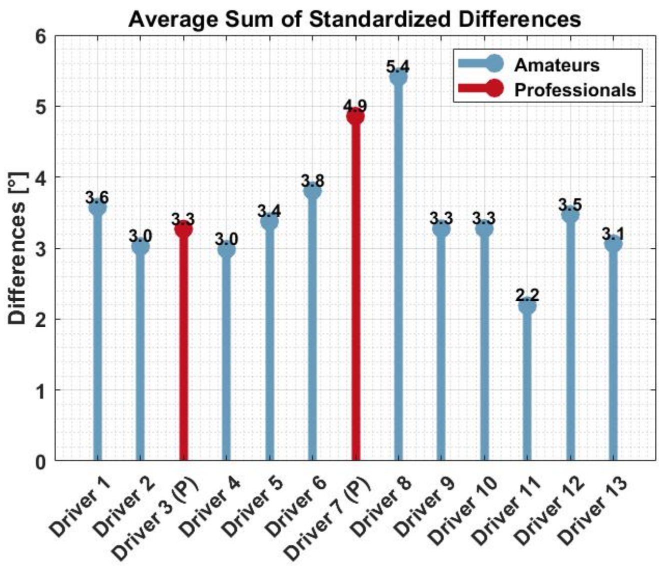

Fig. 4.33 Differences comparison between original and filtered steering

Focusing the attention on the driver 12, he shows the lowest differences among all the drivers. These differences, however, were not justified by an effective superiority of the driver 12, so it was decided to investigate more thoroughly and understand the reason for his greater steering cleanliness. What has been noticed is that the driver 12 showed more regularity, but at the same time he went through the curves at a slower speed, requiring less steering. It was therefore decided to redo the comparison between the drivers, but this time also taking into account other aspects that intervene in a steering phase, such as the imposed steering angle, the steering speed and the traveling

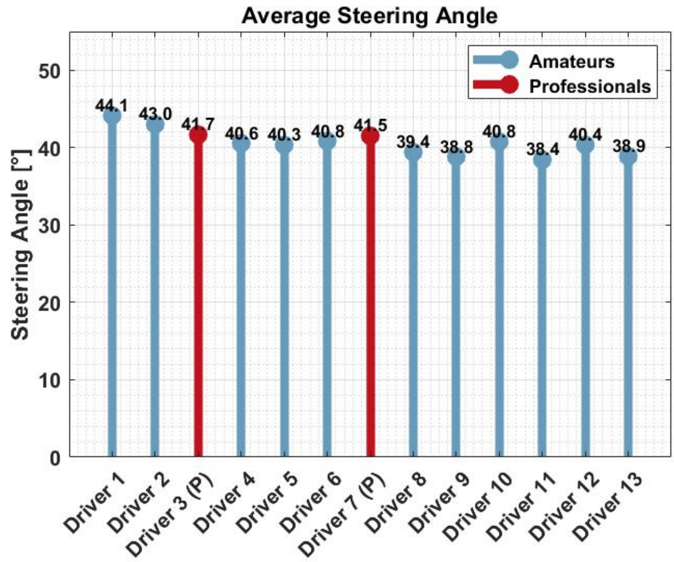

Fig. 4.34 Comparison of average steering values

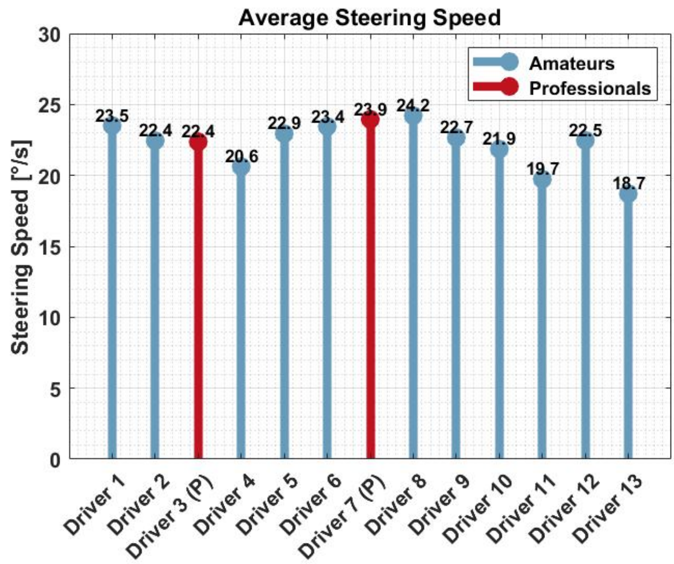

Fig. 4.35 Comparison of average steering speed

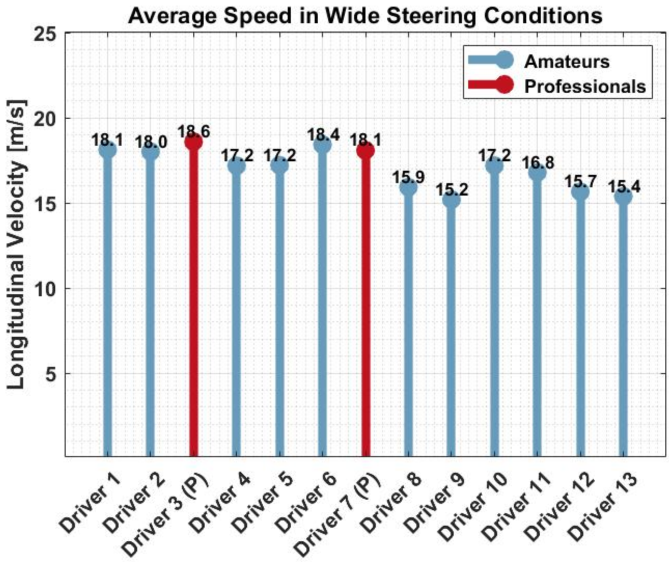

Fig. 4.36 Comparison of average forward speeds under wide steering conditions

speed, as shown in Figures 4.34, 4.35 and 4.36. Hence, the average values of these quantities were evaluated on the single lap for each driver and then these were averaged over all the laps of the single driver.

Two clarifications must be made before analyzing the results:

1. the steering averages have been calculated considering the absolute values;

2. the traveling speed was taken into account only for values of steering angle > 20° or <-20°, assuming it is a threshold for conditions of fair curvature.

At this point the comparisons shown in the previous figures can be critically analyzed. Going first of all to make a check on driver 12, it is evident that compared to professional drivers he travels at lower speeds on average, which allows him to steer less and more slowly. This clearly results in a greater cleaning of the signal, but at the same time in a longer lap time. Looking from a more general point of view, it can be seen that what professional drivers have in common is the high steering speed and the high steering angle values set; moreover, the average steering speed also tends to be quite high. At the same time it can be seen that even some amateur pilots are able to maintain standards very close to those of professional drivers. However, there is a necessary observation to make: when traveling at high speeds, especially in corners as professional drivers do, more steering corrections may be required. In addition, these can be further increased if the drivers take advantage of the curbs, which make the car swing and so greater steering oscillations are inevitable.

It can therefore be concluded that the sum of the differences alone is not a sufficient parameter to judge the performance of a driver, as there are too many factors at play, but by looking at all 4 quantities taken into consideration, it can be said that the optimal behavior to be assumed is that of the professional driver 3, who through medium-high values of steering and steering speed is able to guarantee maximum speed when cornering with a limited steering variability.

4.4 Braking and Acceleration Influence on Performance

The acceleration and braking phases on track can be difficult to adjust for an amateur driver not used to a sports vehicle, as was evident from the testing session and also confirmed by the analysis of the acquired data. In fact, mistakes of inexperienced drivers in the choice of pedals' activation have been noted compared to professionals who showed a more standardized procedure, reaching the peak in the first moments of the accelerations and braking, as it possible to see in Figures 4.37 and 4.38.

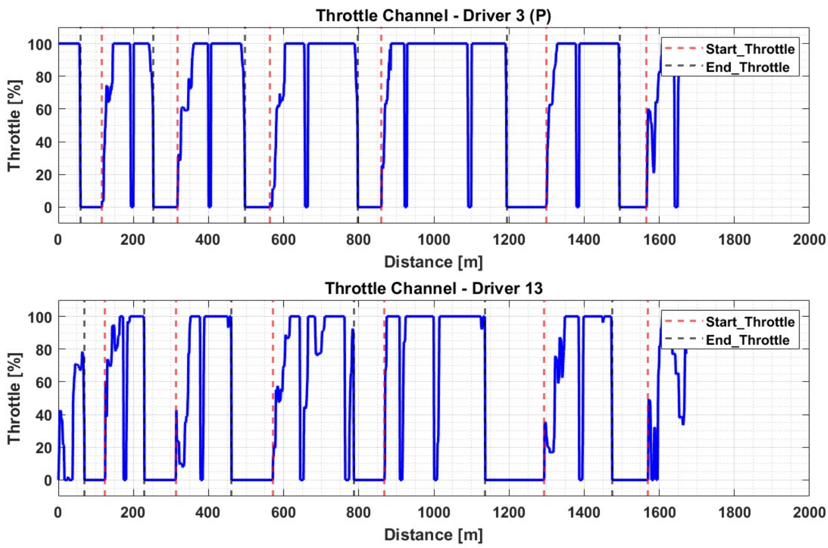

Fig. 4.37 Comparison of throttle signals - Driver 3 (P) vs Driver 13

Following these qualitative considerations, it was decided to explore the aspects highlighted with the aim of identifying indices that would allow more quantitative comparisons to be made.

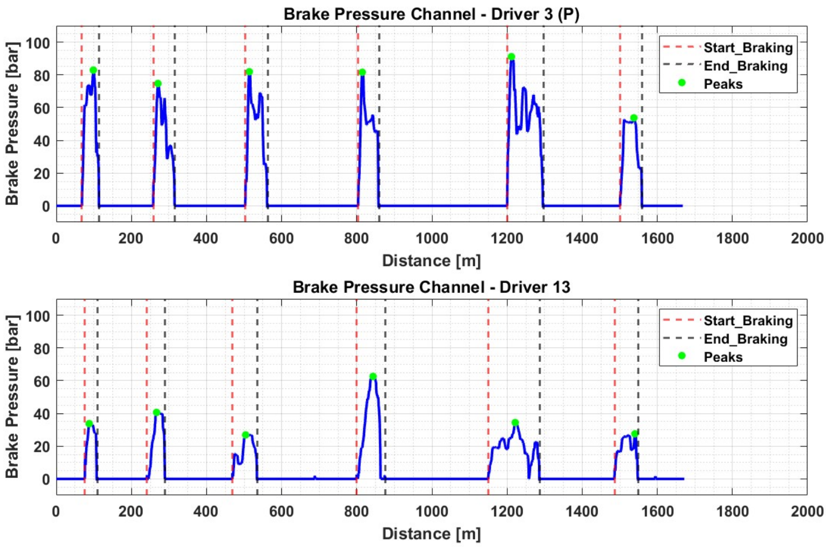

Fig. 4.38 Comparison of brake pressure signals - Driver 3 (P) vs Driver 13

4.4.1 Braking and Acceleration Strategy Indicators

First of all, the braking time and the time to reach the peaks for the six curves have been evaluated by averaging them on all the laps of the individual drivers. Generally, professional pilots showed shorter characteristic times, even if, clearly, braking for less time does not necessarily mean driving better, because it could also mean that the driver has reached the corners with a lower speed and therefore less speed reduction is required. However, considering the combination of both times, professional drivers proved to have excellent consistency in reaching the pressure peak within the first second maintaining shorter braking times than the other pilots, while reaching high cornering speeds.

Another aspect interesting to investigate was the use of the throttle, in fact from comparison plots it was noticed the tendency to keep the pedal pressed longer by professional drivers who in fact reached higher speeds at the entrance of the curves.

To better visualize the differences, it was decided to represent the throttle usage indices at fixed percentages by means of bar graphs (Figure 4.39), where the fractions of work at a certain percentage of the throttle over the entire lap are represented on the ordinates.

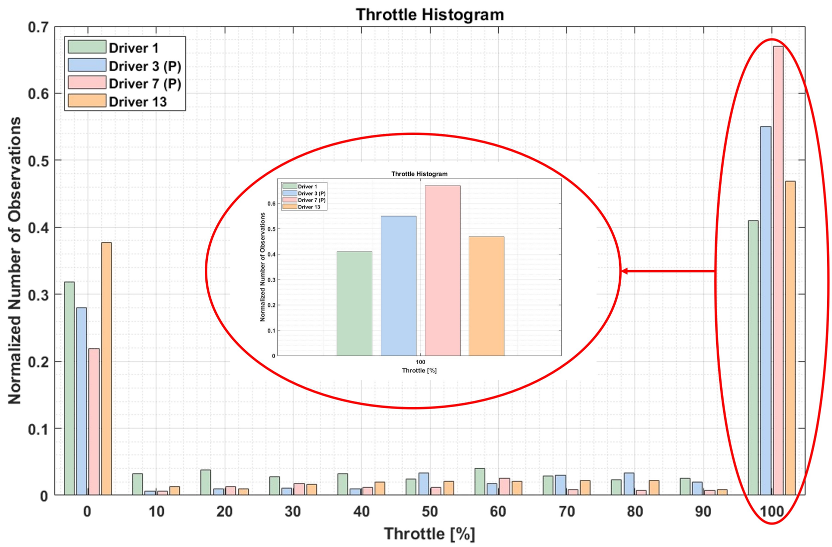

Fig. 4.39 Throttle usage at increasing percentage values

The graph shows the tendency of professional drivers to use more throttle at 100% and less at 0%, which certainly indicates a greater awareness of how to drive on track. To further quantify and confirm these differences, the average throttle percentage values over the entire lap for the different drivers were calculated, these were then averaged over all the laps of the individual drivers and compared (Figure 4.40).

A similar analysis was also conducted on the use of the brake, for which the pressure values reached and the rate of use were compared, assuming that at 0 bar the pedal is not pressed and that a pressure higher than 70 bar is considered high. Once again, a first general idea of the pilots' style can be deduced from the histogram in Figure 4.41.

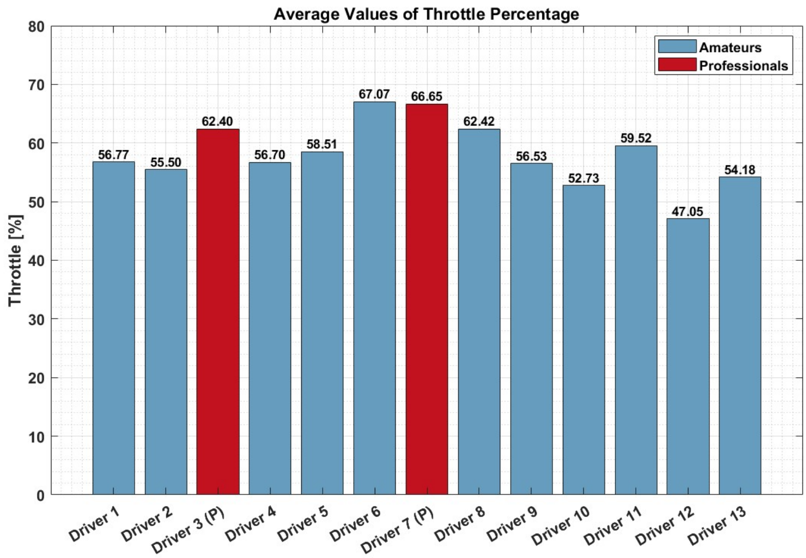

Fig. 4.40 Average throttle percentage

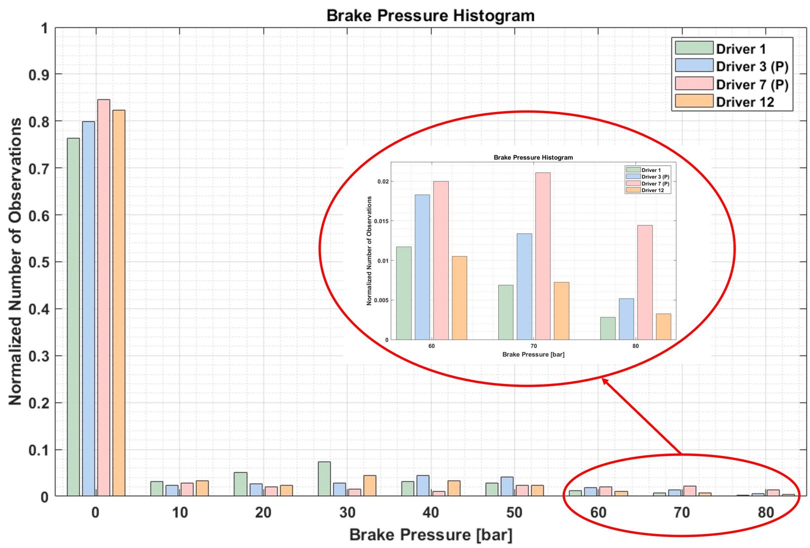

Fig. 4.41 Brake usage at increasing pressure values

In this case, it is interesting to note the high rates of non-use of the brake (0 bar) for professional drivers, which actually are high also for inexperienced ones, since these, accelerating less, also have to brake less. But above all, what is worth noting is the greater frequency of use of the brake at high pressures by racing drivers, as can be seen from the enlargement. Also in this case the aim was to quantify the differences, evaluating the average frequency of non-use of the brake for the riders and comparing the results also considering the average brake pressure values. Looking at the comparison plot in Figure 4.42, professional drivers show higher average pressure values, even if with similar pedal engagement time (if not less), this means that they tend to impose more abrupt braking, reaching high-pressure values.

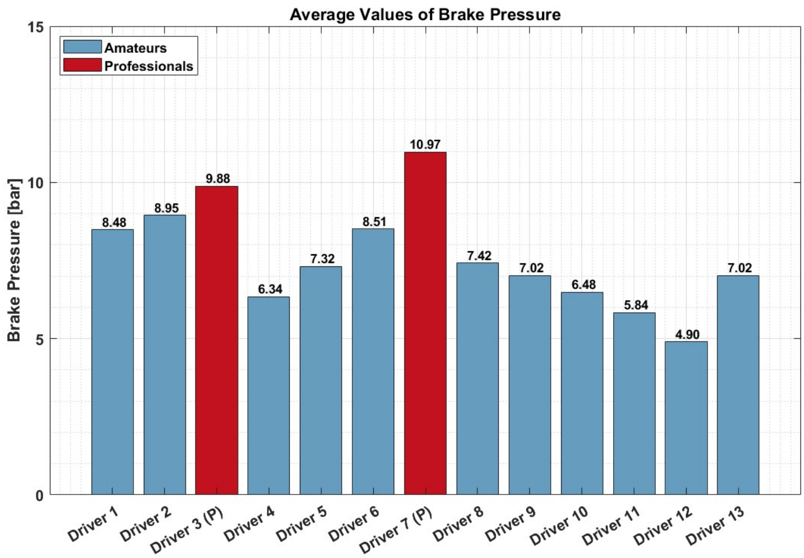

Fig. 4.42 Average brake pressure

It can be concluded that the indicators found allow to highlight differences, even substantial ones, among drivers.

4.4.2 Jerk Study

From the studies conducted so far, it emerged a tendency of professional drivers to drive more firmly, imposing more abrupt braking and acceleration, showing greater responsiveness. The purpose of this paragraph is to propose a method to quantify the aggressiveness of the drivers, understood as the tendency of the pilot to drive at high speeds by imposing heavy acceleration and hard braking, starting from the 'Jerk', defined in physics as the change rate of vehicle acceleration or deceleration with respect to time.

A jerk profile shows how a driver accelerates and decelerates in a particular direction, which is more important in determining the driver's aggressiveness; in particular, it is presumed that more aggressive drivers tend to accelerate faster and thus have higher jerk profiles than non-aggressive drivers [156, 155, 157].

From an initial graphical comparison, the differences between the drivers emerged more in the longitudinal direction, especially in terms of negative acceleration and jerk peaks, than in the lateral direction, as was predictable since the latter is less involved when driving (Figures 4.43 and 4.44).

The comparison showed a greater acceleration variability imposed by the professional drivers than that of the non-professionals, especially in the braking phases where greater distinctions among were noted.

The first global approach, comparing absolute jerk values over the entire lap, was not effective. It was therefore decided to separate the phase with active throttle and the phase with active brake, analyzing separately positive and negative values and so emerged the tendency to use a wider jerk in the braking phase, rather than in the acceleration one, which was also confirmed by the average values of longitudinal jerk, substantially higher during braking (Figure 4.45). In particular, it can be seen that the drivers showing higher average values are the two professionals and driver 6, who has driving simulator experience.

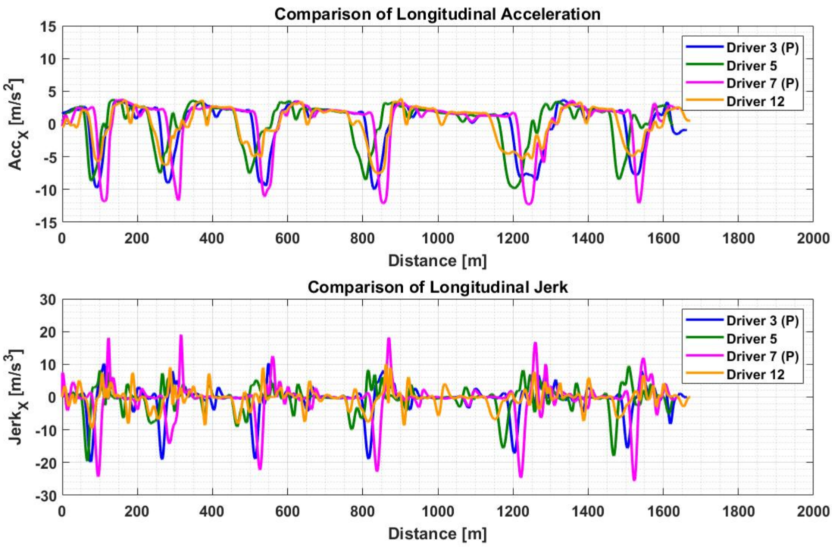

Fig. 4.43 Comparison of longitudinal acceleration and jerk between the drivers

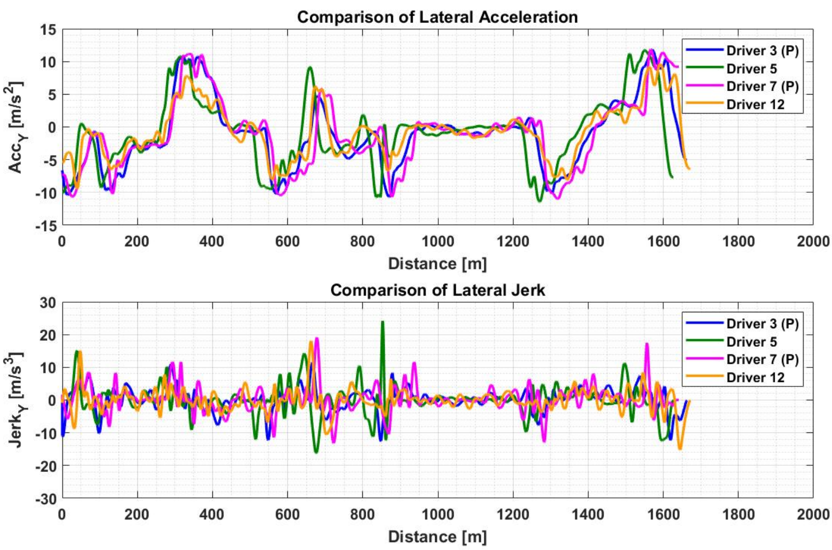

Fig. 4.44 Comparison of lateral acceleration and jerk between the drivers

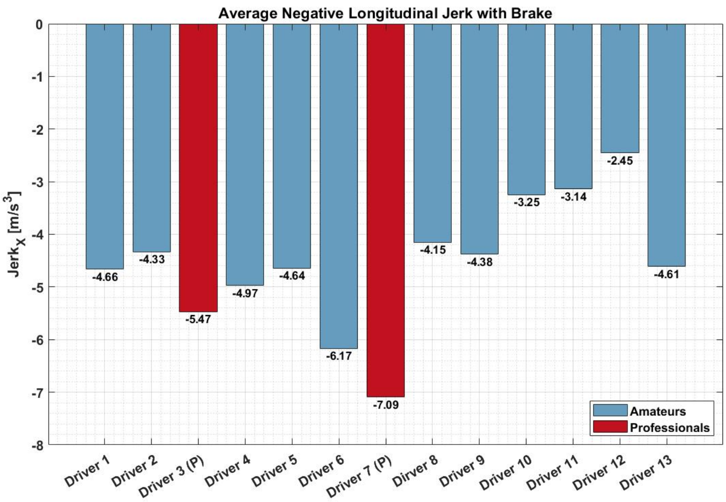

Fig. 4.45 Average negative jerk - Braking phase

Assuming that positive values of longitudinal jerk occur during the acceleration phase or the release phase of the brake pedal, while negative values occur during the braking phase or the release phase of the throttle pedal, since the jerk values are higher in the braking phase, it can be concluded that large positive jerk was generally produced by releasing the brake pedal rather than pressing down the gas pedal, while large negative jerk is generally produced by pressing down the brake pedal rather than releasing the throttle. Furthermore, the differences among drivers are slightly more marked as regards the negative jerk values during braking, this suggests that the differences are characteristic of the initial braking phase and that the professional driving style involves pressing the brake more 'aggressively', thus decelerating more abruptly. This approach was then detailed also on the single curves confirming the same results.

The analysis presented allows to further characterize the drivers' style by also providing information on their readiness and firmness to drive.

4.4.3 Accelerations Ranges Study

There is a final aspect, linked to accelerations, which has a great influence on performance on track, namely how far drivers push the vehicle reaching high accelerations while maintaining control of the vehicle.

To compare drivers' style in terms of acceleration range, the 'G-G Diagram' was used: it is a graph in which the lateral acceleration is reported on the abscissa axis, while the longitudinal acceleration is reported on the ordinate axis [139, 152]. In particular, it was decided to make the driver behaviors objectively comparable by identifying the polynomial curves (symmetrical with respect to the y-axis.) that envelope the points represented in the G-G diagram. These curves were obtained by identifying for each quadrant the arcs enclosing the 90th percentile of the experimental points, and then combining the two upper and the two lower quadrants by averaging the respective percentiles (Figure 4.46).

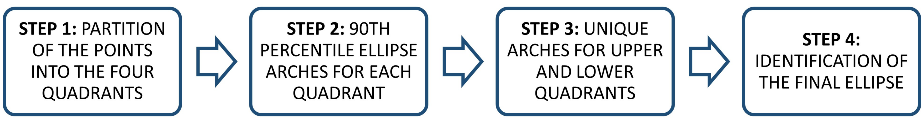

Fig. 4.46 Procedure to identify the 90th percentile enveloping "ellipses"

It should be specified that these curves identified do not define the global tire grip limits, rather they are indicative of the actual accelerations reached by the drivers.

As can be seen from Figure 4.47, the main differences between drivers emerged in the longitudinal direction, which is consistent with the high brake pressure and jerk values shown. Even in the lateral direction, the professional tends to work with greater accelerations, albeit slightly, but what is most noticeable is also a greater number of points concentrated at high acceleration values compared to the amateur whose points are concentrated more towards the center.

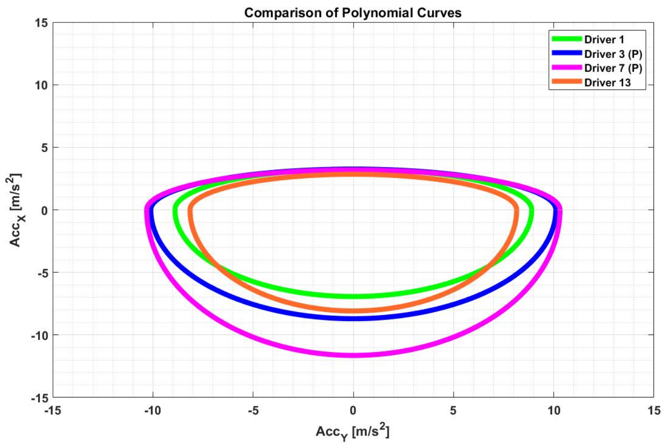

Fig. 4.47 Comparison of polynomial curves among drivers

To numerically compare the results, their areas were calculated for all the laps of all the drivers, then for each driver an identifying value was calculated as the average of the areas over all his laps (Figure 4.48). As expected, the higher average area values correspond to professional drivers and to driver 6, meaning that racing drivers have a greater awareness of the limits of grip and of the vehicle, so they tend to push the car more toward them.

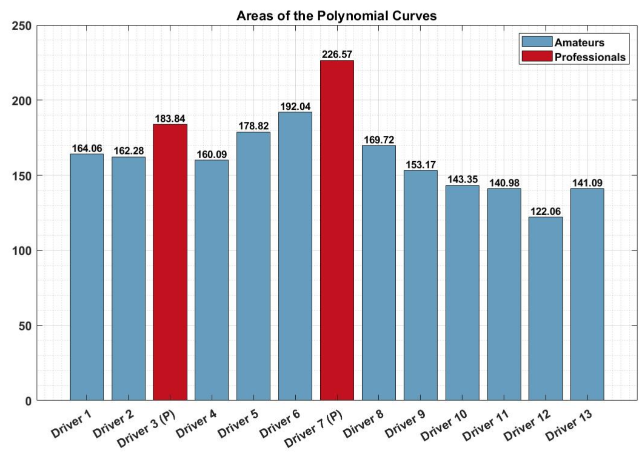

Fig. 4.48 Comparison of average areas of polynomial curves among drivers

Summing up, it can be said that the area is a valid indicator of the pilots' style and therefore it can be added to the list of metrics that satisfy the requirements of objectivity desired.

4.5 Grip Limits

With the last analysis described, it was understood that professional drivers tend to push themselves closer to the grip limits, at least in terms of acceleration. So, it was decided to go deeper in this study to understand how the drivers behave also in terms of forces and slip indices. Before presenting the research conducted, it is appropriate to frame the link between forces and slips and how to maximize performance by obtaining their best combination.

Grip is a consequence of the molecular interactions between tire and road, which develop in the contact patch, and of all the forces that are interchanged in this area. Clearly, the adherence of the tire with the road depends on a considerable number of factors, some that can be mentioned are: the coefficient of friction between the tire and the road; the size of the contact patch; the vertical load on the tire and the longitudinal and lateral forces of interaction; the conditions of pressure and temperature; etc. [180, 181]. This activity is not intended to characterize the grip and contact conditions characteristic of the tires during the test sessions, but the interest is in understanding how much the drivers are aware of adherence to the road and how much they are able to control the vehicle at high speed, especially considering the lateral dynamics which is certainly more difficult to manage than the longitudinal one. To carry out this kind of analysis, it is necessary to evaluate the grip condition, calculating the ratio between the tangential forces and the vertical forces. In addition, also the slip indices have to be evaluated. Both these operations have been carried out thanks to T.R.I.C.K. tool, properly characterized on the reference vehicle used for this activity. From the tire-road contact theory, it was clear that when it comes to skidding, it does not necessarily mean that the driver loses control of the vehicle, indeed certainly in normal driving conditions, not only on the track, there is always an area of the contact patch that is in slippery condition. However, what is important on the track, to optimize performance, is to know what is the maximum degree of slip that the driver can push in order to maximize the forces of interaction with the road, without going further and exceeding the limits of adherence. This is a key factor especially when cornering, because the combination of longitudinal and lateral interaction reduces the adherence available, compared to that available on straights, and therefore working to the limit allows the driver to reach the conditions of maximum grip and travel the curve faster. This problem is less noticeable on straights where the vehicle is usually in ‘power limited conditions’, so it is restrained by the power of the engine to accelerate further, rather than ‘grip limited conditions’ in which the limitation is the friction between road and tire [85]. Aware of the relationship between slip and grip, the aspects mainly examined in this activity were the slip conditions in which the drivers worked, focusing the attention on the lateral conditions, also going to identify an optimal range of slip angle in which to operate to maximize the lateral force and therefore grip when cornering.

4.5.1 Lateral Characteristic Analysis

The study carried out was on lateral interaction characteristics, which represent the trend of the lateral force, dimensionless with respect to the vertical load, as a function of the slip angle. Therefore, they are a representation of the grip available in the lateral direction dependent on the slipping condition. Thanks to the T.R.I.C.K. tool it was possible to obtain these characteristics for all 4 tires and for the 2 axles. Some example plots are shown in Figure 4.49; in particular, in order to have a sufficient number of points for the curves and thus ensure robustness of the results, these characteristics were evaluated on several laps. In the example displayed, the points correspond to 4 laps of the professional driver 3; in general, 4 laps have also been selected for all the other drivers in order to make fair comparisons.

A necessary clarification to make is that these graphs just give an overall view of what is happening for the 4 tires and the 2 axles; by comparing the professional driver 3 with the amateur driver 13 (Figure 4.50), there are differences both in terms of grip and slip angle. In particular, the professional

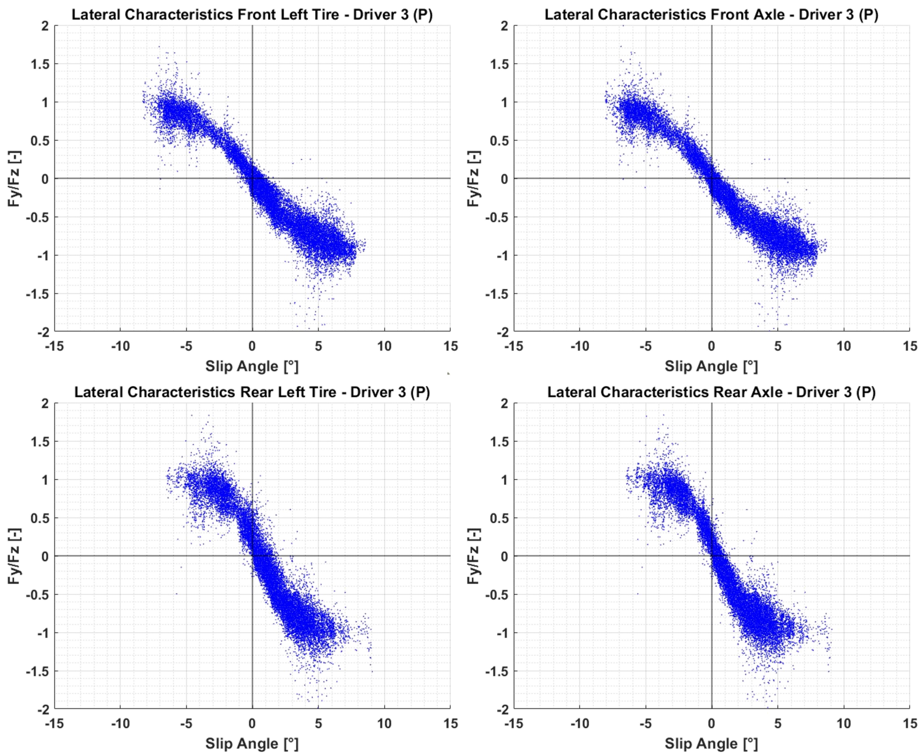

Fig. 4.49 Lateral characteristics evaluated on 4 laps of driver 3

driver tends to reach higher slip values which allow for getting a greater grip. This is more pronounced for positive slip angle values, that, for the adopted convention, correspond to clockwise turns, but it is also normal since the circuit has more curves to the right according to the direction of travel, so there is a greater number of point in the fourth quadrant. However, to make a numerical comparison, the 90th percentiles of the slip angle values were evaluated, distinguishing positive and negative values for the 2 axles. The logic behind it is that a higher percentile value is indicative of a greater number of points at higher slip angles and therefore of a tendency to work at higher slip values, which is precisely the observation raised above.

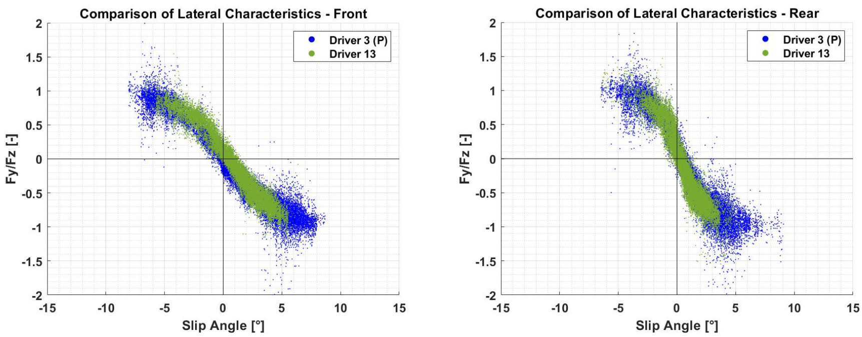

(a) Front Axle (b) Rear Axle

Fig. 4.50 Comparison of lateral characteristics

Always taking into consideration the professional driver 3 and the inexperienced driver 13, in Figure 4.51 the two characteristics of the front axle are shown side by side, with the corresponding percentiles.

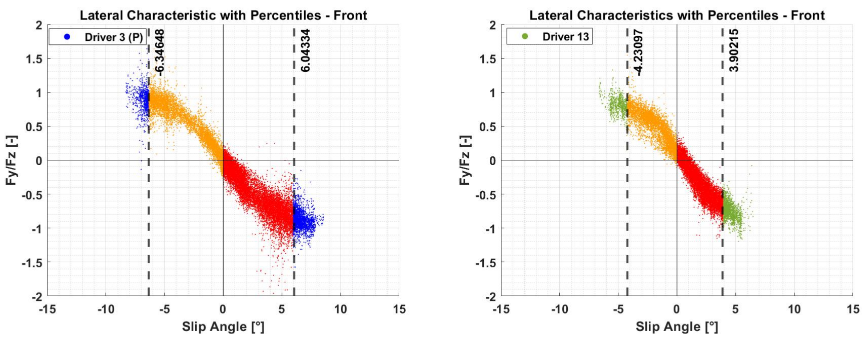

(a) Driver 3 (P) (b) Driver 13

Fig. 4.51 Comparison of percentiles for lateral characteristics. *Orange:* negative slip values below the 90th Percentile. *Red:* positive slip values below the 90th percentile

As can be seen from the numerical values in the figure, the professional driver clearly works more in the non-linear area, therefore far from the origin. This analysis has been extended to all drivers and below, in Figure 4.52, all the results obtained are reported. As for the positive percentiles, they are always greater for the professional driver, confirming the previous considerations. For the negative percentile values, there is a tie between drivers 2 and 3, with 3 slightly prevailing at the front and 2 slightly at the rear. What is actually surprising in this case, is driver 11, especially at the rear, where he shows significantly higher percentile values. However, there is a reason: driver 11 has more than once lost the rear of the vehicle in the left-handed curve 6, thus justifying those high negative slip values. In fact, looking instead at the positive values, he is the second driver with lower percentiles, further demonstrating that those anomalies in the counterclockwise curves are linked to conditions beyond the limit and not controlled. Therefore, in general, it can be said that the percentile itself is a valid indicator of the slip conditions in which the driver in question works.

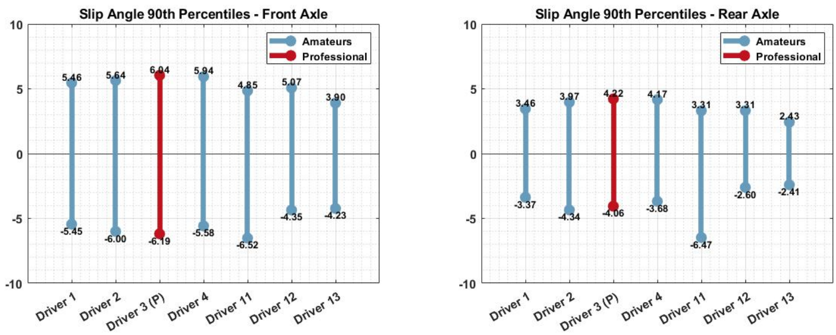

(a) Front Axle (b) Rear Axle

Fig. 4.52 Comparison of lateral characteristics percentiles - Positive and negative values

However, wanting to further deepen the investigation and actually understand the nature of the differences between the drivers, it was decided to take another step forward. As emerged from the theoretical study on lateral characteristics, friction plays an essential role in the shape of the characteristic mainly in the non-linear section, while the linear section, near the origin, is mainly influenced by the stiffness of the tire. Following the maximum grip value, the saturation of the tire occurs, that is the phenomenon for which, with the same vertical load increase, there is not an equal increase in lateral force but rather a smaller one. This clarification was made to further stress the importance of being able to work in a certain range of slip angles that is not too low, because it is necessary to be in the non-linear section to exploit all the friction available, nor too high, to avoid falling back into the saturation zone where there is the risk of losing control of the vehicle. Clearly, this optimal range is not unique, it depends on many factors, including as usual the type of tire and vehicle, the tire-road contact conditions, but in general, it can be said that for sports vehicles, such as the 124 Spider, the maximum lateral grip values are reached in a range of slip angles between 5° and 10° [83]. Given also the results observed in the activity, it was decided to identify the interval as the theoretical optimal range [5°,8°] for positive values of slip angles and [-8°,-5°] for negative values. To make a quantitative comparison, for each driver the percentage of points included in these two intervals on the total has been identified, assuming that higher percentages are indicative of better performance for what has just been said above. The results for the 2 axles are presented in Figure 4.53 and the greater competence of the professional driver is confirmed, so also the percentage parameter can be a useful metric, even if it clearly needs to be adapted to the vehicle and the tires available.

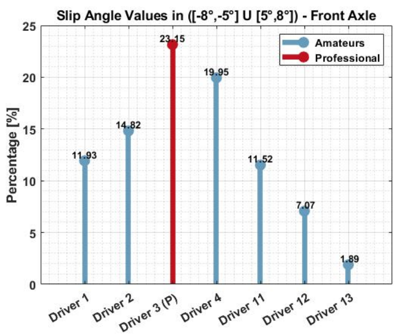

(a) Front Axle

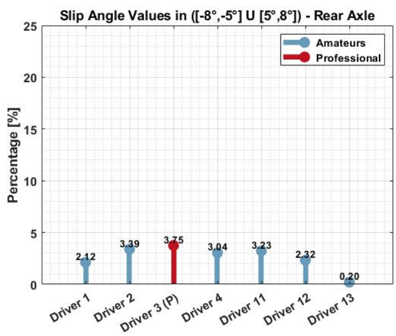

(b) Rear Axle

Fig. 4.53 Comparison of lateral characteristics percentages

An interesting observation is that in this case, even on the rear, driver 3 has a higher percentage of points than driver 11, the reason is that the percentage also takes into account the positive slip values, which compensate for the high negative values. In fact, for further verification, the percentages for the two drivers were calculated even only on the negative values which were substantially higher for driver 11, in line with the previous findings. During this activity, it was decided to take and compare the raw data output from the T.R.I.C.K., for the lateral conditions, without carrying out cleaning operations. The reason is due to the approach that has been followed, that is to identify the most general possible metrics, so making processing of this type, necessarily linked to the quality of the data available and the degree of cleanliness required, would have made the methodology more specific and less standardized.

4.6 Synthesis of Metrics

The final step of this activity was to group all the KPIs identified and establish a level of significance based on their robustness and their influence on the performance on track, in order to classify the drivers through an appropriate synthesis and cataloguing. First of all 3 categories have been defined:

1. Metrics strongly related to performance;
2. Metrics less influential on performance;
3. Metrics more related to style and repeatability than with a direct influence on performance.

In particular, metrics closely related to the trajectory, such as the standard deviation of the racing line-centerline distances and the area enclosing the apex points, belonging to category 3, were not used to draw up the ranking as they were not considered indicative of the quality of the performance. As metrics belonging to the first category, the average speed per lap, the area under the gear chart, average throttle percentage and brake pressure values and finally the area enclosed in the curves obtained from the G-G diagrams were chosen. All others were included in category 2.

After that, for each metric, membership bands have been established in relation to the values assumed by the metrics for the different drivers and for each increasing band the score assigned to the driver increases by one unit. Finally, for all metrics, the scores obtained by the drivers were multiplied by a scale factor obtained as the ratio between the points assigned to the metric for its importance and the maximum score obtainable for that metric.

$$\text{Scale Factor} = \frac{\text{Importance Points}}{\text{Maximum Score}} \tag{4.6}$$

Adding up the scores of all the metrics for the drivers, their final results were obtained. Then a ranking of the drivers was drawn up according to the descending order of scores and this was compared with the ranking obtained from the average lap time values. The basic principle is that having assigned the scores according to the influence of the metrics on the performance and having averaged the values of these metrics on all the good laps for each driver, the resulting ranking should be consistent with that obtained from the average lap times.

In the ranking obtained with the metrics, three categories of drivers can be identified (Table 4.3): professionals (green), intermediates (yellow) and the less practical on track (red).

Comparing this ranking with that obtained from the average times, the results and the identified categories seem to be quite consistent. The top 3 is the same, apart from the two expert drivers who are reversed; for the intermediate class, the positions change but the drivers are the same and the lap times are very close; finally, the last class coincides for the two rankings.

Some clarifications need to be made:

Table 4.3 Driver ranking from metrics and from average lap times with classes division.

DRIVERS RANKING FROM METRICS			DRIVERS RANKING FROM AVERAGE LAP TIME		
1°	DRIVER 7 (P)	25.52	1°	DRIVER 3 (P)	73.12 s
2°	DRIVER 3 (P)	23.04	2°	DRIVER 7 (P)	75.05 s
3°	DRIVER 6	21.43	3°	DRIVER 6	75.32 s
4°	DRIVER 2	17.49	4°	DRIVER 8	76.18 s
5°	DRIVER 8	17.06	5°	DRIVER 5	76.44 s
6°	DRIVER 1	15.19	6°	DRIVER 1	76.64 s
7°	DRIVER 5	15.13	7°	DRIVER 4	77.26 s
8°	DRIVER 9	15.1	8°	DRIVER 2	77.40 s
9°	DRIVER 4	14.17	9°	DRIVER 10	78.36 s
10°	DRIVER 10	13.5	10°	DRIVER 9	79.27 s
11°	DRIVER 11	9.78	11°	DRIVER 11	80.28 s
12°	DRIVER 13	9.76	12°	DRIVER 13	83.10 s
13°	DRIVER 12	5.96	13°	DRIVER 12	85.87 s

1. All the results obtained are average results, so they give a rough indication of what the ranking could be, which is clearly not absolute;

2. The differences among the drivers, especially for those of the same class, are very subtle, so it is normal that the two rankings may be slightly different;

3. The ranking is based on the average lap times, but taking instead the best lap time for each driver, the ranking changes again; for example driver 7 has the best time also lower than that of driver 3, reflecting the positioning obtained by the metrics.

What can be concluded downstream of this synthesis of all the metrics found, is that the purpose of identifying objective and generalized parameters that are able to classify the pilots' style has been achieved, allowing to identify the classes the drivers belong to according to their abilities.

To summarize, in this chapter an original approach to the study of driving style identification was described, with the aim of identifying objective and generalized metrics starting from vehicle data acquired on track. With the goal of characterizing and discerning the skills of professional and amateur drivers, test sessions were planned, involving both experienced and novice drivers, guaranteeing the same driving conditions. In particular, to bring innovation, a methodology involving the use of field data, so not simulated, to identify parameters applicable in various contexts, seemed to be the most suitable for this research. This approach was used for the analysis of the drivers' trajectories, as well as their way of managing the gearbox, pedals and steering and the vehicle at high velocities and accelerations.

The outcomes proved to be satisfactory, making it possible to distinguish three level bands that were also consistent with the results obtained in terms of lap times. It can therefore be said that the identified parameters are effective in classifying driving style and are applicable also in different occasions in which the appropriate instrumentation and data are available. It should be noted that the advice of the professional drivers on track allowed slight improvements for amateurs, although overall they were not found to be decisive. Apart from some developments that can be made to the method, the results achieved are very positive and are a solid starting point for deepening the proposed theme. The proposed methodology represents a concrete tool to understand in an objective way the drivers' skills in order to understand how to improve driver and vehicle performance starting from real data collected on track.

Among the further developments, one could be to extend the evaluation of the KPIs found to a more extensive and varied group of drivers, in order to understand their robustness and effectiveness. In addition, it could be useful to see what happens using different cars and also on more demanding and long circuits. Finally, some metrics could be improved or new ones implemented, for example, related to the comparison of the steering management or to the identification of the maximum grip value through a Pacejka fitting of the characteristics. In this way it would also be possible to define further classification bands for the divers, exceeding the 3 levels identified in the present study, obtaining more precise classifications. With these improvements, the methodology could be successfully applied to scenarios involving only professional drivers, making it possible to identify differences in their driving styles.

Chapter 5

Further Key Phenomena for Performance Understanding

5.1 Introduction

In the previous chapters, two models have been introduced with the aim to characterize the tire-road interaction and the suspension behavior, to obtain additional information to characterize the vehicle performance focusing the attention on the global wheel assembly. Thanks to the studies made in chapter 4, also the influence of the drivers has been exploited, leading to several strategies to improve the driver skills with an objective analysis of their behavior. These two topics alone, however, are not enough to have a complete overview of all the phenomena that directly influence vehicle performance, with a specific reference to tires' grip and wear, whose optimization has always been one of the main factors for winning races. To give a more complete overview of the factors that should be considered in vehicle performance analysis and optimization, in this chapter further macro-topics are presented. First of all, some quantities that could be directly acquired from sensors or easily estimated from models are presented, such as tires' temperatures and pressure, friction powers and contact patches extension. Then, a brief consideration about the ambient conditions is made. Subsequently, a more detailed description of the tire viscoelastic properties evaluation is presented, with a specific focus on an innovative device able to characterize the tire with a complete non-destructive procedure. Finally, road roughness parameters are illustrated, focusing the attention on a novel proposed methodology for micro-roughness parameters estimation.

5.2 Acquired Channels, Estimated Quantities and Ambient Conditions

Generally, on high-performance cars, a big amount of data is collected thanks to dedicated complex acquisition sensor systems. Some of these acquired channels have been deeply treated in chapter 2, but there are a few more that have to be considered in order to understand the vehicle behavior.

One of the quantities, constantly monitored and acquired through appropriate sensors, is the tire temperature, as being able to keep the tires in the optimal thermal window is essential to have excellent vehicle performance and to prevent various issues. Indeed, the description of a tire from a thermal point of view is also fundamental for what concerns the vehicle dynamics. Tires behavior, through which the vehicle exchanges forces with the asphalt, is strongly conditioned by the temperature. The grip, i.e. adherence, and consequently the interaction forces that they are able to exchange, changes as soon as temperature varies. Experimentally it is possible to obtain the temperature values that characterize the tread surface (which is known as Surface Temperature - T_{Surf}) by identifying different reading spots along the width of the tire on which the sensors act (Figure 5.1).

Similarly, it is possible to characterize the temperature of the inner liner (which is known as Inner Liner Temperature - T_{Inner}) by means of TPMS (Tire Temperature and Pressure Monitoring System) devices which provide the evolution over time of the temperature of the inner area of the tire (Figure

Fig. 5.1 Tire tread surface temperature IR sensor

5.2). Furthermore, it is usually necessary to simulate the temperature trend of the bulk layers, which usually is not subject to experimental measurement. This is useful to predict how the behavior of the rubber changes, since the temperature variations can be even several tens of degrees in a few seconds, taking into account the dissipative phenomena linked to the deformations to which the tire is subjected. In this case, advanced thermal models are adopted but, given the purpose of the thesis, they will be omitted.

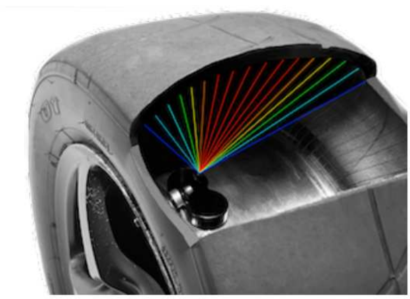

Fig. 5.2 Tire inner liner temperature IR sensor

Additional variables that define the boundary conditions for the phenomenologies described are the air temperature and the asphalt temperature, measured during the different sessions on the track. These two temperatures are, together with the air humidity (generally neglected), the main ambient conditions that directly influence the tire performance; they can be taken into account through direct measurements collected from dedicated sensors mounted on the vehicle, which provides more reliable information, or thanks to stationary sensors that are generally installed on each circuit, that clearly give back some global information on the circuit conditions and not on the specific ambient temperatures around the vehicle when it is running.

Also the tire inflation pressure is of fundamental importance since, through this, specific models are used in order to obtain the characteristic angles of the tire and the tire contact patch area. These quantities mentioned, in the study of the vehicle performance, are fundamental as they affect various factors such as the level of grip obtainable, the way in which the forces are expressed, the achievement of the optimal thermal window of the tire and so on. Internal pressure variations are generally measured using TPMS and they are strictly connected with the tire's thermal evolution during a run. This coupling of temperature and pressure effects makes it quite complex to analyze the single dependencies of these two phenomena with exerted grip and tire degradation. Related to the inflation pressure, there is certainly to consider the contact patch extension. Given the high flexibility of the tire, the extension and the shape of the contact area depend on the applied loads and on operational conditions: the friction of the road affects the deformation of the tire and, hence its *contact patch*. Generally, the footprint is viewed either straight down, or in a plan view, as in figure 5.3.

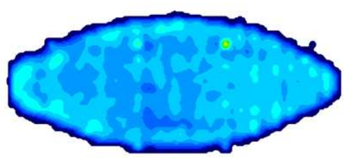

Fig. 5.3 Slick tire contact patch

The tire footprint is highly influenced by the inflation pressure and the camber angle. Indeed, for what concerns the first one, an increase in pressure results in a reduction in the contact area while a reduction causes a footprint increase. The effect of the camber angle on the footprint is due to the inclination of the wheel, which causes a reduction in the footprint, in order to compensate for the negative effects produced by the toe. Clearly, a considerable influence on the contact patch area is also exerted by the vertical load acting on the tires. Dynamic contact patches are generally obtained starting from several indoor tests conducted in different operating conditions (varying normal load, inclination angle and inflation pressure) or using complex models, such as Finite Element Models that consider the global tire structure.

Finally, combining the information related to the interaction forces and the sliding velocities, both calculable using the T.R.I.C.K. 2.0 tool, it is possible to introduce the friction power calculated along the x and y axes.

$$FP_x = F_x v_{s_x} \tag{5.1}$$

$$FP_y = F_y v_{s_y} \tag{5.2}$$

These quantities instantly define the thermal power due to the pneumatic-soil interaction or better to the tangential stresses that, in the contact area in sliding with respect to the ground, perform work that is dissipated in heat. This power will hereinafter be referred to as friction power and it will be indicated with FP_{tot}.

$$FP_{tot} = FP_x + FP_y \tag{5.3}$$

5.3 Viscoelastic Properties Evaluation

In addition to the basic theory introduced in paragraph 1.6, several factors have to be considered to obtain a complete tire viscoelastic characterization. Many theories have been developed in order to explain the complexity of viscoelastic materials and the most relevant of them are illustrated in the next paragraphs.

5.3.1 Frequency and Temperature Influence

The modulus, the energy loss and hysteresis of a viscoelastic material change in response to two parameters: the frequency with which the force is applied and the temperature, which produce opposite effects on the rubber. In particular, whenever the stress frequency is increased at a fixed temperature, the polymer appears in a glassy state; conversely, if the material heats up at a given stress frequency, it becomes softer and the compound exhibits rubbery behavior. These features arise from the balance between molecular velocity and strain rate. If the strain rate is greater than the speed at which the molecular chains are able to move in the polymer structure, the material appears glassy; if instead the strain rate is lower than the molecular speed, the compound exhibits rubbery behavior. In particular, at very low temperatures the rubber is extremely rigid; then when it reaches a certain transition temperature, the molecular bonds of the polymers that constitute it break and consequently the rubber becomes extremely soft at high temperatures. The temperature around which the intermolecular bonds break down is called the *glass transition temperature* and it is indicated as T_g (Figure 5.4). Besides, the motion speed of chains inside the molecular structure is strictly dependent on the specific material temperature. Consequently, the Time–Temperature Superposition Principle (TTSP) is presented [182]. This theory states that, considering for example the Storage Modulus E', at two different temperatures T_1 and T_0 such that $T_1 > T_0$, the value assumed by the modulus at the

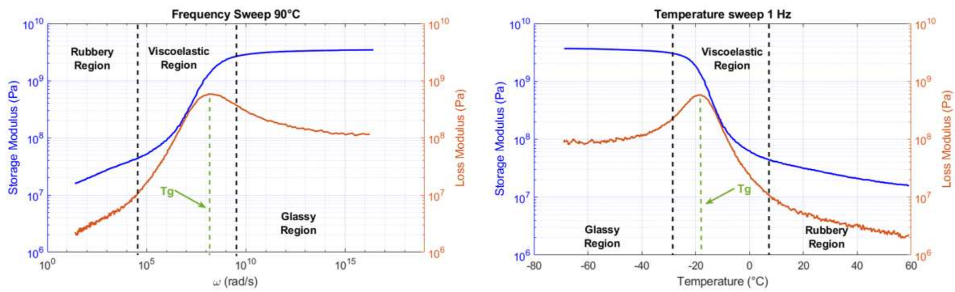

Fig. 5.4 Examples of master curves - frequency and temperature dependence

frequency ω_1 and the temperature T_1 will be the same at the frequency ω_0 and temperature T_0, which is also called reference temperature. In this way, if T_1 is higher than T_0, the molecular processes are faster and it is verified that $\omega_0 < \omega_1$. This phenomenon can be mathematically expressed as follows:

$$E'(\omega_1, T_1) = E'(\omega_0, T_0) \tag{5.4}$$

Materials that satisfy the equation 5.4 are called simple thermologically materials. If the temperature changes, the curve $E' - \omega$ shows a shift, as shown in Figure 5.5, according to the following expression:

$$\omega_0 = \frac{\omega_1}{a_T(T_1)} \tag{5.5}$$

The magnitude $a_T(T)$ is the *shifted factor* and it has the following properties:

$$T_1 > T_0 \rightarrow a_T(T_1) > 1$$

$$T_1 < T_0 \rightarrow a_T(T_1) < 1$$

$$T_1 = T_0 \rightarrow a_T(T_1) = 1$$

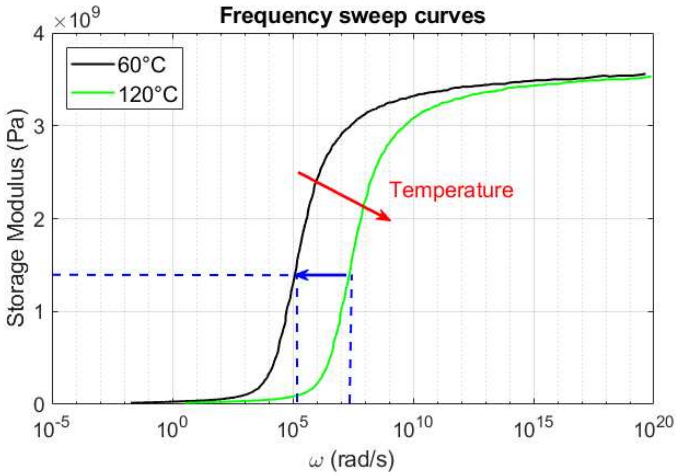

Fig. 5.5 Storage modulus shift

5.3.2 Williams - Landel - Ferry (WLF) Equations

The superposition principle is used to determine the temperature dependency for mechanical properties of linear viscoelastic material in order to know the viscoelastic behavior at a reference temperature T_0. Moreover, the time-temperature superposition avoids the inefficiency of measuring a polymer's behavior over long periods of time at a specified temperature by assuming that at higher temperatures and longer times, the material will behave the same [183].

In order to represent the storage modulus (E') curves at a higher or lower frequency than the reference frequency ω_0, the shift factor, a_T, is evaluated with the relation established by Malcom L. Williams, Robert F. Landel and John D. Ferry, or WLF equation. The empirical WLF equation describing shift factor, a_T, is [184, 185]:

$$\log(a_T) = \log\left(\frac{\omega_0}{\omega}\right) = \frac{-C_1(T-T_0)}{C_2+(T-T_0)} \tag{5.6}$$

In the equation 5.6 the following parameters appear:

- T_0 is the reference temperature for the storage modulus master curve;
- T is an arbitrary temperature;
- ω_0 is the reference frequency associated with the reference temperature T_0;
- ω is the new frequency;
- C_1 and C_2 are empirical constants adjusted to fit the values of the shift factor (a_T).

Differently, if the purpose is to evaluate the storage modulus at different temperatures than the reference ones, the following equation can be used:

$$T = T_0 - \frac{C_2 \log\left(\frac{\omega_0}{\omega}\right)}{C_1 + \log\left(\frac{\omega_0}{\omega}\right)} \tag{5.7}$$

In Equation 5.7 there are the following parameters:

- ω is the frequency at which the new temperature is calculated;
- T is the new temperature;

The WLF coefficients, C_1^* and C_2^*, matching at the new temperature T are evaluated with the following expressions:

$$C_1^* = C_1 \frac{C_2}{C_2 + (T - T_0)} \tag{5.8}$$

$$C_2^* = C_2 + (T - T_0) \tag{5.9}$$

5.4 VESevo: Viscoelasticity Evaluation System Evolved

It is well known that, due to the complexity of the tire vulcanization process, the properties of the tread compound obtained in tire manufacturing can be significantly different from the ones achieved in the laboratory. For this reason, the actual tread mechanical properties are complex to be determined unless the tire tread is destroyed to obtain a specimen on which the Dynamic Mechanical Analysis (DMA) is performed, which usually requires expensive machines and a long time for a full time-temperature characterization of the material [186, 187]. Moreover, in most applications, as well as motorsport ones, the tires are linked to restrictions and they cannot be analyzed by the standard and laboratory procedures. In this scenario, the knowledge of these viscoelastic properties through non-destructive and non-invasive techniques is a key factor for several applications that range from the development of polymers for innovative compounds to vehicle performance and road safety, gaining the attention of industries and academics from different sectors [188–191]. In this research, an innovative device, named VESevo (Viscoelasticity Evaluation System Evolved), able to evaluate in a non-destructive way the viscoelastic properties of the tires, has been used to test the different tires utilized as a reference for this study. The proposed methodology has been developed with the principal aim to characterize the compounds' viscoelasticity directly on tires, with the possibility to perform the tests both in the laboratory and on track.

5.4.1 Innovative Device Description

With the aim to propose a smart solution for non-destructive compounds viscoelastic characterization, the innovative device VESevo has been developed by the Applied Mechanics research group of the Department of Industrial Engineering at the University of Naples Federico II [192]; it allows the char-

Fig. 5.6 VESevo device and acquisition unit

acterization of the tire tread viscoelastic properties and its variations due to cooling or heating and monitoring the performances at progressive mileage or aging depending on vehicle applications. The VESevo can be also very advantageous for tire manufacturers because it could be employed in monitoring the goodness of a huge number of final products in a very short time by the operators compared to the standardized procedures requiring specific and expensive test benches, as well as rolling machines or flat-trac. As depicted in Figure 5.6, the VESevo technology is composed by: an instrument for indentation analysis, an acquisition case, necessary for the management of the acquired signals, and a self-made customized software for raw data acquisition, developed in the LabVIEW environment to find out any acquisition anomalies and check the goodness of a whole test session.

The prototype of the VESevo device and its functional scheme are described in Figure 5.7. The instrument has been designed taking into account a sort of gun-shaped handles for the primary purpose of guaranteeing a high level of ergonomics and stability, allowing the user to carry out many tests

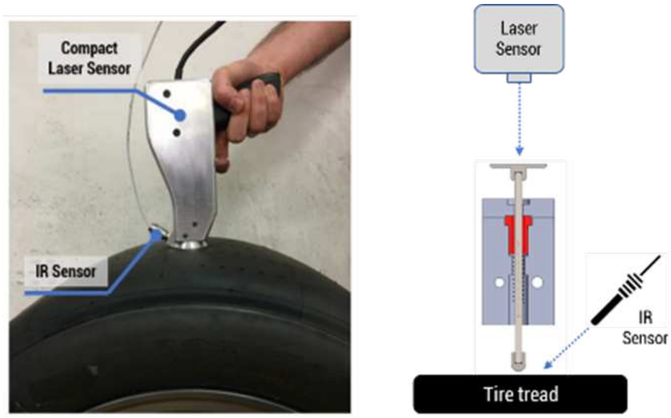

a) b)

Fig. 5.7 VESevo prototype and its conceptual scheme

in the smartest procedure possible with satisfying repeatability. The inner structure of the device is characterized by a steel rod with a semi-spherical indenter. This rod is free to bounce on the material under investigation sliding inside a suitable guide so that the damping phenomena during the motion can be neglected. A spring is arranged in the system in order to guarantee a minimum preload. The free drop motion of the rod always starts from the same initial position thanks to a semi-automatic system based on a magnet: this magnet is mounted on a suitable slider and it is capable of holding the upper plate of the rod and lifting it to the maximum ascent point. This system guarantees the repeatability of the measurements. The motion of the rod is acquired by an integrated optical sensor, with high-frequency response, 100 kHz, and high resolution (10 µm). The temperature of the compound during a single test is also acquired, together with the displacement data, by means of a compact IR pyrometer.

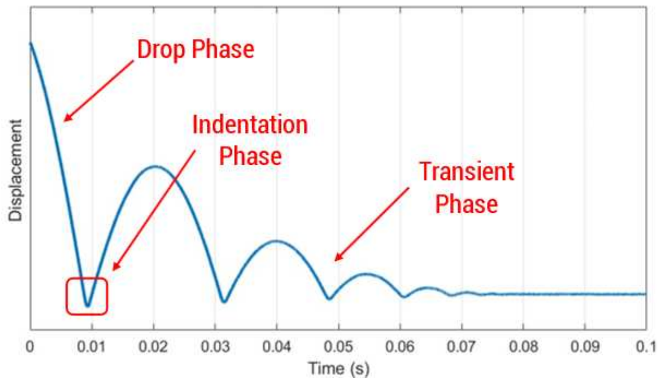

Fig. 5.8 Acquired raw signal on tire tread surface

5.4.2 Testing Procedure and Raw Signal Description

A standardized testing procedure has been set up to perform a single acquisition employing the VESevo; it consists in:

- the positioning of the device vertically to the tire tread compound;
- the indenter is manually raised until a mechanical lock in order to obtain each acquisition with the same starting position and velocity;
- once reached the maximum point, the rod is released thanks to the semi-automatic system and both the rod displacement curve and the compound temperature are shown on the acquisition software.

In Figure 5.8, a typical displacement signal is reported. Here it is noticeable that the rod displacement exhibits different phases characterizing the motion: the drop phase starting from the initial position, the first indentation into the rubber thickness and, then, the transient bounce until the established contact between the indenter and the tread surface.

In order to explore the tread compounds' behavior in dependence on the temperature, the tests can be performed by varying the sample temperature. Typically, the VESevo test session is carried out using the following standard testing procedure:

- about 30 acquisitions at ambient temperature;
- cooling down to about -20°C employing a climatic cell, a freezing spray or any other method capable to keep temperature low and stable and then performing VESevo acquisitions during the natural heating process up to ambient temperature;
- forced heating up to 100°C through a thermal blanket or a professional heating gun, and then carrying out acquisitions down to ambient temperature.

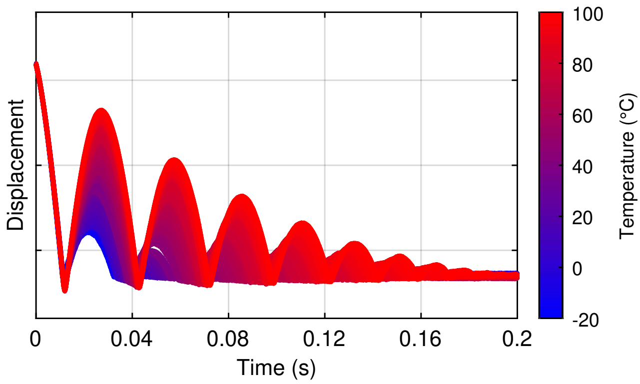

Fig. 5.9 Displacement curves at different temperatures of the tire tread surface.

Figure 5.9 clearly highlights how the temperature strongly affects the rod-sample interaction and consequently the rebound phenomenon both in terms of the amplitude and bounces number reflecting the natural viscoelastic response of the tread compound as a function of the temperature: at low temperatures, high energy dissipation occurs and the material behaves as a glassy solid. Conversely, when the compound is heated up to about 100°C, a progressive decrease of the energy dissipation is observed with a resulting increase in rebounds number and a rubbery behavior clearly emerges. The rod displacement raw signals, acquired throughout the temperature range, contain all the information necessary to extrapolate, through a data processing algorithm, a series of physical temperature-dependent parameters with which is possible to define specific mathematical relationships for the viscoelastic properties evaluation and the full master curves construction. Particularly, the Loss Factor can be defined with the following mathematical relationship obtained by modeling the dynamic response of the steel rod with a second-order damped mass-spring system [190]:

$$\tan\delta = \frac{\omega_s \sigma_c}{K_c} \tag{5.10}$$

where ω_s is the frequency of the damped motion of the rod on the viscoelastic surface while K_c and σ_c represent the equivalent contact stiffness and damping coefficient, respectively.

5.4.3 Experimental Data

In this research activity, several data were collected through the VESevo device, for the viscoelastic characterization of several compounds. This data was used to determine the master curves of the storage modulus and the loss factor for the various compounds. The collected data allows to reconstruct the complete master curves through a fitting process of the experimental values (Figure 5.10. In this way, knowing the solicitation frequency and subsequently, the temperature shifted according to WLF equations, it was possible to obtain the values of the storage modulus and loss factor.

The solicitation frequency was obtained according to the following expression:

$$f = \frac{v_s}{\lambda_{micro}} = \frac{\sqrt{v_{s_x}^2 + v_{s_y}^2}}{\lambda_{micro}} \tag{5.11}$$

where v_s is the sliding velocity obtained from the vector composition of the v_{s_x} and v_{s_y} components while λ_{micro} is the characteristic wavelength of the road profile. After evaluating the solicitation frequency f, it is possible to

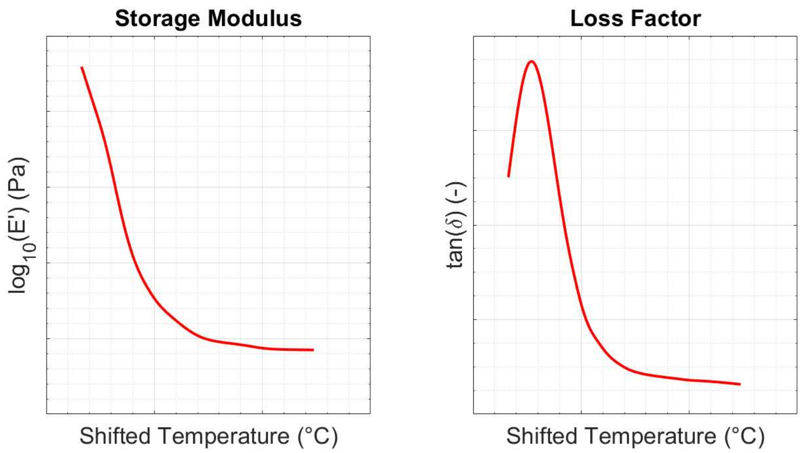

Fig. 5.10 Master curves obtained from the experimental data collected with VESevo

determine the shifted temperature T_s at which to evaluate E' and $\tan(\delta)$ in the master curves through an experimental expression:

$$T_s = T_{Surf} - 8\log_{10}(f) \tag{5.12}$$

5.5 Road Roughness Parameterization

Starting from the global statistical approach presented in paragraph 1.7, adopting several techniques widely described in the literature, it is possible to define different key performance indicators able to describe the characteristics of roughness starting from experimental acquisitions performed with specifically designed instruments. During this research activity, a new methodology for micro-roughness parameters has been developed to overcome the limits of the standard procedures.

5.5.1 Roughness Parameters

The surface roughness is usually characterized by one of the two statistical height descriptors advocated by the American National Standards Institute (ANSI) and the International Standardization Organization (ISO) [193]: the R_a (the center line average or the arithmetic average) and the standard deviation σ (or variance σ^2) or the root mean square R_q (RMS). As already mentioned in the previous section, two other statistical descriptors are skewness and kurtosis.

Considering a generic surface profile $z(x)$, as shown in Figure 5.11, profile heights are measured from a reference line and the center line (or mean line), is defined such that the area between the profile and the mean line, above the line, is equal to that below the mean line.

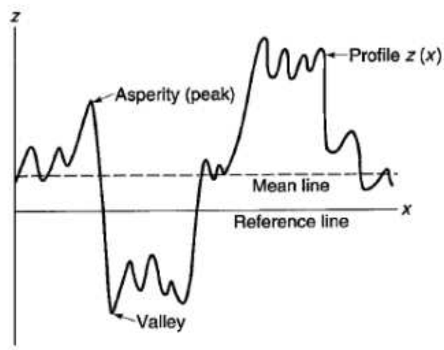

Fig. 5.11 Surface profile $z(x)$

In addition, it is possible to define some statistical height descriptors, in their mathematical form, in this way [194]:

- The center line average R_a is the arithmetic mean of the absolute values of vertical deviation from the mean line through the profile and it is defined as:

$$R_a = \frac{1}{L}\int_0^L |z-m|dx \tag{5.13}$$

where L is the sampling length of the profile and m is the mean, which is defined as $m = \frac{1}{L}\int_0^L z dx$;

- The variance σ^2 is defined as:

$$\sigma^2 = \frac{1}{L}\int_0^L (z-m)^2 dx = R_q^2 - m^2 \tag{5.14}$$

where R_q is the root mean square, which is expressed as

$$R_q^2 = RMS^2 = \frac{1}{L}\int_0^L z^2 dx \tag{5.15}$$

It is evident that if $m = 0$, it is $R_q = \sigma$;

- The skewness of the assessed profile Sk is:

$$Sk = \frac{1}{\sigma^3 L}\int_0^L (z-m)^3 dx \tag{5.16}$$

- The kurtosis of the assessed profile Ku is:

$$Ku = \frac{1}{\sigma^4 L}\int_0^L (z-m)^4 dx \tag{5.17}$$

- The maximum profile peak height of the assessed profile R_p, defined for m profile, is:

$$R_p = \max_{1 \leq j \leq m} Z_{p_j} \tag{5.18}$$

with j = 1,..,m and Z_{p_j} is the height of the j_{th} profile peak within the sampling length;

- The maximum profile valley height of the assessed profile R_v, defined for m profile, is:

$$R_v = \max_{1 \leq j \leq m} Z_{v_j} \tag{5.19}$$

with j = 1,..,m and Z_{v_j} is the depth of the j_{th} profile valley within the sampling length;

- The maximum height of the assessed profile R_z is:

$$R_z = R_p + R_v \tag{5.20}$$

all calculated over a sampling length;

- The mean height of the profile elements of the assessed profile R_c, defined for m profile, is:

$$R_c = \frac{1}{m}\sum_{j=1}^{m} Z_{t_j} \tag{5.21}$$

with j = 1,..,m and Z_{t_j} is the height of the j_{th} profile element within the sampling length;

- The mean width of the profile elements of the assessed profile RS_m, defined for m profile, is:

$$RS_m = \frac{1}{m}\sum_{j=1}^{m} X_{s_j} \tag{5.22}$$

with j = 1,..,m and X_{s_j} is the width of the j_{th} profile element within the sampling length.

These parameters are connected only with the variation of the profile in the vertical direction and, for this reason, they do not provide any information about the slopes, the shares, the sizes or about the frequency and the regularity of their occurrence [193]. Indeed it is possible to have profiles with different frequencies but with the same R_a or R_q values, as shown in Figure 5.12.

For this reason, to have a complete characterization of a profile, amplitude parameters must be integrated with other quantities. In particular, it is fundamental to know the information about the wavelength of the surface λ, which

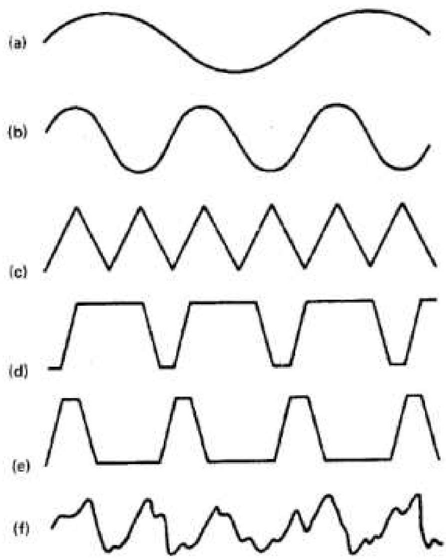

Fig. 5.12 Various surface profile with the same R_a value

is the distance between consecutive corresponding points of the same phase on the wave, such as two adjacent crests, troughs or zero crossings. Therefore some spatial parameters are generally used: the peak (or summit) density N_p, which represents the number of peaks of the profile per unit length and the zero crossing density N_0, which is defined as the number of times the profile crosses the mean line per unit length. Although the profile contains a big range of wavelengths, the wavelength of the profile can be defined as follows [195]:

$$\lambda = 2\pi \frac{\int_0^L |z(x) - m| dx}{\int_0^L |z'(x)| dx} \tag{5.23}$$

where $z'(x)$ is the mean slope of the profile.

5.5.2 Self Affine Surfaces Characterization and Correlation Functions

The term 'self-affinity' was introduced by Mandelbrot when he studied geometrical objects that are statistically invariant under anisotropic dilations[196]. It represents a generalization of the term 'self-similarity' that denotes invariance under isotropic dilation [197]. The statistical self-affinity is due to the similarity in appearance of a profile under different magnifications and such a behavior can be characterized by fractal geometry. The fractal approach has the ability to characterize surface roughness by scale-independent parameters and provides information on the roughness structure at all length scales that exhibit the fractal behavior.

If the profile $z(x)$ of a rough surface without overhangs, i.e. of a vertical cross-section of the surface, is considered, then the surface is self-affine if the transformation $x \rightarrow \Lambda x$, $z \rightarrow \Lambda^H z$ leaves the surface statistically invariant (mathematically it means that a magnification α in the lateral $x-y$ plane corresponds to a magnification in vertical z-direction). The exponent H ($0 \leq H \leq 1$) is called Hurst coefficient and it defines the local fractal dimension D of the surface that represents a quantitative measure of surface irregularity and is evaluated as:

$$D = \delta - H \tag{5.24}$$

where δ is the dimension of the Euclidean space ($\delta = 2$ for two-dimensional surface and $\delta = 3$ for three-dimensional surface). An example of a self-affine profile is shown in Figure 5.13.

In addition to the surface fractal dimension D, two further length scales are necessary to characterize a self-affine surface (Figure 5.14) [198]:

- the correlation length $\xi_{||}$ parallel to the surface, corresponding to the macro wavelength λ_{macro};

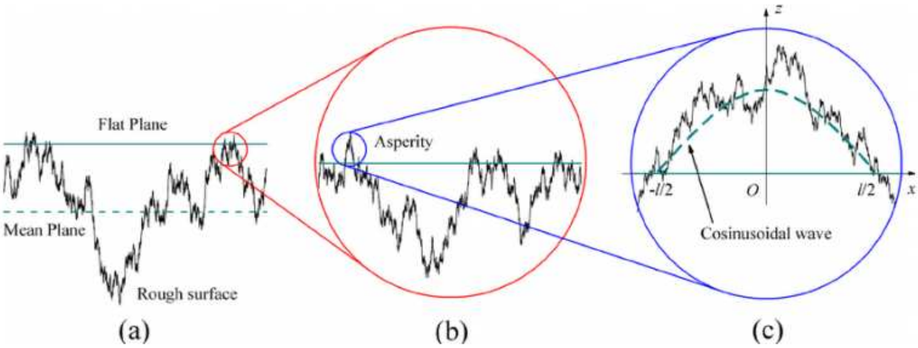

Fig. 5.13 Self-affine profile

- the variance, i.e. the root mean square fluctuations around the mean height:

$$\sigma^2 = \left\langle (z(x) - \langle z \rangle)^2 \right\rangle \tag{5.25}$$

where $\langle z \rangle$ is the mean height of the surface points and $\langle \cdot \rangle$ is the average over the set of observations of surface topography. The variance σ can also be expressed by the correlation length $\xi_\perp$ (also known as peakyness) normal to the surface:

$$\sigma^2 = \frac{\xi_\perp^2}{2} \tag{5.26}$$

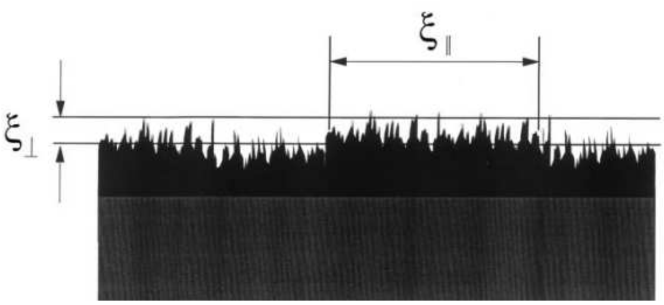

Fig. 5.14 Correlation lengths [198]

For an estimation of surface descriptors, i.e., the correlation lengths $\xi_{\|}$ and $\xi_{\perp}$ and the surface fractal dimension D, it is useful to refer to the correlation functions of the surface. One possibility is to consider the height difference correlation function, $C_z(\lambda)$:

$$C_z(\lambda) = \left\langle (z(x+\lambda) - z(x))^2 \right\rangle \tag{5.27}$$

This function describes the mean square height-fluctuations of the surface with respect to the horizontal length scale λ. For self-affine surfaces, $C_z(\lambda)$ below the horizontal ($\xi_{\|}$) and vertical ($\xi_{\perp}$) cut-off length, follows a power law with exponent $2H$ on small length scales for $\lambda \leq \xi_{\|}$ and approaches the constant value $\xi_{\perp}^2$ for $\lambda > \xi_{\|}$. The relationship between $C_z(\lambda)$ and the surface descriptors $\xi_{\|}$, $\xi_{\perp}$ and H is given by the following expression [197–200]:

$$C_z(\lambda) = \xi_{\perp}^2 \left(\frac{\lambda}{\xi_{\|}}\right)^{2H} \quad for\, \lambda < \xi_{\|} \tag{5.28}$$

Equation 5.28 allows describing the roughness spectrum of self-affine surfaces by only three parameters. If more scaling ranges should be necessary for a reasonable description of surface roughness, the formula can be expanded to any number of scaling ranges with different Hurst exponents. If two scaling ranges appear necessary for describing the different scaling of micro and macro roughness, the function $C_z(\lambda)$ is defined as:

$$C_z(\lambda) = \xi_{\perp}^2 \left(\frac{\lambda}{\xi_{\|}}\right)^{2H_M} \quad for\, \lambda_x < \lambda < \xi_{\|} \tag{5.29}$$

$$C_z(\lambda) = \xi_{\perp}^2 \left(\frac{\lambda_x}{\xi_{\|}}\right)^{2H_M} \left(\frac{\lambda}{\lambda_x}\right)^{2H_m} \quad for\, \lambda < \lambda_x \tag{5.30}$$

Here λ_x is the intersection point of the two scaling ranges while H_m and H_M respectively, give the information about the fractal scaling of micro and macro roughness (Figure 5.15).

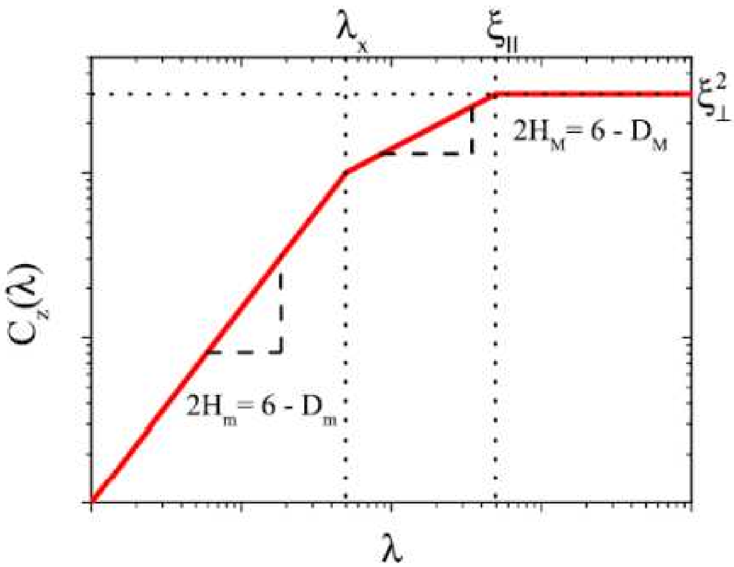

Fig. 5.15 Height Difference Correlation function (HDC) [199]

Another approach is the evaluation of the height correlation function, $\Gamma_z(\lambda)$, also named auto-correlation function:

$$\Gamma_z(\lambda) = \langle z(x+\lambda)z(x)\rangle - \langle z(x)\rangle^2 \tag{5.31}$$

It characterizes the correlations of heights at two different positions and it goes to zero at large distances for $\lambda > \xi_{||}$, where the two heights become uncorrelated. The two correlation functions given in equations 5.27 and 5.31 are related by the equation:

$$C_z(\lambda) = 2(\sigma^2 - \Gamma_z(\lambda)) \tag{5.32}$$

With the large scale behavior ($\lambda > \xi_{\|}$) of $\Gamma_z(\lambda)$ and $C_z(\lambda)$ this equation leads immediately to the identify $\sigma^2 = \frac{\xi_{\perp}^2}{2}$, valid for self-affine surfaces.

An alternative correlation function for describing self-affine rough surfaces is the power spectral density (PSD) [197–199, 6].

For stationary surfaces the Fourier transform of $\Gamma_z(\lambda)$ equals the power spectral density $S(f)$, where f is the spatial frequency (Theorem of Wiener and Khintchin):

$$\Gamma_z(\lambda) = \int_{f_{min}}^{\infty} S(f) e^{2\pi i f \lambda} df \tag{5.33}$$

The minimum frequency f_{min} corresponds to the inverse correlation length $\xi_{\|}$ and it represents the maximum wavelength of the modulations of the surface ($f_{min} = \xi_{\|}^{-1}$).

For one scaling regime the PSD function is identified by the three parameters: $\xi_{\perp}$, $\xi_{\|}$ and H. For two different ranges the PSD is described by the following equations:

$$S_M(\omega) = S_{M,0} \left(\frac{\omega}{\omega_{min}} \right)^{-\beta_M} \quad for\; \omega_{min} < \omega < \omega_x \tag{5.34}$$

$$S_m(\omega) = S_{m,0} \left(\frac{\omega}{\omega_x} \right)^{-\beta_m} \quad for\; \omega > \omega_x \tag{5.35}$$

where:

$$S_{M,0} = \frac{(3 - D_M) {\xi_{\perp}}^2}{2\pi v \xi_{\|}} \tag{5.36}$$

$$S_{m,0} = \frac{(3 - D_M) {\xi_{\perp}}^2}{2\pi v \xi_{\|}} \left(\frac{\omega_x}{\omega_{min}} \right)^{-\beta_M} \tag{5.37}$$

In the equations just presented the following parameters appear:

- v is the sliding velocity;
- ω is the frequency;

- $\beta_M = 2H_M + 1 = 7 - 2D_M$ is the slope of the PSD for lower excitation frequencies caused by large asperities;
- $\beta_m = 2H_m + 1 = 7 - 2D_m$ is the scaling exponent of micro roughness;
- $\omega_{min} = 2\pi v/\xi_{||}$ is the smallest frequency related to the largest length scale $\xi_{||}$;
- $\omega_x = 2\pi v/\lambda_x$ is the crossing frequency micro and macro roughness.

An illustration of the power spectral density $S(\omega)$ for two scaling ranges is shown in Figure 5.16.

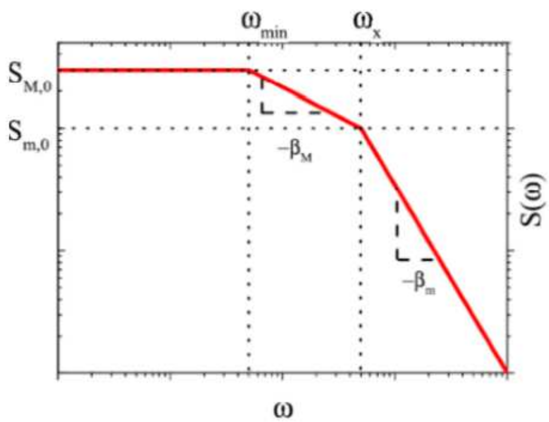

Fig. 5.16 Power Spectral Density (PSD) [199]

In general the 2D power spectral density (C_{2D}) cannot be evaluated from 1D power spectral density (C_{1D}) unless in two cases: isotropic surface roughness or 1D surface roughness. In particular, in the case of a 2D isotropic surface roughness, the power spectral density is evaluated in this way [201]:

$$C_{2D}(q) = \frac{1}{\pi}\int_q^\infty \frac{[-C'_{1D}(q')]}{\sqrt{q'^2 - q^2}}dq' \tag{5.38}$$

where q is the magnitude of the wave vector.

In Figure 5.17, the power spectral density $C_{2D}(q)$ obtained form 2D-data of a track asphal is proposed.

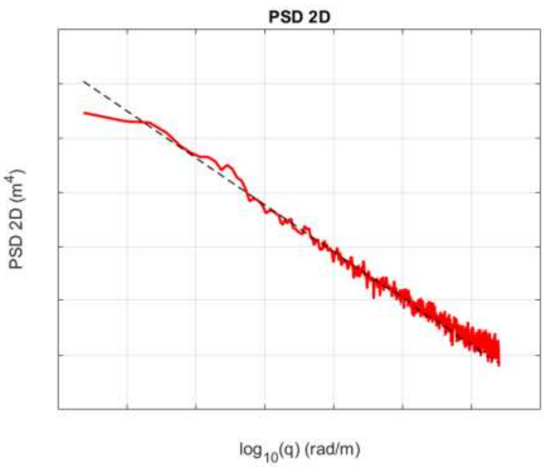

Fig. 5.17 PSD $C_{2D} = C(q)$ for a track asphalt surface obtained from 2D data

Differently, in the case of 1D surface roughness, the power spectral density is evaluated with the following equation:

$$C_{2D}(q) = C_{1D}(q_x)\delta(q_y) \tag{5.39}$$

5.5.3 Minimum Contact Length

If the evaluation of the macro wavelength can be entrusted to the study of the HDC or of the PSD, the same cannot be said for the micro wavelength (λ_{micro}) The theory for micro wavelength evaluation assumes that a profile impacts with a rubber substrate and indents at a height d. Two height distributions are evaluated to indicate every height profile, as shown in Figure 5.18. This is an extension of the Greenwood-Williamson contact theory to self-affine rough surfaces, which assumes that the asperities have the same radius of curvature and that the height of the peaks is stochastically distributed around an average value and it considers randomly distributed Hertz-like contacts with spherical

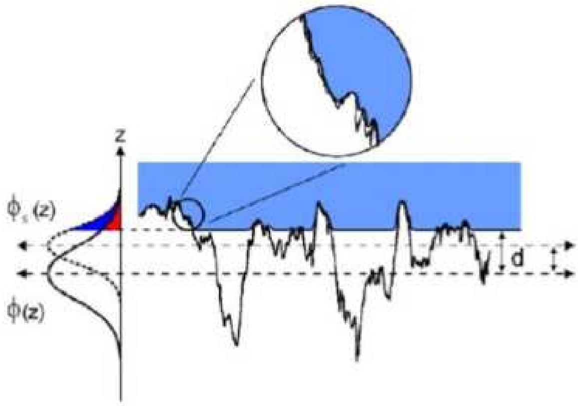

Fig. 5.18 Profile and height distribution [200]

macro asperities on the largest roughness scale of the substrate. The spheres have a curvature radius R, equal to:

$$R = \frac{\xi_{\parallel}^2}{4\pi^2 \xi_{\perp}} \tag{5.40}$$

The following equation allows to evaluate the λ_{micro}:

$$\frac{\lambda_{micro}}{\xi_{\parallel}} \approx \left[\left(\frac{\lambda_x}{\xi_{\parallel}} \right)^{3(D_m - D_M)} \frac{0.09\pi s^{3/2} \xi_{\perp} F_0(t) |E^*(2\pi v/\lambda_{micro})| \tilde{n_s}}{\xi_{\parallel} |E^*(2\pi v/\xi_{\parallel})| F_{3/2}(t_s)} \right]^{\frac{1}{3D_m - 6}} \tag{5.41}$$

where:

- s is an affine parameter, equal to 1.44, characteristic for every rough surface. It establishes the transformation for each eight z of the substrate with height distribution $\Phi(z)$ to a corresponding height z_s for the summit height profile distributions $\Phi_s(z)$ of macroscopic asperities as follows:

$$z_s = z_{max} + \frac{z - z_{max}}{s}$$

with z_{max} the maximum height of the substrate;

- $F_0(t)$ and $F_{3/2}(t_s)$ are the *Greenwood-Williamson function* defined as:

$$F_0(t) = \int_t^{\infty} \Phi(z)dz \tag{5.42}$$

$$F_{3/2}(t_s) = \int_{t_s}^{\infty} (z - t_s)^{3/2} \Phi_s(z)dz \tag{5.43}$$

where $t = d/\tilde{\sigma}$ is the normalized gap distance d between rubber and substrate, referring to the standard deviation $\tilde{\sigma}$ of the height distribution $\Phi(z)$ and the same is for $t_s = d_s/\tilde{\sigma}_s$ where d_s and $\tilde{\sigma}_s$ are the corresponding parameters of the summit height distribution $\Phi_s(z)$ of macro asperities. Considering that the mean value $\langle z \rangle$ of the substrate height function $\Phi(z)$ is zero, the average of the summit height distribution $\Phi_s(z)$ is given by:

$$\langle z_s \rangle = z_{max} \left(1 - \frac{1}{s} \right)$$

In addition the standard deviation of $\Phi_s(z)$, $\tilde{\sigma}_s$, is linked with the origin standard deviation by the affine parameter s:

$$\tilde{\sigma}_s = \frac{\tilde{\sigma}}{s}$$

and hence:

$$t_s = t \cdot s - \frac{\langle z_s \rangle}{\tilde{\sigma}_s}$$

- $\tilde{n}_s = 6\pi\sqrt{3}\lambda_c^2 n_s$, where n_s is the microscopic summit density defined with the following expression: $n_s = m_4/(6\pi\sqrt{3}m_2)$, with m_2 and m_4 the second and fourth moments of the spectrum, evaluated in this way [197]:

$$m_2 = \left\langle \left(\frac{dz}{dx} \right)^2 \right\rangle \tag{5.44}$$

$$m_4 = \left\langle \left(\frac{d^2 z}{dx^2} \right)^2 \right\rangle \tag{5.45}$$

and $\lambda_c \sim 10^{-10}$m is the lowest possible contact length;

- E^* is the dynamic modulus (sum of the storage modulus, E', and the *loss modulus*, E'', multiplied by the imaginary unit i: $E^* = E' + iE''$) evaluated at different wavelengths.

5.5.4 Innovative Methodology for Micro-Roughness Parameters Identification

The idea to develop a new formulation for micro-roughness parameters is born from the need to obtain robust parameters able to completely characterize road roughness. As outlined in the previous paragraph, both λ_{Macro} and λ_{micro} can be evaluated using the HDC function. However, this procedure is affected by the instability of the auto-correlation function (described in Equation 5.31); indeed, this function is strongly dependent on the shape of the roughness profile acquisition and it is not possible to highlight eventual error committed during the measurement. In addition, this estimation, in particular for what concerns the micro parameters, could be also affected by the rugosimeter resolution. Moving toward more complex formulations, like the one proposed by Greenwood-Williamson and described in Equation 5.41, it is not possible to consider only the information related to the road. In fact, this formula contains several parameters associated with the viscoelastic material that has to be coupled with the road during contact interaction. The approach adopted in the development of this innovative formulation is to process road data independently from the other factors, such as the specific tire used with its viscoelastic properties, to obtain a roughness characterization that is independent and could be used also with different cars and in different contexts. To this aim, a simplified analytical methodology has been used starting from the Equation 5.23 [195], applied to several extrapolated "micro-profiles". The reference formula, from which the analytical approach has been developed is the following:

$$\lambda = 2\pi \frac{\int_0^L |z(x) - m| dx}{\int_0^L |z'(x)| dx} \tag{5.46}$$

in which the numerator of the ratio is the profile function, equivalent to the R_a calculation (Equation 5.13), whereas the denominator identifies the slope of the selected profile. To properly apply this Equation 5.46 not only to the entire profile, to evaluate the λ_{Macro}, but also for the λ_{micro} estimation, a robust procedure to extract some portion of the "macro-profile" has been built. To obtain the "micro-profiles" from the rugosimeter acquisition, it is necessary to perform the following steps:

1. Selection of the roughness acquisition;
2. Application of a smoother to the profile to correctly determine the local maxima;
3. Local maxima detection;
4. Extraction of the micro-profiles;
5. Detrend of the extracted micro-profiles;
6. Application of the formula on all the extracted micro-profiles extracted;
7. Mean of the parameters obtained on the different micro-profiles.

After the selection of the reference roughness profile to be processed, a smoother is applied to the profile (Figure 5.19). This is fundamental to correctly identify the local maxima of the profile, considered as the micro-asperities that are in contact with the tire during its motion. Without this operation, it is quite hard to define only the relevant maxima, several issues can be encountered, as shown in Figure 5.20. The smoother, combined with

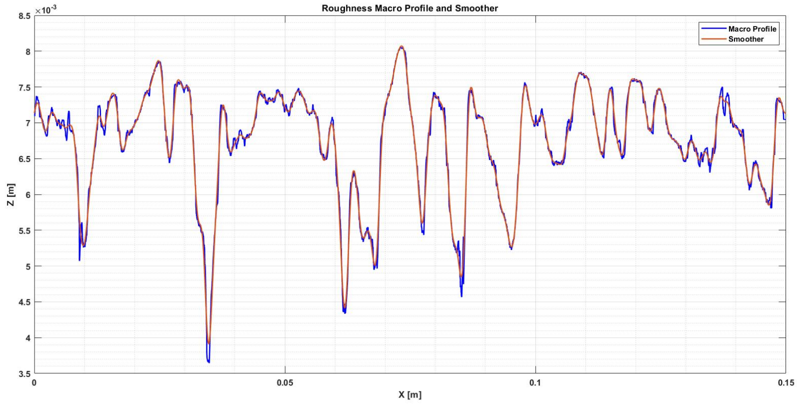

Fig. 5.19 Original vs smoothed macro-profile

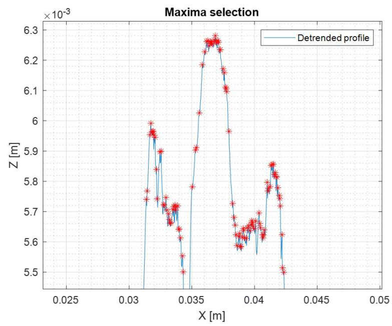

(a) Too many maxima identified

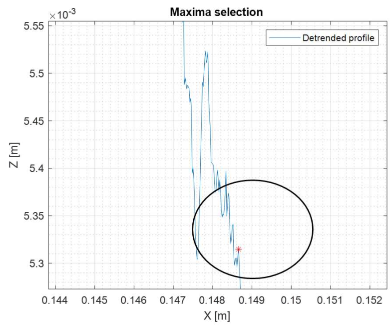

(b) False peak

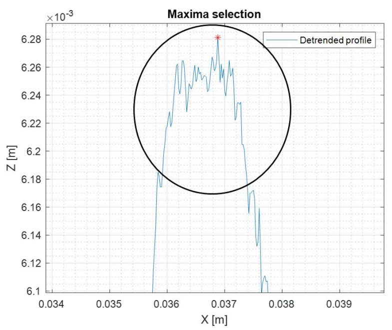

(c) Asymmetrical peak

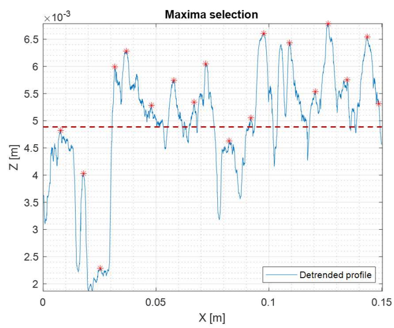

(d) Maxima under the mean value

Fig. 5.20 Errors in local maxima detection the selection procedure, gives the opportunity to select only the relevant peaks, above the mean value of the profile, spaced apart by an adequate minimum interval, determined through the acquisition instrument resolution. In addition, in this way, it is also possible to not consider false peaks and to center the interval of interest on the micro-asperity.

After these preliminary operations, several micro-profiles are extracted from the reference profile 5.21; in order to properly consider the road characteristic of the identified profile, a further detrend operation is performed 5.22 to remove the slope effect due to the macro-roughness of the acquired macro-profile.

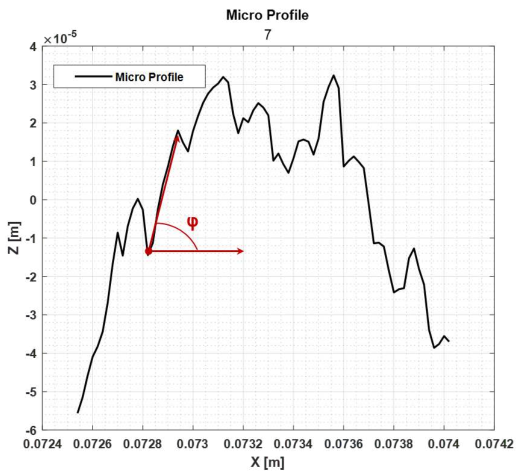

Fig. 5.21 Extracted micro-profile

The presented procedure allows the user to carry out checks on the consistency of the available acquisitions, giving the possibility of discarding the incorrect measurements. After the extraction, it is possible to apply the Equations 5.46 and 5.13 to evaluate the λ_{micro} and Ra_{micro} for the micro-profiles and then to calculate the mean value of these quantities to obtain the micro parameterization of the reference profile.

Applying the analytical approach to the extracted micro-profile and comparing the results obtained with those achievable with the classic HDC func-

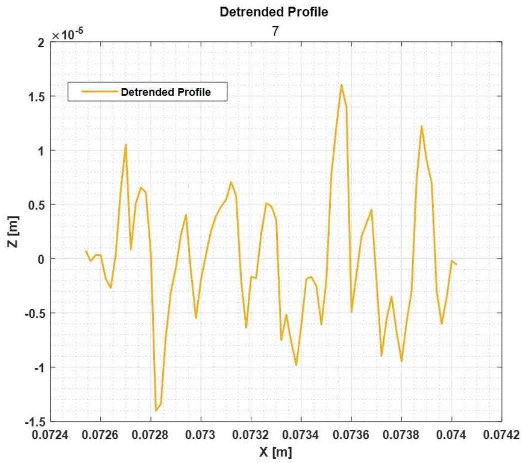

Fig. 5.22 Extracted micro-profile detrended

tion, it is possible to affirm that the innovative procedure gives back more stable results; indeed, considering the average of all the λ_{micro} values obtained from the various scans carried out on a track, obtained by averaging the λ_{micro} values of all the micro-profiles extracted from the single acquisition, it is possible to note how the results present a considerably lower dispersion than to the same values calculated with the application of HDC function (Figure 5.23).

Given the quality of the results obtained through the analytical method, it was decided to apply the same formula also for the evaluation of the λ_{Macro}, obtaining results also in this case much more robust than those obtainable with the HDC, as shown in the Figure 5.24, where it is possible to note the reduced standard deviation for the λ_{Macro} calculated with the Equation 5.46.

The presented procedure, thanks to the quality of the results obtained, it was of fundamental importance for the study of correlation with the target variables illustrated in the next Chapters.

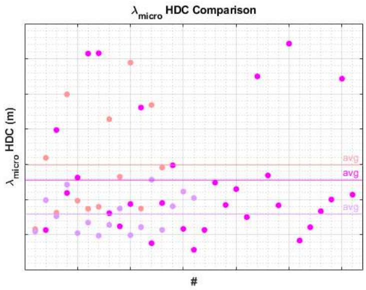

(a) HDC λ_{micro} estimation

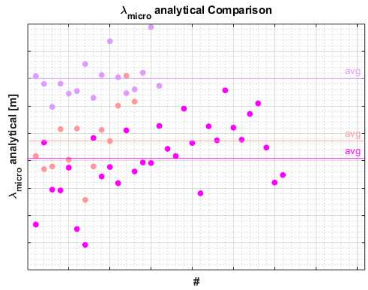

(b) Analytical λ_{micro} estimation

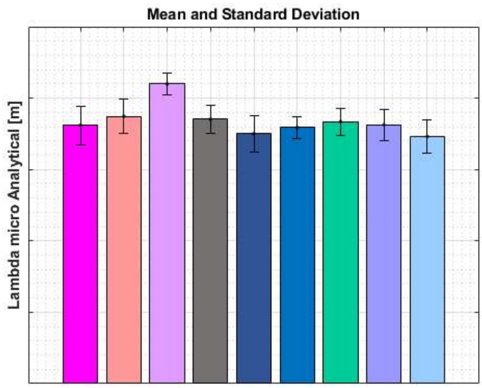

(c) Analytical λ_{micro} estimation, mean values and standard deviations

Fig. 5.23 Comparison between HDC and analytical λ_{micro} estimation

5.5.5 Further Indexes

In the roughness characterization process, additional parameters have been identified in order to describe better the road roughness of the various track. In particular, the following were introduced:

- $Index_{Macro}$ obtained from the ratio between λ_{Macro} and Ra_{Macro}

$$Index_{Macro} = \frac{\lambda_{Macro}}{Ra_{Macro}} \tag{5.47}$$

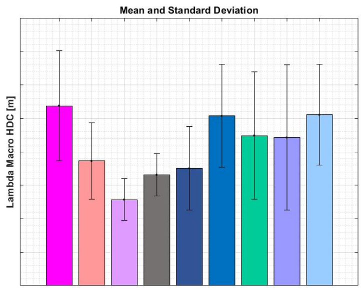

(a) HDC λ_{Macro} estimation

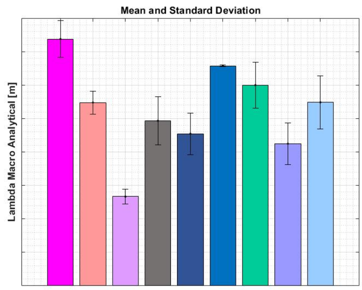

(b) Analytical λ_{Macro} estimation

Fig. 5.24 Comparison between HDC and analytical λ_{Macro} estimation, mean values and standard deviations

- $Index_{micro}$ obtained from the ratio between λ_{micro} and Ra_{micro}

$$Index_{micro} = \frac{\lambda_{micro}}{Ra_{micro}} \tag{5.48}$$

These indices were designed to synthesize combined characteristics that refer to certain wavelengths. Indeed, these quantities, being obtained through a combination of results from different studies, hold different information in a single value. All the quantities presented in this chapter were fundamental in order to obtain some useful information. Indeed, with the aim of getting structured databases through which to carry out several analyses, an appropriate reduction of the telemetry data was done in order to consider only the values relating to particular physical conditions, relevant for the study of vehicle performance, thus excluding all the points characterized by negligible values of the physical quantities presented in this thesis.

Chapter 6

Data Reduction and Database Creation

6.1 Introduction

In this and in the next chapter a complex case study is presented. Exploiting almost all the methodologies already presented in this thesis, the case study has been developed in order to illustrate how it is possible to combine all the data that generally are available in high motorsport competitions to obtain fundamental information to understand and optimize the vehicle's overall behavior. In particular, thanks to the collaboration with an industrial partner, telemetry data, tire viscoelastic properties and road roughness acquisitions have been collected to carry out these analyses. The data have been obtained from two professional drivers adopting the same vehicle configuration, for this reason, the methodology treated in chapters 3 and 4 are not directly applied to the outcomes that will be presented. The main aim of this Chapter is to propose different strategies to extract the relevant information from a big amount of the data of different typologies, stored in different structures. To this purpose, first of all, the Big Data analysis approach will be deepened; then, the target variables, tire grip and tire wear will be described, analyzing both the data pre-processing phase and how it is possible to isolate the data related to the vehicle maximum performance, extracting the data collected in the grip limited zones. Finally, the database creation phase is illustrated in detail, describing the various approaches adopted for data discretization.

6.2 Big Data in Motorsport Field

In the motorsport field, the teams collect large amounts of real-time data to improve the vehicle performance or to predict the same in order to achieve the best result during the race [202]. Thanks to this data, it is possible to evaluate the main parameters concerning the vehicle and tire such as velocities, temperatures, pressures and so on. Telemetry data can be defined as the transmission of real-time data streams from the race car sensors of data in each race. The output is often sent to each team's data processing center in the racetrack pits and simultaneously to the 'remote garage' back in the company (Figure 6.1).

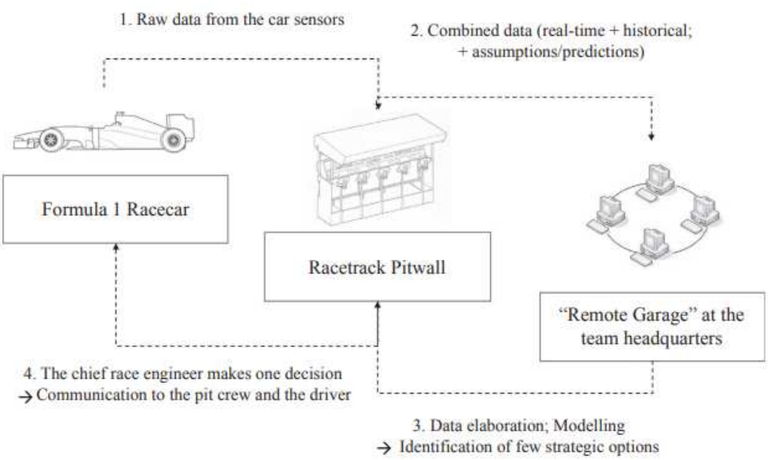

Fig. 6.1 real-time Big Data in motorsport racing [203]

In the information era, Big Data is the common term used to describe the enormous amount of data available on hand to decision markers. Big Data refers to databases, from a few dozen terabytes (TB) to many petabytes (PB) of data, that are too large and complex systems to be used effectively on conventional systems [204]. Most definitions of Big Data are closely connected with the size of data in storage. However, there are other components that play a fundamental role, indeed, the main features that distinguish Big Data, also known as the 'Vs' of Big Data, are the following ones:

- Volume;
- Variety;
- Velocity.

These characteristics constitute a more complete definition that busts the myth that Big Data is only about data volume [205]. In addition, each of the three Vs has its ramifications, as shown in Figure 6.2.

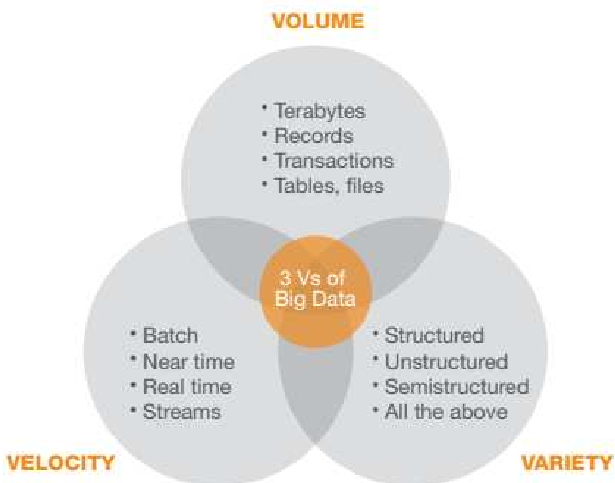

Fig. 6.2 The three Vs of Big Data [205]

Data volume is the primary attribute of Big Data since it refers to its size and how enormous it is. Big Data can be quantified by size in Terabytes or Petabytes (even if is rapidly heading toward Exabytes [206]), but also by counting records, transactions, tables or files. Some organizations find it more useful to quantify Big Data in terms of time, but it is important to understand that the scope of the same affects its quantification too. One of the things that makes Big Data really big is that it is coming from a greater variety of sources than ever before. For this reason, variety is really important since Big Data is remarkably different in terms of formats and types of data, as well as the several kinds of uses and ways of analyzing the data. Finally, velocity refers to the frequency of data generation or the frequency of data delivery [207]. Therefore it is possible to state that Big Data consists of large data sets mainly in the characteristics of volume, variety and speed that require a simplified structure for efficient archiving, manipulation and analysis [208].

Although the main features are the three mentioned above, some researchers and organizations have discussed the addition of other Vs: the veracity, the variability (and complexity) and the value [209]. The veracity, known as the fourth V, focuses on the quality of the data and it characterizes Big Data quality as good, bad or undefined due to data inconsistency, incompleteness, ambiguity, latency, deception and approximations. Variability refers to the variation in the data flow rates, while complexity is connected to the fact that Big Data is generated through a lot of sources. This represents the need to connect, match, clean and transform all the acquired data. Finally, the value is important since the data received in the original form, usually, has a low value compared to its volume. However, a high value can be obtained by analyzing large volumes of such data.

The definition of Big Data given above implies the presence of an interaction between the properties of the data and the need for a properly scaled structure of the same, to obtain the necessary performance and to optimize costs. There are two methodologies for system scaling, known as 'vertical' or 'horizontal' scaling. The first implies increasing the system parameters of the processing speed, storage and memory for better performance. This approach is limited by the need for increasingly sophisticated systems, which involve an increase in time and money for implementation. The second method is to use horizontal scaling to operate with individual resources integrated, with the aim of acting as a single system. Horizontal scaling is the central aspect of the Big Data revolution.

Understanding the data and its problems was fundamental in the work of this thesis. Indeed, in relation to the features indicated above, the main Vs of the available data were the volume (given the considerable amount of data), the variety (considering the different physical nature of the same) and also the acquisition speed (dictated by particular complex sensor systems that acquire data very quickly). In particular, given the characteristics of the same, a series of non-traditional approaches have been adopted in order to better process the starting data (raw data acquired on the track) and extract only the information of interest from this (creating specific databases based on runs, laps or by time data) to analyze the performance of the vehicle in a more easy way.

6.2.1 Big Data Analysis Pipeline

Big Data analysis involves several phases, each one characterized by its own difficulties. One of the most important is the analysis/modeling phase. However, this is of little use without the other phases that characterize the data analysis pipeline. Indeed, although in the analysis phase there are many complexities that are poorly understood since the difficult treatment required, there are different challenges that also extend to the other phases. For example, an important issue concerns the management of Big Data, since this can be affected by noise, is heterogeneous in nature and it is often difficult to identify an initial pattern. For this reason, the management of the provenance of the data with the uncertainty and error that distinguishes it is a crucial aspect [210]. The phases that characterize the Big Data analysis pipeline are shown in Figure 6.3.

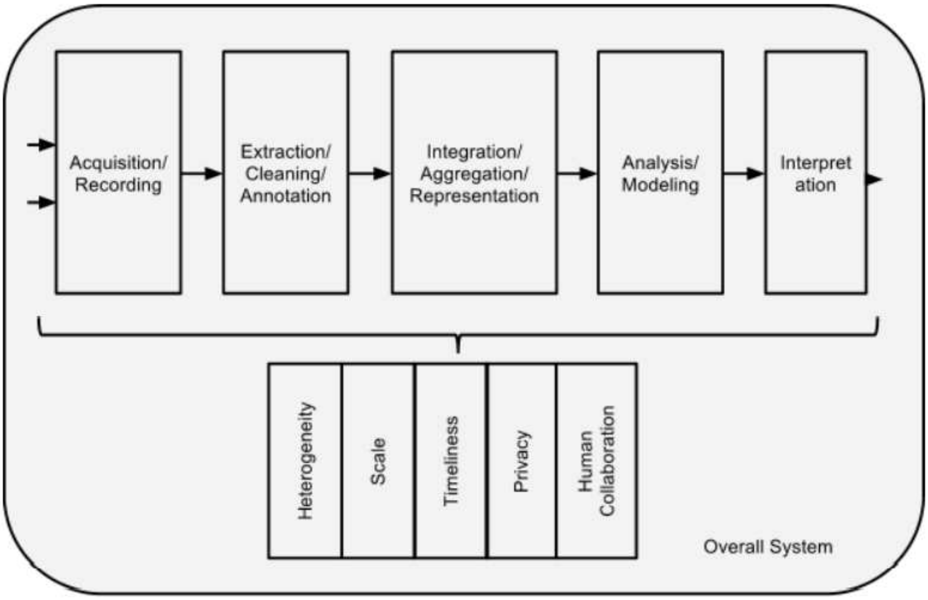

Fig. 6.3 Big Data analysis pipeline [210]

For what concern the acquisition/recording phase, a crucial aspect is that Big Data is recorded from some data-generating source. A lot of this data does not contain useful information and it can be filtered and compressed by orders of magnitude [211]. Therefore a central aspect is to describe which data is recorded, as it is recorded and measured. Recording information about the data is not useful unless this can be used in the other phases of the data analysis pipeline. Indeed, all the phases are connected since an error made in one step can make the results of the following steps anomalous. The second phase of the Big Data analysis pipeline is the extraction/cleaning/annotation phase. The importance of this step is that, usually, the information collected is not in a format ready for analysis. Therefore, an information extraction process is necessary, which is useful to obtain the required quantities and express them in a structured form suitable for analysis [212]. This operation of extraction, cleaning and correct annotation of the data is a particularly critical step, since a mistake in this phase can cause the loss of important data.

For the third phase, it is important to underline that data analysis is considerably more challenging than simply locating, identifying and understanding data. For an accurate analysis, all this has to happen in a completely automated way. This requires that differences in data structure and semantics be expressed in forms that are understandable by the computer, in order to obtain useful information from the data. Therefore, database design is today very important and is carefully executed by professionals since an intelligent database architecture is central to having a clear view of the data [213]. The fourth step is the core of the Big Data analysis pipeline, since it represents the analysis of the information collected previously. As this phase start, the data has to be already integrated, clean, reliable and efficiently accessible, with the aim of implementing various techniques, through the use of appropriate tools, to carry out the necessary studies [214]. The last phase is about the interpretation of the obtained results. The users have to interpret these results and the interpretation involves examining all the assumptions made and retracing the analysis, since there are many possible sources of error. For this reason, the users have to understand and verify the results produced by the computer [215]. Therefore it is possible to state that the result is an end in itself without an appropriate physical-mathematical interpretation of the same.

There are different challenges at all phases of the Big Data analysis pipeline such as heterogeneity, scale, timeliness and privacy [216]. Heterogeneity is the first obstacle given the different nature of the data. Even after data cleaning and error correction, some incompleteness and some errors in data remain and these have to be managed during the data analysis. A big challenge with Big Data is related to managing its size [217]; the use of faster processors has overcome the problem. However, nowadays, there is a fundamental shift underway since data volume is scaling faster than compute resources and CPU speeds are static. Implications of this change potentially touch every aspect of data processing. Connected to the size is the speed. Indeed, the larger the data set to be processed, the longer it will take to analyze. Given a large data set, it is often necessary to find elements in it that meet a specified criterion. In the course of data analysis, this sort of search is likely to occur repeatedly and in most cases, results need to be achieved quickly. Therefore this operation requires a very long time. Considering that in some cases the required times are impracticable, it is necessary to take advantage of appropriate techniques that optimize the times and at the same time provide acceptable results. Another important issue is the privacy with Big Data given that in many cases the acquired data is remarkably sensitive, such as in the case of the motorsport field [218].

6.2.2 Big Data Treatment

The methodologies with which Big Data processing takes place play a remarkably important role. There are several techniques to be able to work with this data, drawn from several disciplines including statistics, computer science and applied mathematics. For example, efficient methods such as cluster analysis, classification, data fusion and integration, genetic algorithms, machine learning and so on are included in the mentioned disciplines. These methods, which are used to identify suitable laws or physical-mathematical models within Big Data, constitute the so-called data mining. Thus, thanks to these techniques it is possible to analyze the data on a large scale in a reasonable time.

Data mining serves a confluence of multiple disciplines, since it is the process of discovering interesting patterns, models and other kinds of knowledge in large data sets [219]; its importance in Big Data analysis is expressed in terms of the computation cost, memory requirement and accuracy of the end results. Clustering is one of the well-known data mining problems, useful to better understand the data [220]. This technique is particularly used in the field of engineering, but it extends to several disciplines of a scientific nature.

There are various types of clustering algorithms and these are classified into hierarchical and partition algorithms. The former are represented through a dendrogram in which each partition is nested within the partition at the next level in order hierarchical, while the latter generates a single data partition, with a specified number of non-overlapping clusters. The most popular clustering algorithm is the k-means algorithm (KMA) [221]. The basic idea of this problem is to separate a set of unlabeled input data into k different groups, hence the name k-means. Differently from clustering, classification relies on a set of labeled input data to construct a set of groups which will then be used to classify the unlabeled input data to the groups to which they belong. These algorithms follow iterative criteria that lead to convergence towards the best result, for example, the criteria of minimal decrease in squared error [222]. To solve the data mining problems that attempt to classify the input data, two of the major goals are cohesion and coupling. The first refers to the principle according to which the distance between each data and the centroid (i.e. the mean) of its cluster should be as small as possible, while the latter refers to the idea that the distance between data that belong to different clusters should be as large as possible [223]. The sum of squared errors (SSE), used as an indicator of the cohesion of data mining results in clustering or classification problems, can be defined as:

$$SSE = \sum_{i=1}^{k} \sum_{j=1}^{n_i} D(x_{ij} - c_i) \tag{6.1}$$

where

- k is the number of clusters;
- n_i is the number of data in the i_{th} cluster;
- x_{ij} is the j_{th} datum in the i_{th} cluster;

- D is the Euclidean distance, which is the most common measure used in data mining problems for the study of the distance between the various points;
- $c_i = \frac{1}{n_i}\sum_{j=1}^{n_i} x_{ij}$ is the mean of the i_{th} cluster;
- $n = \sum_{i=1}^{k} x_{ij}$ is the number of data.

Unlike clustering and classification, which refers to the classification of the input data to k groups, association rules and sequential patterns are focused on relationships between the input data, thanks to the apriori algorithm. However, the great difficulty that is encountered is that of a high computational cost. Therefore it is necessary to use different approaches, such as the application of the genetic algorithm.

A very useful approach of which clustering and classification are part is machine learning. Machine learning algorithms can be used for several mining and analysis problems because they are typically employed as the search algorithm of the required solution. This approach is used for solving two kinds of problems: *supervised learning* and *unsupervised learning*. For what concerns the first one, the supervision in the learning comes from the labeled examples in the training data set and an example of supervised learning is classification. Differently, in the second one, the learning process is unsupervised since the input examples are not class-labeled and an example of unsupervised learning is clustering. The results that can be obtained through machine learning algorithms show that these are an essential part of Big Data analytics. Some problems facing with these are similar to those of the more traditional data mining algorithms. However, one of the solutions is to make them work for parallel computing and this is not very difficult since, fortunately, through machine learning, they can be used for parallel computing.

In this work, the mentioned techniques have been useful in the first phase of data analysis. However, subsequently, the approach changed, moving away from that of a purely statistical nature and moving towards a more basic physical one as it was more suitable for the available data. Among all the different methods, two of these are relevant to the aim of this research activity, the Principal Component Analysis (PCA) and the multiple linear regression.

Principal Components Analysis (PCA)

Multivariate statistics is a mature field with many different methods and many of these are mathematical [224]; it is the simultaneous statistical analysis of a collection of variables, which improves upon separate univariate analyses of each variable by using information about the relationships between the variables. The computations involved in applying most multivariate techniques are considerable and most analyses of multivariate data should involve the construction of appropriate graphs and diagrams. One of the problems with a lot of sets of multivariate data is that there are simply too many variables to make the application of simple techniques successful in providing an informative initial assessment of the data.

Principal Components Analysis (PCA) is a multivariate technique with the central aim of reducing the dimensionality of a multivariate dataset while accounting for as much of the original variation as possible present in the data set. This aim is achieved by transforming to a new set of variables, the principal components, that are linear combinations of the original variables, which are uncorrelated and are ordered so that the first few of them account for most of the variation in all the original variables. The result of a principal components analysis would be the creation of a small number of new variables that can be used as surrogates for the originally large number of variables [225].

The basic goal of principal components analysis is to describe variation in a set of correlated variables, $x^T = (x_1, \ldots, x_q)$, n terms of a new set of uncorrelated variables, $y^T = (y_1, \ldots, y_n)$, each of which is a linear combination of the x variables. The new variables are derived in decreasing order of "importance" in the sense that y_1 accounts for as much as possible of the variation in the original data amongst all linear combinations of x. Then y_2 is chosen to account for as much as possible of the remaining variation, subject to being uncorrelated with y_1, and so on. The new variables defined by this process, $y_1, \ldots, y_n$, are the principal components (Figure 6.4).

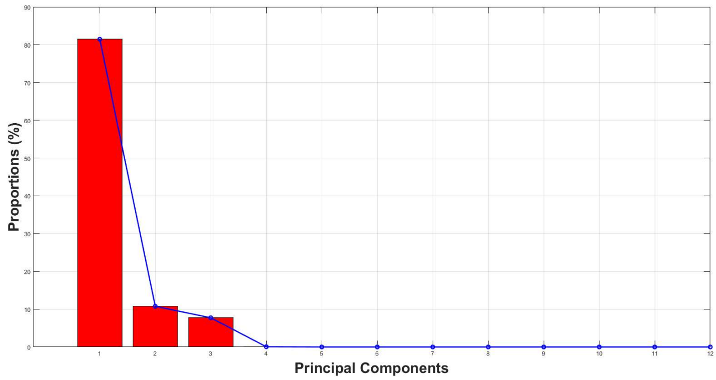

Fig. 6.4 PCA - Principal Components proportions

The general hope of principal components analysis is that the first few components will account for a substantial proportion of the variation in the original variables, $x_1, \ldots, x_q$, and can, consequently, be used to provide a convenient lower-dimensional summary of these variables that might prove useful for a variety of reasons.

The first principal component of the observations is that linear combination of the original variables whose sample variance is greatest amongst all possible such linear combinations. The second principal component is defined as that linear combination of the original variables that accounts for a maximal proportion of the remaining variance subject to being uncorrelated with the first principal component. Subsequent components are defined similarly as in Equation 6.2.

$$y_i = \sum_{j=1}^{q} a_{ij} x_j \tag{6.2}$$

In order to perform a PCA:

- the covariance matrix of the normalized experimental data must be calculated;
- the coefficients a_{ij} the principal components must be calculated as eigenvectors of the covariance matrix;
- evaluate the Principal Components y_i as a linear combination of the eigenvectors with normalized experimental data;
- evaluation of the proportions as follows:

$$Prop_i\% = \frac{\lambda_i}{\sum \lambda} \tag{6.3}$$

where λ_i is the eigenvalue of the correlation matrix.

The PCA made it possible to understand which variables are able to explain the variance of the studied dataset; however, it was preferred to avoid considering the principal components directly in order to not lose contact with the physical evidence represented by the individual variables.

Multiple Linear Regression

Linear Regression is probably one of the most powerful and useful tools available to the applied statistician; this method uses one or more variables to explain the values of another. Statistics alone cannot prove a cause-and-effect relationship but it can show how changes in one set of measurements are associated with changes of the average values in another. This process requires a good understanding of the data and a preliminary study of them as described in previous Chapters. A regression model does not imply a cause-and-effect relationship between the variables. Even though a strong empirical relationship may exist between two or more variables, this cannot be considered evidence that the regressor variables and the response are related in a cause-and-effect manner.

To establish causality, the relationship between the regressors and the response must have a basis outside the sample data, for example, the relationship may be suggested by theoretical considerations. The regression equation is only an approximation to the true functional relationship between the variables of interest. These functional relationships are often based on physical or other engineering or scientific theory, that is, knowledge of the underlying mechanism [226].

A regression model that involves more than one regressor variable is called a multiple regression model. The term "linear" is used because the Equation 6.4 is a linear function of k regressors $\beta_0,\ \beta_1,\ldots\beta_k$ and not because is a linear function of the x's.

$$y=\beta_0+\beta_1 x_1+\beta_2 x_2+\ldots+\beta_k x_k+e \tag{6.4}$$

This model describes a hyperplane in the k - dimensional space of the regressor variables x_j [226]. Models that include interaction effects may also be analyzed by multiple linear regression methods. For example, suppose that the model is:

$$y=\beta_0+\beta_1 x_1+\beta_2 x_2+\beta_{12} x_1\ x_2+e \tag{6.5}$$

If $x_3=x_1\ x_2$ and $\beta_3=\beta_{12}$ then Equation (6.5) can be written as:

$$y=\beta_0+\beta_1 x_1+\beta_2 x_2+\beta_3 x_3+e \tag{6.6}$$

which is a linear regression model.

It is more convenient to deal with multiple regression models if they are expressed in matrix notation. This allows a very compact display of the model, data, and results. y_i is a random variable (response variable) with a distribution that depends on a vector of known explanatory values x_i (predictor or regressor).

$$Y = X\beta + e \tag{6.7}$$

where the independent, normally distributed errors e_i have zero means and constant variances σ^2. Additionally, it usually assumes that the errors are uncorrelated. This means that the value of one error does not depend on the value of any other error.

- Y is a $n \times 1$ vector:

$$\begin{pmatrix} y_1 \\ y_2 \\ \vdots \\ y_n \end{pmatrix}$$

- X is a $n \times (k+1)$ matrix:

$$\begin{bmatrix} 1 & x_{11} & x_{12} & \cdots & x_{1k} \\ 1 & x_{21} & x_{22} & \cdots & x_{2k} \\ 1 & \vdots & \vdots & \ddots & \vdots \\ 1 & x_{n1} & x_{n2} & \cdots & x_{nk} \end{bmatrix}$$

- β is a $(k+1) \times 1$ vector:

$$\begin{pmatrix} \beta_0 \\ \beta_1 \\ \vdots \\ \beta_k \end{pmatrix}$$

- e is a $n \times 1$ vector:

$$\begin{pmatrix} e_1 \\ e_2 \\ \vdots \\ e_n \end{pmatrix}$$

The regression coefficients β are parameters that need to be estimated from the observed data (y_i, x_i). This process is also called fitting the model to the data or "training". Thus regression analysis is an iterative procedure, in which data lead to a model and a fit of the model to the data is produced. The quality of the fit is then investigated, leading either to modification of the model or the fit or to the adoption of the model.

6.3 Wear

Abrasion or wear occurs whenever two bodies slide against each other under friction. Material is transferred from one body to the other and this process can go in both directions. Rubber wear is the result of several different mechanisms that range from rubber oxidation to mechanical delamination. All or part of these mechanisms may be present at the same time thus making it very difficult to build up a predictive and at the same time practical model for rubber wear.

Wear Definition

Rubber wear is a function of a huge variety of external parameters such as the shape of the contacting surfaces, the presence of contaminants between these surfaces, the sliding speed, the normal pressure, the contact temperature, etc. [227].

In particular, it is considered to be the result of energy dissipation due to friction, which can be divided into adhesion and hysteresis. Adhesion occurs when two solid sliding surfaces slide over each other under pressure. Hysteresis occurs during the return to a normal state of a rubber from either compression or expansion [228]. The cause of this is internal friction, since rubber is a viscoelastic material the schematic diagram of friction and wear mechanism shown in Figure 6.5, could be applied also to tires.

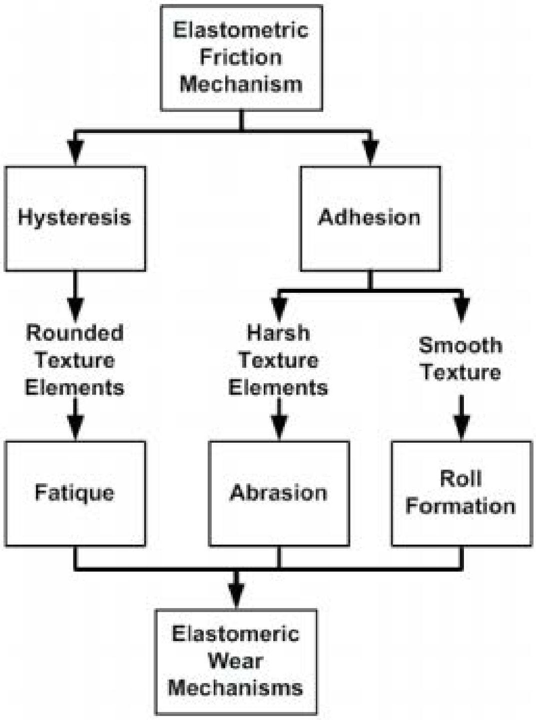

Fig. 6.5 Wear and friction mechanism in tires [228]

Abrasive wear is a product of adhesion and pressure. The result is a temporary bond between the road and the rubber molecules in the tire. The bonds are torn apart due to continuing sliding, which results in abrasive wear. The coarseness of the surfaces affects the amount of contact the surfaces have against each other, smoother surfaces have a larger contact area compared to rough surfaces. On rough surfaces such as asphalt, the roughness might cause local adhesion peaks, due to asperities, resulting in abrasion. Abrasive wear is a function of the texture property, rubber property, vertical load and sliding velocity. The higher the load, the more material will be squeezed between the asperities, increasing the contact area and resulting in stronger bonds and therefore higher abrasive wear. Increasing the sliding velocity tears the bonds apart faster leading to a larger abrasive force which increases the abrasive wear.

Hysteresis wear, instead, originates from the penetration of the asperities into the tire, creating high and low deformation areas, which is illustrated in Figure 6.6. The sliding motion of the rubber creates pressure hysteresis in the tire. This type of wear is relatively mild but it is a continuous process [228].

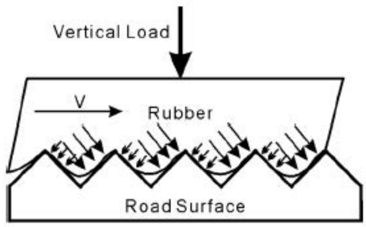

Fig. 6.6 Deformation and forces leading to hysteresis wear [228]

6.3.1 Wear Measurements

The wear data are generally provided in the form of depth detected by reading holes on the tread at the end of each session or run. Since these are different in numbers compared to the conventional division into ribs of the wheel (for each of them several telemetry quantities are acquired) the known values were interpolated. In this way, it was possible to obtain a "virtual" value of the wear at each rib (Figure 6.7). This operation allows obtaining wear values on the "virtual" ribs that can be interpreted as the volumetric loss of material since in this case the spots are equally spaced.

The values thus obtained are then processed in order to obtain an average wear value along the entire length of the tread ($Wear_{Mean}$) and a maximum value corresponding to the maximum wear of the single rib ($Wear_{Max}$). Both of these variables are expressed in percentage terms with respect to the thickness of the tread.

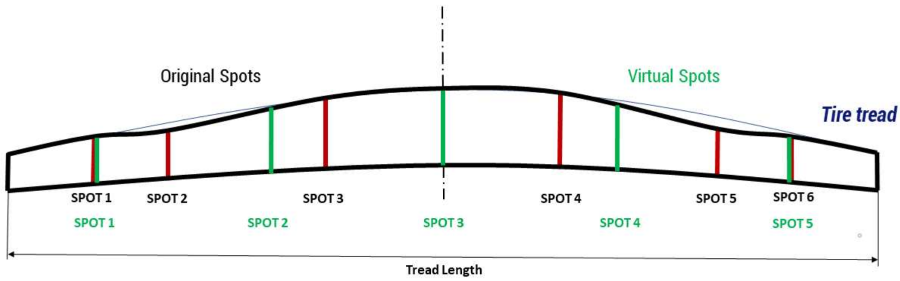

Fig. 6.7 Wear measurements - schematic tread spots

6.3.2 Further Wear Phenomena - Graining and Blistering

One of the most common tire defects seen trackside, the graining, represents itself as a ripple effect in the rubber like many very small tears in the surface of the rubber. It occurs when strips of rubber begin to separate and tear away from each other and then fuse back together due to the heat of the tire. This produces a very uneven surface and damages the integrity of the compound, reducing grip specifically in corners and during braking. It is due to high-frequency stresses to which the tire is subjected when it slips at high speed, therefore with high frequencies, on the roughness of the asphalt. Graining usually occurs when track temperatures are colder than optimum. Blistering, such damage or alteration of the tire occurs in competitions and it is characterized by overheating of the tire tread proximal to the carcass, which leads to the creation of air bubbles inside the tread, which causes it to lift and, in more serious cases, detachment. The phenomena described above are difficult to quantify through KPIs. In the models, therefore, the runs in which the tires show marked signs of irregular wear will be eliminated.

6.4 Grip

Rubber friction is a phenomenon influenced by different variables, often hard and difficult to be measured. In the motorsport field, in particular, the possibil-

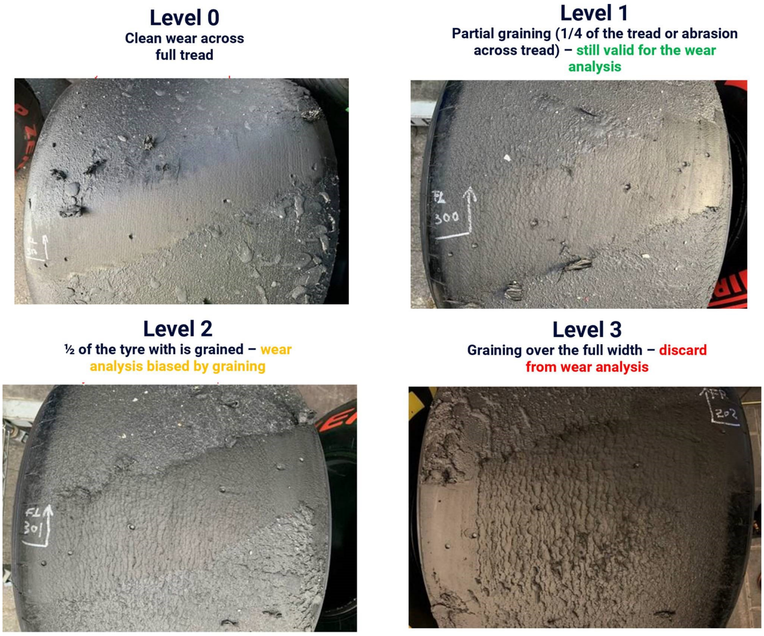

Fig. 6.8 Different levels of graining

ity to maximize the grip, at the different boundary conditions, can represent a key factor to obtain the best performance, for choosing the most suitable compound for each road and weather condition and planning a proper driving strategy, able to make the tires work under the desired conditions. The forces that the tire exchanges with the road are frictional forces and so the theme of friction is a crucial topic in the investigation of all the effects that influence the tire grip performance. Indeed, many theories have been developed in order to better understand the physical phenomena that affect the tire-road interaction [229, 230]. The mechanically effective friction coefficient for rubber materials can result from four main contributions: hysteresis, adhesion, cohesion and hydrodynamic influences. Despite this, however, it is possible to affirm that the cohesion and hydrodynamic contributions can be neglected as they have a much lower impact if compared with the other two. Indeed, by the 1960s, it has been widely accepted that two friction mechanisms develop in the rubber: adhesion (F_a) and bulk deformation hysteresis (F_h) [231]. The first contribution is due to the van der Waals' adhesion of the two surfaces, while the latter one, also called viscoelastic friction, is due to the pulsating deformations the material is exposed to during sliding on the substrate asperities [232]. For what has been said, therefore, it is possible to state that the total friction force is given by the following expression:

$$F = F_a + F_h \tag{6.8}$$

Dividing each component of Equation 6.8 by the vertical load, the corresponding one in terms of friction coefficient is:

$$\mu = \mu_a + \mu_h \tag{6.9}$$

The friction master curve of rubber on a rough track shows, in general, two peaks, as reported in Figure 6.9. One of these occurs at high sliding velocity and it has been mainly attributed to viscoelastic contribution (although at very high speeds the effect of temperature further complicates the study, generally lowering the friction coefficient) and the other one, occurring in general at much lower velocities, is considered attributable to the adhesion.

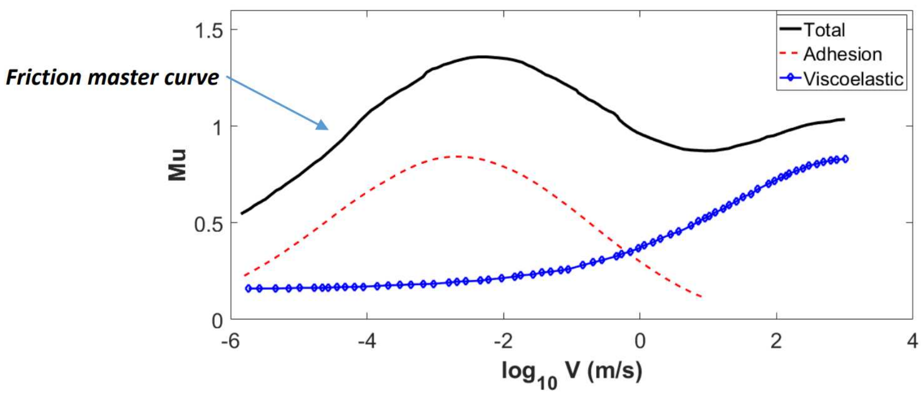

Fig. 6.9 Friction master curve and its contribution [232]

In the world of scientific literature, currently, there are different theories of reference for the analytical evaluation of the two contributions presented in this paragraph [233, 234].

6.4.1 Grip Limited Condition

The overall performance in motorsport is the result of driver-vehicle interaction, which is usually highlighted through the lap time on the track. Given a desired trajectory around a race track, the lap time is minimized by maximizing the average velocity. Two factors limit maximizing the velocity; the first is that the vehicle can be restrained by the power of the engine to accelerate further and this is called power limited, the latter is based on the fact that there is an acceleration limit for the vehicle due to tire-road friction. Track sections where maximizing the velocity would violate this limit are referred to as grip limited conditions[235]. This search for the maximum grip limit that can be explained without losing grip, is one of the main activities that are conducted by the drivers during free practice sessions in order to obtain the best performance from the car.

In particular, the definition of the grip limited zones as areas of interest was useful as it allowed to reduce the size of the collected data. Therefore, a robust definition of this concept made it possible to eliminate data that were not relevant to the overall study of the car's performance and that only affected the volume of the same, making them difficult to handle. This approach also finds a great practical application since, in addition to reducing the amount of data, it is important to study only the conditions for which the car is exhibiting high levels of grip.

Taking up the concept of the adherence ellipse (presented in paragraph 1.2.3, the definition of grip limited lies in identifying all the conditions for which it was possible to establish a narrow region of values close to the border of the ellipse itself. In this way, only the regions relating to high grip values were taken into account, excluding those that were not relevant for the purpose of studying the vehicle performance as they were characterized by low grip values. In addition, for what concerns the study of the grip limited theory, it is important to say that the loss of grip on the lateral side is the most critical case since it is more dangerous to lose grip on the lateral side than in the longitudinal one. For this reason, the study of adherence is of great importance, especially in the analysis of the lateral behavior and the combined one (to understand how the lateral affects the longitudinal). Indeed, during this research activity, less importance is given to the evaluation of the several key performance indicators (KPIs) in pure longitudinal conditions as the lateral behavior represents the most severe operating conditions of the tires.

6.4.2 Grip Limited Zones Identification

The knowledge of the grip values along longitudinal and lateral directions was fundamental in order to identify the grip-limited zones. The study was conducted by analyzing the adherence ellipse of every tire, starting with the identification of the sectors of interest and, subsequently, with the application of specific saturations on some quantities to extract only the significant values. Starting from the adherence ellipse for each tire, the first analysis was based on the division of the same into the following sectors:

- Pure longitudinal sectors;
- Pure lateral sectors;
- Combined interaction sectors.

The presented division was done using the ratio between the lateral force and the longitudinal one:

$$\tan(\theta) = \frac{F_y}{F_x} \tag{6.10}$$

In this way, establishing appropriate θ intervals for the three conditions mentioned, the sectors of interest have been identified. The results obtained with this identification of the sectors are reported in Figures 6.10 and 6.11.

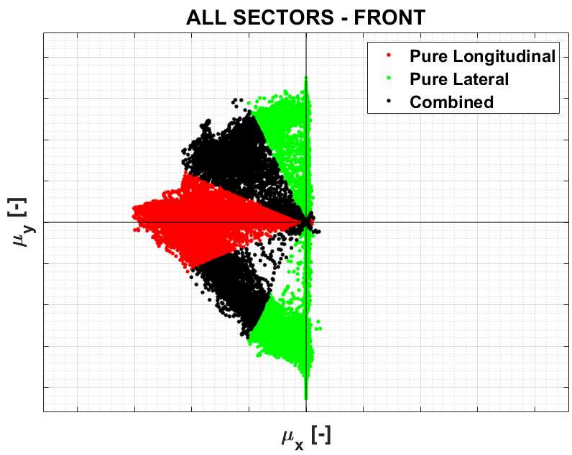

Fig. 6.10 Front adherence ellipse, all sectors

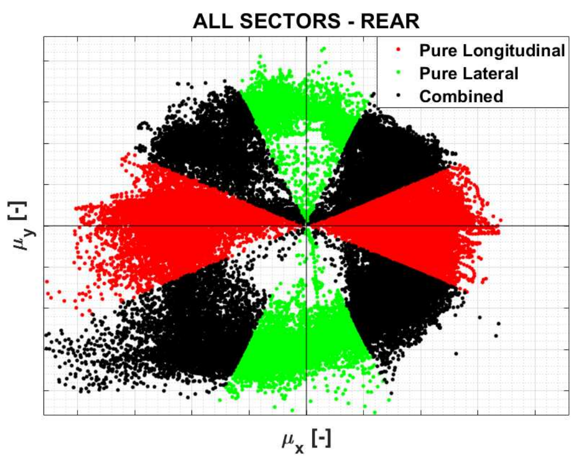

Fig. 6.11 Rear adherence ellipse, all sectors

Once the sectors of interest have been identified, the second phase for the grip limited zones identification involves the application of some thresholds on the following several physical quantities:

- Slip ratio;
- Sideslip angle;
- Longitudinal acceleration;
- Lateral acceleration;
- Longitudinal velocity;
- Vertical load;
- Surface temperature;

In the presented study, for all the sectors, it was imposed:

- Lower and upper limits on surface temperature: to exclude any temperatures that are too low or too high;
- Lower limit on longitudinal velocity: to exclude any samples at low speeds as they are not useful for this application;
- Lower limit on vertical load: this condition serves to neglect acquisitions relating to particular phenomena such as discharge phenomena on the curbs.

In addition to this, for what concerns the pure longitudinal conditions, the other saturations applied were:

- Lower limit on longitudinal acceleration: the pure longitudinal need for high longitudinal acceleration, so a lower limit was imposed since motorsport cars reach very high longitudinal accelerations;

- Lower limit on slip ratio: the pure longitudinal need for a theoretical condition of high slip ratio, so it was maximized as much as possible;
- Upper limit on lateral acceleration: the pure longitudinal need for low lateral acceleration, so an upper limit was imposed since high-performance cars reach very high lateral accelerations;
- Upper limit on sideslip angle: the pure longitudinal need for a theoretical condition of zero slip angle, so it was minimized as much as possible.

Differently from the pure longitudinal, for what concerns the pure lateral, the other saturations were:

- Lower limit on lateral acceleration: the pure lateral need for high lateral acceleration, so a lower limit was imposed since motorsport 1 cars reach very high lateral accelerations;
- Lower and upper limits on sideslip angle: for pure lateral grip limited zone, the interest is on the last zone of the lateral curve, so any slip angles below the lower limit can be neglected. High-performance tires are very stiff so any slip angles greater than the upper limit value represent special conditions that can be neglected for this application;
- Upper limit on longitudinal acceleration: the pure lateral need for low longitudinal acceleration, so an upper limit was imposed since motorsport cars reach very high longitudinal accelerations;
- Upper limit on slip ratio: the pure lateral need for a theoretical condition of zero slip ratio, so it was minimized as much as possible.

Finally, the combined interaction was identified by putting lower and upper limits on all the quantities presented above for the pure interactions in order to exclude any values that are too high or too low. The results obtained with the application of the saturations presented for the various sectors are shown in Figures 6.12 and 6.13.

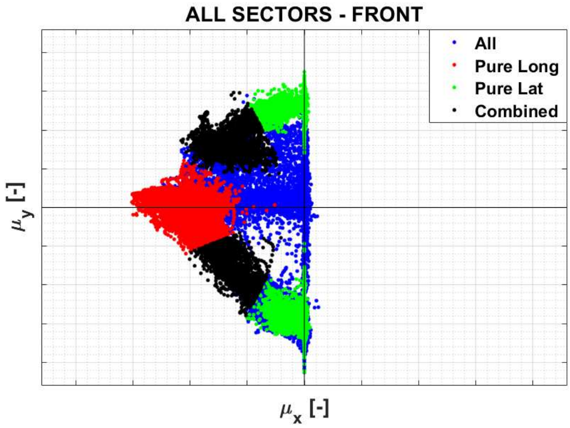

Fig. 6.12 Front adherence ellipse all sectors with saturations

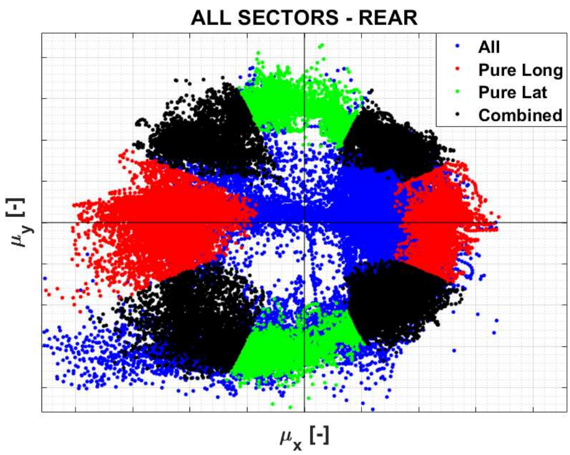

Fig. 6.13 Rear adherence ellipse all sectors with saturations

In addition, as already mentioned in the previous section, most attention was paid to the lateral and combined sectors as they represent the most severe operating conditions of the tires. For this reason, the pure longitudinal was not considered in the extraction of relevant data in this condition and, in this way, it was also possible to reduce the total amount of data. From what has been said, it is clear that the real sectors of interest, used to obtain values of various quantities constituting appropriate reference databases on which various analyses have been made, are only the pure lateral and the combined ones, as shown in Figures 6.14 and 6.15.

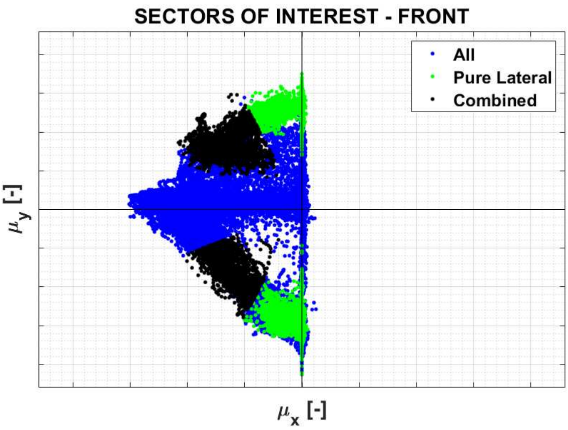

Fig. 6.14 Front adherence ellipse sectors of interest with saturations

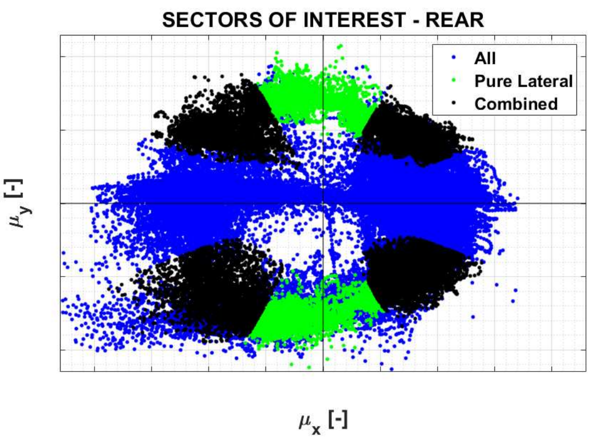

Fig. 6.15 Rear adherence ellipse sectors of interest with saturations

Once the data reduction was completed through the individuation of the grip limited zones procedure and the exclusive consideration of the same, it was possible to build suitable databases with only the information necessary to carry out the analyses of interest on the vehicle performance.

6.5 Database Creation

During this activity, several databases were created in order to collect all the available data in a more manageable structure for performing some specific analysis. The data used for the construction of the datasets comes from the acquisitions made during the real race (R) session (even if in some specific circumstances the data acquired during the other characteristic sessions of the entire race weekend were also found to be useful). For each event, road roughness profiles and vehicle telemetry data were provided and the wear levels of the individual sets of tires used were disclosed. In particular, the reduction of telemetry data, referring only to grip-limited conditions, combined with roughness and viscoelastic data, has made it possible to obtain very large databases, each one containing information relating to some specific approaches, which were used in order to better understand various physical phenomena, also associated with the main problems encountered over the course of the race itself. Indeed, it was decided to process the data in different ways in order to extrapolate some key performance indicators relating to individual laps, some key performance indicators relating to global runs and some key performance indicators relating to a time by time data evolution and collect them in related datasets.

Each dataset was obtained through a specific algorithm which after processing the various data, also organize the same in a rectangular format table, in which the elements of each row correspond to the values of a particular observation and the elements of the columns correspond to the values taken by a specific variable. In addition, each row refers to a single tire of the car and the databases collected the information for all the tires and for both the drivers too (so both the cars). From what has been said, it is clear that the structures obtained in this way can be defined as multivariate databases, whose generic form is shown in Table 6.1.

Table 6.1 Multivariate dataset

Observations	**Variable** 1	**...**	**Variable** q
1	$x_{1,1}$	$\cdots$	$x_{1,q}$
$\vdots$	$\vdots$	$\vdots$	$\vdots$
n	$x_{n,1}$	$\cdots$	$x_{n,q}$

where:

- n is the number of available observations;
- q is the number of variables present in the database;
- $x_{i,j}$ denotes the value of the j_{th} variable for the i_{th} observation.

Considering the different areas of analysis and the information necessary to characterize the single observation, the organization of the columns of the database was modeled in the following way:

- a preliminary section containing a series of general information about the event;
- a section containing the values recorded during the event of several telemetry quantities;
- a section containing the characteristic values of the main roughness indicators;
- a final section containing the information about the main viscoelastic quantities.

Table 6.2 Structure of the databases

Observations	**General Information**	**Telemetry Data**	**Roughness Indicators**	**Viscoelastic Data**
	$Info_1 \ldots Info_h$	$Tel_1 \ldots Tel_m$	$Rough_1 \ldots Rough_l$	$Visco_1 \ldots Visco_p$
1	$[Info_{1,1}] \ldots [Info_{1,h}]$	$[Tel_{1,1}] \ldots [Tel_{1,m}]$	$[Rough_{1,1}] \ldots [Rough_{1,l}]$	$[Visco_{1,1}] \ldots [Visco_{1,p}]$
2	$[Info_{2,1}] \ldots [Info_{2,h}]$	$[Tel_{2,1}] \ldots [Tel_{2,m}]$	$[Rough_{2,1}] \ldots [Rough_{2,l}]$	$[Visco_{2,1}] \ldots [Visco_{2,p}]$
$\ldots$	$\ldots$	$\ldots$	$\ldots$	$\ldots$
n	$[Info_{n,1}] \ldots [Info_{n,h}]$	$[Tel_{n,1}] \ldots [Tel_{n,m}]$	$[Rough_{n,1}] \ldots [Rough_{n,l}]$	$[Visco_{n,1}] \ldots [Visco_{n,p}]$

These databases were extracted for the available data and their general structure is well represented in Table 6.2.

By structuring the databases as presented in Table 6.2, three types of databases have been developed, each one with its characteristics:

- Database by runs, in which each sample is obtained by extracting representative KPIs of the entire run, calculating sums and means of the quantities considered;

- Database by laps, in which each sample is obtained by extracting representative KPIs of the entire lap, calculating sums and means of the quantities considered;

- Database by time, in which each sample correspond to the specific acquisitions sample, considering only acquisitions in grip-limited zones.

6.5.1 General Information

The general information reported in the database provides an overview of the observation under analysis. The information reported in this section of the database is presented in table 6.3.

Table 6.3 General information contained in the database

Name	**Description**
Year	The year of the event considered
Race	The track of the event considered
Driver	The driver who carried out the run/lap in analysis
Compound	The compound used during the run/lap in analysis
Corner	The tire to which the row refers
Laps Number	The number of good laps of the run in analysis
Lap Time	The proper or the average lap time
Run Distance	The number of total kilometers of the run in analysis

For what concerns Laps Number and Run Distance, they are not present in the database by lap and by time; the Lap Time, instead, is evaluated as the average value between the lap times of all the good laps that characterize the run in analysis, whereas it is the lap time of the proper lap considered in the database by lap and it is omitted in the database by time.

6.5.2 Telemetry Data

The second section of the database presents, for each observation, the main telemetry data and several key performance indicators, which were essential to have a global vision of the car's performance for the run analyzed. Furthermore, some of the main quantities were considered only in grip-limited conditions (GLim)), some have been evaluated in a global condition (G) and others in both conditions, whereas the track temperature $T_{Track_{avg}}$ and the external air temperature $T_{Air_{avg}}$ are independent from the vehicle conditions (In). For the database by time all the quantities are evaluated only in grip limited conditions. In the run and lap databases, both mean values and their standard deviations are evaluated, whereas for the database by time only the punctual values are inserted. The table 6.4 summarizes these indicators.

For what concerns the T_{Surf} and T_{Inner} channels, these were obtained as a mean among all the values acquired from the several sensors, in order to have a single reference channel for the mentioned quantities. Similarly, for the CP_{area}, this is evaluated as the mean value among the channels of the contact areas of the various ribs considered for the tire. The Friction Power along the two axes and the total one (FP_x, FP_y and FP_{tot}), the Sliding Distance and are calculated as a cumulative value in the run/lap.

Table 6.4 Telemetry data in the database

Name	Unit of Measure	Conditions
$T_{Track_{avg}}$	$^{\circ}C$	In
$T_{Air_{avg}}$	$^{\circ}C$	In
$T_{Surf_{avg}}$	$^{\circ}C$	GLim and G
$T_{Surf_{std}}$	$^{\circ}C$	GLim and G
$T_{Inner_{avg}}$	$^{\circ}C$	GLim and G
$T_{Inner_{std}}$	$^{\circ}C$	GLim and G
$a_{y_{avg}}$	m/s^2	GLim
$a_{y_{std}}$	m/s^2	GLim
$F_{x_{avg}}$	N	GLim
$F_{x_{std}}$	N	GLim
$F_{y_{avg}}$	N	GLim
$F_{y_{std}}$	N	GLim
$F_{z_{avg}}$	N	GLim
$F_{z_{std}}$	N	GLim
$v_{s_{x_{avg}}}$	m/s	GLim and G
$v_{s_{x_{std}}}$	m/s	GLim and G
$v_{s_{y_{avg}}}$	m/s	GLim and G
$v_{s_{y_{std}}}$	m/s	GLim and G
FP_x	W	G
FP_y	W	G
FP_{tot}	W	G
$Sliding\,Distance$	m	G
$Pressure_{avg}$	Pa	G
$CP_{area_{avg}}$	mm^2	G
γ_{avg}	deg	GLim

6.5.3 Roughness Indicators

The third section of the database by runs presents, for each observation, the road roughness indicators of the track. These values are characteristic of the circuit under analysis and they were evaluated by referring to the experimental data using the procedure described in Chapter 5.

Table 6.5 Roughness indicators in the database

Name	**Unit of Measure**
λ_{Macro}	mm
λ_{micro}	mm
$Hurst\,Coefficient$	$(-)$
Ra_{Macro}	mm
Ra_{micro}	mm
$Peakyness$	mm
$Skewness$	$(-)$
$Kurtosis$	$(-)$
$Index_{Macro}$	$(-)$
$Index_{micro}$	$(-)$

In particular, the roughness profiles were loaded into a specific tool that evaluates a PSD (Power Spectral Density), an HDC (Height Difference Correlation Function) and some parameters related to the profile with the analytical approach. In addition, as pre-processing of the data, a cleaning operation was carried out to eliminate anomalous trends linked to incorrect acquisitions. Once this was done, the roughness indicators are evaluated as the mean value of KPIs of the data extracted from the various acquisitions along the several locations of the track. Therefore, once the circuit under analysis is fixed, the indicators used to describe the road roughness are constant. The quantities that characterize this section of the database are shown in Table 6.5.

6.5.4 Viscoelastic Data

The fourth section of the database presents, for each observation, the main viscoelastic indicators. These are strictly related to the compound used and they are summarized in Table 6.6. In particular, the viscoelastic properties are evaluated in correspondence of the shifted temperature in order to take into account the real operating conditions.

Table 6.6 Viscoelastic data in the database

Name	**Unit of Measure**
f	Hz
T_s	$°C$
$E'(T_s)$	MPa
$\tan(\delta)(T_s)$	$(-)$

Chapter 7

Vehicle Performance Analysis and Optimization

7.1 Introduction

In this final Chapter, the synthesis of the various works carried out is presented, focusing on practical strategies for analyzing and optimizing performance by studying the dependence on the extracted KPIs on the identified target variables.

For what concerns tire wear, starting from the runs database, after a series of preliminary correlations aimed at identifying the most influential parameters of tire degradation, two statistical predictive models of wear are described in detail. For the study of grip, instead, different correlations are analyzed in detail, with the aim of identifying the mutual dependence of the most relevant KPIs and providing useful and practical information about the tire's optimal thermal working range.

7.2 Preliminary Wear Correlations

In order to highlight the most relevant KPIs, deeply linked to the wear phenomenon, several preliminary correlation studies were carried out on the runs database, the only one directly comparable with the wear measurements. A good correlation with sliding phenomena has been identified. The dependence between mean wear and friction power was then analyzed, considering the accumulated energy dissipated in the entire run. Preliminary studies on telemetry data show that the friction power values between the front and rear tires differ significantly; for this reason, correlations have been found separately for the two axles.

Starting from the Mean Wear Percentage vs Total Friction Power plot, an interpolating line has been defined for each circuit (Figure 7.1).

In order to find a robust correlation among wear, friction power, temperature and road indexes the following procedure has been carried out:

1. Two reliability indexes have been identified to obtain further information on the robustness of the wear/friction correlation:

    - R_1 - Obtained normalizing the RMSE among the experimental points on the plot Wear vs FP_{tot} and the linear fitting; it is used to weight fittings with other performance indicators.
    - R_2 - Obtained normalizing the number of consistent experimental points on the plot Wear vs FP_{tot}; it is used to remove circuits with a lower number of acquisitions from the fittings.

2. The slopes and the quadratic coefficients obtained for each circuit were compared with several temperature indicators with the aim to find other correlations.

3. Finally, the residuals between the fitting line and the experimental points obtained from the combination among wear, friction power and

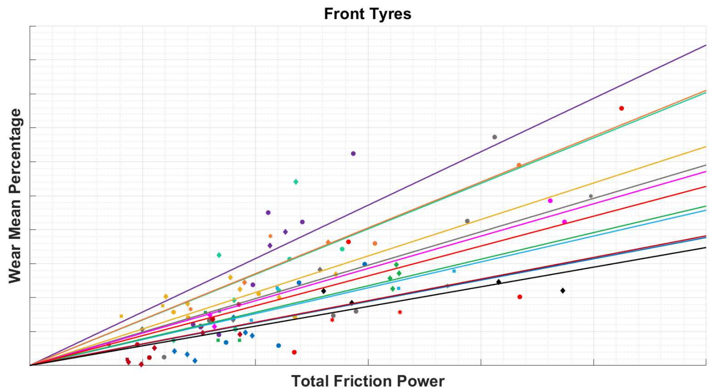

(a) $Wear_{Mean}$ vs FP_{tot} - Front tires

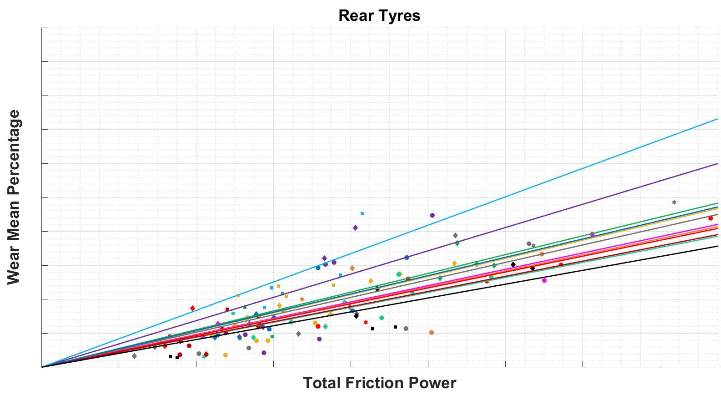

(b) $Wear_{Mean}$ vs FP_{tot} - Rear tires

Fig. 7.1 $Wear_{Mean}$ vs FP_{tot} - Each colour represents a different circuit

temperature were plotted against the road indexes already evaluated for each circuit.

With the circuit line slopes an additional analysis was carried out with the aim to correlate the wear phenomenon and the friction power with road and temperature indicators highlighting a good correlation with tread surface temperatures (Figure 7.2).

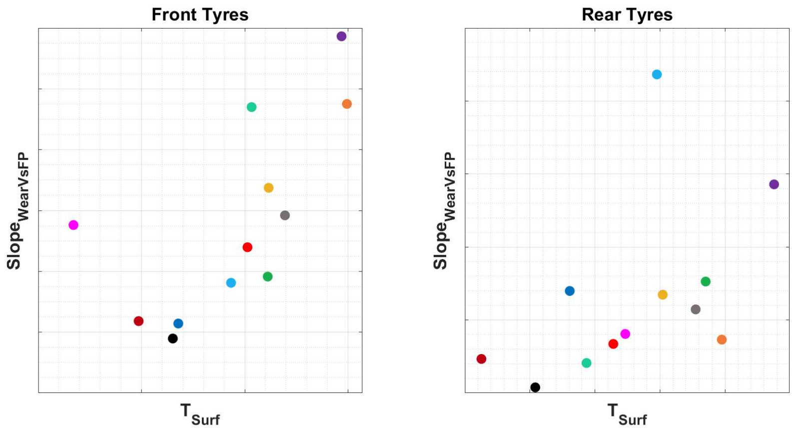

Fig. 7.2 $Wear_{Mean}$-FP_{Tot} slope vs T_{Surf}

It was noticed that residuals show several good correlations with road indexes, but only for rear tires (Figures 7.3 and 7.4). This means that for the front tires, the wear is influenced by further phenomena.

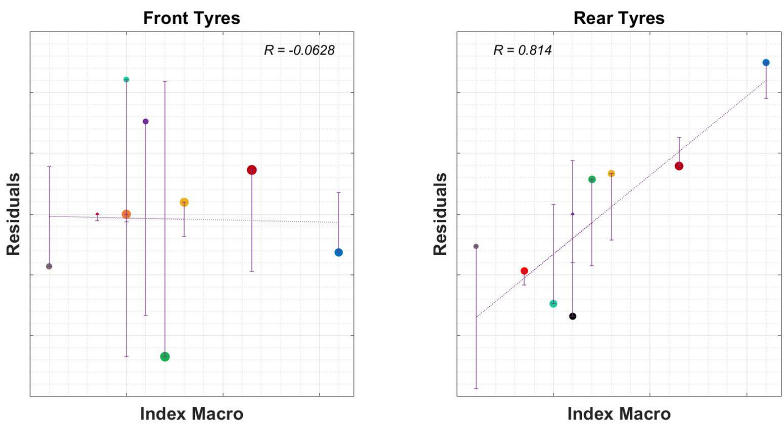

Fig. 7.3 Residuals vs Index Macro

Thanks to the procedure illustrated it was possible to highlight the main phenomena that contribute to the determination of wear energy generated

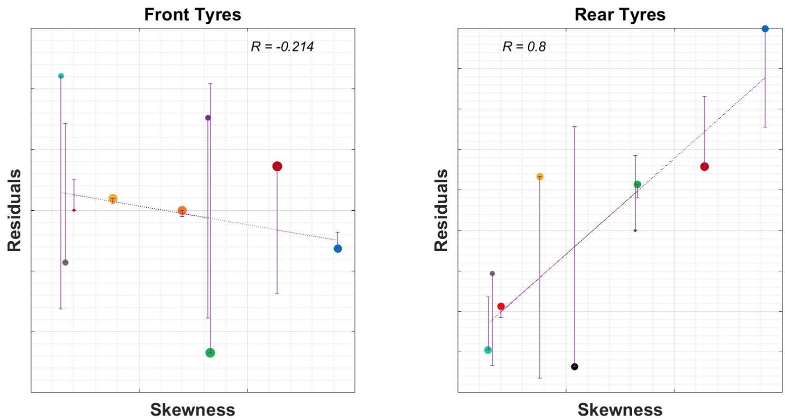

Fig. 7.4 Residuals vs Skewness

due to friction, thermal phenomena linked to the surface temperature of the tires and the influence of the road parameters characteristic of each circuit. These phenomena are well correlated with each other as regards the rear tires whereas for what concerns the front tires, the correlations with the road indexes are not yet robust, probably because of secondary wear phenomena such as graining or blistering.

7.3 Wear Statistical Models

After these preliminary analyses, wear predictive models have been developed. In general, the first phase coincides with the training of the model which corresponds to the identification of the coefficients b_j which guarantee the best fit of the input data. The part of the dataset that is used here represents a portion of the entire available dataset and is suitably selected to avoid any overfitting phenomena. The quality of the model obtained is evaluated using the goodness of fit indicators.

There is no assurance that the equation that provides the best fit to existing data will be a successful predictor. Furthermore, the correlative structure between the regressors may differ in the model-building and prediction data. This may result in poor predictive performance for the model. Proper validation of a model developed to predict new observations should involve testing the model in that environment before it is released to the user. Then a good validation of a regression model should include a study of the coefficients to determine if their signs and magnitudes are reasonable. This phase requires that the model's prediction performance be investigated. Both interpolation and extrapolation modes should be considered. Three types of procedures are useful for validating a regression model [226]:

1. Analysis of the model coefficients and predicted values including comparisons with prior experience, physical theory, and other analytical models or simulation results.

2. Collection of new (or fresh) data with which to investigate the model's predictive performance.

3. Data splitting, that is, setting aside some of the original data and using these observations to investigate the model's predictive performance.

The final intended use of the model often indicates the appropriate validation methodology. Thus, validation of a model intended for use as a predictive equation should concentrate on determining the model's prediction accuracy.

The most effective method of validating a regression model with respect to its prediction performance is to collect data as the complementary part of the one used in the training and directly compare the model predictions against them. If the model gives accurate predictions of new data, the user will have greater confidence in both the model and the model-building process. Sometimes these new observations are called confirmation runs. A large number of observations is desirable to give a reliable assessment of the model's prediction performance.

In order to define the input variables for the wear statistical models, first of all, a correlation matrix was assessed between all the performance indicators and the target ($Wear_{Mean}$). The wear phenomenon is not directly related to a single variable. For this reason, the preliminary analysis carried out so far has been fundamental to identify the relevant input variables that are not directly correlated. The dataset was divided into two parts to obtain a portion usable for the training phase and the rest for validation. The implemented routine guarantees a random selection of the observations while preserving the proportion between the different circuits and it will be used for the generation of all the datasets of the following models. This allows you to have a training dataset that explores all possible operating conditions. In this way, for the validation of the statistical models, an approach of type 2 is adopted whereas to assess the prediction performance of the models on unseen data the procedure of type 3 has been followed.

The entire run dataset was split into two parts:

1. Front tires - Run Database;
2. Rear tires - Run Database;

It was noticed that front and rear tires present different levels of friction powers and, in addition, the rear wear data were more robust and reliable. A smaller amount of starting input variables was selected based on previous analysis. In particular, six input variables were selected trying to take into account all the different areas of investigation (telemetry, road roughness and viscoelasticity), as shown in Table 7.1.

7.3.1 Statistical Wear Model - Front Tires

The front tires dataset presents some issues:

- smaller amount of samples due to non-functioning telemetry sensor;
- higher distribution of the mean wear percentage values;
- some samples are affected by graining.

Table 7.1 6 Input - Wear Model

Input Variable		**Unit of measure**
$Skewness$		$(-)$
$Kurtosis$		$(-)$
$T_{Surf_{Avg}}$		$^{\circ}C$
FP_{TOT}		W
CP_{Area}		mm^2
$tan(\delta)(T^*)$	$Loss\ Factor(Shifted)$	$(-)$

The results obtained starting from the front tire data are shown in Figure 7.5 in which the comparison between the experimental wear acquisitions, labelled as Acquired Wear, and the model outputs, indicated as Training, is shown. There is a drastic reduction in the number of observations due to the subdivision of the dataset which inevitably limits training performance. However, the subdivision made it possible to understand in which portion of the dataset phenomena that alter the modeling of degradation were most manifested.

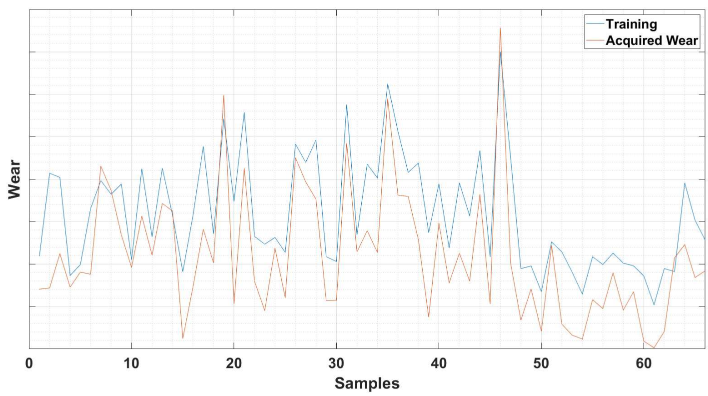

Fig. 7.5 Front tires wear model - Training

The model, albeit with many uncertainties especially in correspondence with the high wear values, proves to be capable of predicting unseen data

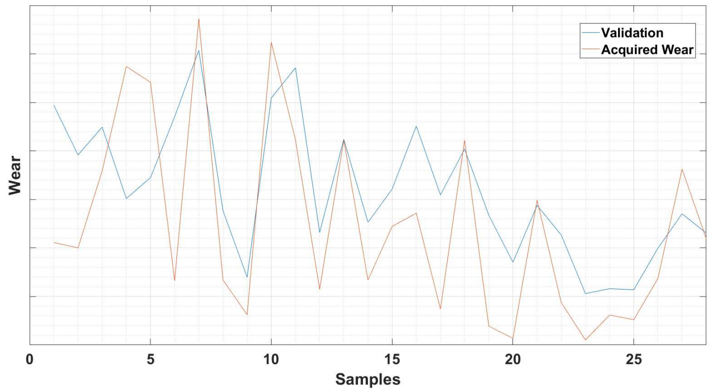

Fig. 7.6 Front tires wear model - Validation

with acceptable RMSE (Figures 7.6 and 7.7). However, the predictive performances appear to be extremely influenced by the presence of corollary phenomena (such as graining) and the other criticalities described, which in some cases lower the quality of the model.

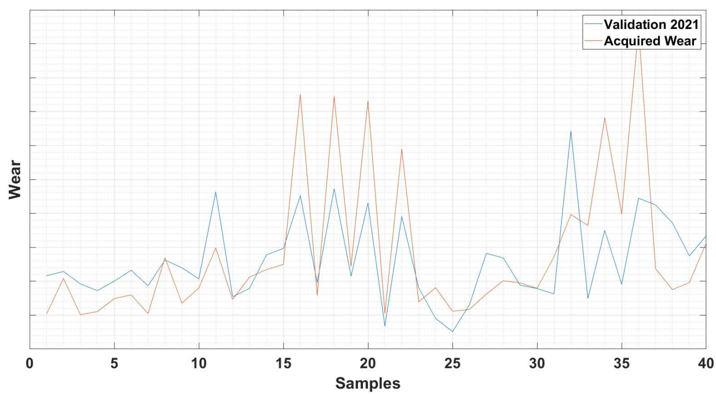

Fig. 7.7 Front tires wear model - Validation on further data

Table 7.2 Front tires wear model - statistics

Phase	RMSE	R^2	R^2_{Adj}
TRAINING	7.5	0.778	0.752
VALIDATION	15.398	0.353	0.206
VALIDATION ON FURTHER DATA	15.96	0.429	0.345

7.3.2 Statistical Wear Model - Rear Tires

The improved reliability of the data relating to the rear wheels allowed to build a larger dataset than that of the front wheels which results in a higher number of observations. The training phase, therefore, appears more capable of fitting the experimental data and making the model robust. The scarce presence of unexpected phenomena also allowed obtaining better results in the subsequent validation phases compared to the previous model.

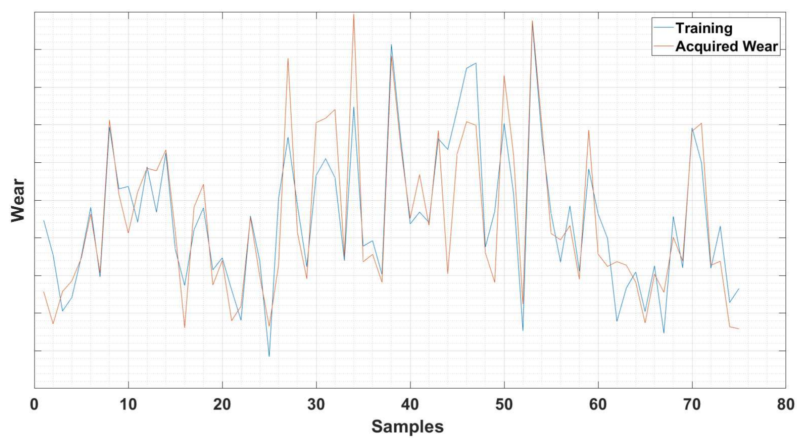

Fig. 7.8 Rear tires wear model - Training

The rear tire Wear Model proposed, as it is possible to see from the shown plots and from the *RMSE* values reported in Table 7.3, presents very reduced errors, with validation on further data (unknown to the model) comparable

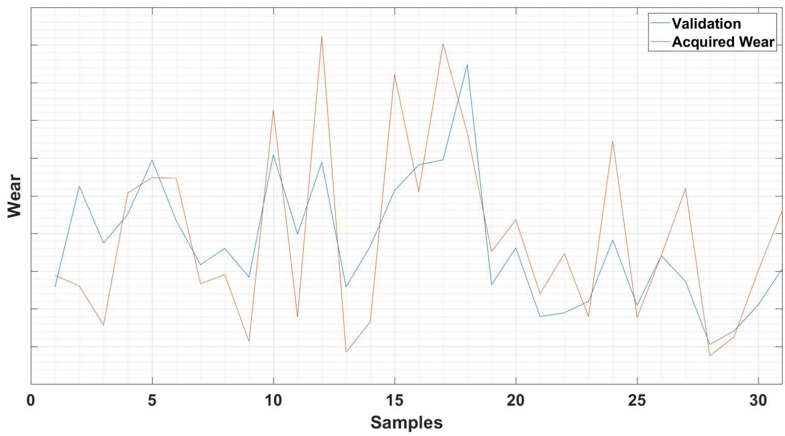

Fig. 7.9 Rear tires wear model - Validation

to the validation on the starting data. These results confirm that the chosen inputs are able to represent the complexity of the wear phenomenon.

Table 7.3 Rear tires wear model - statistics

Phase	RMSE	R^2	R^2_{Adj}
TRAINING	4.84	0.807	0.787
VALIDATION	8.2955	0.5148	0.4178
VALIDATION ON FURTHER DATA	9.014	0.235	0.135

To summarize, starting from the preliminary correlative analysis, it has been possible to identify the main KPIs that can be used as inputs for a predictive model of wear on a statistical basis. The need to use the by-run database as input led to a limited number of observations which made the training process more complicated to adapt the model to the different possible combinations of conditions. Furthermore, the strategy of dividing the data between the front and rear wheels made it possible to identify the effects of disturbance phenomena not contemplated in the model. Nevertheless, results in wear prediction are reliable in almost all the operating conditions, but the

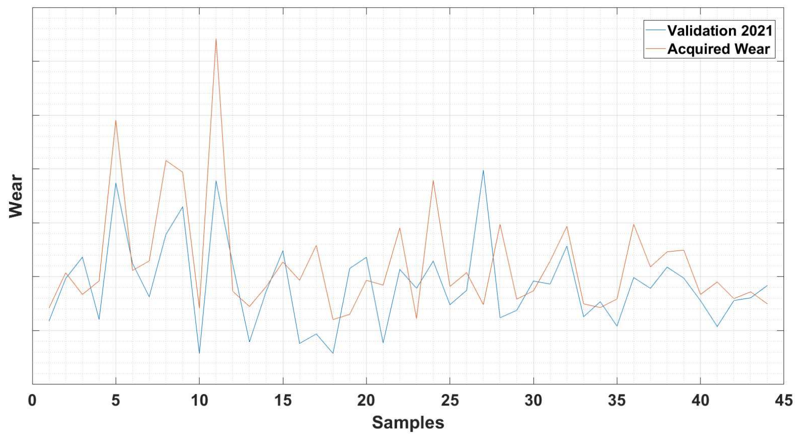

Fig. 7.10 Rear tires wear model - Validation on further data

linearity hypothesis constitutes a limit for the model, since the dependence among wear and surface temperature or other variables is certainly more complex from a physical point of view, but in the model operating range (not explicitly mentioned, for confidentiality reason) it does not seem to cause large inaccuracies of the latter.

7.4 Grip-Temperature Dependence

The tire-road friction coefficient is highly influenced by working temperature, showing a dependence commonly described by a bell-shaped curve [181]. In racing and sports tires, this trend is particularly evident and depending on the employed tread compound the curves are characterized by different peaks and respective temperature values.

Motorsport tires are generally characterized by an optimal thermal working range. Indeed, in order to best exploit the potential offered by the car, while maintaining low wear levels, drivers must constantly try to keep within the optimal window for tire temperatures. In particular, low working range compounds (LWR), often called soft, offer their optimal performance at lower temperatures if compared with the high working range ones (HWR), commonly defined as hard and, maximizing hysteretic and adhesive grip components thanks to their lower dynamic modulus, are able to reach higher friction level. The grip-temperature relationship is shown in Figure 7.11.

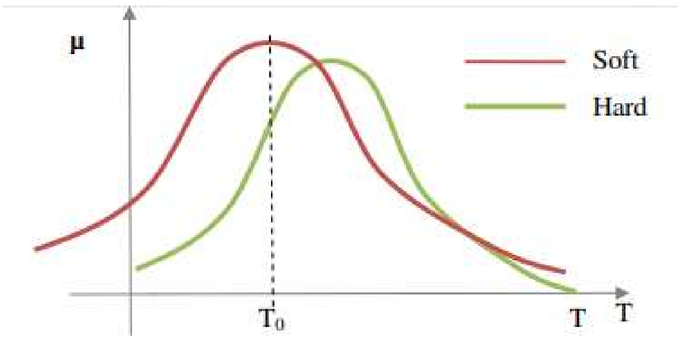

Fig. 7.11 Grip - temperature trend for LWR (soft) and HWR (hard) compounds

Commonly the analysis concerning the tire friction coefficient and temperature are based on the thermal data experimentally available [181]. In this activity, the temperature used to look for the relationship between this and the grip was the surface temperature (previously a percentage combination of the surface temperature and that of the inner liner was considered but this proved to be decidedly ineffective for identifying the already mentioned relationship).

7.4.1 Enveloping Parabolas

In order to better understand the grip-temperature relationship an analysis of the friction variation with respect to the surface temperature has been carried out. This analysis had the aim of characterizing the compound from a performance point of view, in order to understand how to make it work better and it allowed to highlight differences between different compounds. In this way, it was possible to choose the right compound according to the requirements and external conditions. The methods used to find the grip-temperature relationship are based on the evaluation of an enveloping parabola for each compound and for each axle and it was applied to the races data. The starting point of these methodologies was to consider the pure lateral condition for the grip, in order to find the relationship mentioned between the pure lateral grip and the surface temperature. These analyses were carried out by maintaining a time-by-time approach.

Derivative Method

Once the pure lateral conditions have been identified and the grip value plotted with respect to the surface temperature for all the available data, the first method used was based on the division of the reference temperatures into several intervals of fixed and equal amplitude and, subsequently, each temperature column was divided into fixed grip ranges equal to each other. In this way, several reference areas were obtained. An example of the identification of a reference area for one compound and one axle is shown in Figure 7.12, in which every color refers to a specific track. In the reported figure it is possible to observe the red box, which is an example of a reference area for a specific temperature column in relation to a characteristic grip interval.

Subsequently, the number of points acquired within the considered area was assessed. In this way it was possible to obtain three reference values for each area:

- average range temperature;
- average range grip;
- number of points acquired within the range.

. In particular, through the knowledge of these three quantities, it was possible to obtain a series of Gaussian fitted curves for each temperature column. Each Gaussian refers to a specific temperature range (highlighted by the color) and shows the trend of the number of points acquired as the grip value increases. These curves represent the starting point for the construction of

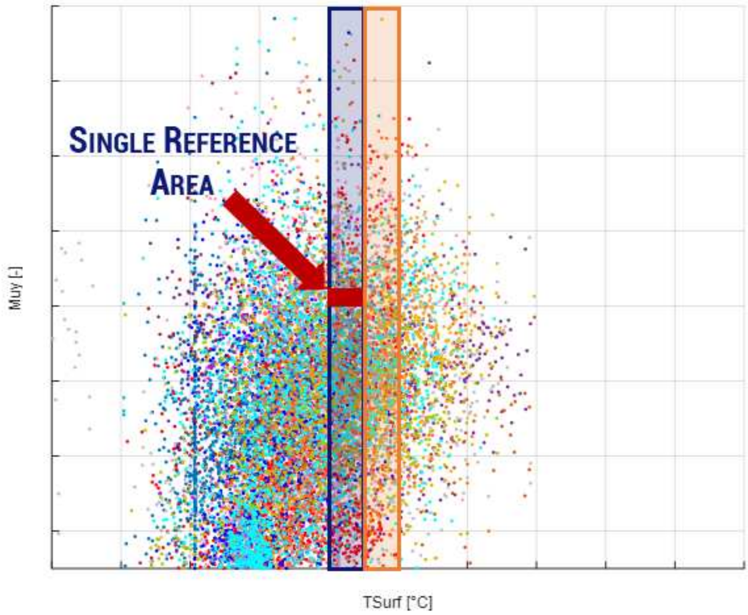

Fig. 7.12 Reference areas evaluation

the enveloping parabolas. The Gaussian curves obtained, in relation to Figure 7.12, are reported in Figure 7.13.

Thus, having obtained the various Gaussians, two kinds of approaches related to the derivative method were developed. The first one was based on the identification of a global point density threshold in order to evaluate robust grip values for each reference temperature interval (reference values were taken on the descending stretches of Gaussian to identify area high grip zones since there is a low point density). From this analysis, it has been possible to observe that not all the Gaussians exceed the threshold value in ordinate, as the latter identifies temperature intervals for which there are not enough acquired points. The representation of the envelope parabola with the fitting points and the acquired data is shown in Figure 7.14.

As shown in Figure 7.14, the parabola thus evaluated has a too-pronounced curvature, highlighting a too-high decrease in grip, especially at low surface

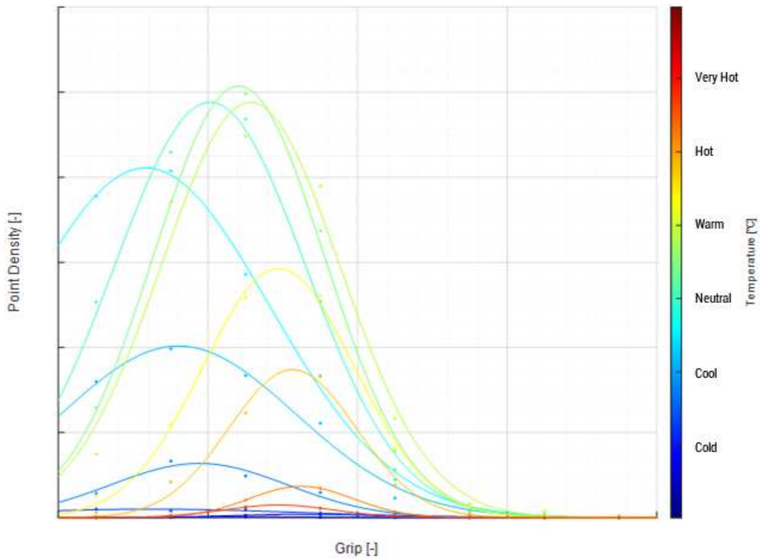

Fig. 7.13 Gaussian curves

temperatures. Therefore, with the intention of solving this problem, improving the trend of the enveloping parabola, a more structured approach was attempted in order to identify a more robust envelope.

The second approach adopted is conceptually similar to the first. The main difference lies in the identification of the threshold for the Gaussians. Indeed, in this case, the derivative was evaluated for each Gaussian and a threshold was set for each curve at the minimum point of the derivative. In this way, the identified threshold point density value strictly depends on the distribution of the points acquired for the single reference temperature range. The representation of what has been said is shown in the following figure:

Once the various points of intersection have been obtained, also in this case the enveloping parabola has been evaluated. The latter is shown in figure 7.16.

Thanks to this second approach, it was possible to evaluate a more robust and realistic envelope parabola, with a coherent global trend. Indeed, as

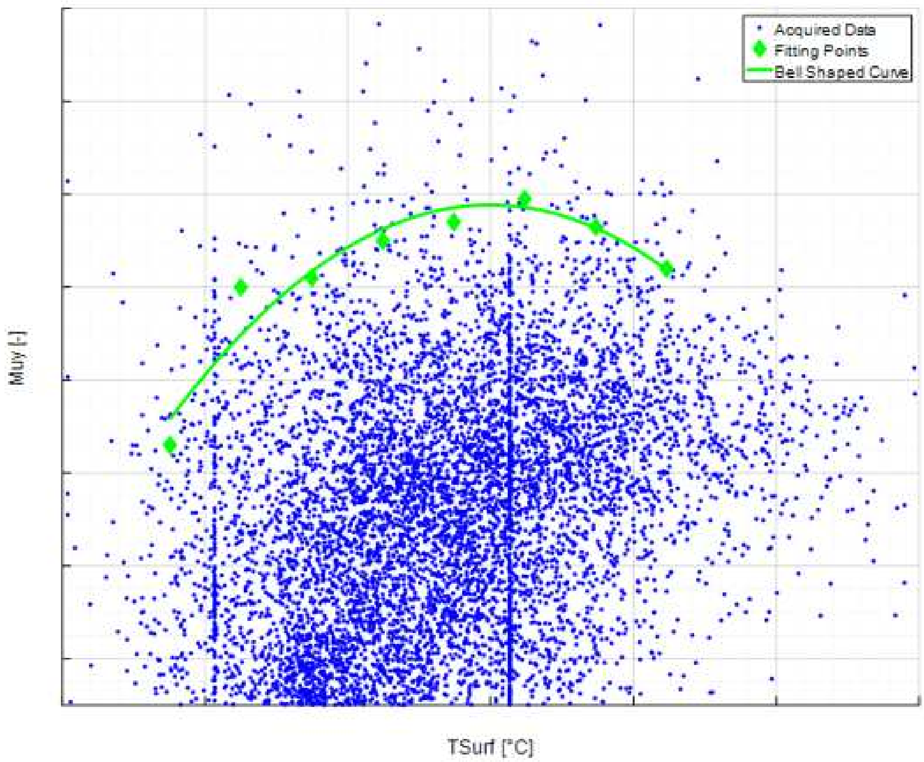

Fig. 7.14 Enveloping parabola: first approach

can be observed, the shape of the enveloping parabola is decidedly more robust and therefore this second approach was considered more valid if compared with the first one. Therefore, thanks to the method introduced for the identification of the grip-temperature bell-shaped curve, it was possible to obtain the maximum grip relative to the single compound and the single axle and the surface temperature at which this is reached. Furthermore, this methodology has made it possible to identify the optimal thermal windows in which the specific compound for the axle in question works. In particular, the optimal working windows in terms of temperature were obtained by

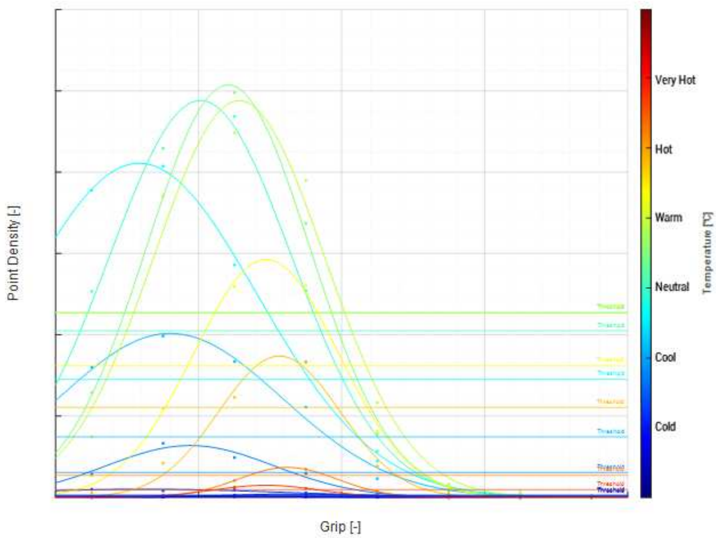

Fig. 7.15 Gaussian curves with each threshold

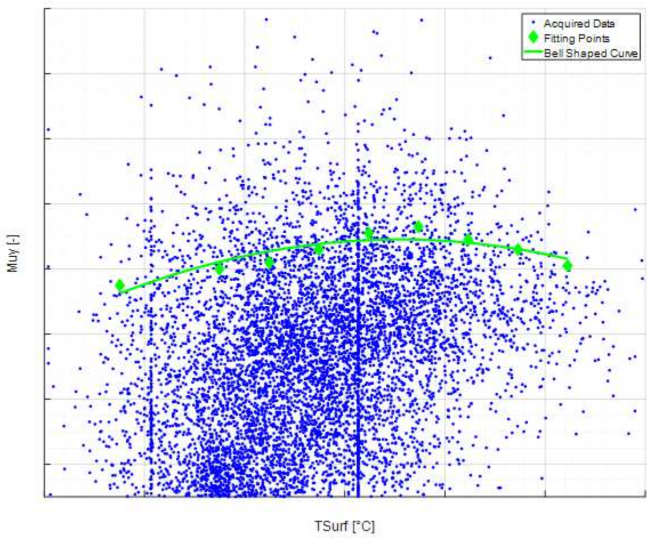

Fig. 7.16 Enveloping parabola: second approach

applying a tolerance with respect to the maximum grip of a few percentage points. This methodology has also made it possible to compare the various compounds in order to better understand the relationship among the same. An example of two parabolas obtained with this second approach for two different compounds (considering the same axle) is shown in Figure 7.17, in which each color indicates a compound.

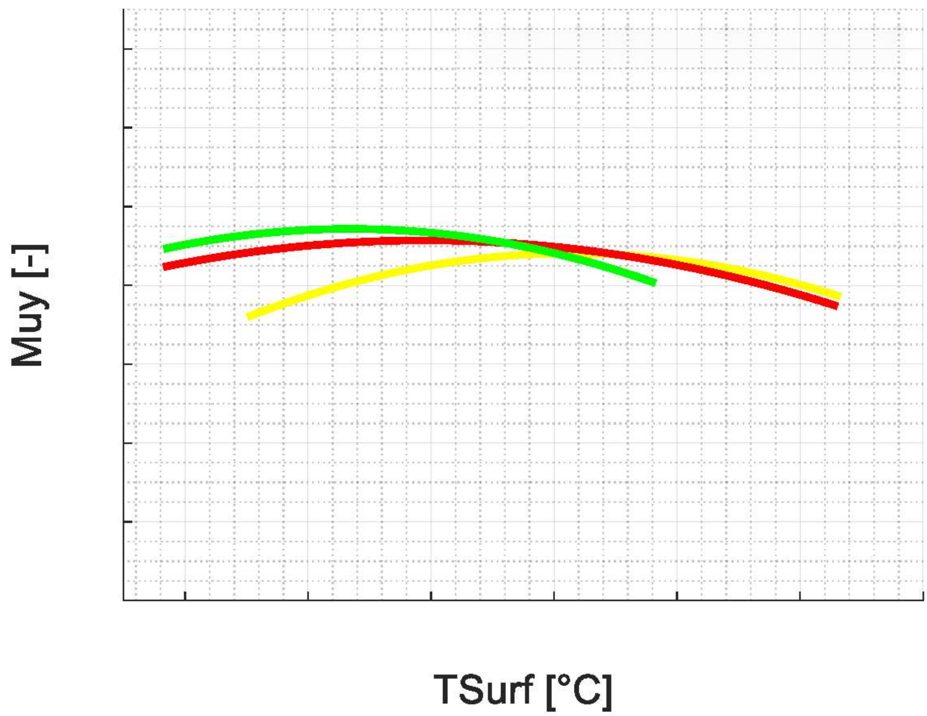

Fig. 7.17 Enveloping parabolas: compounds comparison

From Figure 7.17, it is possible to observe how the compound related to the green curve shows a great grip immediately, but its performance drops very quickly as the temperature rises. Hence, it has the narrowest working range. Furthermore, this compound has a higher grip than the compound related to the red curve and the latter has a greater grip than the compound related to the yellow curve. Finally from this figure, it is possible to observe that the compound related to the red curve is the most stable from a performance point of view with respect to surface temperature.

The presented methodology, although robust and effective for the description of the grip-temperature dependence, requires a sufficiently large number of points and a fairly extended temperature range. Indeed, the starting points, from which the reference areas are identified, are related to all the tracks (as shown in Figure 7.12). Therefore this methodology cannot be extended to an analysis relating to single circuits. Having fewer data for a single track, it was decided to design a new method to be used in order to obtain a reliable result and also for the identification of the parabolas for the single circuit.

k-Means Clustering Method

The second method was developed with the intention of obtaining the enveloping parabolas for the single circuits (which is not possible with the derivative method given the small amount of data for the single tracks). This method involves the use of k-means, which is a distance-based algorithm that divides a dataset into K distinct and non-overlapping groups by minimizing the sum of the Euclidean quadratic distances between the observations and the centroid of the group. The use of k-means clustering served to identify the points with the highest grip and a subsequent division of these points into temperature ranges. The problem with this algorithm is that the initial conditions are chosen randomly and this causes it to return a local optimum. To bring this local optimum as close as possible to the ideal global one, it was important to repeat the algorithm several times, changing the initial conditions each time. For each iteration, the within-cluster sums of point-to-centroid distances were calculated. Finally, the solution with the lowest within-cluster sums of point-to-centroid distances was taken. By using a large number of repetitions, it was possible to get very close to the global optimum point, so as to minimize the effect linked to the randomness of the initial conditions.

Another issue to consider with this type of clustering was related to the fact that the number of clusters was chosen in advance by the user. For this reason, in order to reduce the user influence to validate the goodness of the choice, it was used the silhouette method. The silhouette value for each point is a measure of how similar that point is to other points in the same cluster, compared to points in other clusters. The silhouette values range from -1 to 1: a high silhouette value indicates that the point is well-matched to its own cluster and poorly matched to other clusters. If many points have a low or negative silhouette value, then the clustering solution might have too many or too few clusters. An example of a clustering quality check with the silhouette method is shown in Figure 7.18. As regards the choice of the variables on which to base the division into clusters, since the target is to identify the points with the highest grip, the absolute value of the ratio between the lateral and vertical force and the absolute value of the slip angle has been chosen. As already mentioned, these two quantities were considered in conditions of pure lateral dynamics.

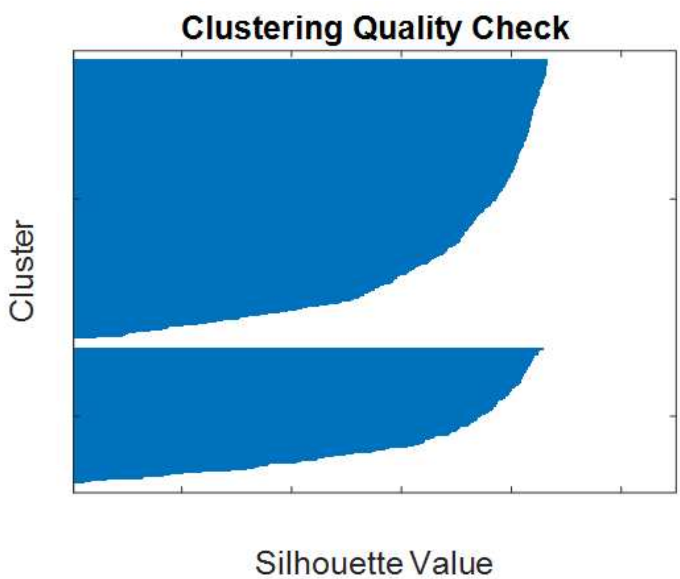

Fig. 7.18 Clustering quality check: silhouette method

In Figure 7.19, it is possible to clearly see how the two clusters were well divided and how no points were excluded.

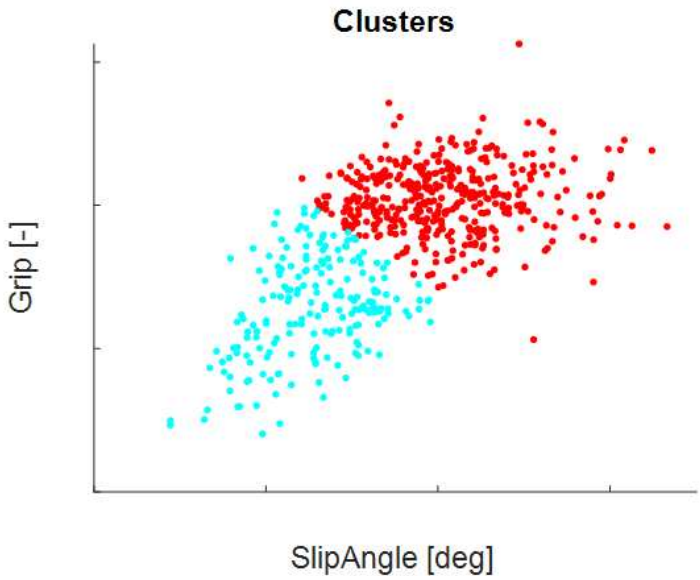

Fig. 7.19 Number of clusters

After determining the clusters, the new method takes the one with the highest medium grip. Subsequently, the points of this cluster were then divided into temperature columns (similar to as presented for the derivative method). Within each of these columns, a low percentage of the points with the highest grip were extracted, so as to reduce the effect of anomalies (considering the maximum it could happen to consider grip values related to not very robust conditions) and the average grip value of the points extracted was calculated. Furthermore, the number of points present within each column was also calculated so as to avoid taking into account non-robust situations. In this way, the grip-temperature pairs were obtained. These pairs allowed the identification of the grip-temperature parabola by means of a fitting. An example of an envelope parabola obtained using this method for one track, fixing both the axle and the compound, is shown in figure 7.20.

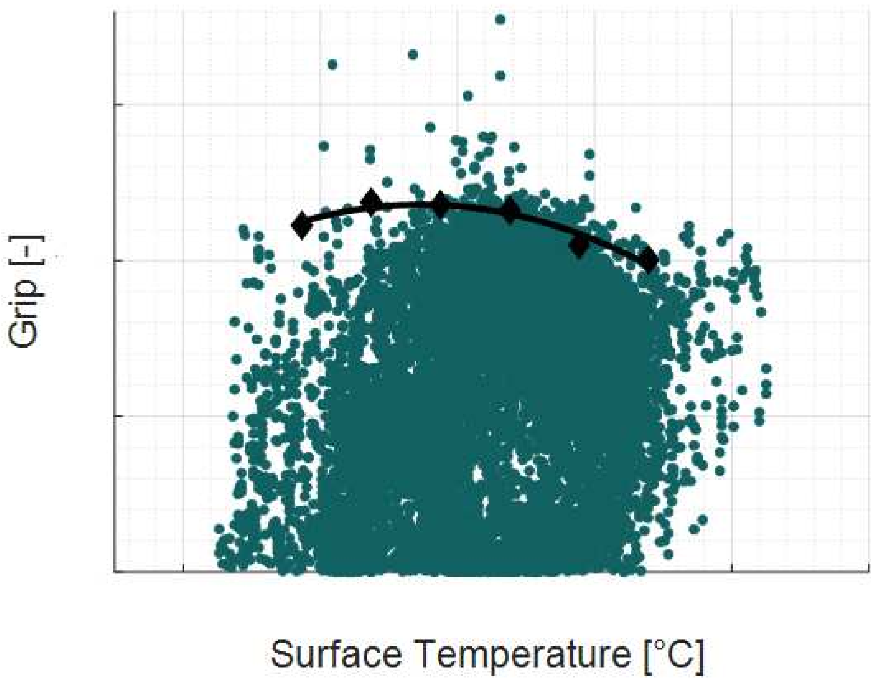

Fig. 7.20 Enveloping parabola: k-means clustering

With this method it was possible to compare the parabolas obtained for the two axles, fixing both the track and the compound or to compare the parabolas obtained for more compounds, fixing both the track and the axles or to compare the parabolas obtained for more tracks, fixing both the axles and the compounds. The k-means method has also been applied in order to have the indicative parabola of several tracks at the same time in order to make other kinds of comparisons. In particular, once this method was developed, it was also possible to compare the characteristic parabolas of the single track with that characteristic one of the data on all circuits, fixing the axle and the compound. An example of a comparison of this type is shown in figure 7.21, in which the pink parabola is of the single track and the black is the one obtained on all the tracks.

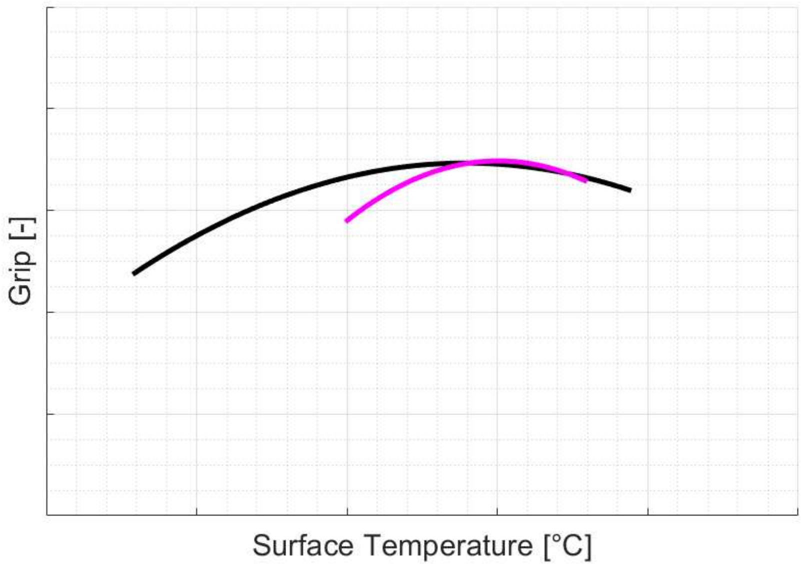

Fig. 7.21 k-means enveloping parabolas: comparison between one track and the other ones

The comparison of the grip parabolas obtained for the different track shows how different maximum grip levels are reached, in correspondence with different thermal ranges, generally below the parabola of the single compound obtained with the derivative method. To explain these differences it is necessary to use the other data available, in order to highlight further dependencies.

7.5 Grip-Roughness-Viscoelasticity Correlations

Thanks to the innovative procedure for calculating λ shown in paragraph 5.5.4, it was possible to calculate robust λ_{Macro} and λ_{micro} values for different circuits. Referring to Figures 7.22 and 7.23, it is possible to state that there is no direct correlation between the macro and micro scales; indeed, comparing the different circuit values, they a completely different behavior: high levels of λ_{Macro} corresponds to lower values of λ_{micro} and vice-versa. For this reason, the combined use of these two KPIs could provide interesting suggestions for defining the effect of roughness on the maximum grip.

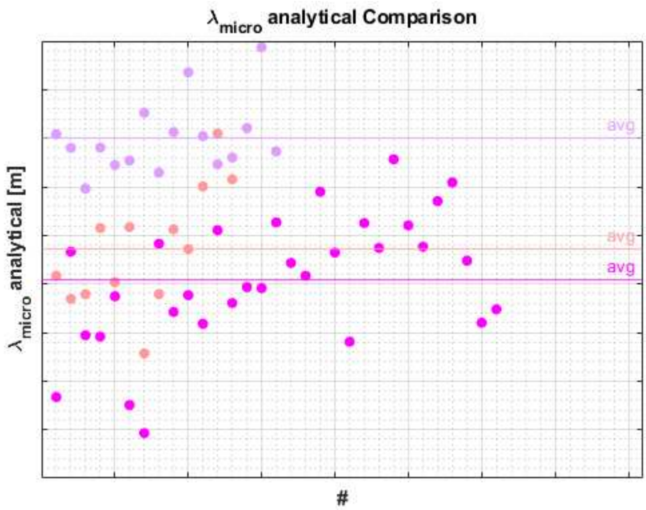

Fig. 7.22 Analytical λ_{micro} estimation

Starting from these considerations, a correlation was sought between these parameters and the maximum grip, obtained as the average value between the different values per circuit present in the database by time. In particular, the dependence can be synthesized as in Equation 7.1:

$$\mu = k_1 \lambda_{micro} + k_1 \lambda_{Macro} + k_3 \tag{7.1}$$

The estimate of the average grip values on the individual circuits obtained through the linear regression just presented, shows excellent results (Figure 7.24), explaining the reason for the different maximum grip levels obtainable for the various circuits analyzed.

Finally, once the dependencies with temperature and roughness have been highlighted, to complete the performance analysis it is also necessary to

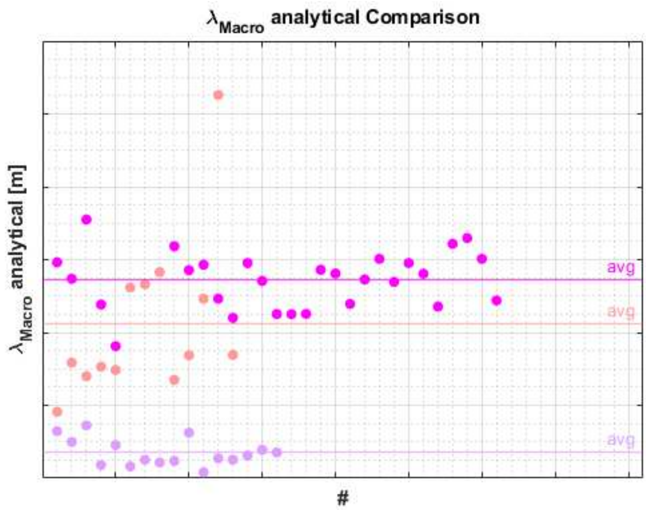

Fig. 7.23 Analytical λ_{Macro} estimation

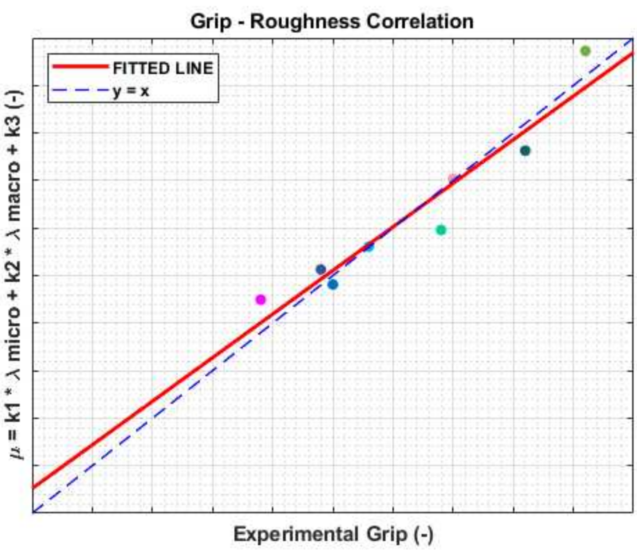

Fig. 7.24 Grip vs Roughness parameters correlation

investigate the dependencies with the viscoelastic properties. Through the various KPIs extracted and cataloged in the database by time, it is possible to identify the real operating point on the master curve by applying the WLF equation. In Figures 7.25 and 7.26, the operating points for the front and rear tires on the master curves are shown, evaluated in two specific conditions extracted from the database by time.

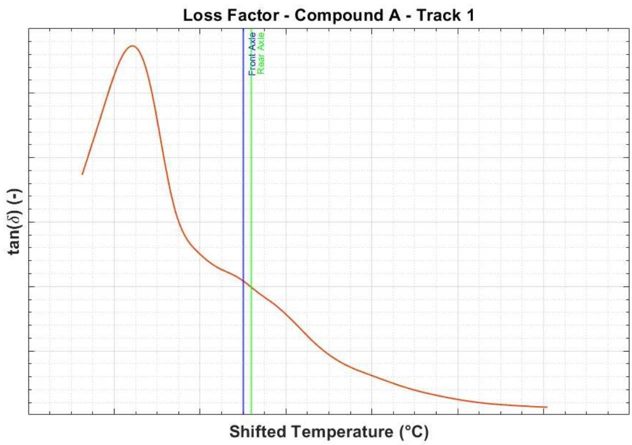

Fig. 7.25 Operating points - Compound A - Track 1

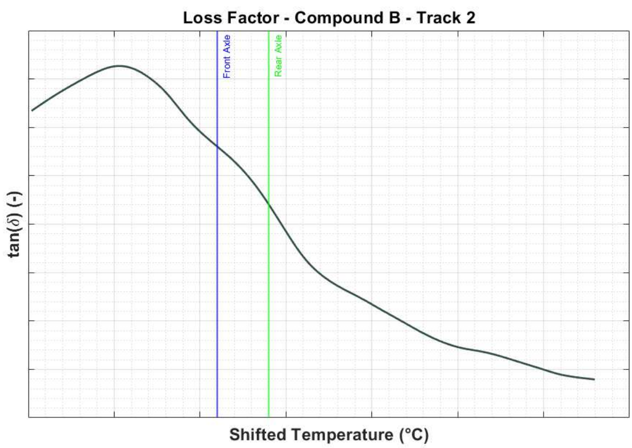

Fig. 7.26 Operating points - Compound B - Track 2

Figure 7.25 shows that the operating temperatures of the two axles are more or less the same, with a balanced behavior of the vehicle also from a thermal point of view. Furthermore, it is possible to note how the temperatures of the axles fall in a slightly sloping area of the master curve, identifying a stable operating point with the viscoelastic characteristics of compound A which varies little. Figure 7.26, instead, shows a completely different condition in which the two axles work at different temperatures and in points in which the viscoelastic characteristics of compound B vary significantly (the section of the master curve is quite sloping).

The results obtained have a direct practical application, because thanks to the possibility of identifying the real operating point, directly connected to the target grip variable, it is possible to define in detail the various optimal thermal working ranges, also influenced by the roughness properties of the chosen circuit.

Conclusions and Further Developments

Innovative methodologies to study and optimize vehicle performance, taking into account the vehicle and its sub-components, the drivers' skills and other relevant external key factors, such as tire viscoelasticity and road roughness, have been presented. Starting from the vehicle analysis, two different tools have been developed, respectively, to evaluate tire-road interaction forces and to properly characterize the suspension behavior. These tools have been developed starting from simple vehicle models, properly parameterized according to the information available, exploiting their modularity and versatility. The implemented equations were validated through the use of simulations obtained from more complex vehicle models, which confirmed the robustness of the chosen approach. The goodness of the results obtainable through the use of T.R.I.C.K. 2.0 and of the Virtual 7-Post is also confirmed by the physical consistency of the calculated quantities. With the aim of further improving the performance of these two tools, a further validation campaign on real data obtained on the track or on real test benches could be conducted.

Subsequently, shifting attention to the driver, it was possible to define a series of objective and generalized metrics, thanks to the data collected on the track, under the same conditions, for amateur and professional drivers. Thanks to the study of the direct interaction of the driver with the vehicle, the acceleration and braking ranges and the grip actually achieved, a classification of these drivers has been defined by giving a specific weight to all the identified KPIs, clearly defining three bands of drivers with three different skill levels, perfectly matching their lap times.

Then, to complete the overview of the phenomena directly involved in the definition of vehicle performance, an innovative device for estimating the viscoelastic properties of tires, the VESevo, has been presented. It is capable of carrying out tests directly on the track, overcoming the limits of the standard characterization procedures commonly adopted. With the same objective, a new methodology for the characterization of road micro-roughness has been proposed, starting from the extraction of small portions of the profile; the results obtained with this procedure are more robust and have allowed a clear identification of the differences between the various circuits analyzed.

After that, all the data collected has been stored in different databases according to the different targets of the activity. Through the definition and study of the target variables, it was possible to reduce the size of the databases by focusing attention only on the maximum performance conditions of the vehicle. Thanks to the adoption of these databases, two statistical models of wear have been developed, one for each axle, based on the combination of only 6 relevant KPIs which take into account the various factors explored during this research activity. For what concerns the grip, however, after an extensive study linked to the dependence on the temperature, it was possible to define operating procedures capable of highlighting the correlation with the parameters λ_{Macro} and λ_{micro}, leading to the identification of the effective working points on the viscoelastic curves of the various compounds. The procedures illustrated within this thesis can be effectively applied within motorsport contexts, providing further insights on how to modify vehicle operating conditions in order to maximize grip and reduce tire degradation.

Among the future developments of this work, there is certainly the validation of the procedures developed on further experimental data obtained in different scenarios, not exclusively coming from the world of motorsport. By refining the data acquisition and processing techniques, further key performance indicators could be defined, in order to develop grip and wear models starting from complete analytical formulations.

List of figures

List of tables

References

[1] Jörge Segers, editor. *Analysis Techniques for Racecar Data Acquisition*. Sae International, 2014.

[2] G Capone, D Giordano, M Russo, M Terzo, and F Timpone. Ph. an. ty. mha: a physical analytical tyre model for handling analysis–the normal interaction. *Vehicle System Dynamics*, 47(1):15–27, 2009.

[3] Massimo Guiggiani. *The Science of Vehicle Dynamics*. Springer International Publishing AG, 2014.

[4] Hüsnü Dal and Michael Kaliske. Bergström–boyce model for nonlinear finite rubber viscoelasticity: theoretical aspects and algorithmic treatment for the fe method. *Computational mechanics*, 44:809–823, 2009.

[5] Mokarram Hossain, Duc Khoi Vu, and Paul Steinmann. Experimental study and numerical modelling of vhb 4910 polymer. *Computational Materials Science*, 59:65–74, 2012.

[6] BNJ Persson. Theory of rubber friction and contact mechanics. *The Journal of Chemical Physics*, 2001.

[7] Andrea Genovese, Flavio Farroni, Antonio Papangelo, and Michele Ciavarella. A discussion on present theories of rubber friction, with particular reference to different possible choices of arbitrary roughness cutoff parameters. *Lubricants*, 7(10):85, 2019.

[8] Rao V Dukkipati. *Vehicle dynamics*. CRC Press, 2000.

[9] Dieter Schramm, Manfred Hiller, and Roberto Bardini. Vehicle dynamics. *Modeling and Simulation. Berlin, Heidelberg*, 151, 2014.

[10] Bo NJ Persson. Rubber friction: role of the flash temperature. *Journal of Physics: Condensed Matter*, 18(32):7789, 2006.

[11] Aleksandr Sakhnevych. Multiphysical mf-based tyre modelling and parametrisation for vehicle setup and control strategies optimisation. *Vehicle System Dynamics*, 60, 09 2021.

[12] Jim Waldo. Embedded computing and formula one racing. *IEEE Pervasive Computing*, 4(3):18–21, 2005.

[13] Bernard Marr. *Big data in practice: how 45 successful companies used big data analytics to deliver extraordinary results*. John Wiley & Sons,, 2016.

[14] Gerard George, Martine R Haas, and Alex Pentland. Big data and management. *Academy of management Journal*, 57(2):321–326, 2014.

[15] Jasmine Zakir, Tom Seymour, and Kristi Berg. Big data analytics. *Issues in Information Systems*, 16(2), 2015.

[16] José L Torrecilla and Juan Romo. Data learning from big data. *Statistics & Probability Letters*, 136:15–19, 2018.

[17] Tobias Abthoff. Big data technologies in automotive development. *ATZelektronik worldwide*, 11(5):42–47, 2016.

[18] Alan Neville Gent and Joseph D Walter. *Pneumatic tire*. 2006.

[19] Reza N Jazar. Road dynamics. In *Advanced Vehicle Dynamics*, pages 297–350. Springer, 2019.

[20] Francesco Calabrese, Flavio Farroni, and Francesco Timpone. A flexible ring tyre model for normal interaction. *complexity*, 7(9), 2013.

[21] C Allouis, F Farroni, A Sakhnevych, and F Timpone. Tire thermal characterization: test procedure and model parameters evaluation. In *Proceedings of the World Congress on engineering*, volume 2, 2016.

[22] Edwin W Hines. Indicator device for indicating tread wear and tire incorporating the indicator, December 30 1975. US Patent 3,929,179.

[23] Cx K Batchelor and GK Batchelor. *An introduction to fluid dynamics*. Cambridge university press, 2000.

[24] P Bosch, D Ammon, and F Klempau. Tyre models-desire and reality in respect of vehicle development. *Darmstdter Reifenkolloquium, October*, 2002.

[25] Marco Viehweger, Cyrano Vaseur, Sebastiaan van Aalst, Manuel Acosta, Enrico Regolin, Angel Alatorre, Wim Desmet, Frank Naets, Valentin Ivanov, Antonella Ferrara, et al. Vehicle state and tyre force estimation: demonstrations and guidelines. *Vehicle system dynamics*, 59(5):675–702, 2021.

[26] Daniel Chindamo, Basilio Lenzo, and Marco Gadola. On the vehicle sideslip angle estimation: a literature review of methods, models, and innovations. *applied sciences*, 8(3):355, 2018.

[27] Laura R Ray. Nonlinear tire force estimation and road friction identification: Simulation and experiments. *Automatica*, 33(10):1819–1833, 1997.

[28] Fredrik Gustafsson. Slip-based tire-road friction estimation. *Automatica*, 33(6):1087–1099, 1997.

[29] Moustapha Doumiati, Alessandro Correa Victorino, Ali Charara, and Daniel Lechner. Onboard real-time estimation of vehicle lateral tire–road forces and sideslip angle. *IEEE/ASME Transactions on Mechatronics*, 16(4):601–614, 2010.

[30] Moustapha Doumiati, Alessandro Victorino, Ali Charara, and Daniel Lechner. Estimation of vehicle lateral tire-road forces: a comparison between extended and unscented kalman filtering. In *2009 European Control Conference (ECC)*, pages 4804–4809. IEEE, 2009.

[31] Damrongrit Piyabongkarn, Rajesh Rajamani, John A Grogg, and Jae Y Lew. Development and experimental evaluation of a slip angle estimator for vehicle stability control. *IEEE Transactions on control systems technology*, 17(1):78–88, 2008.

[32] Yung-Hsiang Judy Hsu, Shad M Laws, and J Christian Gerdes. Estimation of tire slip angle and friction limits using steering torque. *IEEE Transactions on Control Systems Technology*, 18(4):896–907, 2009.

[33] Ricardo De Castro, Rui Araujo, and Diamantino Freitas. Optimal linear parameterization for on-line estimation of tire-road friction. *IFAC Proceedings Volumes*, 44(1):8409–8414, 2011.

[34] Rajesh Rajamani, Gridsada Phanomchoeng, Damrongrit Piyabongkarn, and Jae Y Lew. Algorithms for real-time estimation of individual wheel tire-road friction coefficients. *IEEE/ASME Transactions on Mechatronics*, 17(6):1183–1195, 2011.

[35] Jadranko Matuško, Ivan Petrović, and Nedjeljko Perić. Neural network based tire/road friction force estimation. *Engineering Applications of Artificial Intelligence*, 21(3):442–456, 2008.

[36] Manuel Acosta and Stratis Kanarachos. Tire lateral force estimation and grip potential identification using neural networks, extended kalman filter, and recursive least squares. *Neural Computing and Applications*, 30(11):3445–3465, 2018.

[37] Guillaume Baffet, Ali Charara, and Daniel Lechner. Estimation of vehicle sideslip, tire force and wheel cornering stiffness. *Control Engineering Practice*, 17(11):1255–1264, 2009.

[38] Juqi Hu, Subhash Rakheja, and Youmin Zhang. Real-time estimation of tire–road friction coefficient based on lateral vehicle dynamics. *Proceedings of the Institution of Mechanical Engineers, Part D: Journal of Automobile Engineering*, 234(10-11):2444–2457, 2020.

[39] Hongyan Guo, Hui Liu, Zhenyu Yin, Yulei Wang, Hong Chen, and Yingjun Ma. Modular scheme for four-wheel-drive electric vehicle tire-road force and velocity estimation. *IET Intelligent Transport Systems*, 13(3):551–562, 2019.

[40] Nan Xu, Hassan Askari, Yanjun Huang, Jianfeng Zhou, and Amir Khajepour. Tire force estimation in intelligent tires using machine learning. *IEEE Transactions on Intelligent Transportation Systems*, 2020.

[41] MG Pottinger. The flat-trac ii® machine, the state-of-the-art in tire force and moment measurement. *Tire Science and Technology*, 20(3):132–153, 1992.

[42] Tianli Gu, Bo Li, Zhenqiang Quan, Shaoyi Bei, Guodong Yin, Jinfei Guo, Xinye Zhou, and Xiao Han. The vertical force estimation algorithm based on smart tire technology. *World Electric Vehicle Journal*, 13(6):104, 2022.

[43] Jin-Oh Hahn, Rajesh Rajamani, and Lee Alexander. Gps-based real-time identification of tire-road friction coefficient. *IEEE Transactions on Control Systems Technology*, 10(3):331–343, 2002.

[44] Jorge Villagra, Brigitte Dâ€™Andréa-Novel, Michel Fliess, and Hugues Mounier. A diagnosis-based approach for tire–road forces and maximum friction estimation. *Control engineering practice*, 19(2):174–184, 2011.

[45] Flavio Farroni. Trick-tire/road interaction characterization & knowledge-a tool for the evaluation of tire and vehicle performances in outdoor test sessions. *Mechanical Systems and Signal Processing*, 72:808–831, 2016.

[46] Guido Napolitano Dell'Annunziata, Basilio Lenzo, Flavio Farroni, Aleksandr Sakhnevych, and Francesco Timpone. A new approach for estimating tire-road longitudinal forces for a race car. In *IFToMM World Congress on Mechanism and Machine Science*, pages 3601–3610. Springer, 2019.

[47] Flavio Farroni, Guido Napolitano Dell'Annunziata, Aleksandr Sakhnevych, Francesco Timpone, Basilio Lenzo, and Mauro Barbieri. Towards trick 2.0–a tool for the evaluation of the vehicle performance through the use of an advanced sensor system. In *Conference of the Italian Association of Theoretical and Applied Mechanics*, pages 1093–1102. Springer, 2019.

[48] Roberto Lot, Vittore Cossalter, and Matteo Massaro. Real-time roll angle estimation for two-wheeled vehicles. In *Engineering Systems Design and Analysis*, volume 44847, pages 687–693. American Society of Mechanical Engineers, 2012.

[49] Ivo Boniolo, Michele Norgia, Mara Tanelli, Cesare Svelto, and Sergio M Savaresi. Performance analysis of an optical distance sensor for roll angle estimation in sport motorcycles. *IFAC Proceedings Volumes*, 41(2):135–140, 2008.

[50] JM Badalamenti and GR Doyle Jr. Radial-interradial spring tire models. 1988.

[51] KM Captain, AB Boghani, and DN Wormley. Analytical tire models for dynamic vehicle simulation. *Vehicle System Dynamics*, 8(1):1–32, 1979.

[52] Jerzy Kisilowski and Zbigniew Lozia. Modelling and simulating the braking process of automotive vehicle on uneven surface. *Vehicle System Dynamics*, 15(sup1):250–263, 1986.

[53] JR Kilner. Pneumatic tire model for aircraft simulation. *Journal of Aircraft*, 19(10):851–857, 1982.

[54] Konghui Guo. Tire roller contact model for simulation of vehicle vibration input. Technical report, SAE Technical Paper, 1993.

[55] V Misun. Loads on lorries' driving systems due to road unevenness. In *Proceedings: International Technical Conference on the Enhanced Safety of Vehicles*, volume 1992, pages 203–210. National Highway Traffic Safety Administration, 1992.

[56] Chunlai Zhao and Mengyan Zang. Analysis of rigid tire traction performance on a sandy soil by 3d finite element–discrete element method. *Journal of Terramechanics*, 55:29–37, 2014.

[57] Sh Taheri, C Sandu, S Taheri, E Pinto, and D Gorsich. A technical survey on terramechanics models for tire–terrain interaction used in modeling and simulation of wheeled vehicles. *Journal of Terramechanics*, 57:1–22, 2015.

[58] F Farroni, A Sakhnevych, and F Timpone. Physical modelling of tire wear for the analysis of the influence of thermal and frictional effects on vehicle performance. *Proceedings of the Institution of Mechanical Engineers, Part L: Journal of Materials: Design and Applications*, 231(1-2):151–161, 2017.

[59] Sunrong Gong. Study of in-plane dynamics of tires. *Ph. D. Thesis*, 1993.

[60] Seongho Kim, Parviz E Nikravesh, and Gwanghun Gim. A two-dimensional tire model on uneven roads for vehicle dynamic simulation. *Vehicle system dynamics*, 46(10):913–930, 2008.

[61] Christian Oertel and Andreas Fandre. Ride comfort simulations and steps towards life time calculations: Rmod-k tyre model and adams. 1999.

[62] Sven TH Jansen, Lennard Verhoeff, Robert Cremers, Antoine JC Schmeitz, and Igo JM Besselink. Mf-swift simulation study using benchmark data. *Vehicle System Dynamics*, 43(sup1):92–101, 2005.

[63] AJC Schmeitz, IJM Besselink, and STH Jansen. Tno mf-swift. *Vehicle System Dynamics*, 45(S1):121–137, 2007.

[64] AJC Schmeitz and WD Versteden. Structure and parameterization of mf-swift, a magic formula-based rigid ring tire model. *Tire Science and Technology*, 37(3):142–164, 2009.

[65] IJM Besselink and AJC Schmeitz. The mf-swift tyre model: Extending the magic formula with rigid ring dynamics and an enveloping model. *JSAE review*, 26(2):245–252, 2005.

[66] Michael Gipser. Ftire: a physically based application-oriented tyre model for use with detailed mbs and finite-element suspension models. *Vehicle system dynamics*, 43(sup1):76–91, 2005.

[67] A Gallrein and M Bäcker. Cdtire: a tire model for comfort and durability applications. *Vehicle System Dynamics*, 45(S1):69–77, 2007.

[68] Chongfeng Wei, Oluremi A Olatunbosun, and Mohammad Behroozi. Simulation of tyre rolling resistance generated on uneven road. *International journal of vehicle design*, 70(2):113–136, 2016.

[69] Ch Oertel. On modeling contact and friction calculation of tyre response on uneven roads. *Vehicle System Dynamics*, 27(S1):289–302, 1997.

[70] CW Mousseau, GM Hulbert, and SK Clark. On the modeling of tires for the prediction of automotive durability loads. *Vehicle System Dynamics*, 25(S1):466–488, 1996.

[71] N Balaramakrishna and R Krishna Kumar. A study on the estimation of swift model parameters by finite element analysis. *Proceedings of the Institution of Mechanical Engineers, Part D: Journal of Automobile Engineering*, 223(10):1283–1300, 2009.

[72] Zoran Constantinescu, Cristian Marinoiu, and Monica Vladoiu. Driving style analysis using data mining techniques. *International Journal of Computers, Communications & Control (IJCCC)*, V:654–663, 12 2010.

[73] Nadezda Karginova, Stefan Byttner, and Magnus Svensson. Data-driven methods for classification of driving styles in buses. *SAE Tech. Pap*, 04 2012.

[74] Rui Wang and Srdjan M. Lukic. Review of driving conditions prediction and driving style recognition based control algorithms for hybrid electric vehicles. In *2011 IEEE Vehicle Power and Propulsion Conference*, pages 1–7, 2011.

[75] Leonhard Hermansdorfer, Johannes Betz, and Markus Lienkamp. Benchmarking of a software stack for autonomous racing against a professional human race driver. *CoRR*, abs/2005.10044, 2020.

[76] Stefan Löckel, André Kretschi, Peter van Vliet, and Jan Peters. Identification and modelling of race driving styles. *Vehicle System Dynamics*, 60(8):2890–2918, 2022.

[77] Adrian Remonda, Eduardo Veas, and Granit Luzhnica. Comparing driving behavior of humans and autonomous driving in a professional racing simulator. *PLOS ONE*, 16:1–37, 02 2021.

[78] Peter M. van Leeuwen, Stefan de Groot, Riender Happee, and Joost C. F. de Winter. Differences between racing and non-racing drivers: A simulator study using eye-tracking. *PLOS ONE*, 12(11):1–19, 11 2017.

[79] Naman Singh Negi, Peter Van Leeuwen, and Riender Happee. Differences in driver behaviour between race and experienced drivers: A driving simulator study. In *VEHITS*, pages 360–367, 2019.

[80] Wei Han, Wenshuo Wang, Xiaohan Li, and Junqiang Xi. Statistical-based approach for driving style recognition using bayesian probability with kernel density estimation. *IET Intelligent Transport Systems*, 13(1):22–30, 2019.

[81] Dominik Dörr, David Grabengiesser, and Frank Gauterin. Online driving style recognition using fuzzy logic. In *17th International IEEE Conference on Intelligent Transportation Systems (ITSC)*, pages 1021–1026, 2014.

[82] Bohua Sun, Weiwen Deng, Jian Wu, Yaxin Li, Lei Fu, and Liang Xu. Research on the classification and identification for personalized driving styles. Technical report, SAE Technical Paper, 04 2018.

[83] Keith Bugeja, Sandro Spina, and Francois Buhagiar. Telemetry-based optimisation for user training in racing simulators. In *2017 9th International Conference on Virtual Worlds and Games for Serious Applications (VS-Games)*, pages 31–38. IEEE, 2017.

[84] Yilu Zhang, William C. Lin, and Yuen-Kwok Steve Chin. Driving skill characterization: A feasibility study. In *2008 IEEE International Conference on Robotics and Automation*, pages 2571–2576, 2008.

[85] Julian von Schleinitz, Thomas Schwarzhuber, Lukas Wörle, Michael Graf, Arno Eichberger, Wolfgang Trutschnig, and Andreas Schröder. Race driver evaluation at a driving simulator using a physical model and a machine learning approach. *arXiv*, 2022.

[86] Yulong Lei, Ke Liu, Yao Fu, Xingzhong Li, Zhenjie Liu, and Shaohua Sun. Research on driving style recognition method based on driver's dynamic demand. *Advances in Mechanical Engineering*, 8(9), 2016.

[87] Clara Marina Martinez, Mira Heucke, Fei-Yue Wang, Bo Gao, and Dongpu Cao. Driving style recognition for intelligent vehicle control and advanced driver assistance: A survey. *IEEE Transactions on Intelligent Transportation Systems*, 19(3):666–676, 2018.

[88] Massimo Canale and Stefano Malan. Analysis and classification of human driving behaviour in an urban environment*. *Cognition Technology and Work*, 4:197–206, 09 2002.

[89] Tarek Ouali, Nirav Shah, Bill Kim, David Fuente, and Bo Gao. Driving style identification algorithm with real-world data based on statistical approach. Technical report, SAE Technical Paper, 2016.

[90] Lina Xia and Zejun Kang. Driving style recognition model based on nev high-frequency big data and joint distribution feature parameters. *World Electric Vehicle Journal*, 12(3), 2021.

[91] Brendan Rodgers. *Rubber compounding: chemistry and applications*. CRC press, 2015.

[92] Anu Mary Joseph, Benny George, KN Madhusoodanan, Rosamma Alex, et al. Current status of sulphur vulcanization and devulcanization chemistry: Process of vulcanization. *Rubber Science*, 28(1):82–121, 2015.

[93] James E Mark, Burak Erman, and Mike Roland. *The science and technology of rubber*. Academic press, 4 edition, 2013.

[94] Roderic Lakes and Roderic S Lakes. *Viscoelastic materials*. Cambridge university press, 2009.

[95] Piaras Kelly. *Solid mechanics part I: An introduction to solid mechanics*. University of Auckland, Solid Mechanics Lecture Notes, 2013.

[96] John D Ferry. *Viscoelastic properties of polymers*. John Wiley & Sons, 1980.

[97] Alan Neville Gent and Joseph D Walter. *Pneumatic tire*. Mechanical Engineering Faculty Research, 2006.

[98] Prasanta Sahoo and Tapan Kr Barman. Ann modelling of fractal dimension in machining. In *Mechatronics and manufacturing engineering*, pages 159–226. 2012.

[99] William Mendenhall, Robert J Beaver, and Barbara M Beaver. *Introduction to probability and statistics*. Cengage Learning, 2012.

[100] Marko Sedlaček, Bojan Podgornik, and Jože Vižintin. Correlation between standard roughness parameters skewness and kurtosis and tribological behaviour of contact surfaces. *Tribology international*, 2012.

[101] Flavio Farroni, Nicolò Mancinelli, and Francesco Timpone. A real-time thermal model for the analysis of tire/road interaction in motorcycle applications. *Applied Sciences*, 10(5):1604, 2020.

[102] Flavio Farroni, Michele Russo, Aleksandr Sakhnevych, and Francesco Timpone. Trt evo: Advances in real-time thermodynamic tire modeling for vehicle dynamics simulations. *Proceedings of the Institution of Mechanical Engineers, Part D: Journal of Automobile Engineering*, 233:095440701880899, 11 2018.

[103] F. Farroni and A. Sakhnevych. Tire multiphysical modeling for the analysis of thermal and wear sensitivity on vehicle objective dynamics and racing performances. *Simulation Modelling Practice and Theory*, 117:102517, 2022.

[104] Flavio Farroni, Raffaele Lamberti, Nicolò Mancinelli, and Francesco Timpone. Trip-id: A tool for a smart and interactive identification of magic formula tyre model parameters from experimental data acquired on track or test rig. *Mechanical Systems and Signal Processing*, 102:1–22, 03 2018.

[105] Francesco Timpone. *An Application of TRIP-ID: MF Identification Tool for an Automobile Tire Interaction Curves Dataset*, volume 68, page 100. Springer, 2018.

[106] Flavio Farroni, Lorenzo Mosconi, Aleksandr Sakhnevych, and Francesco Timpone. *Trick real time. a tool for the real-time onboard tire performance evaluation*, pages 1020–1032. Springer, 2020.

[107] Young Soo Suh. Laser sensors for displacement, distance and position, 2019.

[108] Joseph Katz. Aerodynamics of race cars. *Annual Review of fluid mechanics*, 38(1):27–63, 2006.

[109] Simon McBeath. *Competition Car Aerodynamics 3rd Edition*. Veloce Publishing Ltd, 2017.

[110] Jianfeng Wang, Hao Li, Yiqun Liu, Tao Liu, and Haibo Gao. Aerodynamic research of a racing car based on wind tunnel test and computational fluid dynamics. In *MATEC Web of Conferences*, volume 153, page 04011. EDP Sciences, 2018.

[111] Christopher P Rahaim, Alain J Kassab, and Robert J Cavalleri. Coupled dual reciprocity boundary element/finite volume method for transient conjugate heat transfer. *Journal of thermophysics and heat transfer*, 14(1):27–38, 2000.

[112] Peter Aschwanden, Jürg Müller, and Ulrich Knörnschild. Experimental study on the influence of model motion on the aerodynamic performance of a race car. *SAE Transactions*, pages 736–743, 2006.

[113] Iyasu Jiregna and Goftila Sirata. A review of the vehicle suspension system. *Journal of Mechanical and Energy Engineering*, 4(2), 2020.

[114] WF Milliken, DL Milliken, EM Kasprzak, and LD Metz. Race car vehicle dynamics: Problems, answers and experiments. *Dynamics*, 265:5Control267, 1995.

[115] Seong-Jun Park and Jeong-Hyun Sohn. Effects of camber angle control of front suspension on vehicle dynamic behaviors. *Journal of Mechanical Science and Technology*, 26(2):307–313, 2012.

[116] Takahiko Yoshino and Hiromichi Nozaki. About the effect of camber control on vehicle dynamics. Technical report, SAE Technical Paper, 2014.

[117] Marco Gadola, Daniel Chindamo, and Basilio Lenzo. Revisiting the mechanical limited-slip differential for high-performance and race car applications. *Engineering Letters*, 29(3):824–839, 2021.

[118] H. Winner E. Kutluay. Validation of vehicle dynamics simulation models - a review. *Vehicle System Dynamics*, 47(2):186–200, 2014.

[119] M. Chouksey S.K. Sharma. Numerical studies using full car model for combined primary and cabin suspension. *Procedia Technology*, 23(1):171–178, 2016.

[120] Serge Klein, Rene Savelsberg, Feihong Xia, Daniel Guse, Jakob Andert, Torsten Blochwitz, Claudia Bellanger, Stefan Walter, Steffen Beringer, Janek Jochheim, et al. Engine in the loop: closed loop test bench control with real-time simulation. *SAE International journal of commercial vehicles*, 10(1):95–106, 2017.

[121] Nurzaki Ikhsan, Rahizar Ramli, and Anuar Alias. Analysis of kinematic and compliance of passive suspension system using adams car. *UM Research Repository*, 2014.

[122] G. Bitsch K. Dressler, M. Speckert. Virtual durability test rigs for automotive engineering. *Vehicle System Dynamics*, 47(4):387–401, 2009.

[123] Károly Jármai and Betti Bolló, editors. *Characterization of the Vehicle Roll Movement with the Dynamic Chassis Simulator*. Springer International Publishing, 2018.

[124] *Suspension System Testing and Tuning with the Use of a Four-Post Rig*, 1998.

[125] *Testing a Formula SAE Racecar on a Seven-Poster Vehicle Dynamics Simulator*, 2002.

[126] Henri Kowalczyk. Damper tuning with the use of a seven post shaker rig. *SAE Transaction*, 111(6):1182–1193, 2002.

[127] *Track Simulation and Vehicle Characterization with 7 Post Testing*, 2002.

[128] *Development of a Virtual 7-Post Test Rig for Experimental Validation*, volume Design Engineering and Computers and Information in Engineering, Parts A and B of *ASME International Mechanical Engineering Congress and Exposition*, 2006.

[129] Giandomenico Di Massa Sergio Della Valle. *Dinamica dei sistemi meccanici*. Edizioni Scientifiche e Artistiche, 2016.

[130] Jacob Pieter Den Hartog. *Mechanical vibrations*. Courier Corporation, 1985.

[131] Tristan M Ericson and Robert G Parker. Planetary gear modal vibration experiments and correlation against lumped-parameter and finite element models. *Journal of sound and vibration*, 332(9):2350–2375, 2013.

[132] Y Taskin, N Yagiz, and I Yuksek. Lumped parameter identification of a quarter car test rig. In *Journal of Physics: Conference Series*, volume 410, page 012089. IOP Publishing, 2013.

[133] Apichan Kanjanavapastit and Aphirak Thitinaruemit. Estimation of a speed hump profile using quarter car model. *Procedia-Social and Behavioral Sciences*, 88:265–273, 2013.

[134] Anirban C Mitra and Nilotpal Benerjee. Ride comfort and vehicle handling of quarter car model using simulink and bond graph. In *Proceedings of the 1st International and 16th National Conference on Machines and Mechanisms (iNaCoMM2013)*, 2013.

[135] Daniel Garcia-Pozuelo, Antonio Gauchia, Ester Olmeda, and Vicente Diaz. Bump modeling and vehicle vertical dynamics prediction. *Advances in Mechanical Engineering*, 6:736576, 2014.

[136] V Niola and G Quaremba. The gear whine noise and vibro-acoustic emission of gear-box. In *Proceedings of the 11th WSEAS international conference on robotics, control and manufacturing technology, and 11th WSEAS international conference on Multimedia systems & signal processing*, pages 138–143. Citeseer, 2011.

[137] Mahmoud Rababah and Atanu Bhuyan. Passive suspension modeling and analysis of a full car model. *International Journal of Advanced Science and Engineering Technology*, 3(2):250–261, 2013.

[138] Louis Hand and Janet Finch. Analytical mechanics, 2000.

[139] William F. Milliken and Douglas L. Milliken. *Race Car Vehicle Dynamics*. Sae International, 1995.

[140] John Dixon. *Tires, suspension and handling*. SAE, 1996.

[141] Reza N Jazar. *Vehicle dynamics*, volume 1. Springer, 2008.

[142] RA GUIDO and L Della Pietra. *Lezioni di Meccanica applicata alle macchine*. Cuen, 1998.

[143] Dan B Marghitu. *Mechanical engineer's handbook*. Elsevier, 2001.

[144] John C Dixon. *The shock absorber handbook*. John Wiley & Sons, 2008.

[145] John C Dixon. *Suspension geometry and computation*. John Wiley & Sons, 2009.

[146] Paolo Biscari, Tommaso Ruggeri, Giuseppe Saccomandi, and Maurizio Vianello. *Meccanica razionale*, volume 138. Springer Nature, 2022.

[147] Jorge Sergers. *Analysis techniques for racecar data acquisition*. SAE, 2014.

[148] Anirban C Mitra, Ajay Rajput, Vinay Satish, and Shubhali Mhatre. Development and analysis of passive suspension model with half sine wave road bump for different suspension parameters. In *AIP Conference Proceedings*, volume 2469, page 020023. AIP Publishing LLC, 2022.

[149] VI-GRADE. *VI CarRealTime 19.0, Documentation*, 2019.

[150] Julian von Schleinitz, Lukas Wörle, Michael Graf, Andreas Schröder, and Wolfgang Trutschnig. Analysis of race car drivers' pedal interactions by means of supervised learning. In *2019 IEEE Intelligent Transportation Systems Conference (ITSC)*, pages 4152–4157, 2019.

[151] Lukas Wörle, Julian von Schleinitz, Michael Graf, and Arno Eichberger. Driver detection from objective criteria describing the driving style of race car drivers. In *2019 IEEE Intelligent Transportation Systems Conference (ITSC)*, pages 1198–1203. IEEE, 2019.

[152] Florian Goy, Jochen Wiedemann, T Völkl, G Delli Colli, J Neubeck, and W Krantz. Development of objective criteria to assess the vehicle performance utilized by the driver in near-limit handling conditions of racecars. In *16. Internationales Stuttgarter Symposium*, pages 1213–1231. Springer, 2016.

[153] Wm Mitchell, Roger Schroer, and Dennis B Grisez. Driving the traction circle. In *Motorsports Engineering Conference & Exposition*, number 2004-01-3545, 1998.

[154] Paul A Theodosis and J Christian Gerdes. Generating a racing line for an autonomous racecar using professional driving techniques. In *Dynamic Systems and Control Conference*, volume 54761, pages 853–860, 2011.

[155] Fred Feng, Shan Bao, James R. Sayer, Carol Flannagan, Michael Manser, and Robert Wunderlich. Can vehicle longitudinal jerk be used to identify aggressive drivers? an examination using naturalistic driving data. *Accident Analysis & Prevention*, 104:125–136, 2017.

[156] Yi Lu Murphey, Robert Milton, and Leonidas Kiliaris. Driver's style classification using jerk analysis. In *2009 IEEE Workshop on Computational Intelligence in Vehicles and Vehicular Systems*, pages 23–28, 2009.

[157] Anup Doshi and Mohan M. Trivedi. Examining the impact of driving style on the predictability and responsiveness of the driver: Real-world and simulator analysis. In *2010 IEEE Intelligent Vehicles Symposium*, pages 232–237, 2010.

[158] Zhixia Li, Madhav Chitturi, Andrea Bill, and David Noyce. Automated identification and extraction of horizontal curve information from geographic information system roadway maps. *Transportation Research Record: Journal of the Transportation Research Board*, 2291:80–92, 12 2012.

[159] Citlalli Gámez Serna, Alexandre Lombard, Yassine Ruichek, and Abdeljalil Abbas-Turki. Gps-based curve estimation for an adaptive pure pursuit algorithm. In Grigori Sidorov and Oscar Herrera-Alcántara, editors, *Advances in Computational Intelligence*, pages 497–511, Cham, 2017. Springer International Publishing.

[160] Alessandro Rucco, Giuseppe Notarstefano, and John Hauser. An efficient minimum-time trajectory generation strategy for two-track car vehicles. *IEEE Transactions on Control Systems Technology*, 23(4):1505–1519, 2015.

[161] Efstathios Velenis and Panagiotis Tsiotras. Minimum time vs maximum exit velocity path optimization during cornering. In *2005 IEEE international symposium on industrial electronics*, pages 355–360. Citeseer, 2005.

[162] F. Braghin, F. Cheli, S. Melzi, and E. Sabbioni. Race driver model. *Computers & Structures*, 86(13):1503–1516, 2008.

[163] Matteo Botta, Vincenzo Gautieri, Daniele Loiacono, and Pier Luca Lanzi. Evolving the optimal racing line in a high-end racing game. In *2012 IEEE Conference on Computational Intelligence and Games (CIG)*, pages 108–115, 2012.

[164] Bassam Alrifaee and Janis Maczijewski. Real-time trajectory optimization for autonomous vehicle racing using sequential linearization. In *2018 IEEE Intelligent Vehicles Symposium (IV)*, pages 476–483, 2018.

[165] D. Antonelli, L. Nesi, G. Pepe, and A. Carcaterra. A novel approach in optimal trajectory identification for autonomous driving in racetrack. In *2019 18th European Control Conference (ECC)*, pages 3267–3272, 2019.

[166] Luigi Cardamone, Daniele Loiacono, Pier Luca Lanzi, and Alessandro Pietro Bardelli. Searching for the optimal racing line using genetic algorithms. In *Proceedings of the 2010 IEEE Conference on Computational Intelligence and Games*, pages 388–394, 2010.

[167] Nitin R. Kapania, John Subosits, and J. Christian Gerdes. A sequential two-step algorithm for fast generation of vehicle racing trajectories. *Journal of Dynamic Systems, Measurement, and Control*, 138(9), 06 2016.

[168] John C. Kegelman, Lene K. Harbott, and J. Christian Gerdes. Insights into vehicle trajectories at the handling limits: analysing open data from race car drivers. *Vehicle System Dynamics*, 55(2):191–207, 2017.

[169] Raymond Brach and Matthew Brach. The tire-force ellipse (friction ellipse) and tire characteristics. Technical report, SAE Technical Paper, 2011.

[170] Hans Pacejka. *Tire and vehicle dynamics*. Elsevier, 2005.

[171] Hans B Pacejka and Egbert Bakker. The magic formula tyre model. *Vehicle system dynamics*, 21(S1):1–18, 1992.

[172] Steve Corrigan HPL. Introduction to the controller area network (can). *Application Report SLOA101*, pages 1–17, 2002.

[173] Karl Henrik Johansson, Martin Törngren, and Lars Nielsen. Vehicle applications of controller area network. In *Handbook of networked and embedded control systems*, pages 741–765. Springer, 2005.

[174] Zhonghao Li, Da Wang, and Qiao Kang. The development of data acquisition system of formula sae race car based on can bus communication interface and closed-loop design of racing car. *Wireless Communications and Mobile Computing*, 2021, 2021.

[175] Guido Lopez and Anthony Seaber. The theory and practice of race vehicle data acquisition and analysis in motor sports engineering education. In *2009 Annual Conference & Exposition*, pages 14–1257, 2009.

[176] Luca Baldisserri, Riccardo Bonetti, Francesco Pon, Leandro Guidotti, Maria Giulia Losi, Roberto Montanari, Francesco Tesauri, and Simona Collina. Motorsport driver workload estimation in dual task scenario. In *Sixth International Conference on Advanced Cognitive Technologies and Applications*. Citeseer, 2014.

[177] Noraimi Azlin Mohd Nordin, Zati Aqmar Zaharudin, Mohd Azdi Maasar, and Nor Amalina Nordin. Finding shortest path of the ambulance routing: Interface of a* algorithm using c# programming. In *2012 ieee symposium on humanities, science and engineering research*, pages 1569–1573. IEEE, 2012.

[178] Edy Winarno, Wiwien Hadikurniawati, and Rendy Nusa Rosso. Location based service for presence system using haversine method. In *2017 international conference on innovative and creative information technology (ICITech)*, pages 1–4. IEEE, 2017.

[179] Vinayak Hegde, TS Aswathi, and R Sidharth. Student residential distance calculation using haversine formulation and visualization through googlemap for admission analysis. In *2016 IEEE International Conference on Computational Intelligence and Computing Research (ICCIC)*, pages 1–5. IEEE, 2016.

[180] Flavio Farroni, Michele Russo, Riccardo Russo, and Francesco Timpone. A physical-analytical model for a real-time local grip estimation of tyre rubber in sliding contact with road asperities. *Proceedings of the Institution of Mechanical Engineers, Part D: Journal of Automobile Engineering*, 228(8):955–969, 2014.

[181] Vincenzo Maria Arricale, Francesco Carputo, Flavio Farroni, Aleksandr Sakhnevych, and Francesco Timpone. Experimental investigations on tire/road friction dependence from thermal conditions carried out with real tread compounds in sliding contact with asphalt specimens. In *Key Engineering Materials*, volume 813, pages 261–266. Trans Tech Publ, 2019.

[182] F Povolo and M Fontelos. Time-temperature superposition principle and scaling behaviour. *Journal of materials science*, 1987.

[183] Roderic S Lakes. Viscoelastic measurement techniques. *Review of scientific instruments*, 75(4):797–810, 2004.

[184] Malcolm L Williams, Robert F Landel, and John D Ferry. The temperature dependence of relaxation mechanisms in amorphous polymers and other glass-forming liquids. *Journal of the American Chemical society*, 1955.

[185] Robert F Landel. A two-part tale: the wlf equation and beyond linear viscoelasticity. *Rubber chemistry and technology*, 79(3):381–401, 2006.

[186] Kevin P Menard and Noah R Menard. *Dynamic mechanical analysis*. CRC press, 2020.

[187] Kwang Soo Cho. Theory of linear viscoelasticity. In *Viscoelasticity of Polymers*. Springer, 2016.

[188] A Sakhnevych, A Genovese, A Maiorano, F Timpone, and F Farroni. An ultrasound method for characterization of viscoelastic properties in frequency domain at small deformations. *Proceedings of the Institution of Mechanical Engineers, Part C: Journal of Mechanical Engineering Science*, 235(23):7180–7191, 2021.

[189] Francesca Lionetto, Francesco Montagna, and Alfonso Maffezzoli. Ultrasonic dynamic mechanical analysis of polymers. *Applied Rheology*, 15(5):326–335, 2005.

[190] Andrea Genovese and Sebastian Rosario Pastore. Development of a portable instrument for non-destructive characterization of the polymers viscoelastic properties. *Mechanical Systems and Signal Processing*, 150:107259, 2021.

[191] John W Schultz. Dielectric spectroscopy in analysis of polymers. *Encyclopedia of Analytical Chemistry: Applications, Theory and Instrumentation*, 2006.

[192] Flavio Farroni, Andrea Genovese, Antonio Maiorano, Aleksandr Sakhnevych, and Francesco Timpone. Development of an innovative instrument for non-destructive viscoelasticity characterization: Vesevo. In *The international conference of IFToMM ITALY*, 2020.

[193] Bharat Bhushan. *Modern tribology handbook, two volume set*. CRC press, 2000.

[194] Geometrical Product Specifications. Surface texture: profile method—terms, definitions and surface texture parameters. *International Organization for Standardization*, 4, 1997.

[195] ES Gadelmawla, Monir M Koura, Talal MA Maksoud, Ibrahiem M Elewa, and HH Soliman. Roughness parameters. *Journal of materials processing Technology*, 2002.

[196] Benoit B Mandelbrot. *The Fractal Geometry of Nature*. WH Freeman New York, 1977.

[197] Manfred Klüppel and Gert Heinrich. Rubber friction on self-affine road tracks. *Rubber chemistry and technology*, 2000.

[198] G Heinrich, M Klüppel, and Thomas A Vilgis. Evaluation of self-affine surfaces and their implication for frictional dynamics as illustrated with a rouse material. *Computational and Theoretical Polymer Science*, 2000.

[199] Andrej Lang and Manfred Klüppel. Influences of temperature and load on the dry friction behaviour of tire tread compounds in contact with rough granite. *Wear*, 2017.

[200] André Le Gal and Manfred Klüppel. Investigation and modelling of rubber stationary friction on rough surfaces. *Journal of Physics: Condensed Matter*, 2007.

[201] Giuseppe Carbone, Boris Lorenz, Bo NJ Persson, and Alexander Wohlers. Contact mechanics and rubber friction for randomly rough surfaces with anisotropic statistical properties. *The European Physical Journal E*, 2009.

[202] Adam Joseph Mourad, Prescott Jeanne Delzell, and Patrick Conner McCabe. Automation of data analysis in formula 1. 2019.

[203] Paolo Aversa, Laure Cabantous, and Stefan Haefliger. When decision support systems fail: Insights for strategic information systems from formula 1. *The Journal of Strategic Information Systems*, 27(3):221–236, 2018.

[204] Wayne R Kubick. Big data, information and meaning. *Applied Clinical Trials*, 21(2):26, 2012.

[205] Philip Russom et al. Big data analytics. *TDWI best practices report, fourth quarter*, 19(4):1–34, 2011.

[206] Venkat N Gudivada, Ricardo Baeza-Yates, and Vijay V Raghavan. Big data: Promises and problems. *Computer*, 48(03):20–23, 2015.

[207] Nada Elgendy and Ahmed Elragal. Big data analytics: a literature review paper. In *Industrial conference on data mining*, pages 214–227. Springer, 2014.

[208] Wo L Chang, Nancy Grady, et al. Nist big data interoperability framework: Volume 1, definitions. 2019.

[209] Amir Gandomi and Murtaza Haider. Beyond the hype: Big data concepts, methods, and analytics. *International journal of information management*, 35(2):137–144, 2015.

[210] Divyakant Agrawal, Philip Bernstein, Elisa Bertino, Susan Davidson, Umeshwas Dayal, Michael Franklin, Johannes Gehrke, Laura Haas, Alon Halevy, Jiawei Han, et al. Challenges and opportunities with big data 2011-1. 2011.

[211] Klaus Lyko, Marcus Nitzschke, and Axel-Cyrille Ngonga Ngomo. Big data acquisition. In *New horizons for a data-driven economy*, pages 39–61. Springer, Cham, 2016.

[212] MZH Jesmeen, J Hossen, S Sayeed, CK Ho, K Tawsif, Armanur Rahman, and E Arif. A survey on cleaning dirty data using machine learning paradigm for big data analytics. *Indonesian Journal of Electrical Engineering and Computer Science*, 10(3):1234–1243, 2018.

[213] Martin Strohbach, Jörg Daubert, Herman Ravkin, and Mario Lischka. Big data storage. In *New horizons for a data-driven economy*, pages 119–141. Springer, Cham, 2016.

[214] Edward Curry. The big data value chain: definitions, concepts, and theoretical approaches. In *New horizons for a data-driven economy*, pages 29–37. Springer, Cham, 2016.

[215] Tilman Becker. Big data usage. In *New horizons for a data-driven economy*, pages 143–165. Springer, Cham, 2016.

[216] Hiba Sebei, Mohamed Ali Hadj Taieb, and Mohamed Ben Aouicha. Review of social media analytics process and big data pipeline. *Social Network Analysis and Mining*, 8(1):1–28, 2018.

[217] T Nasser and RS Tariq. Big data challenges. *J Comput Eng Inf Technol 4: 3. doi: http://dx. doi. org/10.4172/2324*, 9307(2), 2015.

[218] Alexandru Adrian Tole et al. Big data challenges. *Database systems journal*, 4(3):31–40, 2013.

[219] Jiawei Han, Jian Pei, and Hanghang Tong. *Data mining: concepts and techniques*. Morgan kaufmann, 2022.

[220] Tian Zhang, Raghu Ramakrishnan, and Miron Livny. Birch: an efficient data clustering method for very large databases. *ACM sigmod record*, 25(2):103–114, 1996.

[221] K Krishna and M Narasimha Murty. Genetic k-means algorithm. *IEEE Transactions on Systems, Man, and Cybernetics, Part B (Cybernetics)*, 29(3):433–439, 1999.

[222] Anil K Jain, M Narasimha Murty, and Patrick J Flynn. Data clustering: a review. *ACM computing surveys (CSUR)*, 31(3):264–323, 1999.

[223] Chun-Wei Tsai, Chin-Feng Lai, Han-Chieh Chao, and Athanasios V Vasilakos. Big data analytics: a survey. *Journal of Big data*, 2(1):1–32, 2015.

[224] Daniel Zelterman. *Applied Multivariate Statistics with R*. Springer International Publishing, 2015.

[225] Brian Everitt and Torsten Hothorn. *An Introduction to Applied Multivariate Analysis with R*. Springer-Verlag New York, 2011.

[226] Douglas C. Montgomery, Elizabeth A. Peck, and G. Geoffrey Vining. Introduction to linear regression analysis, fifth edition. *International Statistical Review*, 2013.

[227] Francesco Braghin, Federico Cheli, Stefano Melzi, and Ferruccio Resta. Tyre wear model: Validation and sensitivity analysis. *Meccanica*, 2006.

[228] J. Veen. An analytical approach to dynamic irregular tyre wear. 2007.

[229] HW Kummer. Unified theory of rubber friction. *Pennsylvania State University, Engineering Research Bulletin*, 1966.

[230] AR Savkoor. On the friction of rubber. *Wear*, 8(3):222–237, 1965.

[231] Robert Horigan Smith. *Analyzing friction in the design of rubber products and their paired surfaces*. CRC press, 2008.

[232] Andrea Genovese, Francesco Carputo, Michele Ciavarella, Flavio Farroni, Antonio Papangelo, and Aleksandr Sakhnevych. Analysis of multiscale theories for viscoelastic rubber friction. In *Conference of the Italian Association of Theoretical and Applied Mechanics*, pages 1125–1135. Springer, 2019.

[233] Valentin L Popov et al. *Contact mechanics and friction*. Springer, 2010.

[234] Michele Ciavarella. A simplified version of persson's multiscale theory for rubber friction due to viscoelastic losses. *Journal of Tribology*, 140(1):011403, 2018.

[235] Julian von Schleinitz, Thomas Schwarzhuber, Lukas Wörle, Michael Graf, Arno Eichberger, Wolfgang Trutschnig, and Andreas Schröder. Race driver evaluation at a driving simulator using a physical model and a machine learning approach. *arXiv preprint arXiv:2201.12939*, 2022.

Appendix A

T.R.I.C.K. Model Equations

In this appendix all the equations implemented in the first release of the T.R.I.C.K. [45] are briefly reported, in order to compare the original formulations with those implemented in the T.R.I.C.K. 2.0, deeply discussed in the chapter 2. In particular, the resolution of these equations starts after the pre-processing phase, described in section 2.2.3.

A.1 Vertical Forces Evaluation

When the vehicle is stationary or advancing with uniform rectilinear motion with constant steering angle, it is defined in static conditions and the so-called static loads W_F and W_R weigh on the two axles which, in the absence of appreciable aerodynamic actions, depend only on the position of the center of gravity:

$$W_F = \frac{mgb}{l} \tag{A.1}$$

$$W_R = \frac{mga}{l} \tag{A.2}$$

where m is the vehicle sprung mass, a and b are the front and rear wheelbase. The static loads, since gravity acceleration is considered negative, are directed in the positive direction, as they represent the reactions of the road on the vehicle.

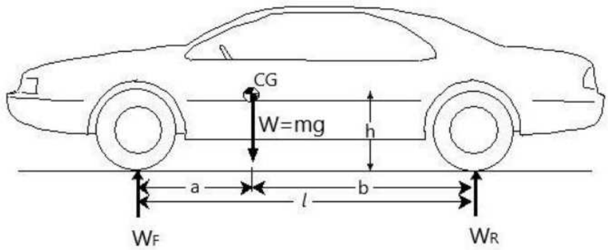

Fig. A.1 Static loads acting on the vehicle

It should be noted that the values just found represent the global static contribution for each axle and to obtain the single contribution of each wheel, right or left, it is necessary to divide these values by two. During braking, a force of inertia directed at the front arises, which involves a forward variation of the load (the front becomes heavier and the rear becomes lighter); in more precise terms, there is an increase of the vertical load on the front axle and a corresponding decrease on the rear one; clearly, the exact opposite happens in acceleration; these vertical forces variations are called longitudinal load transfer.

Longitudinal load transfers can be evaluated using the following formula:

$$\Delta F_{z_{Long}} = \frac{mha_x}{l} \tag{A.3}$$

where h is the CoG height and l is the wheelbase. Therefore, the longitudinal load transfer linearly depends on the longitudinal acceleration and is greater the smaller the wheelbase and the greater the height of the center of gravity from the ground.

When the velocity vector is varied, not in the module as before but in the direction, lateral friction forces, acting at the tire-road contact point, and an inertia force, acting in the center of gravity of the vehicle, are generated. These forces are overall in equilibrium with each other, but the moment they involve, due to the distance between the application points of the forces, is not in equilibrium. The presence of this moment means that the overall load acting on the tires, which does not change, must be transferred from one side of the vehicle to the other to balance this moment and ensure that the balance is respected; in particular, the external tires are subject to an increase in load, vice-versa the external ones. Therefore, in addition to longitudinal load transfers, lateral ones have to be introduced. Lateral load transfers are related to lateral acceleration and they can be split into two contributions, the first linked to structural components (suspension control arms), the second linked to elastic elements (springs and torsion bars). For lateral equilibrium equations [3], it results:

$$\Delta F_{z_{Lat-F-Struct}} = (ma_y b + N)\left(\frac{d_F}{l}\right)\left(\frac{1}{t_F}\right) \tag{A.4}$$

$$\Delta F_{z_{Lat-R-Struct}} = (ma_y a - N)\left(\frac{d_R}{l}\right)\left(\frac{1}{t_R}\right) \tag{A.5}$$

$$\Delta F_{z_{Lat-F-Spring}} = \left(\frac{ma_y(h-d)}{t_F}\right)\left(\frac{k_{\Phi F}}{k_{\Phi F}+k_{\Phi F}}\right) \tag{A.6}$$

$$\Delta F_{z_{Lat-R-Spring}} = \left(\frac{ma_y(h-d)}{t_R}\right)\left(\frac{k_{\Phi R}}{k_{\Phi F}+k_{\Phi F}}\right) \tag{A.7}$$

where d_F and d_R are the heights of the roll centers, d is the height of the roll axis at the abscissa of the center of gravity, t_F and t_R are the front and rear tracks, $K_{\Phi i}$ is the roll stiffness and N is the yaw torque. Obviously, the global lateral load transfers are given by the sum of the contributions expressed in the equations just written. Furthermore, in addition to static loads and load transfers, when the vehicle is in motion the aerodynamic effects on the vertical loads cannot be neglected. These can be assessed as follows:

$$Aerodown_F = \frac{1}{2}\rho A_v U^2 C_{zF} \tag{A.8}$$

$$Aerodown_R = \frac{1}{2}\rho A_v U^2 C_{zR} \tag{A.9}$$

where ρ is the air density, A_v is the vehicle master section and C_{zi} is the downforce coefficient. Assuming that the aerodynamic forces, longitudinal load transfers and static loads on the individual axles are equally distributed over the two wheels, it is possible to evaluate the overall vertical load as follows:

$$F_{zFL} = \frac{W_F}{2} - \frac{\Delta F_{z_{Long}}}{2} - \Delta F_{z_{Lat-F}} + \frac{Aerodown_F}{2} \tag{A.10}$$

$$F_{zFR} = \frac{W_F}{2} - \frac{\Delta F_{z_{Long}}}{2} + \Delta F_{z_{Lat-F}} + \frac{Aerodown_F}{2} \tag{A.11}$$

$$F_{zRL} = \frac{W_R}{2} - \frac{\Delta F_{z_{Long}}}{2} - \Delta F_{z_{Lat-R}} + \frac{Aerodown_R}{2} \tag{A.12}$$

$$F_{zRR} = \frac{W_R}{2} - \frac{\Delta F_{z_{Long}}}{2} + \Delta F_{z_{Lat-R}} + \frac{Aerodown_R}{2} \tag{A.13}$$

A.2 Lateral Forces Evaluation

In a vehicle integral reference system, axle lateral forces, respecting vehicle lateral dynamic equilibrium, can be calculated by resolving the following equations system:

$$\begin{cases} F_{yF} = (ma_y - F_{yR}) \\ F_{yR} = \frac{ma_y a + J_z \frac{dr}{dt}}{l} \end{cases} \tag{A.14}$$

It can be assumed that in a quite wide range of working conditions, the distribution of axle lateral forces on the two sides is proportional to the same axle vertical forces distribution. So, the lateral forces on each tire are:

$$F_{yFL} = F_{yF}\frac{F_{zFL}}{F_{zFL}+F_{zFR}} \tag{A.15}$$

$$F_{yFR} = F_{yF}\frac{F_{zFR}}{F_{zFL}+F_{zFR}} \tag{A.16}$$

$$F_{yRL} = F_{yR}\frac{F_{zRL}}{F_{zRL}+F_{zRR}} \tag{A.17}$$

$$F_{yRR} = F_{yR}\frac{F_{zRR}}{F_{zRL}+F_{zRR}} \tag{A.18}$$

A.3 Longitudinal Forces Evaluation

Under the same hypotheses, it is possible to consider vehicle longitudinal dynamic equilibrium to estimate longitudinal interaction forces. Differently from lateral forces calculation, wheels inertial effects, aerodynamic drag and tire rolling resistances contributions must be considered. Aerodynamic drag resistance force is expressed by:

$$Aerodrag = \frac{1}{2}\rho A_v U^2 C_x \tag{A.19}$$

Regarding rolling resistance, it is a function of vertical load and wheel speed by means of vehicle characterization data. Furthermore, the wheel rotation inertial resistant contribution, reported on the ground, is:

$$F_{WIR_{ij}} = \frac{I_{w_i}\frac{d\Omega_{ij}}{dt}}{R_{r_i}} \tag{A.20}$$

Given these premises, it is possible to evaluate the longitudinal interaction forces, distinguishing the cases of traction and braking, considering a rear-wheel drive vehicle and observing that it can be assumed, based on the experimental results obtained in the track testing sessions, that in a quite wide range of working conditions the distribution of axle longitudinal forces on the two sides can be considered proportional to the same axle vertical forces distribution, as follows:

- Traction (measured $a_x > 0$)

$$F_{xFL} = F_{RollRes_{FL}} + F_{WIR_{FL}} \tag{A.21}$$

$$F_{xFR} = F_{RollRes_{FR}} + F_{WIR_{FR}} \tag{A.22}$$

$$\begin{aligned} F_{xRL} = {} & F_{RollRes_{RL}} + F_{WIR_{RL}} + (ma_x - Aerodrag + \\ & - F_{RollRes_{FL}} - F_{WIR_{FL}} - F_{RollRes_{FR}} - F_{WIR_{FR}}) \frac{F_{zRL}}{F_{zRL} + F_{zRR}} \end{aligned} \tag{A.23}$$

$$\begin{aligned} F_{xRR} = {} & F_{RollRes_{RR}} + F_{WIR_{RR}} + (ma_x - Aerodrag + \\ & - F_{RollRes_{FL}} - F_{WIR_{FL}} - F_{RollRes_{FR}} - F_{WIR_{FR}}) \frac{F_{zRR}}{F_{zRL} + F_{zRR}} \end{aligned} \tag{A.24}$$

- Braking (measured $a_x < 0$)

$$F_{xFL} = \frac{1}{2}(ma_x - Aerodrag) \frac{F_{zFL} + F_{zFR}}{F_{zFL} + F_{zFR} + F_{zRL} + F_{zRR}} \tag{A.25}$$

$$F_{xFR} = \frac{1}{2}(ma_x - Aerodrag) \frac{F_{zFL} + F_{zFR}}{F_{zFL} + F_{zFR} + F_{zRL} + F_{zRR}} \tag{A.26}$$

$$F_{xRL} = \frac{1}{2}(ma_x - Aerodrag) \frac{F_{zRL} + F_{zRR}}{F_{zFL} + F_{zFR} + F_{zRL} + F_{zRR}} \tag{A.27}$$

$$F_{xRR} = \frac{1}{2}(ma_x - Aerodrag) \frac{F_{zRL} + F_{zRR}}{F_{zFL} + F_{zFR} + F_{zRL} + F_{zRR}} \tag{A.28}$$